Development of Small Peptide Amphiphile Based Supramolecular Hydrogels for Various Potential Applications

by

Nilotpal Singha

Department of Chemistry
Indian Institute of Technology Guwahati
Guwahati, Assam - 781039
India

A Thesis Submitted in Partial Fulfillment of the Requirements for the degree of

Doctor of Philosophy
In
Chemistry

IIT Guwahati, April 2019

Dedicated
To
My Parents

Declaration

I hereby declare that the matter embodied in this thesis is the result of investigations carried out by me in the Department of Chemistry, Indian Institute of Technology Guwahati, India, under the guidance of Dr. Debapratim Das. In keeping with the general practice of reporting scientific observations, due acknowledgments have been made wherever the work described is based on the findings of other investigators.

(Nilotpal Singha)

भारतीय प्रौद्योगिकी संस्थान गुवाहाटी

INDIAN INSTITUTE OF TECHNOLOGY GUWAHATI

Dr. Debapratim Das
Associate Professor
Department of Chemistry
Contact: + 91 361 258 3301
Fax: + 91 361 258 2349
E-mail: ddas@iitg.ac.in

3rd April, 2019

To whom it may concern.

This is to certify that the thesis entitled "**Development of small peptide amphiphile based supramolecular hydrogels for various potential applications**" submitted by Nilotpal Singha (Roll No. 146122001) for the award of Ph.D. degree to IIT Guwahati, is absolutely based on his own research work and that neither this thesis nor any part of it has been submitted for any degree/diploma or any academic award anywhere before.

(Dr. Debapratim Das)

Acknowledgments

This thesis is the last milestone of my journey in acquiring my Ph.D. and has been kept on track which is also governed by the support and encouragement of numerous people including my lab mates, well-wishers, friends, and various institutions. I would like to thank all those people who made this thesis successful and a remarkable experience for me. Also, it is a great opportunity to express my gratitude to all those who contributed in several ways to the victory of this study.

Prior to all, I would like to express my sincere gratefulness to my supervisor Dr. Debapratim Das. This work would not have been accomplished in the absence of his guidance, scholarly inputs, consistent encouragement and unconditional support that I received throughout the research work. I am truly honored and blessed to have been a part of his research team and I fruitfully overcame many obstacles which assisted me to learn a lot from his research expertise. His unflinching courage and conviction always inspire me, and I anticipate to continue further research with his gallant thoughts. He has been by my side always whenever and wherever I needed. He is known for his amicability and positive disposition. Thank you, Sir, for all your immense support, enthusiasm, and dedication.

Besides my supervisor, I would like to give special thanks to my doctoral committee members: Dr. Sunanda Chatterjee, Dr. Debasis Manna, and Dr. Dipankar Srimani for their encouragement, insightful comments, and suggestions.

I am grateful to the collaborators for deploying me their expertise and instinct to my scientific and technical problems: Dr. Antara Dasgupta, Dr. Anindita Ukil (University of Calcutta, India), Dr. Ranajit Ghosh (CMERI, India), Dr. Ananya Debnath (IIT Jodhpur, India).

I would like to thank the Department of Chemistry, IIT Guwahati for availing me the innumerable facilities. Also, I am thankful to IIT Guwahati for financial support.

I would also like to extend huge, warm thanks to my past and present lab mates Dr. Julfikar Hassan Mondal, Dr. Sahnawaz Ahmed, Bapan Pramanik, Payel Dowari, Dr. Subhajit Ghosh, Basab Kanti Das, Dr. Tanur Sinha, Sumit Chowdhuri, Supriya for providing an amusing and fun-filled environment. I am especially grateful to Dr. Julfikar Hassan Mondal and Dr. Sahnawaz Ahmed for their initial guidance, support, and motivation in the lab. My heartfelt thanks to Payel, Bapan, and Basab for their cooperation during the course of my work.

My special acknowledgments go to my friends, Ayan, Rajat, Utsab, Mostakim, Rana, Subas, for their support during my research endeavor. I am indebted to Milan Mahadani for his valuable help with TEM analysis.

I sincerely thank all the research scholars and the technical staffs of the Department of Chemistry for their help and friendship. I would like to express my gratitude to all others who are associated with my work directly or indirectly at IIT Guwahati.

Abstract

The thesis **"Development of small peptide amphiphile based supramolecular hydrogels for various potential applications"** deals with the development of new short peptide amphiphile based hydrogels with the help of different aromatic functional groups.

Chapter 1 is a brief introduction of peptide-based hydrogels with up to date literature review.

Chapter 2 describes the hydrogelation mechanism of a peptide amphiphile (**PA-1**) conjugated to naphthalene diimide (NDI) and its application in both cell imaging as well as intracellular pH sensing.

Chapter 3 deals with another naphthalene diimide (NDI) appended peptide amphiphile (**PA-2**) and its application in sensing the VOC with the help of carbon quantum dots.

Chapter 4 describes the untraditional unique behaviors of a pyrene containing short tri-peptide (**PyKC**) based hydrogel.

Chapter 5 contains the potential application of **PyKC** hydrogel in the protection and retention of enzymes' geometrical conformation and activity respectively from different extreme conditions like denaturants, temperature, acid, and base.

List of Abbreviations

Abbreviations

ADI	Arylene Diimide
NDI	Naphthalene Diimide
NMR	Nuclear Magnetic Resonance
ESI-Ms	Electrospray Ionization Mass Spectrometry
UV-Vis	Ultraviolet–Visible Spectroscopy
FL	Fluorescence
λ_{max}	The wavelength in the absorption spectrum where the absorbance is maximum
MAC	Minimum Aggregation Concentration
MeOH	Methanol
EtOH	Ethanol
ACN	Acetonitrile
DMSO	Dimethyl Sulfoxide
DMF	N,N-Dimethylformamide
THF	Tetrahydrofuran
DIPEA	N,N-Diisopropylethylamine
TEA	Triethylamine
NaOH	Sodium Hydroxide
FESEM	Field Emission Scanning Electron Microscopy
FETEM	Field Emission Transmission Electron Microscopy
AFM	Atomic force microscopy
FTIR	Fourier-transform Infrared Spectroscopy
DLS	Dynamic Light Scattering
ζ	Zeta potential
PBS	Phosphate Buffer
Tris	Tris(hydroxymethyl) aminomethane
CD	Circular Dichroism
ICD	Induced circular Dichroism
PA	Peptide Amphiphile
G'	Storage Modulus
G"	Loss Modulus
MGC	Minimum Gelation Concentration
T_g	Gel Melting Temperature
D_2O	Deuterium Oxide
d_6-DMSO	Deuterated Dimethyl Sulfoxide
nM	Nanomolar

μM	Micromolar
mM	Millimolar
ppm	Parts Per Million
μg/mL	Microgram Per Milliliter
HRTEM	High Resolution Transmission Electron Microscopy
DFT	Density Functional Theory
Phe	Phenylalanine
Trp	Tryptophan
Tyr	Tyrosine
ECM	Extra Cellular Matrix
MTT	3-(4,5-Dimethylthiazol-2-Yl)-2,5-Diphenyltetrazolium Bromide
VOC	Volatile Organic Compound
SMHG	Supramolecular Hydrogel
PHG	Polymeric Hydrogel
CQD	Carbon Quantum Dot
PVA	Polyvinylalcohol
CV-lipase	Lipase from *Chromobacterium viscosum*
CR-lipase	Lipase from *Candida rugosa*
PXRD	Powder X-ray Diffraction
TCEP	Tris(2-carboxyethyl)phosphine hydrochloride
GSH	Glutathione
HPLC	High Performance Liquid Chromatography
I-V	Current-Voltage
MD	Molecular Dynamic
HBTU	Hexafluorophosphate Benzotriazole Tetramethyl Uronium
HOBT	Hydroxybenzotriazole
TFA	Trifluoroacetic acid
Py	1-Pyrenebutyric acid
Wt%	10 mg/mL

Contents

Chapter - 1

Introduction

1.1 Prelude

Often and often, whenever someone starts lecturing about supramolecular chemistry, he/she must have been starting with this phrase- 'Chemistry beyond molecules', a short but very decent definition of the context.[1] Back in 1894, when Emil Fischer had proposed the famous 'Lock and Key' model to explain the enzyme-substrate mechanism, two tenets have come in front- 'molecular recognition' and 'supramolecular function', which afterward are included as a topic of a new subject identified as supramolecular chemistry.[1] While traditional chemistry explains strong covalent irreversible bonding, supramolecular chemistry deals with the weak, reversible noncovalent interactions and intermolecular forces between the molecules in space. In the way of unveiling many biological processes, this subject has gradually drawn the attention of a major part of chemists and biologists. It includes molecular self-assembly, folding, molecular recognition, host-guest chemistry, mechanically-interlocked molecular architectures, and dynamic covalent chemistry. Amongst these supramolecular systems, hydrogels are one sub-section which gained tremendous attention owing to their wide-spread applications.

The present thesis primarily deals with one of the most promising soft-materials, "supramolecular hydrogels" prepared from small peptides. Below is a brief about the hydrogels and the present status of such materials in terms of their preparation, mechanistic details and various applications.

1.2 Hydrogels

The appropriate use of covalent and noncovalent interactions to develop soft-materials, like hydrogels, polymers, foams etc., has become an eminent strategy in material science to construct highly demanding functional materials for a wide variety of applications ranging from biotechnology to electronics.[2]

The process of the development of such soft-materials via covalent or noncovalent interactions among the constituent molecules or building blocks is termed as molecular self-assembly.[3] A variety of molecular building blocks, such as high molecular weight natural or synthetic polymers (polyethylene glycol), and biopolymers (proteins[4], polysaccharides[5], hyaluronic acid, collagen, fibrin) has been the center of interest for this purpose for a long period of time. However, over the last few decades, due to their biocompatibility, biodegradability, and biofunctionality with a variety of applications[6], small molecular weight and especially the peptide-based hydrogels have emerged as one of the most promising soft-materials in this field. A hydrogel can be precisely defined as a

three-dimensional (3D) polymeric cross-linked hydrophilic network that is able to absorb a large amount of water while maintaining a semisolid (viscoelastic) state.[7-9] The applications of hydrogel include tissue engineering (where hydrogels are used as 3D scaffolds to support the growth of cultured cells, mimicking extracellular matrix),[10] controlled drug delivery (where hydrogel matrices are used as a reservoir as well as regulator of drugs to release in a sustained manner),[11-13] wound healing,[14-15] cartilage repairing,[16] bio-printing,[17] bio-mineralisation,[18] contact lenses,[10] template for nanofabrication[19] etc. However, the main challenge in supramolecular chemistry is to construct the well-defined architectures with tuneable properties to cover such a wide range of applications. Hence, to achieve the smart soft-materials, one needs to be accustomed to the rules that govern the molecular assembly of specific monomeric building blocks.

1.2.1 Polymeric hydrogels

Polymeric hydrogels (PHG) are the type of soft-materials which has not only pervaded in the daily life in different form of applications such as soap, shampoo, toothpaste, hair gel, contact lenses etc., and also in many industrial applications, such as oil recovery, pharmaceutical, agriculture, textile, and water treatment.[20] PHGs are a kind of hydrogels which can swell in water and can hold a large amount of it, sometimes more than 400 times its original weight, without dissolution.[21] They are even termed as "superabsorbent polymer hydrogels".[22] Moreover, solvent molecules of these hydrogels remain in dynamic motion with the solvent outside and both solvent and solute can pass through the gel. Polymeric hydrogels are mainly formed by permanent crosslinks between the polymer chains via irreversible covalent bonds such as Michael addition,[23] Schiff base formation,[24-25] photopolymerization of thiol and terminal alkenes,[26] free-radical chain-growth photopolymerization,[27] enzyme-catalyzed reactions[28-29] and 1,3 dipolar cycloaddition between azides and alkynes etc.[30] Moreover, these chemical crosslinks can be fine-tuned to change the mechanical strength in order to obtain tough and stable hydrogels. A few important molecules that have so far been used as monomers to prepare PHGs with great applications are Hydroxyethyl methacrylate (HEMA) and its derivatives like Hydroxyethoxyethyl methacrylate (HEEMA), Hydroxy diethoxyethylmeth-acrylate (HDEEMA), Methoxyethyl methacrylate (MEMA), MEEMA, MDEEMA, Ethylene glycol dimethacrylate (EGDMA), N-vinyl 2-pyrrolidone (NVP), N-isopropyl AAm (NIPAAm), Vinyl acetate (VAc), Acrylic acid (AA), N-(2-hydroxypropyl) methacrylamide (HPMA), Ethylene glycol (EG), PEG acrylate (PEGA), PEG methacrylate (PEGMA), PEG diacrylate (PEGDA), PEG dimethacrylate (PEGDMA), cross-linking agent such as epichlorohydrin (ECH), N,N'-Methylene-bis-acrylamide(N,N'-MBAAm)(BIS) and divinyl sulfone (DVS) etc.[22]

1.2.2 Supramolecular hydrogels

Instead of their vast ranging applications from biotechnology to industry, PHGs are failed to show their potential in the biomedical field mainly due to their toughness and the irreversible properties. They are sometimes brittle, opaque and non-biodegradable in nature; moreover, unable to self-heal once the cross-links are broken, thus limiting their applications.[31] On the other hand, supramolecular hydrogels (SMHGs) are of great interest because of their bio-compatibility, bio-degradability, bio-stability and better bio-functionalities (e.g., bio-activity, self-healing ability, shape memory ability)[32] compared to PHGs. Interestingly, individually weak but collectively strong and reversible non-covalent interactions including hydrogen bonding, π–π stacking, metal-ligand coordination, electrostatic and hydrophobic interactions are the driving forces that construct SMHGs.[10] In contrast to PHGs, SMHGs are mechanically weaker but possess the reversible sol-gel transition ability in response to various stimuli, like, change in pH, redox agents, enzymes, bioactive molecules, etc. More importantly, the dynamic nature of physical hydrogels confers them two advantageous inherent properties, 1) shear thinning (viscous flow under shear stress) and 2) self-healing (time-dependent recovery upon relaxation),[33] which makes them a smart carrier of many therapeutic agents (e.g., drugs, proteins, genes) in the human body. On the other hand, their water retention ability and biocompatibility make them suitable for being used as the matrices for tissue regeneration. The building blocks for SMHGs include low molecular weight molecules, e.g., short peptides, peptide amphiphiles, hydrophilic macrocyclic hosts, synthetic molecules tagged with supramolecular motifs, 3G dendrimers etc.[32]

1.2.3 Supramolecular polymeric hydrogels

Instead of covalent cross-linking, the incorporation of specific and dynamic non-covalent reversible stimuli-responsive supramolecular interactions to promote the cross-linking between the polymeric chains pushes the polymeric hydrogels up to much smarter hybrid soft material named supramolecular polymeric hydrogel (SMPHG). The rational covalent attachment of supramolecular motifs to the polymeric chains of PHGs added some extra physicochemical properties like reversibility, biodegradability, and self-healing ability into their inherent strong covalent properties. In recent years, supramolecular polymeric hydrogels have been emerged as one of the most demanding and promising soft materials, hence, become a center of interest for many groups. In most cases, host-guest complexation is used as a non-covalent interaction to make the polymeric cross-links. In this context, α, β, γ– cyclodextrins (**fig. 1.1A-B**) and cucurbit[n]uril (**fig. 1.1C**) are the first choices as macrocyclic hosts, which can accommodate some selected guests depending upon

their nature and cavity size. **Fig. 1.1C** shows the hydrogelation using hosts like free CB[8] functionalized polymers. Mostly, hydrophobic interactions, van der Waals forces, electrostatic interactions, and hydrogen bonding are involved in host-guest complexation. Moreover, other supramolecular driving forces, e.g., hydrogen bonding, metal-ligand complexation, ionic and biomimetic interactions can also be utilized to obtain stimuli-responsive smart physical polymeric hydrogels.[33]

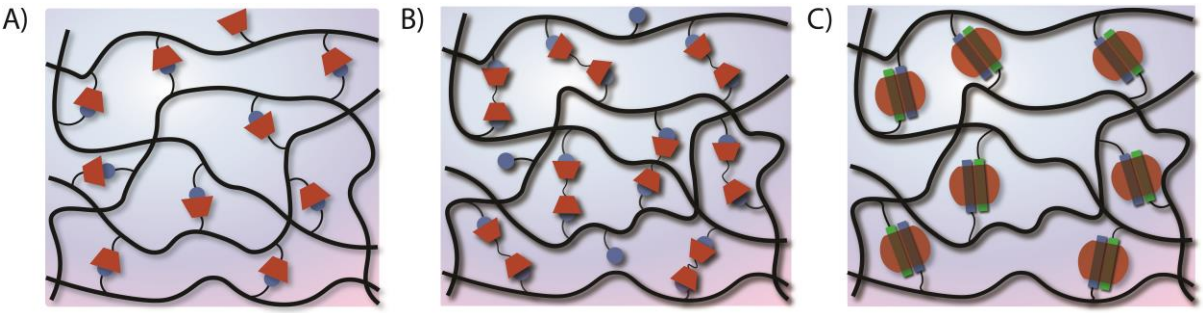

Fig 1.1 Schematic representation of hydrogelation due to Host-Guest complex formation from (A) both CD (host) and guest functionalized polymer, and (B) only CD functionalized polymer. (C) The hydrogelation from guest functionalized polymeric chain that undergoes ternary complexation inside CB[8] to form SMHG.[33]

1.3 Peptide-based hydrogels

Being constructed from natural amino acids peptides are always of great interest and hence, a huge amount of work has been reported so far on peptide self-assembly leading to hydrogel as well. The major portion of supramolecular hydrogels is reported based on *short* or long peptides mainly because of the inherent properties of the amino. Designing a smart peptide with rationally selected amino acids to attain the precise balance in hydrophilicity and hydrophobicity is the only trick that can give rise to such strong self-assembly driven hydrogels.[34] The self-assembly of peptides leading to hydrogelation is a hierarchical process, so-called "Bottom-up" route.[3] In solution, depending on the sequence of peptides, all the supramolecular forces, majorly hydrogen bonding and $\pi-\pi$ stacking can lead to the formation of ordered secondary structures including α–helices, β–sheets, β–hairpins and coiled-coil, which under appropriate physical conditions (or stimuli) self-assemble to form nano-fibers.[10] Elongation of these fibers in 3D space leads to thicker and longer fibers, which eventually entangles into 3D fibrillar network of hydrogel matrix. The understanding of the secondary structures of peptides and their hierarchical self-assembly processes unveiled the possibility to design, synthesize and modulate the properties of self-assembling peptides. Therefore, today hydrogelation from synthetic peptides is not a serendipitous observation anymore.[3]

1.3.1 Hydrogels based on secondary structural motifs

The ongoing biological studies on the structures and functions of proteins have revealed numerous peptide epitopes that could serve as functional motifs for supramolecular hydrogelation.[35] These long oligopeptides composed of minimum 8 to 16 amino acid residues are very much capable of showing conformational flexibility to assist the supramolecular forces in constructing secondary structures. Though most of the oligopeptide hydrogels are reported to be comprised of β-sheets or β–hairpins, nonetheless, there are few reports indicating α-helices can also show higher-order self-assembly to form hydrogels.

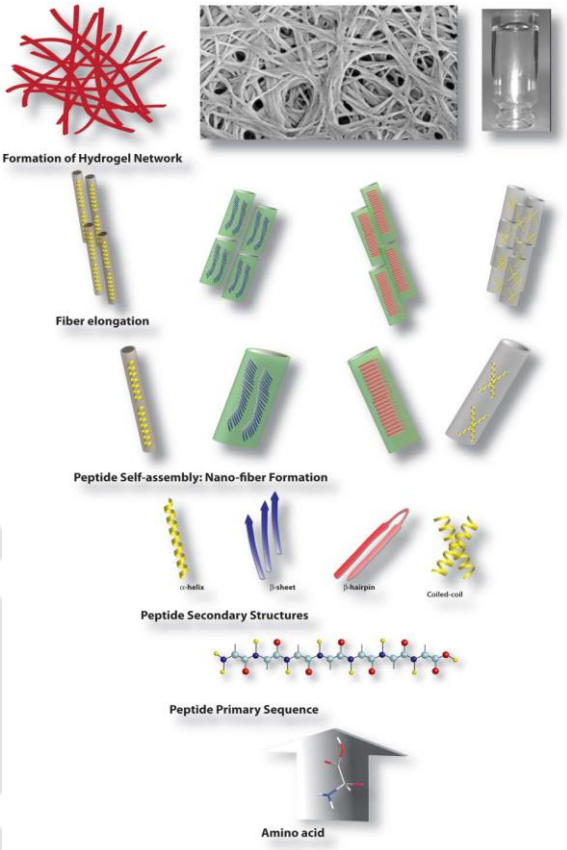

Fig. 1.2 Schematic representation of the "bottom-up" process for the formation of hydrogel, where amino acids and peptide molecules are seated at the bottom and fibers are at the top.[3]

β-sheet forming peptides

The β-sheet (**fig. 1.3a**) is one of the most common and regular secondary structures in proteins. β-the sheet is formed by the intermolecular hydrogen bonding between lateral β-strands. Using at least two or three hydrogen bonds as backbone the β-strands get connected and give rise to twisted, pleated β-sheets. Further aggregation of β-sheets leads to fibers which eventually results in gelation.

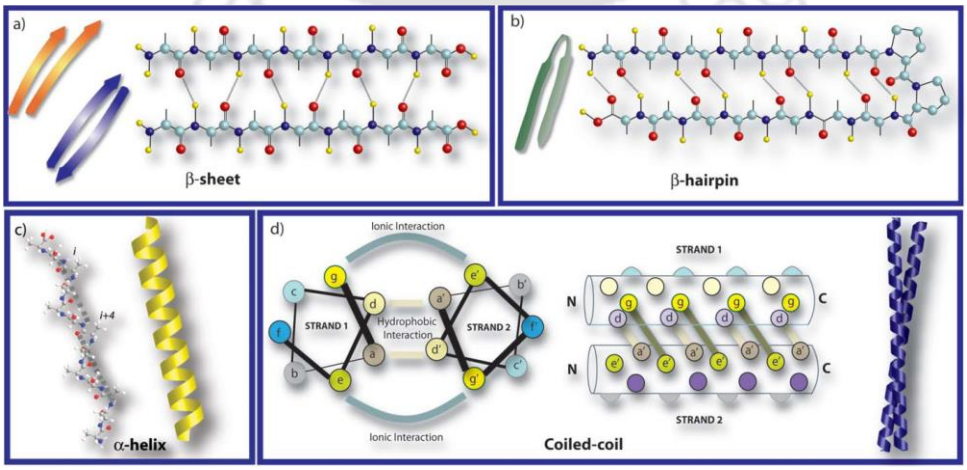

Fig. 1.3 The secondary structures of peptides: (a) β-sheet, (b) β-hairpin, (c) α-helix and (d) coiled-coil.[3]

Many human diseases, particularly Alzheimer's disease in the brain, is nothing but a terrible consequence of β-sheet induced aggregation and fibrillation from so-called Aβ-peptide.[36] To achieve the self-assembled β-sheet tapes Boden and co-workers proposed some conditions. According to their perspective, three criteria should be fulfilled: (a) attractive forces, like, hydrophobic, electrostatic, hydrogen-bonding between side chains of cross-strands, (b) lateral recognition between adjacent β-strands to drag their self-assembly to one dimension and avoid heterogeneous aggregation of β-sheet structures, and (c) strong solvent adhesion of the surface of tapes to control solubility.[37] Using these assumptions they have initially reported two peptides **1.1** and **1.2** (**fig.1.4**), which form a hydrogel in water. They have also achieved the hydrogel constructed of antiparallel β-sheets from the peptides **1.3** and **1.5** at low pH whereas, **1.4** and **1.6** at higher pH.[38] A series (**1.7-1.10**) of amphiphilic and acidic β-sheet forming peptides (AAβPs) has been prepared by Rapaport *et al.* (**fig. 1.4**) at near neutral pH.[39] Zhang *et al. have* synthesized a series (**1.11-1.16**) of β-sheet forming amphiphilic peptides (**fig. 1.4**), which are discussed in detail in the section 1.3.3.1.[40-42]

Peptide	*Primary Structure*	*Label*
P_{11}- I	CH_3CO-QQRQQQQQQQ-NH_2	1.1
P_{11}- II	CH_3CO-QQRFQWQFEQQ-NH_2	1.2
P_{11}- 4	CH_3CO-QQRFEWEFEQQ-NH_2	1.3
P_{11}- 8	CH_3CO-QQRF$\overset{*}{O}$WOFEQQ-NH_2	1.4
P_{11}- 9	CH_3CO-SSRFEWEFESS-NH_2	1.5
P_{11}- 12	CH_3CO-SSRFOWOFESS-NH_2	1.6
P_{LD}- 5	Pro-Asp-$(Leu\text{-}Asp)_5$-Pro	1.7
P_{LE}- 5	Pro-Glu-$(Leu\text{-}Glu)_5$-Pro	1.8
P_{FD}- 5	Pro-Asp-$(Phe\text{-}Asp)_5$-Pro	1.9
P_{FE}- 5	Pro-Glu-$(Phe\text{-}Glu)_5$-Pro	1.10
EAK8	H_2N-AEAEAKAK-COOH	1.11
EAK12	CH_3CO-AEAEAKAKAEAE-$CONH_2$	1.12
EAK16	CH_3CO-AEAEAKAKAEAEAKAK-$CONH_2$	1.13
KLD12	CH_3CO-KLDLKLDLKLDL-$CONH_2$	1.14
RADA16-I	CH_3CO-RADARADARADARADA-$CONH_2$	1.15
RADA16-II	CH_3CO-RARADADARARADADA-$CONH_2$	1.16

$\overset{*}{O}$ = Ornithine

Fig. 1.4 Sequences of some β-sheet forming peptides.

β-hairpin forming peptides

Another common secondary structure of proteins is β-hairpin (**fig. 1.3b**), which is found to be shaped like a hairpin formed from a series of hydrogen bonds between two β-strands.[3] The first report on hydrogelation from a series of β-hairpin-forming peptides is delivered by Schneider *et al.* [43-52] (**fig. 1.5**).

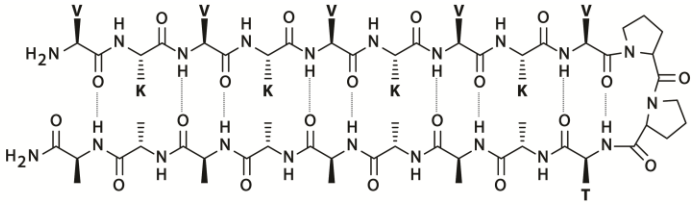

Peptide	*Sequence*	*Label*
MAX1	VKVKVKVKV^{D}*P*PTKV**K**VKVKV-NH_2	1.17
DMAX1	VKVKVKVKV^{L}*P*PTKV**K**VKVKV-NH_2	1.18
K15Q	VKVKVKVKV^{D}*P*PTKV**Q**VKVKV-NH_2	1.19
K15T	VKVKVKVKV^{D}*P*PTKV**T**VKVKV-NH_2	1.20
K15E	VKVKVKVKV^{D}*P*PTKV**E**VKVKV-NH_2	1.21
MAX2	VKVKVKVKV^{D}*P*PTKVK**T**KVKV-NH_2	1.22
MAX3	VKVKVK**T**KV^{D}*P*PTKVK**T**KVKV-NH_2	1.23
MAX6	VKVKVKVKV^{D}*P*PTKVK**E**KVKV-NH_2	1.24
MAX7	VKVKVKVKV^{D}*P*PTKVK**C**KVKV-NH_2	1.25
MAX8	VKVKVKVKV^{D}*P*PTKV**E**VKVKV-NH_2	1.26
SPP1	VKVKV^{D}*P*PTKVKVKVKVKVKV-NH_2	1.27
SPP2	VKVKVKV^{D}*P*PTKVKVKVKVKV-NH_2	1.28
SPP3	VKVKVKVKVKV^{D}*P*PTKVKVKV-NH_2	1.29

Fig. 1.5 Sequences of some β-hairpin forming peptide amphiphiles.[43-52]

Using two β-strands constructed of alternative hydrophilic and hydrophobic amino acids, and a central tetra-peptide (-**VDPPT**-) with type II′ β-turn propensity this group has furnished the β-hairpin structure (**fig. 1.5**). Hence, to achieve a β-hairpin structure one should design a β-turn which is flanked by two β-strands. However, these peptides are fully soluble and attain random coil conformation in solution phase. Although an external stimulus initiates the intramolecular folding of the peptide to a β-hairpin conformation which undergoes rapid self-assembly forming a highly cross-linked β-sheet-rich hydrogel.[3] Following the same strategy and structural motif, they have constructed several β-hairpin containing hydrogels.

α-helix forming peptides

The α-helix is a key building block of protein structures.[3] The α-helix is formed by winding the polypeptide backbone into a right-handed helix with a periodicity of 3.6 amino acids per turn, and it is stabilized by internal backbone hydrogen bonding between the carbonyl oxygen atoms of residues 'i' with the amide hydrogen of residues four along the chain, (i+4) (**fig. 1.3c**). For simplicity, Woolfson *et al.* have shown the *heptad* rule to design the α-helix peptides, and it says that the incorporation of nonpolar residues at positions ***a*** and ***d*** of a linear *heptad* repeat peptide $(abcdefg)_n$ places their side-chains along one face of a helix and drives the formation of helical assemblies.[53] Unlike β-structures, the hydrogen-bonding associated with α-helices are intramolecular in nature and α-helices can be treated more as discrete building blocks. There are only a few examples were rationally designed peptide hydrogelators have been reported in which the self-assembly is generated from α-helical structures.[54-55] However, more specifically, hydrogels are achieved when two or three α-helices co-assemble to form coiled-coil structures (**fig. 1.3d**), which is a very common phenomenon in native proteins.

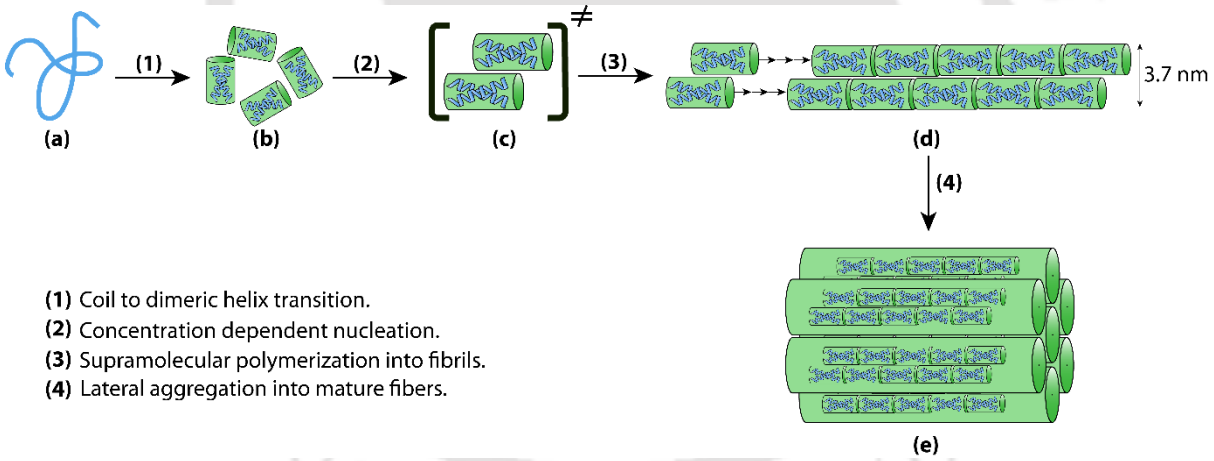

Fig. 1.6 Mechanism of the formation of the coiled-coil structure followed by fibrillation.

1.3.2 Short peptide-based hydrogels

The exploration of oligopeptides in self-assembly to form hydrogels in water opened a new area of interest to the same field, which is di/tri-peptide based hydrogels. Since the first ever example has come out a century ago by Gortner and Hoffman from a dibenzoyl cystine moiety (**1.30**), [56] this field has remained as a special topic till now. Most notably, the N-terminally protected phenylalanine or tyrosine moieties are found to be efficient as well as mostly studied hydrogelators in the last two decades. The simple conjugation of aromatic moieties (fluorenyl, naphthyl or pyrenyl) to the N-

terminal of amino acids by amide bond can deliver the essential supramolecular interactions required in self-assembly to end with a hydrogel.

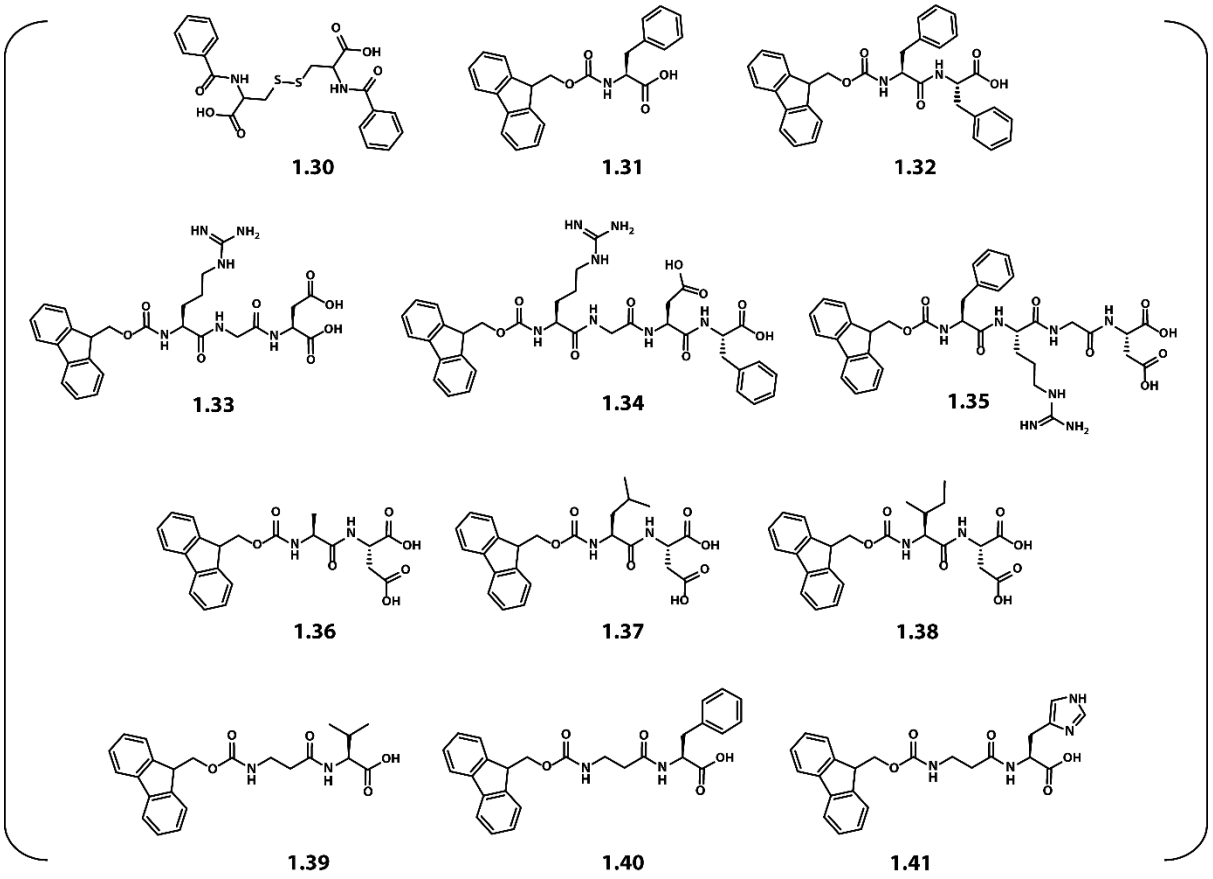

Fig. 1.7 Fmoc protected short peptide hydrogelators.

The pioneer of this field, Bing Xu and co-workers were the first to demonstrate the hydrogelation from Fmoc protected single phenylalanine/tyrosine.[57-59] Further, Nillson group and Gazit *et al.* had carried on studying the hydrogelation of Fmoc-Phe (**1.31**) and its analogs. Especially, the latter group has done some advanced studies on the self-assembly of Fmoc-FF (**1.32**), which showed tubular and amyloid-like structures. Being taken from the Aβ-peptide sequence this di-peptide has been explored a lot due to its fascinating characteristics. Even the mechanical strength of the gel from this peptide exceeded the strength from longer oligopeptides. Conjugating 'Fmoc' group to the N-terminal of a cell penetrating peptide motif Arg-Gly-Asp (RGD) the same group has reported hydrogelation from molecules **1.33**, **1.34** and **1.35** (**fig 1.9**).[60] Apart from Phe or Tyr moieties, hydrogelations from Fmoc-Leu-Asp (**1.37**) and its analogs Fmoc-Ala-Asp (**1.36**), Fmoc-Ile-Asp (**1.38**) has also been reported by Janmey *et al.*[61] Later on, many groups have started focussing on designing and synthesizing non-peptide molecules that mimic the structure and functions of peptides to restrict the proteolysis.[62] In the investigation of such a non-peptide molecule, Xu *et al.* have found

β-Alanine as a suitable one for the job.[63] Further, using Fmoc in the N-terminal of the 'β-alanine' Banerjee *et al.* have developed two hydrogelators, Fmoc-βAla-Val-OH (**1.39**) and Fmoc-βAla-Phe-OH (**1.40**), which form transparent, stable, self-supporting hydrogels at physiological pH.[64] Few examples of Fmoc-protected peptide hydrogel are shown in **fig. 1.7**.

Though Fmoc-peptides were effective for hydrogelation, the inherent cytotoxicity of the Fmoc group limits their application in the biomedical field. As suitable alternatives for Fmoc as π-stacking group, 2-(naphthalene-2-yloxy)acetic acid, 2-(naphthalene-2-yl)acetic acid and 2-naphthoic acid were selected and used at the N-terminal of a series (**1.42-1.44**) of peptides developed by Xu *et al.* to form hydrogels with more efficiency as well as more bio-compatibility (**fig. 1.8**).[65]

A significant amount of work has also been carried out with Boc-protected di-peptide based hydrogels. Banerjee *et al.* have first reported a series of peptides containing N-Boc-Leu-Phe (**1.45**), N-Boc-Phe-Leu (**1.46**), N-Boc-Leu-Leu (**1.47**), which form thermoreversible pH-sensitive hydrogels showing nanofibrillar network with antiparallel β-sheet structure.[66] Some examples of naphthalene and Boc protected peptide hydrogels are shown in **fig 1.8**.

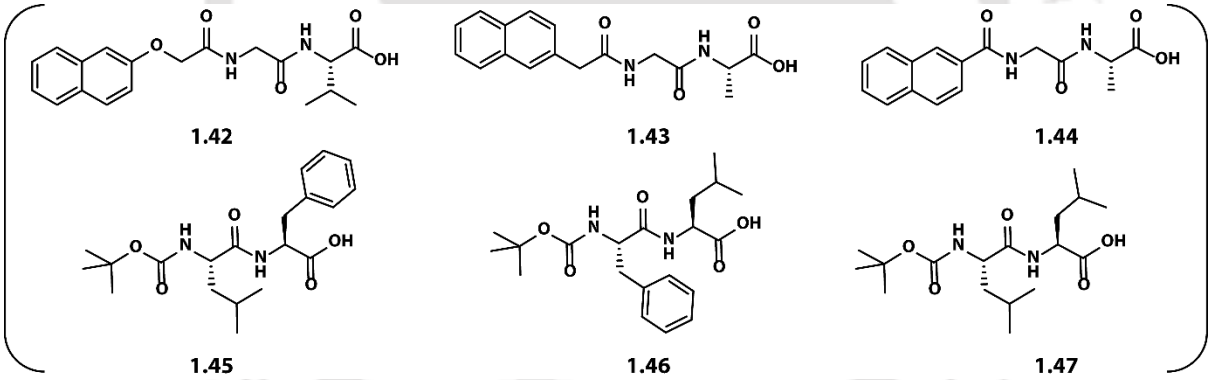

Fig. 1.8 Naphthyl and Boc protected short peptide hydrogelators.

1.3.3 Peptide amphiphile based hydrogels

Peptide amphiphiles (PAs) are always being one of the fascinating classes of molecules that too self-assemble, leading to the formation of highly demanding nano-structures. Nano-structures including fibrils, nanotubes, micelles, and vesicles are of great importance when it comes to the applications in biotechnology and bio-medical engineering.[67] The typical PAs are constructed of two different kinds of blocks: 1) a hydrophilic peptide segment and 2) an optional hydrophobic segment (alkyl chain, lipid, polymer or polypeptide).[68] PAs can also be made of an alternating hydrophilic and hydrophobic amino acids, which ultimately turns into a β-sheet forming motif. The PAs are

categorized into two major categories: 1) amphiphilic peptides, made of only amino acids and 2) lipidated peptide amphiphiles.

1.3.3.1 Amphiphilic peptides (PAs)

These type of PAs are comprised of amino acids only, where both the hydrophilic and hydrophobic domains are present. These domains can be arranged in different ways, either alternatively or as a di-block (where one of the two blocks contains a series of nonpolar and the other one contains a series of polar amino acids).[3] As mentioned earlier in section 1.3.1, Schneider et al. reported a series of amphiphilic peptides of the first type where a 20 residue peptide sequence of alternating Val-Lys repeats (**fig. 1.5**) resulted in β-hairpin structures.[38-47] At basic pH, the exterior face of the peptide is lined with hydrophilic lysine while the interior face is lined with hydrophobic valine, which provides stability to the β-hairpin leading to the self-assembly to form a hydrogel. Zhang introduced a concept based on ionic self-complementary peptides where he mentioned about several moduli (I, II, III, and IV) depending on the alternation of charges.[69] For example, in case of modulus I, the (+) positively- and (-) negatively-charged amino acid residues are alternated by one (+ - + - + - + - and - + - + - + in the complementary peptide). Consecutively, for modulus II, III, IV etc., charges are alternated by two, three, four etc. (++--++--, +++---and +++++----etc.). The peptides designed in these fashions are mostly the self-assembling β-sheet forming motifs, which undergo a spontaneous association to organize well-ordered nano-fibers. **K**L**D**L**K**L**D**L**K**L**D**L (**1.14**, KLD12-I)[41] and Ac-**R**A**D**A**R**A**D**A**R**A**D**A-$CONH_2$ (**1.15**, RADA16-I)[42] is the well-known examples of modulus I type. Two such examples of 16 amino acid peptides, which fall under modulus II are A**R**A**R**A**D**A**D**A**R**A**R**A**D**A**D** (**1.16**, RAD16-II,) and **E**A**E**A**K**A**K**A**E**A**E**A**K**A**K**A (**1.13**, EAK16-II).[40] The second type of amphiphilic peptides are developed in a di- or tri-block fashion where a hydrophobic amino acid stretch is connected to a hydrophilic domain to build up a new type of PA. A few examples of di-block polypeptides that undergo self-assembly to hydrogelation are K_xL_y (**1.48**), K_xV_y (**1.49**), E_xL_y (**1.50**) (K=Lysine, L=Leucine, V=Valine, E=Glutamate).[70] Interestingly, these hydrogels are enzymatically degradable, injectable and stable both in presence and absence of ionic species.

1.3.3.2 Lipidated peptide amphiphiles (LPAs)

Connecting a hydrophobic tail to a hydrophilic peptide residue of different functional domains introduces important hydrophobic interaction to the peptide, which facilitates in self-organization of the molecule. A lipidated peptide amphiphile behaves more like a surfactant which first self-assembles to micelles or bilayer structures in aqueous systems at a particular concentration. Further

increase in the concentration leads to nanofibers or tube formation, which leads to the formation of a hydrogel by 3D entanglement.[3] Stupp and co-workers, one of the pioneers of this field, has first shown the way to design a lipidated PA (LPA **1.51, fig. 1.9**) which is comprised of five regions.[18] The different functionalities of those five regions are described in table 1.1.

Table 1.1. Different regions and the functions of LPA **1.51**.

Regions	***Functions***
Region 1	The alkyl chain brings hydrophobic interaction.
Region 2	The thiol groups are prone to dimerize itself by oxidation to induce polymerization.
Region 3	Glycine units provide flexibility.
Region 4	Phosphorylated serine unit binds to Ca^{2+} to mineralize.
Region 5	-RGD segment is well-known as cell adhesive ligand.

In a similar fashion, Hartgerink *et al.* demonstrated a three domain lipidated PA (LPA **1.52, fig. 1.9**). Keeping both the alkyl chain and cell adhesive ligand (-**RGDS**) almost unchanged they have modified the central domain by introducing **GTAGLIGQ,** a matrix metalloprotease (MMP) cleavable sequence.[71] The PA initially self-assembles into small aggregates under neutral pH, and the addition of calcium ions converts these into extremely long cylindrical micelles leading to hydrogelation. Another lipidated PA (**1.53, fig. 1.9**) composed of both the cell-binding **GRGDSP** domain and the synergistic **PHSRN** domain has been reported by the Kokkoli group.[72] Using diacetylene group in the lipid part Stupp *et al.* showed the hydrogelation of **1.54** (**fig. 1.9**) under UV light (254 nm).[73]The PA self-assembles into nanofibers in aqueous medium and form hydrogels at a concentration of 6 mM or higher. Apart from long peptide sequences, short positively charged amino acid-based lipidated PAs are also reported. Das *et al.* have established tryptophan based amphiphile (**1.56**, **fig. 1.10**) to form a hydrogel.[74] Further, the same group has extended their work to di-peptide based hydrogelators by adding proline or phenylalanine with the tryptophan along with the C-16 alkyl chain (**1.57-1.60**).[3]

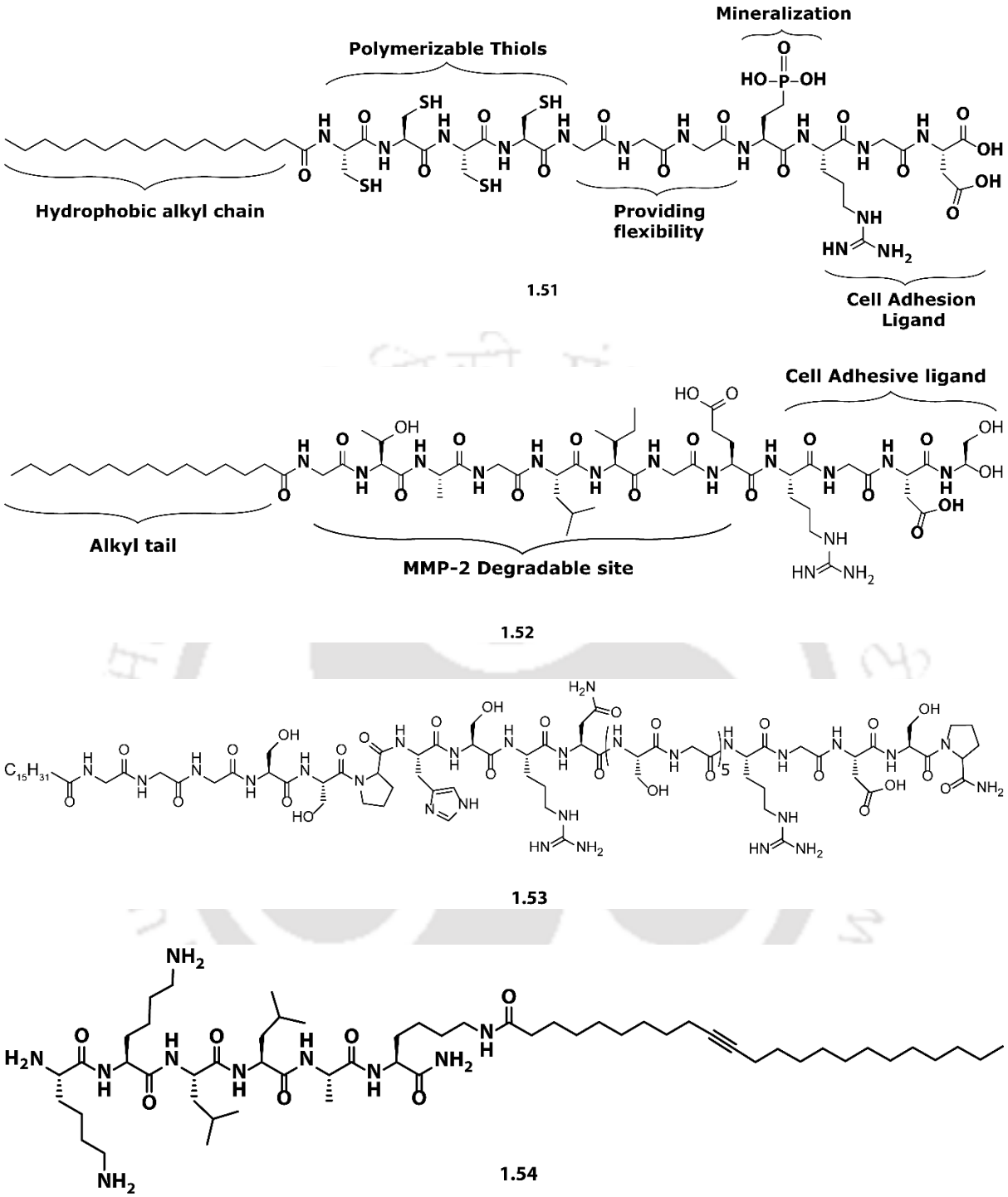

Fig. 1.9 Chemical structures of some lipidated peptide amphiphiles.

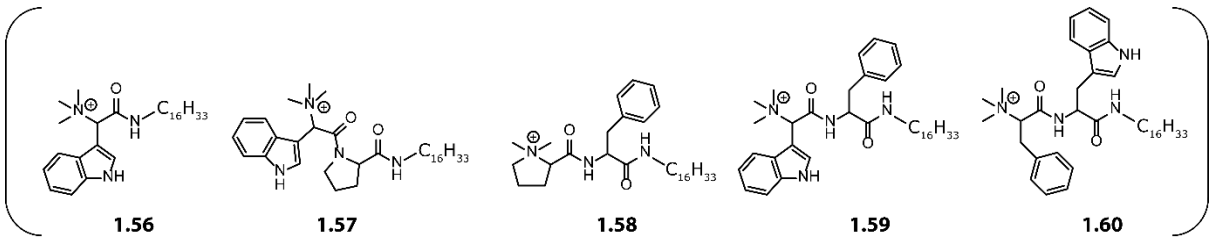

Fig. 1.10 Tryptophan based lipidated peptide hydrogels.

1.3.4 Peptide amphiphiles with different substitutions

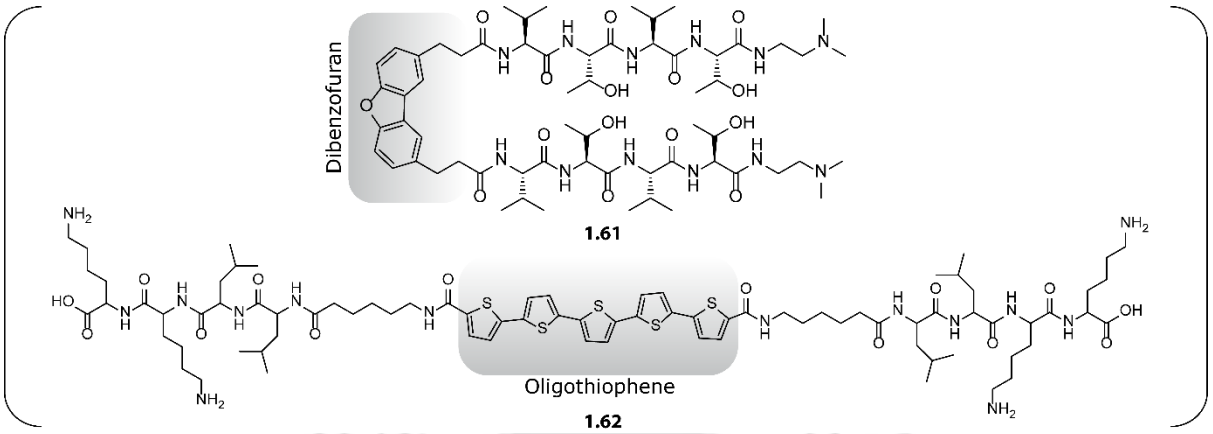

Fig. 1.11 Bolaamphiphilic peptide hydrogelators conjugated with unnatural aromatic functional moieties.

However, the possibility to incorporate non-natural amino acids or aromatic/non-aromatic functional moieties at any position of a peptide sequence is particularly valuable for the introduction of an increased level of functionality in the assemblies.[75] In recent years, organic self-assembled nano-materials have been well developed for various applications of supramolecular hydrogels. Though there are a lot of reports regarding various non-traditional functional material conjugated peptide hydrogels, a few have been identified as peptide amphiphile. Some of those functional moieties are dibenzofuran, oligothiophene, naphthalene diimide.[35] Interestingly, all of them are aromatic in nature and so can be a good candidate to replace aromatic amino acids like Phe or Trp or Tyr. Besides, both oligothiophene and naphthalene diimide are semiconducting in nature, hence highly demanding in organic electronic devices like photovoltaic cells. **Fig. 1.11** shows the examples of bolaamphiphiles (**1.61, 1.62**), where two hydrophilic peptide segments are connected through the hydrophobic as well as aromatic π-conjugating functional moieties leading to the formation of β-sheet structure, which eventually gives rise to hydrogelation in water at low concentrations. Following Stupp's work on oligothiophenes, some other groups started investigating on NDI-peptide based hydrogels (**fig. 1.12**). Parquette et al. have found that Fmoc-KK(NDI) (**1.46**) can self-assemble to hydrogelation.[76] Further, Ulijn et al. have reported hydrogelation of NDI-Y (**1.47**) and NDI-YF-NH_2 (**1.48**) in Phosphate buffer.[77] Lin et al. have reported the nano-fibrillar hydrogelation from NDI-FF (**1.49**), NDI-FG (**1.50**), NDI-GG (**1.51**) and NDI-GF (**1.52**) under acidic condition,[78] similarly, NDI-Lys (**1.53**), NDI-Glu (**1.54**) and NDI-Ser (**1.55**) are also able to produce the same at different pHs.[79] In each of these peptide amphiphiles, one end of the NDI moieties is functionalized by a C8 alkyl chain.

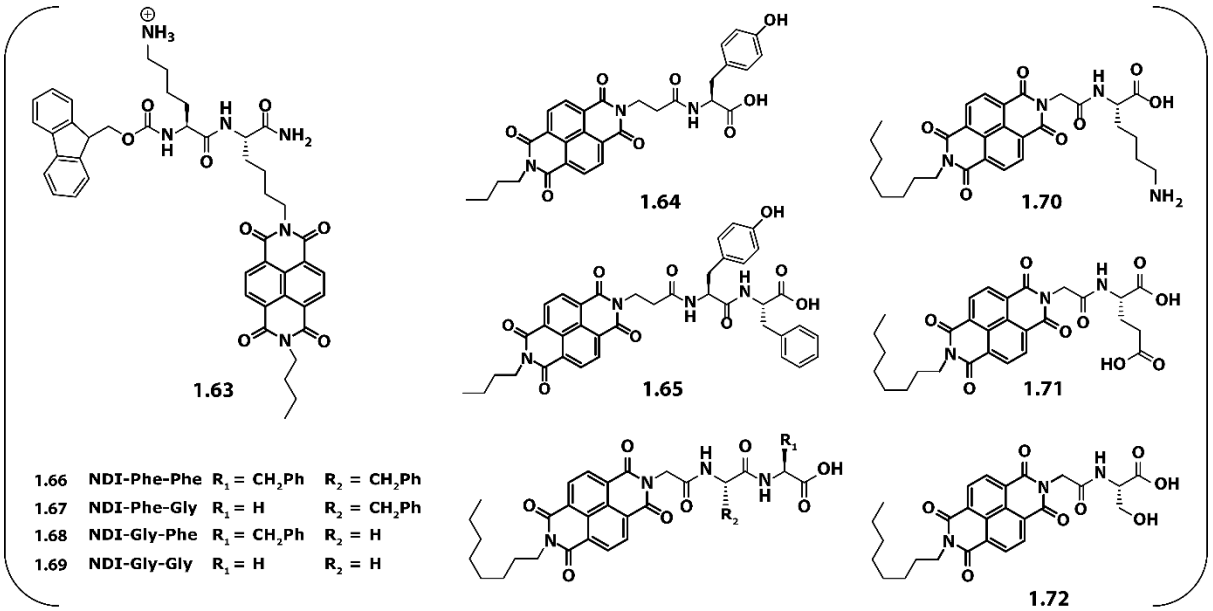

Fig. 1.12 Naphthalene diimide (NDI) based peptide hydrogelators.

1.4 Applications of PA hydrogels

Undoubtedly, hydrogels are being utilized by mankind in many ways starting from home to industry. The gelators can be rationally designed and modified to get a smart functional soft-material. Hence, developing a functional material out of peptides is no more a difficult job nowadays. The PAs, due to their lipidated nature, can easily penetrate or even rupture the cell membrane of particular interest. Hence, focus on PA, few important applications are discussed in this report.

1.4.1 Tissue Scaffolds

Hardly a man can be found unknown of the fact that each and every part of a human body is made of soft tissues in natural, which are artificially resembled with the hydrogels, particularly peptide-based hydrogels.[35] Therefore, peptide hydrogels, because of their large water content and fibrous protein like morphology, are considered as the best tissue scaffold or extracellular matrix (ECM) mimicking material in the field of Bio-engineering. ECM, which is made of proteoglycans, water, minerals, and fibrous proteins, not only provides the structural support to the cells embedded within a tissue but also guides their proliferation. Hence, using peptide-based hydrogels as the scaffold for tissue, 3D cell culture has drawn massive attention in the last few years.

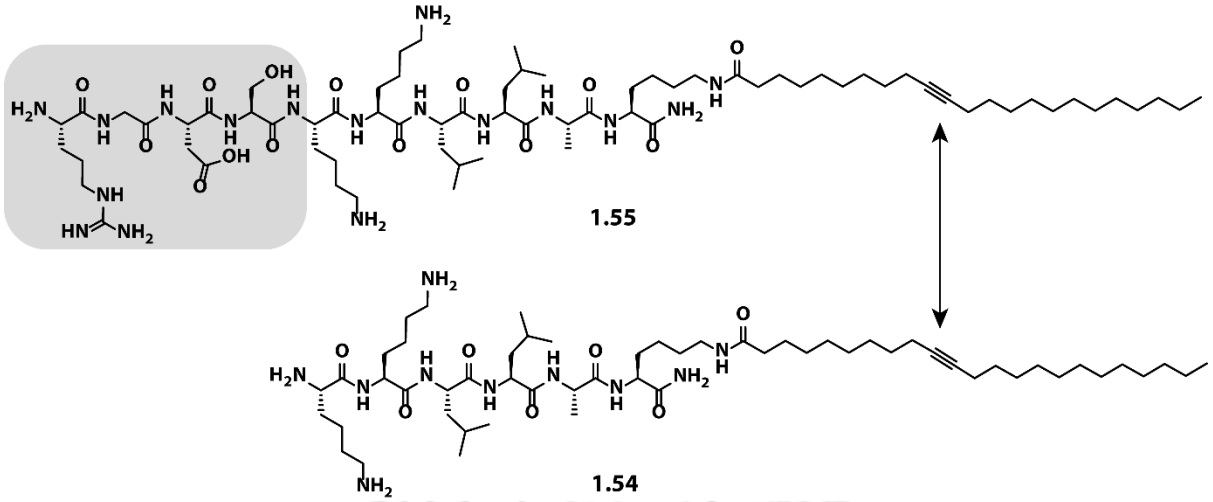

Fig. 1.13 The mixture of these two lipidated peptide amphiphiles acts as ECM.

In this regard, a short tri-peptide sequence derived from fibronectin, which is attached to most of the successful ECM mimicking hydrogels is Arg-Gly-Asp (RGD), the so-called cell adhesive ligand.[36] For example, a simple peptide hydrogelator, Fmoc-RGD, has displayed excellent performance in 3D cell culture.[80] Stupp and co-workers have shown some exciting results by designing a few lipidated peptide amphiphiles using this sequence. For example, hydrogels from molecule **1.51** and a 4:1 mixture of **1.55/1.54** molecules showed some promising applications as ECM.[74] Moreover, the hydrogels from the β-hairpin and β-sheet PAs reported by Schneider (**fig. 1.5**) and Zhang et al. (**1.14, 1.15, 1.16, fig. 1.4**) respectively are also demonstrated as potential scaffolds for tissue engineering.

1.4.2 Drug-Delivery vehicles

Owing to the biocompatibility, non-cytoxicity and porous fibrillar network of the peptide-based hydrogels they can encapsulate bio-macromolecules, including proteins, DNA and hydrophilic or hydrophobic drugs. Therefore, they are the efficient candidates for drug loading, targeted drug delivery and controlled drug release, which collectively make them the perfect drug-delivery vehicles. These systems can be applied into bodies in different ways, e.g., oral, ocular, rectal, epidermal and subcutaneous injection. Thus, the injectability of a semi-solid hydrogel, which means the transition from gel to sol upon applying sufficient stress and the vice versa upon releasing the stress, can be considered as one of the important properties of peptide-based hydrogels.[3] In this regard, the contribution of PA nano-structures is quite extraordinary. For example, the β-hairpin-forming PAs (**1.19** and **1.23, fig. 1.5**), reported by Schneider et al., showed direct encapsulation and control release of FITC-dextran macromolecule.[81] Moreover, the hydrogel from PA **1.23**, by showing local delivery of curcumin, became an excellent drug vehicle. Later on, Zhang et al. have found the β-sheet forming PA hydrogel Ac-$(RADA)_4$-$CONH_2$ (RADA16-I), which is able to encapsulate as well as

release a variety of proteins (e.g., lysozyme, trypsin inhibitor, BSA, and immunoglobulin G) in a controlled way with much efficiency.[11] Zhang and Jiang et al. reported a transparent hydrogel from Fmoc-FFRGDF sequence, which acted as an implanted carrier, delivers an antiproliferative model drug (5-fluorouracil, 5-FU) in rabbit eyes and inhibits postoperative scarring formation.[82] Saiani et al. showed the hydrogelation from an antiparallel β-sheet forming octapeptide, FEFEFKFK, which was further used to deliver of two commercial drugs, lidocaine, and flurbiprofen.[83]

1.4.3 Antimicrobial hydrogels

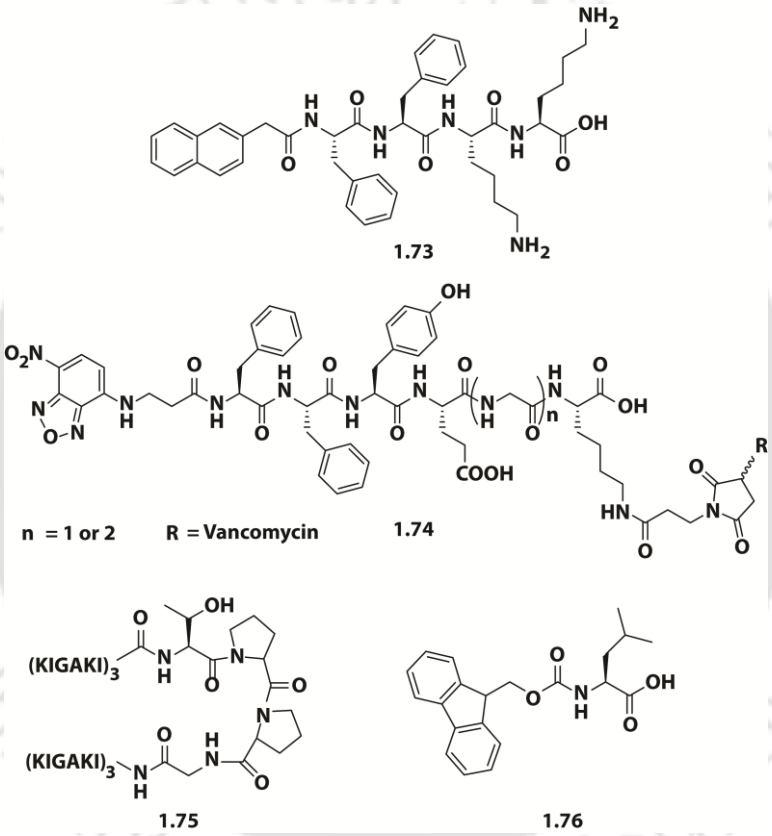

Fig. 1.14 Examples of antimicrobial peptides.

Antimicrobial agents always need to be upgraded with time to fight against the smart multi-drug-resistant bacteria causing infectious diseases. Hence, the demand for novel antimicrobial peptides and that driven hydrogels is no less than antimicrobial agents available in the market. To this end, few peptide amphiphiles have shown some promising results.[35] Those PAs, having the property of killing either or both Gram-positive and Gram-negative bacteria, are allowed to self-assemble to form an antibacterial hydrogel on purpose of some practical applications. For example, PA **1.17** (MAX1, **fig. 1.5**), which is introduced by Schneider *et al.* as one of the *β*-sheet peptide-based

hydrogels, also exhibits antimicrobial activity against both Gram-positive (*Staphylococcus epidermidis, Staphylococcus aureus, and Streptococcus pyrogenes*) and Gram-negative bacteria (*E. coli and Klebsiella pneumonia*) without incorporating exogenous antimicrobial agents.[84] Laverty *et al.* has produced a hydrogel from **1.73** (**fig. 1.14**), which is able to show 94% damage of *S. epidermidis* along with a little hemolytic side effect.[85] Yang and Wang *et al.* synthesized FF or FFY based peptides conjugated with vancomycin (**1.74**) and showed their antibacterial property.[86] Zhao *et al.* have designed a peptide, in which, a central tetra-peptide linker is flanked by two Gram-positive antibacterial sequences $(KIGAKI)_3$-NH_2 (**1.75**). The peptide forms hydrogel with β-hairpin conformation and effectively inhibits the *E. coli* proliferation.[87] Further, Chen and Li et al. have found the antimicrobial activity against Gram-positive bacteria by cell-wall and membrane disruption from the coassembly of Fmoc-Phe (**1.31**) and Fmoc-Leu (**1.76**). This type of hydrogel may potentially be used as an antimicrobial coating in clinical devices and wound dressings.[88]

1.4.4 Templates for nanofabrication

Production of nanostructured materials is a fundamental requirement in today's technological advancement. In this regard, molecular self-assembly undoubtedly plays a crucial role.[89-90] The biggest advantage of applying self-assemblies as a template for nano-fabrication is that the self-assembly process can be fine-tuned and consequently nano-materials of different shape and sizes can be prepared from the same material. Peptide-based materials play a superior role in this regard owing to their easily tunable functionality and morphology.[89-90]The nanostructures fabricated from peptides are gaining attention owing to their simple chemical and biological modification and easy availability for bottom-up fabrication.[91] Peptide Self-assemblies can produce various nano-structures like fiber,[40] tubes,[92] tapes,[93] belts,[94] ribbon[95] etc. In the presence of appropriate precursors, these shapes can be used as a template to produce the nano-materials. Various such materials have already been produced using this particular technique. One such example is the formation of hollow single walled silica nanotube from a simple peptide amphiphile based hydrogel (**fig. 1.15**).[96]

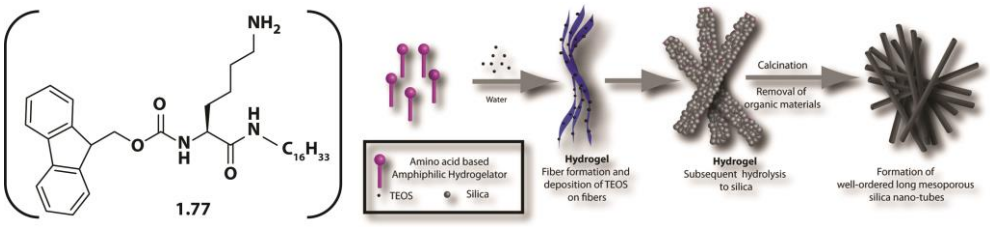

Fig. 1.15 Molecular structure of PA and pictorial representation of the possible mechanism of nanotube formation.

1.4.5 Cell-Imaging

Nowadays cell-imaging is an inevitable technique for the diagnosis of internal diseases and various therapeutic procedures. Though radiolabelled small molecules or macromolecules are initially utilized as a probe for such purposes, because of their low specificity or limited target permeability, those are mostly failed to keep the success.[97] The ideal probes are expected to have high affinity, high specificity, as well as long retention to the binding site along with the biocompatibility. In the quest for such probes, the small peptides have come out as a promising material fulfilling all requirements. The synthesis of peptide probes is also very straight forward- it only requires the attachment of a fluorophore to the peptide chain. Bing Xu has reported a peptide probe for imaging the cancer cell (HeLa), using 4-nitro-2,1,3-benzoxadiazole (NBD) and phosphorylated tyrosine residue as fluorophore and trigger responsive motif respectively. The probe shows bright fluorescence in the aggregated state while it is lower in the monomeric state.[98]

1.4.6 Probable future applications

Encapsulation and Storage of Biomolecules

Proteins are prone to get denatured even due to minute changes in the environment and thereby lose their activity. Protecting proteins and biomolecules from the environment as well as from various denaturant is a challenging task. Various methods, including immobilization of proteins on a solid support, chemical modification, using molecular chaperons or polymeric hydrogels etc. have been applied for this purpose.[99-106] However, the reported methods are usually low in efficiency and could not provide a long life to the proteins under antagonistic conditions. Peptide-based hydrogels can play a crucial role in this regard as they can efficiently encapsulate biomolecules within the cross-linked network structure. A tightly entangled network can be a suitable hiding place for a biomolecule where due to limited availability of space, the biomolecules cannot unwind themselves and thereby remained protected. Additionally, due to the confinement, the biomolecules remain protected from the external stimuli and retain their activity even after exposure to those stimuli for a long time. However, to the best of my knowledge, no such effort has so far been reported.

Application in Organo-electronics and Gas Sensing Devices

Though biomolecular interfaces have already started getting attention in electronic devices, peptides are yet to be exploited properly.[107] A number of related studies by means of natural

materials highlight the perspective of this methodology to create new properties and applications.[108-109] However, it still remains a difficult task to fabricate nanowires or other types of 1D nanostructures with well-defined morphology and molecular arrangement.[111] The main difficulty lies in the fact that a successful 1D fabrication demands a tight correlation between the self-assembling kinetics or thermodynamics and the molecular design and engineering, which in turn usually requires a strong interplay between chemical synthesis, materials fabrication, and physical characterization, in search of optimal crystalline structure and optoelectronic properties that relate to broad range of applications in nanodevices.[110] Connecting natural self-assembling sequences with synthetic organic semiconductors offer a more promising way to use the peptide assemblies in the conductive components of electronic devices. In this regard, small peptide-based hydrogelators could be of tremendous help as the arrangement of the constituent molecules in the nano-fibers can easily be fine-tuned for these systems. Our group have recently shown the role of the morphology toward the semiconducting behavior of organic semiconductors.[111-113] Systems can be planned where the desired morphologies can be achieved along with functional groups which can selectively bind with a specific gas molecule and thus provide a signal to detect the presence of the gas. Thus, these peptide-based hydrogels can be utilized toward the creation of selective and sensitive volatile organic gas sensors in the near future.

1.5 The present thesis

In the present thesis, we have presented three short peptide-based hydrogels designed purposefully for different applications. All three peptides fall under the category of peptide amphiphiles and more specifically, lipidated peptide amphiphiles. Two of them belong to NDI-peptide conjugate class of peptides whereas, the other one is a pyrene conjugated short peptide. Most interestingly, they are composed of not more than 7 residues and forming the transparent hydrogels with minimum gelation concentration (MGC) below 2 wt%. In the next section, I have touched the gist of my works, which are elaborately discussed later in the subsequent chapters of the thesis.

Chapter 2 is comprised of the hydrogelation behavior and application of a lipidated peptide amphiphile (**PA-1**). The peptide was rationally designed to use the emission behavior of NDI for cell imaging and the RGDS sequence for its cell-penetrating ability. The peptide undergoes three step self-assembly process to form a self-supporting hydrogel. The mechanism behind the gelation process is studied in detail with the help of various instrumental techniques. The peptide was applied successfully toward cell imaging and importantly, it was found to be effective for sensing the intracellular pH as well.

Chapter 3 describes another lipidated peptide amphiphile (**PA-2**) very similar to that from **Chapter 2**. However, the incorporation of NDI, in this case, was purposefully made to utilize its semiconducting behavior toward volatile organic gas sensing. Similar to **PA-1**, this molecule is also capable of forming a self-supporting hydrogel in water. The mechanism of the gelation is revealed through various instrumental techniques. A composite hydrogel was formed using the gelator, polyvinyl alcohol, and carbon quantum dots. The xerogel of the composite hydrogel was then tested for its VOC sensing ability. The device prepared out of the composite xerogel was found to be an efficient and selective sensor of p-xylene. The sensing was ultrafast and can be achieved at room temperature. Notably, this is the first example of an all-organic sensor for p-xylene.

The work described in **Chapter 4** is about a unique peptide-hydrogelator. A tri-peptide (**PyKC**) containing a pyrene unit, lysine, and cysteine is capable of forming a thixotropic hydrogel in water and in a buffer of pH 8. Interestingly, when dispersed in water, the hydrogel remained insoluble for more than 18 months. Moreover, the hydrogel showed unprecedented confinement property as it does not allow any movement of solvent or solute to and from the hydrogel. The insolubility was quantitatively tested in a various aqueous medium and organic solvents and the hydrogel was found to be insoluble in most of the systems. Importantly, the gel was found to be soluble in the presence of some biomolecules which makes it a potential candidate for biomedical applications. The gelation mechanism and the insolubility property of the hydrogel were thoroughly studied with the help of various analytical techniques and theoretical calculation and all these results are discussed in **Chapter 4** in detail.

Chapter 5 describes the application of the **PyKC** hydrogel described in **Chapter 4**. The tightly knitted network formed by the **PyKC–**hydrogel and its unique confinement property were used to effectively protect enzymes from denaturation for a long period of time. Lipases from two different sources were encapsulated in the **PyKC-**hydrogel and subjected to various denaturing agents and stimuli like urea, methanol, high temperature etc. Surprisingly, the encapsulated enzymes were able to retain their activities even after prolonged exposure to these denaturants. In this chapter, all the results related to these studies are described in detail.

Chapter - 2

Hydrogelation from a Peptide Amphiphile (**PA-1**) Conjugated to Naphthalene Diimide and Its Application in Both Cell Imaging and Intracellular pH Sensing

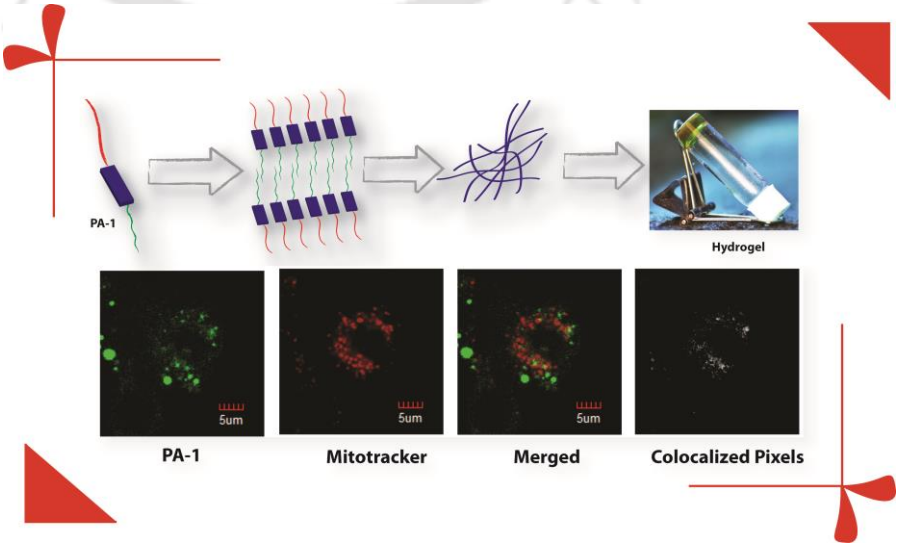

2.1 Introduction

Self-assembly of a diverse range of molecules has afforded competent and attractive approaches for designing various supramolecular constructs.[114,115] Utilizing this concept, various nano-architectures can potentially be developed through structural manipulation at the molecular level. Among all the different types of molecules being explored for developing self-assembly, peptide-based molecules have found widespread use.[35,116-118] Peptide-conjugated amphiphiles (PAs) usually possess the capability of forming a variety of nano-architectures ranging from micelles, capsules, and vesicles to nano-fibers, ribbons, and tubes in aqueous solutions.[3,34,75,119] Over the years, PAs have emerged as a new class of molecules owing to their remarkable self-assembly properties and potential applications in biomedical and other fields. PAs, be they amphiphilic peptides, lapidated peptides, or supramolecular peptide amphiphiles, are commonly capable of efficient self-assemblies to form various nanostructures and hydrogels.[120,121] These self-assemblies have found applications in biomineralization, tissue engineering, drug delivery, and functional nanomaterials to name a few.[18,96,122-126]

On the other hand, arylene diimides like perylene diimide (PDI) and naphthalene diimide (NDI) possess remarkable properties like electron affinity, molecular planarity, redox behavior, DNA intercalation, antimicrobial, and anticarcinogenic and hold promise for creating supramolecular functional materials.[111,127–134] Among the arylene diimide, NDI is of particular interest owing to its smaller size and ease of synthesis. Careful improvisation and incorporation of the characteristic properties of both NDIs and short peptides in conjugated structures could lead to enhanced water solubility and also control over the aggregation behavior through directional H-bonding interactions.[131] Moreover, combining the inherent fluorescence property of NDI with appropriate peptide sequences can lead to a new generation of materials for in vivo and in vitro sensing. This could eventually lead to the generation of forward-looking materials capable of exhibiting a variety of potential applications as biomaterials. In the recent past, several studies have been found to be reported on the self-assembly of different types of NDI derivatives in aqueous or organic medium for the development of functional materials with interesting applications.[135–142] However, as per the record, there are only a few reports on NDI-based hydrogels and few describing the self-assembly of NDI–peptide conjugates for the development of supramolecular soft functional materials.[76,77,143–147]

To this end, the development of fluorescent nanostructures capable of penetrating the cell membrane and acting as a cell imaging agent is an important area of research. Various fluorophore-appended peptides have been utilized for imaging and monitoring self-assembly inside live cells.[97,98,148] As the fluorescence technique provides insight into both physiological and pathological

processes in real-time, the development of new fluorescent peptide-based hydrogels with the advantages of fluorescence and self-assembly is highly desirable for biomedical applications. NDI, having strong emission as well as self-assembly properties, could be an ideal candidate to develop such a probe. Moreover, with appropriate peptide conjugation, the self-assembly of NDI-peptide conjugates can be fine-tuned in a pH-dependent manner,[149] which in turn might allow one to probe the intracellular pH as well. In this study, we have exploited the aforementioned strategy toward developing a soft material like hydrogels by attaching an NDI moiety to a short peptide.

We report an asymmetric NDI-based hydrogelator formed by attaching a C_6H_{13}- alkyl chain to one end and a GKRGDS peptide sequence to the other (Scheme 1). The RGDS fragment has been incorporated with the aim to introduce its cell adhesion and cell penetrating properties and, henceforth, to play the twin role of a structural component as well as a biological ligand.[150,151] This peptide amphiphile (**PA-1**, **scheme 2.1A**) was found to efficiently self-assemble in water at physiological conditions and form a fibrous network, which further formed a self-supportive hydrogel. Detailed analyses of the formation of the hydrogel revealed a stepwise mechanism where the molecules undergo a three-step hierarchical aggregation process. The noncovalent forces such as hydrophobic interactions, π-π stacking, and hydrogen bonding are behind the self-assembly process. This water-soluble conjugate was found to be nontoxic and cell permeable, was used for cell imaging, and has an extended biological application to assess intracellular pH.

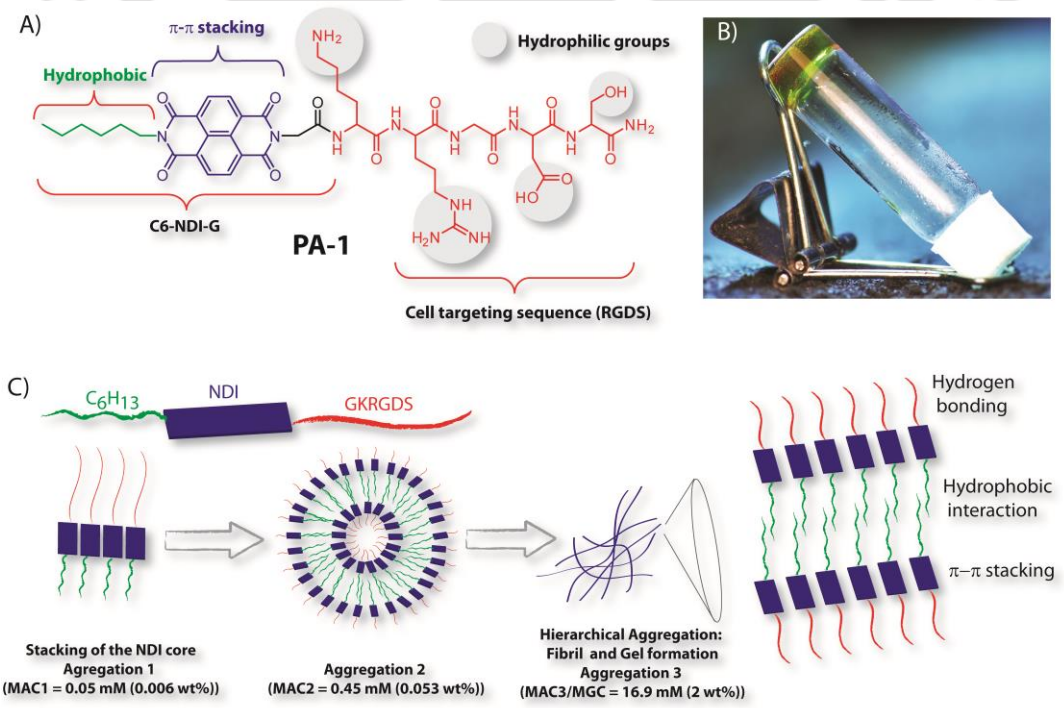

Scheme 2.1 (A) Chemical structure of **PA-1** showing different interactions and functional sites in them, (B) Photograph of a 2 wt % (16.9 mM) hydrogel of **PA-1** in water under UV light, and (C) Pictorial presentation of the stepwise hierarchical aggregation of **PA-1** to form a hydrogel.

2.2 Results and Discussion

2.2.1 Design, synthesis, and gelation

PA-1 (**scheme 2.1A**) was rationally designed to incorporate possible noncovalent interaction sites to promote self-assembly in the aqueous medium. The chemical structure can be divided into three parts: the hydrophobic tail, π-π interaction region in the form of NDI, and the cell adhesive sequence (RGDS).[150,151] The peptide sequence not only contributes to the biofunctionality of the PA but at the same time provides enough hydrophilicity to solubilize the molecule in water as well as hydrogen bond donor-acceptor to give stability to the aggregated structure. The presence of two positive (lysine and arginine) and one negative (aspartic acid) amino acid side chain functionality in the peptide sequence introduces pH responsiveness to the system. **PA-1** was synthesized following the route mentioned in **scheme 2.2**. The **C6-NDI-G** part was synthesized utilizing an earlier reported synthetic protocol.[77] This fragment of the peptide was then attached to the main peptide sequence via SPPS using the "Fmoc" strategy on Rink amide resin. The crude product was purified using reverse phase HPLC to obtain the desired product in good yield (63%) and characterized using NMR and ESI-MS techniques (m/z = 951.45 $[M+H]^+$ and 476.23 $[M]^{2+}$). Dissolution of **PA-1** in water by shaking and then incubation at room temperature provided a transparent hydrogel (**scheme 2.1B**). The minimum gelation concentration (MGC) as noted was 16.9 mM (2 wt %, 16.9 mM). Notably, the help of no other organic solvent was required for solubilization and gelation of **PA-1**. The hydrogel remained stable under ambient conditions over a long period of time (more than 3 months). FESEM and TEM analysis of matured (24 h) hydrogel samples showed the presence of a fibrous network (**fig. 2.1A** and **B**). The fibers are a few micrometers long with a diameter of ~100 nm.

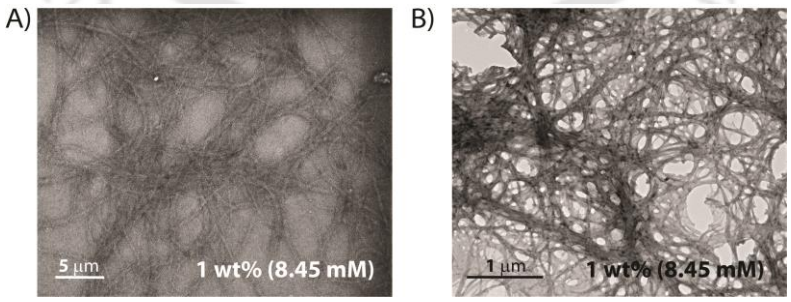

Fig. 2.1 (A) FESEM and (B) TEM images of the aqueous gel at 1 wt% (8.45 mM) concentration. Images were taken from 72 h matured samples.

2.2.2 Stepwise aggregation

For the mechanistic details of the hydrogelation of **PA-1** to be determined, the spectroscopic properties of **PA-1** in water were evaluated. The UV absorption of this NDI-peptide conjugate in water showed two well-resolved absorption bands at 362 and 383 nm with a shoulder at 345 nm, which is characteristic of the A_{0-0}, A_{0-1}, and A_{0-2} transitions arising from the NDI core.[152,153] **Fig. 2.2A** shows the absorption spectra of **PA-1** with increasing concentration. It was observed that, with increasing concentrations of the peptide conjugate, absorbance increases without any shifting or broadening of peaks. However, the absorption (for both 362 and 383 nm) vs concentration plot (**fig. 2.2B**) shows an inflection point in the enhancement of absorption. The change was observed at a concentration of 0.050 mM. Similarly, the fluorescence emission spectra (**fig. 2.2C**) of aqueous solutions of **PA-1** with increasing concentration exhibited (λ_{ex} = 360 nm) two emission bands near 392 and 413 nm whose intensities were found to increase up to a concentration of around 0.050 mM and then gradually decrease (**fig. 2.2C**).

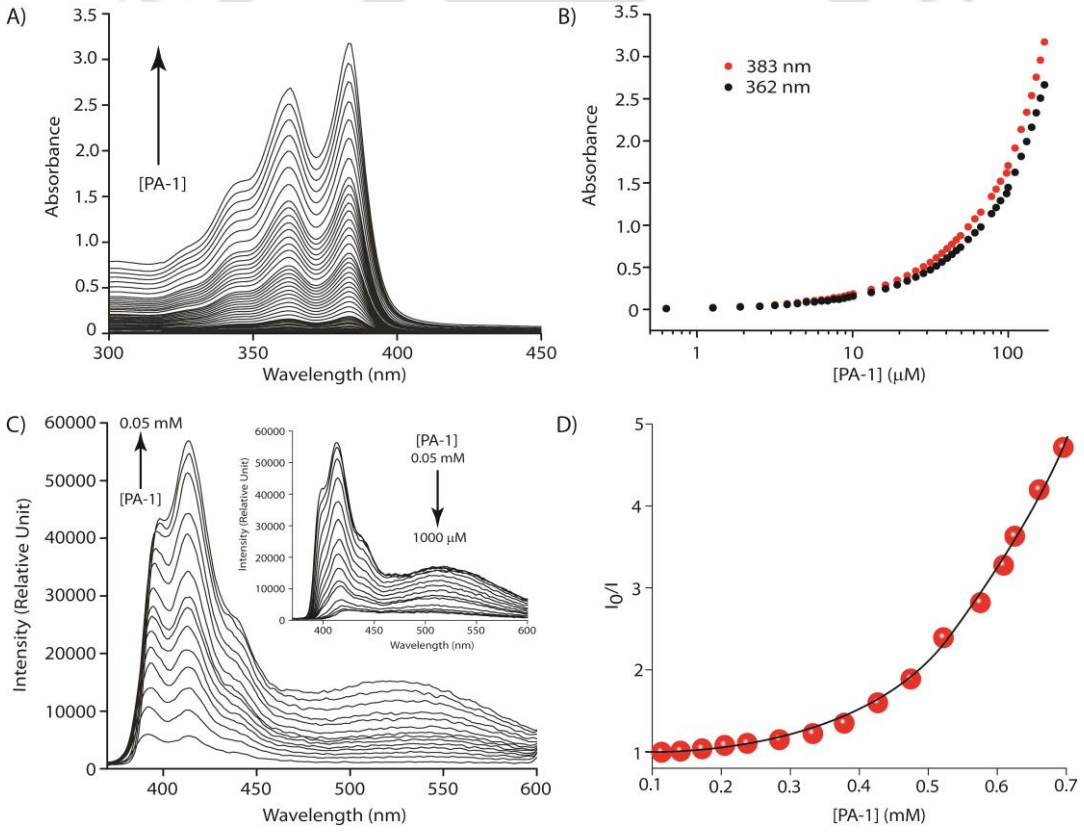

Fig. 2.2 Concentration dependent (A) absorption and (C) emission spectra of **PA-1**. Dependence of (B) absorption at 383 and 362 nm and (C) emission at 413 nm on the concentration of **PA-1**. (D) I_0/I vs concentration of the **PA-1** plot as obtained from the emission spectra; I_0 = emission intensity at 413nm when [**PA-1**] = 0.05 mM and I = emission intensity at 413 nm at any concentration above 0.05 mM.

The inflection point in the absorption spectra can be considered as the minimum aggregation concentration (MAC1) and this is a typical feature for NDI-based molecules where the NDI group forms aggregates through π-π interaction. A broad peak appearing in the emission spectra centered

at ~500 nm signifies the π-π stacking and was further confirmed through recording the excitation spectra of a 0.075 mM solution of **PA-1** at 392, 413, and 500 nm (**fig. 2.3A**). Though the first two wavelengths resulted in excitation spectra matching with the absorption profile, the spectrum recorded at 500 nm was broad and structureless. The broad spectra confirm the aggregation at this concentration as well.

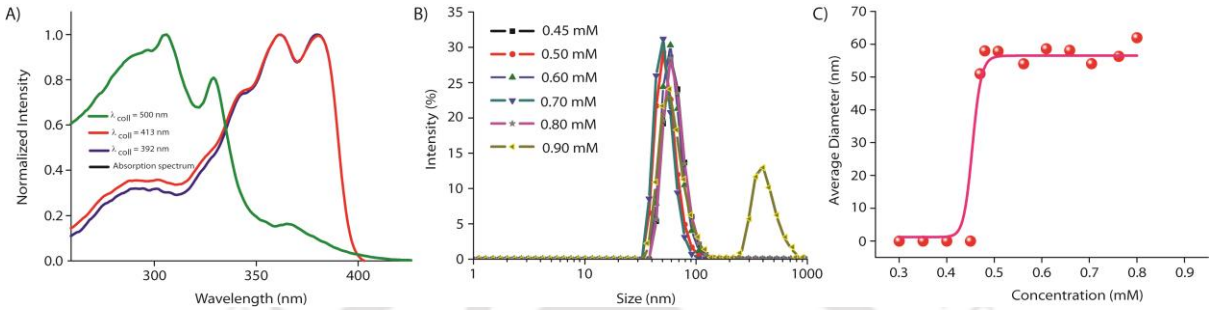

Fig. 2.3 (A) Normalized excitation spectra of an aqueous solution of **PA-1** (75 μM) collected at 500, 413 and 392 nm and merged with its corresponding absorption spectrum. (B) Intensity-weighted distribution of particles obtained from DLS measurements of aqueous solutions of **PA-1** at different concentrations (dilution from 0.9 mM), (C) Average particle sizes obtained at varying concentrations of **PA-1.** The experiments were carried out at room temperature.

However, analysis of samples just above MAC1 (0.075 mM) by FESEM showed no clear morphology. Further, the samples were analyzed by DLS, and interestingly, a very small distribution of around 3-5 nm-sized particles was observed (data not shown). All these results indicate that, above MAC1, the molecules start stacking and aggregates are formed, but the size and population of molecules in these aggregates are very small and the aggregates are formed due to π-π stacking of the NDI core as shown in **scheme 2.1C**. These results also indicate a possible multistep hierarchical aggregation of **PA-1** molecules to form the observed nano-fibers in the hydrogel state.

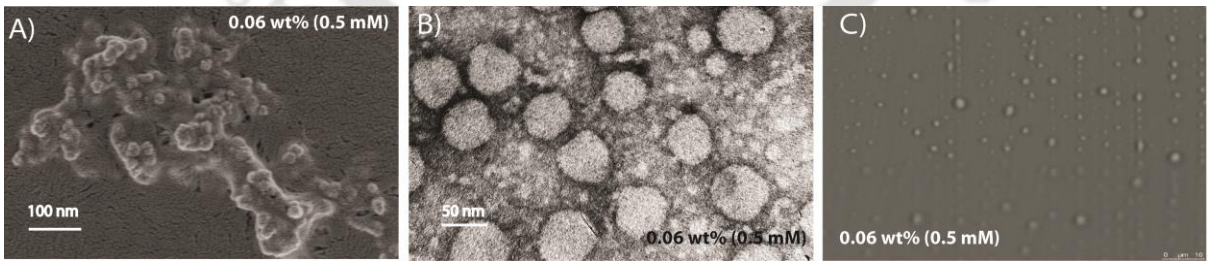

Fig. 2.4 (A) FESEM, (B) TEM, and (C) CLSM images of aqueous solution of **PA-1** at 0.06 wt% (0.5 mM) concentration. Images were taken from 72 h matured samples.

For the self-assembly process to be analyzed further, 0.9 mM (beyond this concentration, the solution was viscous) aqueous solution of **PA-1** was analyzed by DLS measurements, and two clear size distributions centered at 60 nm (major) and 392 nm (minor) were observed (**fig. 2.3B**). This solution was subjected to stepwise dilution and monitored by DLS measurements. Dilution of the

solution to 0.8 mM leads to the disappearance of the minor distribution at 392 nm. The distribution at 60 nm persisted until 0.45 mM concentration, and with further dilution, no measurable particles were obtained (only a negligible distribution at 3 nm). A concentration-dependent particle size distribution plot (**fig. 2.3C**) shows a sharp jump in the average diameter at ~0.45 mM, which remains unchanged until 0.8 mM. The experiment was repeated three times to ensure reproducibility. In addition, for the minimum aggregation concentration to be confirmed, the surface tension of the solution of **PA-1** with increasing concentration was recorded (**fig. 2.5A**).[154] Two distinct inflection points were obtained in the surface tension vs concentration plot at ~57 and 0.46 mM. This inflection points closely match the data obtained from the UV absorption and dilution experiments. The dilution experiment along with surface tension measurements clearly point toward a second order aggregation above 0.45 mM concentration, which can be termed MAC2. FESEM, TEM, and CLSM images of the sample of 0.5 mM concentration showed spherical aggregates of 50-60 nm diameter (**fig. 2.4A-C**).

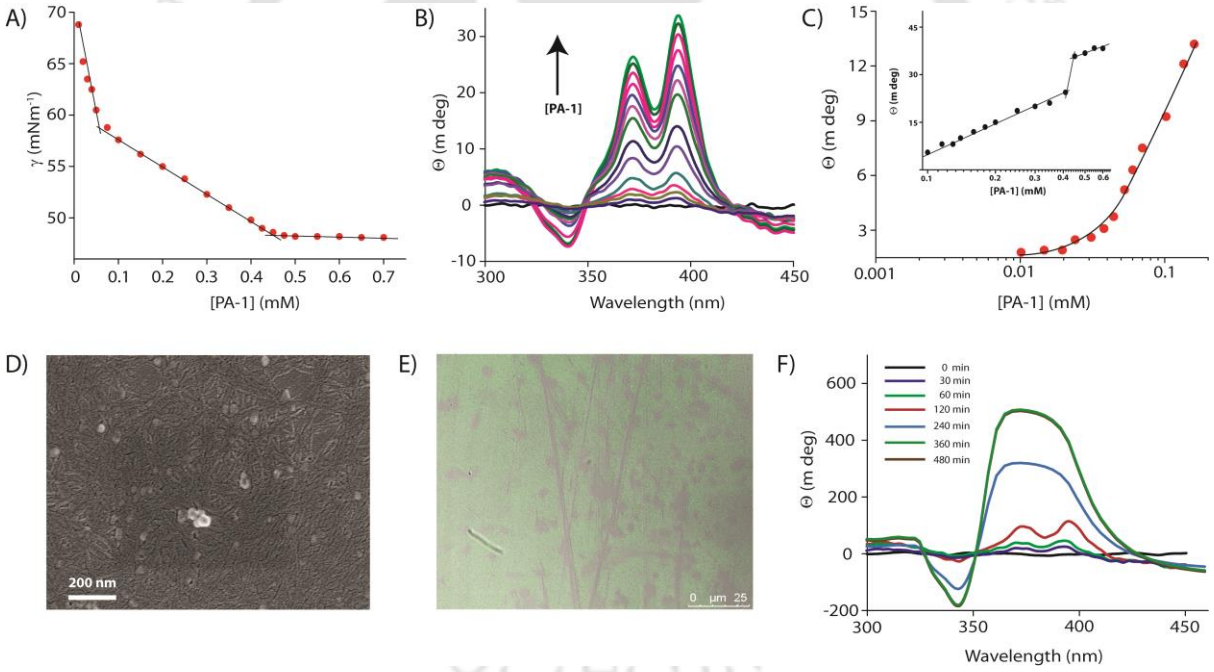

Fig. 2.5 (A) Surface tension vs concentration plot for **PA-1** in water. (B) CD spectra of **PA-1** at different concentrations. (C) Dependence of the CD intensity at 392 nm with **PA-1** concentration (0.01-0.15 mM and in the inset, 0.1-0.6 mM range). (D) FESEM image of a 0.9 mM **PA-1** solution in water (72 h matured) showing the presence of both spherical and fibrous morphologies. (E) CLSM images of 0.9 mM aqueous solutions of **PA-1**. (F) CD spectra of a 1 wt% solution of **PA-1** at a different time interval.

For further information about this secondary aggregation to be obtained, the emission data was re-evaluated. The intensity at MAC1 (0.050 mM) was observed to be the highest in the concentration-dependent study; it was considered as I_0, and subsequent intensities (above MAC1) were considered as I. When I_0/I is plotted against concentration, a clear inflection point at 0.442 mM is observed for both the emission bands (392 and 413 nm) as can be seen in **fig. 2.2D**. The close coincidence of this

value with MAC2 observed from dilution experiment suggests that, above this concentration range, the molecules undergo a second order organization.

For more insight to be obtained on the second order aggregation and MAC2, we employed circular dichroism. A concentration-dependent study of **PA-1** in water provided some interesting results. The CD spectrum of **PA-1** reveals that the peptide part adopted a random coil conformation. However, the presence of the chiral peptide sequence certainly affected the aggregation of the NDI core. Though there is no induced circular dichroism (ICD) observed up to a concentration of ~0.010 mM, above this concentration the ICD is clearly visible (**fig. 2.5B**). A bisignate peak starts appearing above this concentration with a negative-to-positive crossover near the absorption maxima (350 nm).[155,156] The negative-to-positive switch indicates the formation of a right-handed helical aggregate.[156] Upon increasing the concentration up to 0.6 mM, the intensity of this bisignated band increases. However, when the intensity of the peaks are plotted against the concentration of **PA-1**, two sharp changes in the intensities are observed at concentrations of 0.050 and 0.45 mM (**fig. 2.5C**). These jumps in the intensities indicate possible changes in the aggregation patterns at these concentrations. Interestingly, these two concentrations precisely match with MAC1 (0.050 as mM, observed from UV) and MAC2 (0.45 mM, as observed from the dilution experiment), respectively.

In the present system, **PA-1** presumably self-assembles in three steps as shown in **scheme 2.1C**. The NDI core of the molecule formed smaller aggregates through π-π stacking, and the minimum concentration at which this aggregation behavior was observed was termed MAC1 (0.050 mM). Upon increasing the concentration, these smaller aggregates further assemble to form spherical aggregates of ~60 nm diameter above MAC2 (0.45 mM). These spherical aggregates presumably undergo third-order aggregation to form the fibers that eventually lead to the formation of the fibrous network of the hydrogel. Monitoring the third-order aggregation is difficult as the system becomes viscous and most of the analytical techniques cannot be utilized. However, in the case of DLS measurements, the appearance of a minor distribution of 392 nm (**fig. 2.3B**) at 0.9 mM concentration is an indication of the third-order aggregation. The experiment was repeated several times to confirm the presence of the distribution at ~400 nm. Unfortunately, measurements with samples of higher concentration resulted in erroneous results owing to the viscous nature of the samples. Presumably, the spherical aggregates (60 nm) formed above MAC2 further aggregated to form fibers, and at 0.9 mM concentration, both types of aggregates were present. For this to be proven, FESEM and CLSM images of the sample (0.9 mM) were recorded, and as expected, spherical aggregates of ~50-60 nm, as well as some small fiber-like structures, could be seen in the sample after careful analysis (**fig. 2.5D** and **E**). Upon increasing the concentration, the fibers elongated in length, formed longer fibers, and finally resulted in hydrogelation. The minimum gelation concentration can thus be termed MAC3.

As the gelation of **PA-1** takes several hours, to obtain insight into the possibility of any effect of assembly time in addition to a concentration that may be contributing to aggregation, we performed a time-dependent CD study. The intensity of the CD signal corresponding to the NDI core (325-475 nm) was enhanced with time up to 6 h (**fig. 2.5F**). However, the signal became structureless and broad. After 6 h, no further change was observed in the CD signal. As the solution became viscous after 8 h, measurements could not be performed after this time period. From this study, it may be concluded that the molecules aggregate in a thermodynamically controlled fashion, [111] and the fibers obtain their optimal structure at 6 h and subsequently, the hierarchical aggregation of the fibers leads to the formation of the gel network.

2.2.3 Supramolecular interactions involved in the aggregation

To obtain insight into the supramolecular interactions involved in the aggregation process, we performed a ^{1}H NMR study of the hydrogel. A 25.35 mM (3 wt %, 25.35 mM) hydrogel formed in D_2O was subjected to temperature variation (**fig. 2.6A**). At room temperature, all the peaks appeared broad and structureless. With an increase in temperature, the aromatic protons, ^{1}H signals from the amino acid residues, as well as the peaks corresponding to the aliphatic hydrocarbon chain showed a downfield shift. Along with the shift, the peaks also showed proper splitting. The downfield shift continued until 65 °C, but after that, no further change was observed.[74,157] The temperature after which no further downfield shift could be observed can be considered as the melting temperature for the hydrogel. Importantly, the melting temperature of the 3 wt % (25.35 mM) hydrogel of **PA-1**, as measured by the vial inversion method, was found to be 63 °C and closely matches with the temperature observed from the NMR study (65 °C). The observed chemical shifts are the result of breaking the noncovalent interactions involved in the aggregation process. As external energy is provided to the aggregated structure, the π-π stacking between the NDI moieties break, and the protons shifted to higher chemical shift values.[96] The same explanation is also applicable for the hydrocarbon chains, which were bound together through hydrophobic interactions at a lower temperature. An increase in temperature breaks this hydrophobic packing and the protons appear at their respective unbound positions. A similar effect of temperature on the protons corresponding to peptide sequence suggests a probable hydrogen bonding interaction between the amino acids.

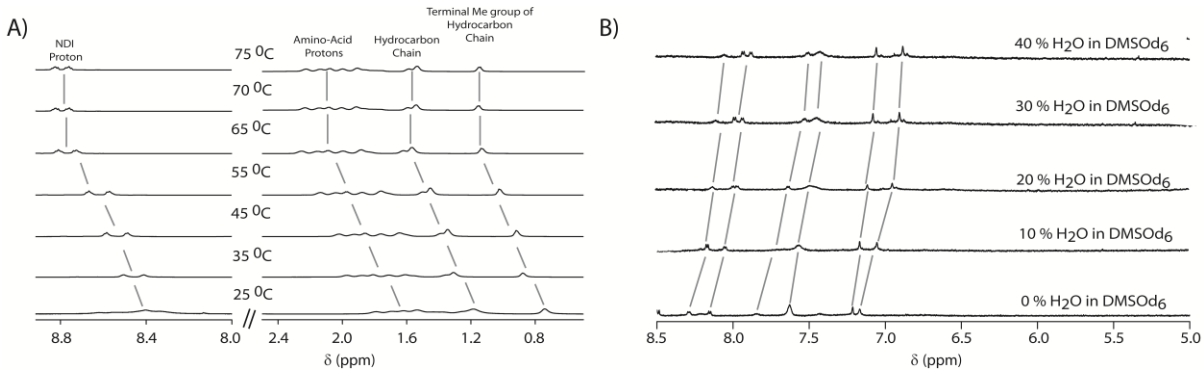

Fig. 2.6 ^{1}H NMR spectra of **PA-1**- (A) in D_2O at increasing temperature and (B) in DMSO-d_6 with increasing H_2O content. [**PA-1**] = 3 wt % (25.35 mM). All samples are matured for 72 h.

To verify the involvement of hydrogen bonding in the aggregation process, we performed another set of NMR studies. Proton NMR was recorded for solutions of **PA-1** in DMSO-d_6 (a solvent where the molecule does not aggregate) with varying amounts of water. As can be seen in **fig. 2.6B**, four of the amide protons from the peptide sequence could be identified in DMSO-d_6. As the water content increases, an upfield shift is observed for all of these protons.[74,157] In the presence of water, intermolecular hydrogen bonding between the DMSO-d_6 and amide NHs start breaking as well as the extent of hydrogen bonding between water and NHs is enhanced with more water molecules. Though measurements could not be performed beyond 40% water, these results clearly show the involvement of hydrogen bonding in the aggregation of **PA-1**.

2.2.4 pH sensitivity

The presence of two positively and one negatively charged side chain functionalities makes the hydrogel pH responsive. HCl and NaOH solutions (1 M, 10 µL) were placed separately at the top of two hydrogel samples (2 wt %, 16.9 mM in water). Within a few hours, the sample with acid on top melted to a clear solution, whereas the other sample remained unchanged. For understanding pH sensitivity, the absorption, emission, and CD spectra of **PA-1** were recorded at different pH levels. Drastic changes were observed both in the absorption as well as emission behavior of **PA-1** as we move from acidic to basic pH (**fig. 2.7A** and **B**). With increasing pH value, both absorption and emission intensities of all peaks decreased. However, up to pH 7, no change in the $A_{0\text{-}0}/A_{0\text{-}1}$ ratio, a measure of aggregation, was observed as it remained constant at 1.19.[153,158] Interestingly, in the basic domain, the ratio decreased dramatically, and at pH 11, it reached a value of 0.85, which signifies strong π-π stacking between the NDI groups. Moreover, a blue-shift of the absorption peaks by 25nm was observed along with broadening of the peaks. The shift in the $A_{0\text{-}0}/A_{0\text{-}1}$ ratio in the case of basic medium, as well as the blue shift, signifies strong H-type aggregation of the NDI core through π-π stacking in this case.[159,160]

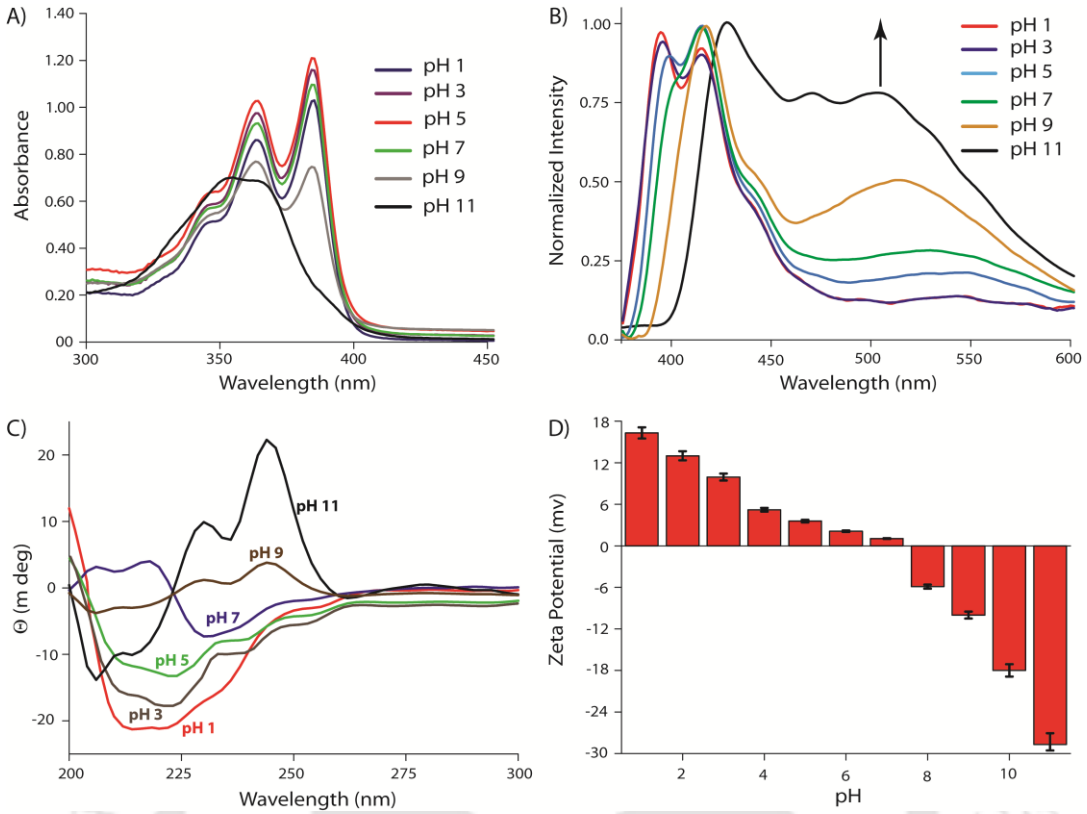

Fig. 2.7 (A) Absorption, (B) emission, and (C) CD spectra of 75 μM solutions of **PA-1** in buffers of different pH. (D) Zeta potential values of 0.5 mM solutions of **PA-1** in buffers of different pH. All experiments were carried out at ambient temperature.

A similar observation was also obtained in the case of emission spectra (**fig. 2.7B**). At higher pH, the broad peak at ~500 nm resulting from aggregation becomes more prominent, suggesting strong aggregation of the molecules in basic pH. The effect of pH on the CD spectra was monitored, and interesting results were obtained. Solutions of **PA-1** (0.075 mM, above MAC2) in buffers of different pH were subjected to CD analyses. Notably, at highly acidic conditions, the peptide adopts α-helical arrangement as observed from the CD signals (**fig. 2.7C**). With increasing pH values, though the α-helical CD pattern remains, the intensity decreases, and at pH 7, a random coil-type arrangement is observed. The random coil nature is maintained in the entire basic range with continuous enhancement of the signal intensity. For the overall charge on the surface of the aggregates to be verified, ζ-potentials of the solutions were measured (**fig. 2.7D**). Under highly acidic conditions, the overall charge was observed to be positive and remained positive up to pH 7. In the higher pH region, the ζ-potential value decreases, and a negative overall charge is observed in the entire range up to pH 11.

The above results describe the role of the amino acid side chains in the formation of the hydrogel. Under acidic conditions, the overall charge on a single molecule is (+2); thus, the molecule becomes highly soluble, and the aggregation process is affected. Higher solubility effectively leads to higher MAC3 (MGC), and thus in the presence of acid, the 1 wt % (8.45 mM) gel melts (the MGC

noted at pH 5 is ~4 wt % (33.8 mM)). The overall charge remains (+2) up to pH 7. However, in basic pH, the overall charge becomes (-1), which decreases the solubility of the molecule and results in the formation of the gel at a lower concentration.

2.2.5 Rheology

It is essential to understand the mechanical properties of the hydrogels as the mechanical strength or elastic behaviors are directly linked to their applications. To evaluate the mechanical properties of the hydrogel at neutral pH, we measured the rheology of a 2 wt % (16.9 mM) hydrogel. A linear viscoelastic frequency sweep response of **PA-1** hydrogel shows plots of G′ and G″ (where G′ is dynamic storage moduli and G″ is loss moduli) versus angular frequency (ω) (**fig. 2.8**). It is found that G′ and G″ do not vary significantly within the applied range of ω and G′ > G″, suggesting high elasticity of the hydrogels.

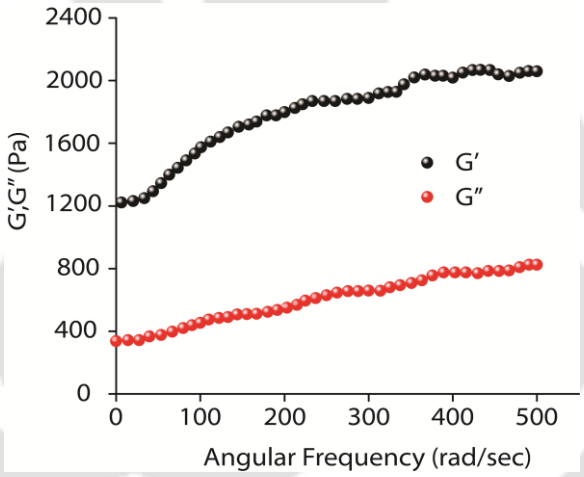

Fig. 2.8 Frequency sweep of dynamic shear modulus for 2 wt % (16.9 mM) 72 h matured hydrogel of **PA-1**.

2.2.6 Cytotoxicity

To evaluate the toxicity of **PA-1**, we performed MTT assays on RAW264.7 murine macrophages (**fig. 2.9A**). Compound **PA-1** was administered to the cells at different concentrations (0.001–0.5 mM) for 4 h, and cell viability was assessed. No significant changes were observed in cell viability as ascertained by MTT assay ($p > 0.05$, **fig. 2.9A**). The nontoxic nature of the peptide amphiphile makes it an ideal candidate for biomedical applications.

2.2.7 Intracellular localization

The noncytotoxic nature of the PA encouraged us to test its ability for intracellular localization and pH sensing inside live cells as discussed in the Introduction. Macrophages being characteristic phagocytic cells are more advantageous to discern this phenomenon in general, and thus they were chosen for the cell-based studies. Intracellular localization studies showed a scattered cytoplasmic distribution of **PA-1** (**fig. 2.9B**). As the compound showed prominent aggregation properties in solution upon increasing the pH of the solution, we tried to understand whether this property of the compound can be used to determine the pH at different cellular locations. To this end, lambda scan mode from 400 to 600 nm was employed at an excitation wavelength of 350 nm. In both region of interest **ROI-1** and **ROI-2**, three bands appeared at approximately 450, 500, and 580 nm (**fig. 2.10C** and **D**).

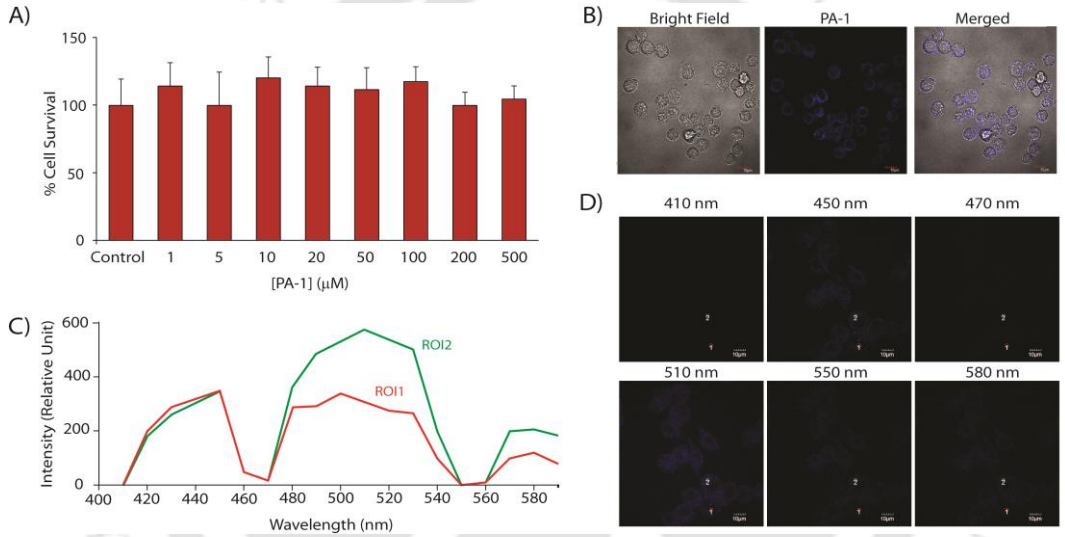

Fig. 2.9 (A) Cell viability using MTT assay and (B) staining of RAW264.7 cells using **PA-1** (blue). The cells were merged over the bright field to ascertain intracellular localization. (C) The emission intensity vs wavelength plots of a Lambda scan over the shown region and (D) the corresponding images at the indicated wavelengths.

In the case of **ROI-2**, the band at 500 nm is much higher than that in the case of **ROI-1**. As seen in the case of the pH-dependent emission property analyses of **PA-1**, the band at ~500 nm signifies the presence of aggregated molecules. These observations support the fact that, at specific locations within the cell (**ROI-2**), the probe aggregated strongly due to the presence of an alkaline atmosphere; thus, the intensity of the band at ~500 nm was enhanced significantly, whereas, in neutral or lower pH, the aggregation is not pronounced and effectively resulted in a lower intensity band at 500 nm (**ROI-1**). Thus, the molecule can be utilized to effectively probe the intracellular pH. To further understand the subcellular localization of this compound, we looked for its colocalization with that of MitoTracker, a fluorescent probe that labels mitochondria. We chose mitochondria above other organelles as the mitochondrial matrix is alkaline due to constant transport of protons across the inner membrane by the components of the electron transport chain, and **PA-1** showed

aggregating properties in solution upon increasing pH. The microscopic data revealed good correspondence between the luminescence pattern of the compound and MitoTracker (**fig. 2.10**). These results unequivocally demonstrate that **PA-1** is cell permeable and has an extended biological application to assess intracellular pH or subcellular staining.

2.2.8 Cellular uptake.

To understand the mechanism of uptake of **PA-1**, we incubated cells at different conditions like lowering of temperature or serum deprivation or in the presence of inhibitors. Uptake was nearly abolished at 4 °C (94.2% decrease with respect to control), indicating either membrane rigidification or energy depletion can play a role in the uptake process.

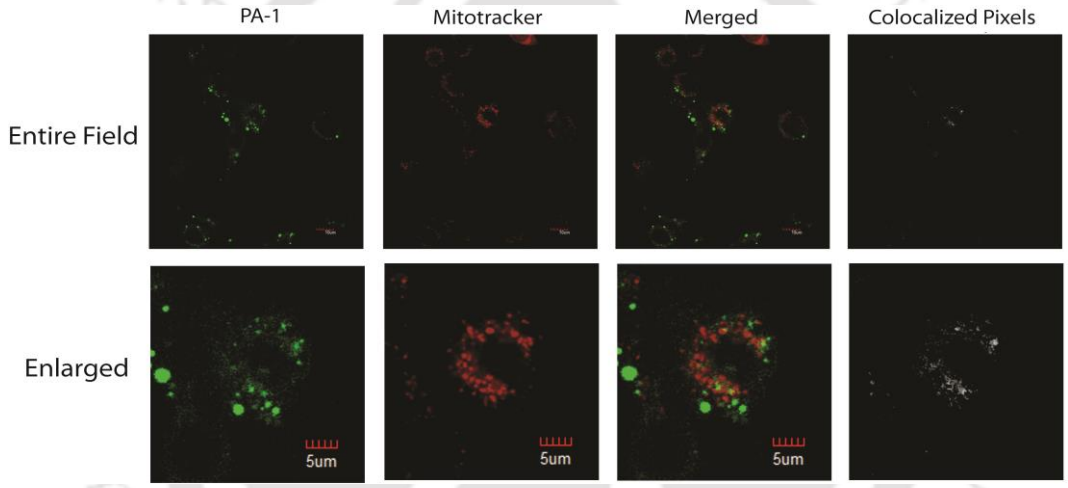

Fig. 2.10 Subcellular localization of the compound (green) was ascertained using MitoTracker (red) by analyzing the merged images. The colocalized pixels give an idea of the degree of correspondence between the luminescence of the green and red pixels.

To understand the same, we treated the cells with 2-D-deoxyglucose, which showed a 62.8% decrease in **PA-1** uptake with respect to control, indicating that energy depletion indeed plays important roles in **PA-1** uptake (**fig. 2.11**). On the other hand, serum starvation showed a 39.1% decrease with respect to control, indicating serum proteins have roles in the uptake mechanism, albeit to a lesser extent. In contrast, cholesterol depletion or inhibition of actin polymerization resulted in a similar (54.9 or 56.1%, respectively) decrease in cellular uptake of **PA-1** as opposed to control, indicating that membrane composition or actin polymerization can both play important roles in the uptake of **PA-1**. The fluidity of the membrane changes upon cholesterol depletion resulting in disruption of lipid rafts, which affects the internalization of particles. Actin polymerization also plays important roles in phagocytic processes. A similar decline observed upon treatment with these inhibitors and the fact that these are energy-dependent processes, ATP

depletion would definitely result in a higher decline in uptake. Overall, the results indicate that phagocytosis- mediated uptake may be the major mechanism by which **PA-1** is internalized within the cells. How other cell types might behave in the uptake of this molecule is subject to further study. However, there are studies that have shown that nanostructures are maximally engulfed by macrophages in contrast to other cells, but uptake of nanoparticles was seen in all of them, albeit to a lesser extent.[161]

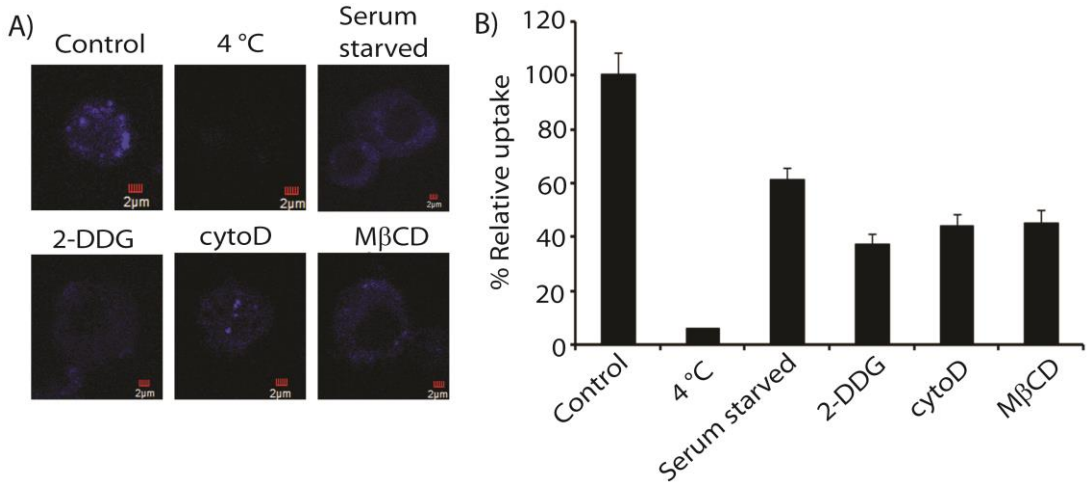

Fig. 2.11 Mechanism of uptake of **PA-1** by macrophages. (A) Representative image of cells exposed to different conditions (4 °C or serum starved) or treated with inhibitors (50 μM 2-deoxy-D-glucose (2 DDG), 5 mM MβCD, 2 μM cytoD, and (B) fluorescence intensity of the images acquired depicted as percent relative uptake.

The uptake may also be influenced by its functional group, uptake kinetics, differentiation of the cell in context, and opsonization by serum proteins.[162] Thus, different cells may behave differently in the uptake of the nanomaterials in context and warrants detailed study for individual cell types. However, future work with this PA warrants investigation as to whether they are immunogenic in nature to be used for drug-release purposes, which can further be studied using the macrophage cells.

2.3 Conclusion

In the process of looking for NDI-appended peptides, we have developed a new low molecular weight asymmetric NDI-capped peptide amphiphile, **PA-1**. The peptide formed a strong hydrogel in water. The hydrogel is formed following a three-step aggregation mechanism involving π-π stacking, hydrophobic interactions, and hydrogen bonding as the main supramolecular forces. Extremely smaller aggregates with a low population of the molecules were formed at a very low concentration through stacking of the NDI core. With increasing concentration, the smaller aggregates were transformed into spherical aggregates of ~60 nm diameter. Hierarchical

aggregation of these spherical aggregates further leads to the formation of fibers that eventually form the fibrous network capable of immobilizing water molecules to form the hydrogel. The hydrogel was found to be pH sensitive, and at higher pH, the aggregation was found to be stronger than that under acidic conditions. **PA-1** was found to be non-toxic as ascertained by MTT assay. The PA functioned as contrast agents for cell imaging, and intracellular localization studies showed a scattered cytoplasmic distribution of the compound. As the compound again showed stronger aggregation in vitro upon increasing the pH of the solution, we were able to exploit this property of the compound to determine the pH at different cellular locations. Furthermore, uptake of **PA-1** seems to be an active phagocytic process as treatment with 2-deoxy-D-glucose, MβCD, or cytoD greatly affected its internalization in macrophages. These results unequivocally demonstrate that **PA-1** is actively taken up by the cells, is nontoxic, and has an extended biological application to assess intracellular pH.

2.4 Experimental Section

2.4.1 Materials

Fmoc-rink amide resin and protected amino acids were purchased from GL Biochem (China). HBTU, diisopropylethylamine (DIPEA), 1,4,5,8-naphthalenetetracarboxylic acid dianhydride (NDA), n hexylamine, 2-deoxy-D-glucose, methyl-β-cyclodextrin (MβCD), cytochalasin D, and 3-(4,5 dimethylthiazol-2-yl)-2,5-diphenyltetrazolium bromide (MTT) were obtained from Sigma-Aldrich (USA). Glycine and piperidine were purchased from Merck (India) and used without further purification. HPLC-grade dimethylformamide (DMF) and acetonitrile were procured from Spectrochem (India) and Fisher Scientific (India), respectively. MitoTracker Red CMXRos was procured from Molecular Probes (USA). For sample preparation, Milli-Q water with a conductivity of less than 2 μS cm^{-1} was used. Chromatographic purification of **PA-1** was performed on Ultimate 3000 (Dionex). ESI-MS was performed with a Q-tof-micro quadrupole mass spectrophotometer (Micromass). UV-Vis data was recorded with a PerkinElmer Lambda 35 spectrometer. Circular dichroism (CD) experiments were performed on a Jasco J-1500 spectropolarimeter. Fluorescence measurements were performed with a Fluoromax-4 spectrofluorometer (HORIBA). Dynamic light scattering and zeta potentials were measured using Zetasizer Nano-ZS90 (Malvern). Confocal laser scanning microscopic (CLSM) images were recorded on a TCS SP8 microscope from Leica, Germany.

2.4.2 Synthesis and characterization

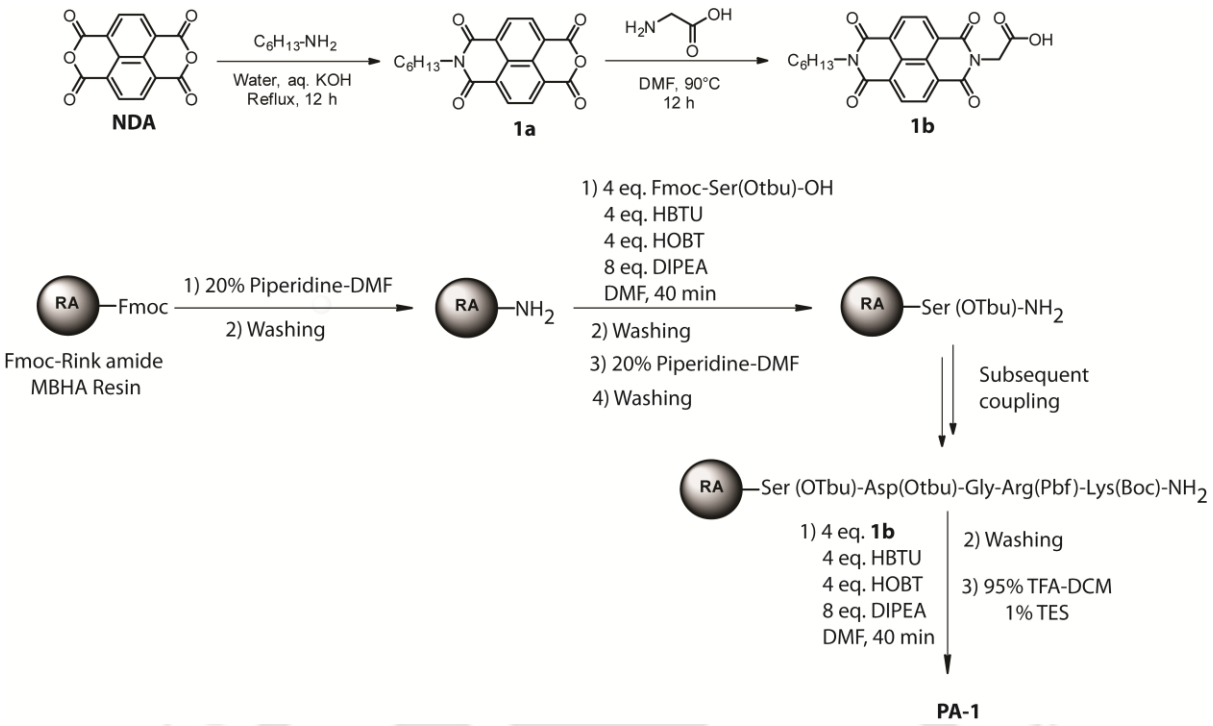

Scheme 2.2 Synthetic Route for **PA-1**.

2.4.2.1 Synthesis of 1a:

1,4,5,8- naphthalenetetracarboxylic acid dianhydride (2.0 g, 7.46 mmol) was taken in a 500 mL round bottom flask and 350 mL of water was added to the solid. 1 M aqueous KOH solution (35 mL) was then added to the mixture and heated with vigorous stirring until the compound completely dissolved. Once the solution became clear, the pH was adjusted to 6.4 by adding 1 M H_3PO_4. To this solution, n-hexylamine (0.98 ml, 7.46 mmol) was added and the pH of the solution was again adjusted to 6.4 with 1M H_3PO_4. The mixture was refluxed overnight. It was then allowed to cool to room temperature and filtered. To the filtrate, acetic acid (5 mL) was added to afford a solid precipitate, which was then filtered and washed with more water and dried over silica gel under vacuum to get 1.47g (56% yield) of **1a** as an off-white solid.

^{1}H NMR (600 MHz, DMSO-d_6,): δ/ppm = 8.56-8.54 (d, J =12Hz, 2H), 8.19-8.18 (d, J = 6Hz, 2H), 4.04-4.01 (t, J = 9Hz, 2H), 1.65-1.61 (m, J = 6Hz, 2H), 1.35-1.28 (m, J = 6Hz, 6H), 0.86-0.84 (t, J = 6Hz, 3H).

2.4.2.2 Synthesis of 1b:

1a (1 g, 2.85 mmol) was first dissolved in dimethylformamide (DMF,15mL), by heating at 60 °C followed by the sequential addition of Glycine (0.44 g, 5.87 mmol) and DIPEA (0.98 ml, 5.87 mmol). The reaction mixture was heated at 90 °C with stirring for 12 h. The solvent was evaporated under

vacuum and the crude residue was suspended in 2:1 water/methanol (100 mL) and the pH of the solution was adjusted to 3 by adding hydrochloric acid (6N). The obtained solid was thoroughly washed with water by centrifugation and then dried over silica gel under vacuum to afford 0.8 g (69% yield) of **1b** as a deep brown solid.

^{1}H NMR (600 MHz, DMSO-d_6,): δ/ppm = 8.67 (s, 4H), 4.65 (s, 1H), 4.04-4.02 (t, J = 9Hz, 2H), 1.65-1.61 (m, J = 6Hz, 2H), 1.35-1.28 (m, J = 6Hz, 6H), 0.86-0.84 (t, J = 6Hz, 3H).

2.4.2.3 Synthesis of PA-1:

PA-1 was prepared manually by the solid-phase peptide synthesis (SPPS) technique using Rink amide MBHA resin and Fmoc strategy. The C6-NDI-G (**scheme 2.1A**) unit was prepared separately in solution phase using the earlier reported synthetic protocol (Supporting Information).[41] After the deprotection of Rink amide resin with a 20% piperidine/DMF solution, Fmoc-Ser(OtBu)-OH was introduced and coupled to the resin followed by Fmoc deprotection and coupling of the next Fmoc amino acids following the sequence. In a typical coupling, 4 eq of protected amino acid (with respect to the loading of the resin), 4 eq of HBTU, and 8 eq of DIPEA were taken in 5 mL of DMF (for 0.1 mmol scales) and stirred for 5 min prior to addition of the mixture to the resin. The reaction mixture was shaken for 40 min and the resin was washed several times with DMF. The Fmoc deprotection and coupling were repeated until the designed peptide sequence was obtained. After Fmoc deprotection of the N-terminal Fmoc-Lys(Boc)-OH, the C6-NDI-G residue was finally coupled to the N-terminal of the peptide sequence. Fmoc deprotection reactions were carried out using DMF solution containing piperidine (20%, v/v) for 15 min followed by thorough washing with DMF five times. Cleavage from the resin and deprotection of the protecting groups on the side-chains were performed concurrently with a mixture of 95% trifluoroacetic acid (TFA) in dichloromethane containing 1% triethylsilane (TES). After rotary evaporation, the cleaved peptides were precipitated with cold diethyl ether, washed thrice with cold ether, and then lyophilized. The crude peptide was purified using semi-preparative HPLC on a Luna 5 µm (C18) column (Phenomenex) using a gradient of acetonitrile and water as the eluent for 20 min. Overall yield after purification was 63%.

^{1}H NMR (600 MHz, D_2O,): δ/ppm = 8.66–8.62 (q, J = 12 Hz, 4H), 5.02–4.99 (d, J = 18 Hz, 1H), 4.92–4.90 (d, J = 12 Hz, 1H), 4.59–4.57 (t, J = 6 Hz, 2H), 4.38–4.35 (m, J = 6 Hz, 3H), 4.10–4.07 (t, J = 6 Hz, 2H), 3.95–3.80 (m, 6H), 3.22 (s, 1H), 3.12–3.10 (t, J = 6 Hz, 2H), 3.03–3.01 (t, J = 6 Hz, 3H), 2.83 (s, 1H), 2.75–2.71 (m, J = 6 Hz, 3H), 1.92–1.76 (m, J = 6 Hz, 5H), 1.74–1.67 (m, J = 6 Hz, 5H), 1.64–1.59 (m, J = 6 Hz, 3H), 1.54–1.44 (m, J = 6 Hz, 3H), 1.42–1.38 (m, J = 6 Hz, 2H), 1.36–1.28 (m, J = 6 Hz, 5H), 0.87–0.85 (t, J = 6 Hz, 3H) ppm. **ESI-MS** calcd for $[M + H]^+$ $C_{43}H_{58}N_{12}O_{13}$: 951.01, found: 951.45 $[M + H]^+$ and 476.23 $[M]^{2+}$.

2.4.3 Sample preparation

The solution of **PA-1** for different instrumental analyses was prepared by dissolving the required amount in Milli-Q water and kept at room temperature before characterization. All experiments were performed at room temperature unless otherwise mentioned.

2.4.4 Preparation of the hydrogel

In a typical experiment, 20 mg of the peptide was dissolved by shaking in 1 mL of HPLC grade water (pH 7) in a glass vial with i.d. of 10 mm at room temperature. The vial was allowed to stand without any disturbance. After 24 h, a transparent gel was obtained that did not flow downward upon inversion of the glass vial. NMR Spectroscopy. ^{1}H NMR spectra were recorded in heavy water (D_2O), DMSO-d_6, or a DMSO-d_6/water system on an Ascend 600 MHz (Bruker, Coventry, UK). In the case of the temperature dependent NMR study of the hydrogel, a 72 h mature hydrogel of **PA-1** (3 wt %, 25.35 mM) in D_2O was used, and the temperature was varied from 295 to 348 K. Whenever necessary, spectra were appropriately water suppressed for clarity.

2.4.5 DLS and Zeta Potential

The particle sizes of the samples were measured at 298 K using a 632.8 nm He-Ne laser. The samples were prepared in water, filtered through appropriate filters to remove dust particles if present, and then allowed to settle for 24 h before the measurement.

2.4.6 Field Emission Scanning Electron Microscopy (FESEM)

FESEM samples were prepared by casting 10 µL of **PA-1** solutions on a silicon wafer and dried over $CaCl_2$ in a desiccator overnight before analyzing the samples on a Gemini SEM 300 (Sigma Zeiss) instrument.

2.4.7 Transmission Electron Microscopy (TEM)

TEM samples were prepared by casting 5 µL of **PA-1** solutions on a 300 mesh Cu grid with a thick carbon film (Pacific Grid Tech, USA) and held in the air for 2-3 min. Excess solution was then blotted with tissue paper. With a drop of 2% uranyl acetate solution, the sample was negatively stained before removing the excess liquid with filter paper and finally dried over $CaCl_2$ in a desiccator. The images were recorded on a JEM-2100 (JEOL) microscope.

2.4.8 Circular Dichroism (CD)

CD spectra of aqueous solutions of **PA-1** at various concentrations and pH were recorded by using a 1.2 mL quartz cuvette of 0.5 mm path length with a J-1500 (Jasco) spectropolarimeter at RT. Spectra were collected at 1 nm intervals and 1 nm bandwidth from 200 to 600 nm.

2.4.9 Surface Tension

The surface tension of the surfactants at the air/water interface was measured using a tensiometer (Jencon, India) by du Noüy ring detachment method. Previously prepared concentrated aqueous solutions of the surfactants were added progressively with Hamilton syringes to a measured quantity of water, gently stirred for 2 min, and kept in a constant-temperature bath for 10 min without disturbance to reach equilibrium. The surface tensions of these solutions were then measured in triplicate while maintaining the temperature. The measurement could not be performed beyond 0.7 mM concentration as erroneous data was obtained above that concentration probably due to the high viscosity of the solution.

2.4.10 Rheology

Rheology was measured using Anton PaarRC102 Rheometer (MCR 301, Austria). Oscillating rheology was used to quantify the final mechanical properties of the **PA-1** hydrogel. For the study, 1 mL of hydrogel was utilized. A 50 mm cone plate with a 1° angle configuration was used, and the temperature was set constant at 25 °C. Storage (G′) and loss (G″) moduli were measured at 0.01% strain with an angular frequency range from 0.1 to 300 rad/s.

2.4.11 Cell Culture

The murine macrophage cell line RAW 264.7 was maintained at 37 °C/5% CO2 in RPMI 1640 (Invitrogen Life Technologies, Carlsbad, CA) supplemented with 10% FBS (Gibco BRL, Grand Island, NY), penicillin (100 U/ml), and streptomycin (100 µg/mL).

2.4.12 MTT Assay

For the effect of the compound on cell viability to be assessed, the MTT assay was performed. Briefly, 104 cells were plated in a 96-well plate and treated with different concentration of the compound for 4 h. Thereafter, MTT was added and incubated at 37 °C for 4 h. The formazan crystals were

dissolved in the solubilization buffer, and absorbance was recorded at 570 nm. The extent of cell viability was ascertained as the percent decrease in viability with respect to control or untreated cells.

2.4.13 Cellular and Subcellular Localization

Cells were plated onto the coverslips at a density of 103 cells and treated with compound for 4 h. For colocalization experiments, cells were first incubated with MitoTracker Red-CMXRos and then treated with the compound as mentioned earlier. The cells were then fixed and mounted on slides. For the uptake mechanism of **PA-1** to be ascertained, different inhibitors or treatments were used to block internalization pathways. First, 50 μM 2-deoxy-D-glucose, 5 mM MβCD, and 2 μM cytoD were used to deplete cells of ATP, cholesterol, or inhibit actin polymerization. For the roles of serum protein in the uptake of **PA-1** to be studied, cells were washed with serum-free media before the addition of the **PA-1** in unsupplemented medium. Then, the cells were kept at 4 °C before the addition of **PA-1** to understand whether low temperature affects the uptake of the nanoparticles. Cells were processed as mentioned before and visualized under an Olympus IX81 microscope equipped with (N.A. 1.45) objective. The images thus captured were processed using an Olympus Fluoview (Tokyo, Japan) (version 3.1a) and analyzed by ImageJ program downloaded from National Institutes of Health (//rsb.info.nih.gov) and mounted using Adobe Photoshop software.

2.4.14 Lambda Scanning

For the confocal lambda scan study, cells were incubated with 500 μM of the compound and incubated for 4 h at 37 °C. Thereafter, the cells were fixed and mounted on a glass slide, and lambda scan was performed where the samples were excited at 350 nm and images were acquired in the emission range of 400–600 nm. Different regions of interest (ROI) of the acquired image were selected manually, and the corresponding emission spectra were processed using Olympus Fluoview (Tokyo, Japan) (version 3.1a) and mounted using Adobe Photoshop software.

भारतीय प्रौद्योगिकी संस्थान गुवाहाटी
Indian Institute of Technology Guwahati

Chapter – 3

Carbon Quantum Dot/Peptide Composite Xerogel Based Sensor: Ultra-fast, Highly Sensitive and Selective toward p-Xylene at Room Temperature

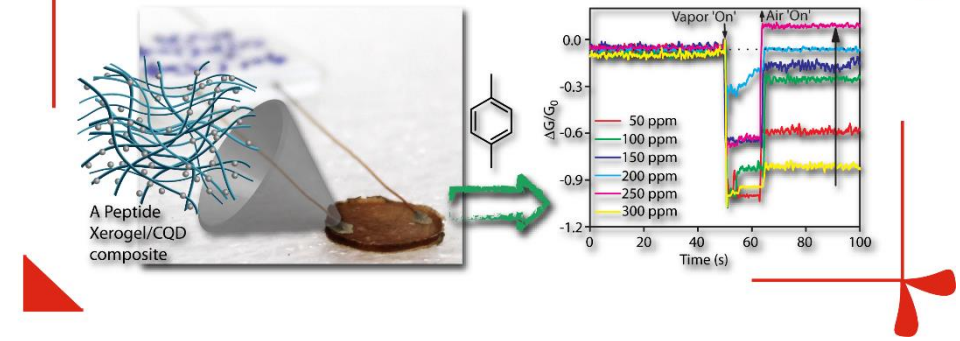

3.1 Introduction

Considering the severe consequences of inhaling toxic volatile organic compounds (VOCs) present in the environment, it is important to have a compact monitoring device and there is currently great interest in R&D to develop such systems. So far, the gas sensing and especially, the VOC sensing relies on metal oxide semiconductors.[163] Metal oxide based sensors have advantages of high sensitivity, ease of fabrication and cost-effectiveness.[164] However, most of the metal oxide semiconductors show strong responses to ethanol and thus loses the selectivity toward the organic aromatic hydrocarbon vapors.[163,165] Amongst the toxic aromatic hydrocarbons (AHCs), xylene is one of the most common representatives and causes damage to the central nervous system and respiratory system.[166] Chemical similarity of benzene, toluene, and xylene makes it extremely challenging to design materials which can selectively sense xylene. Though very limited, semiconducting metal oxide based selective sensors toward xylene is reported in the literature.[167] Xylene exists in three different isomeric forms (ortho, meta, and para), and selective sensing of these isomers separately is even more challenging. Indeed, only a few such reports are available where isomer specific sensor for xylene is developed.[167(b-e)] However, most of them are metal oxide based sensors and can only be operated at an elevated temperature with long response/recovery time.[167(b-d)]

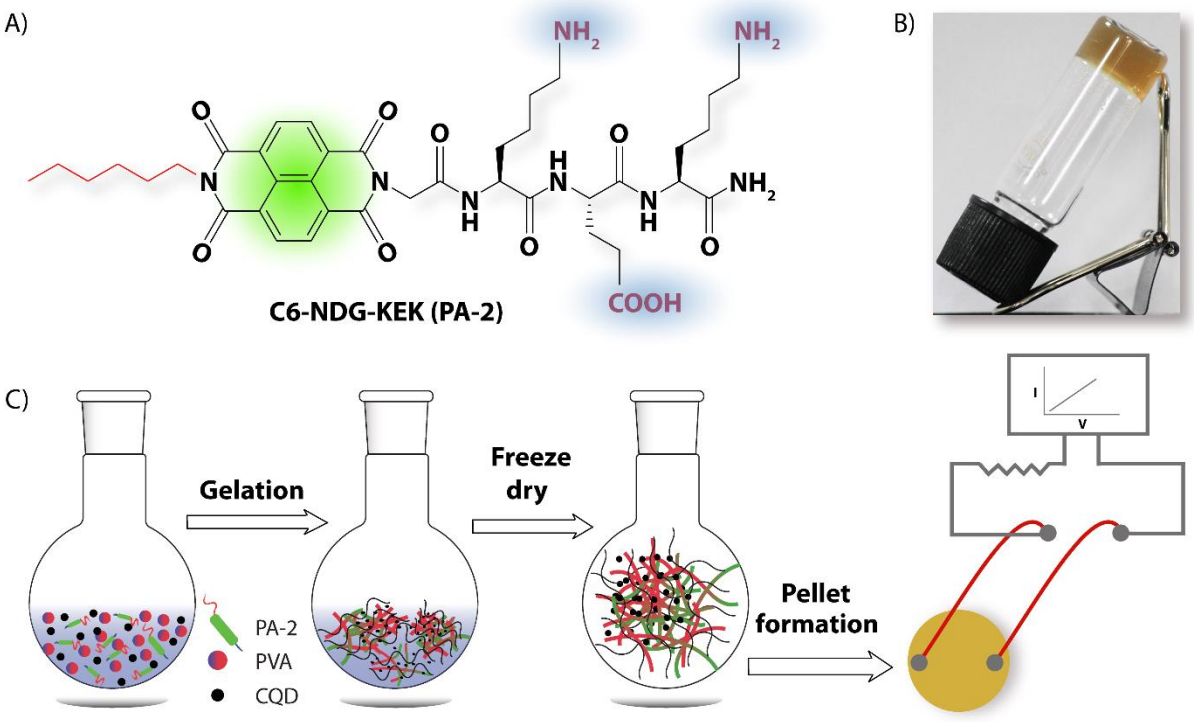

Scheme 3.1 (A) Chemical structures of **PA-2** (B) Pictorial presentation of hydrogelation of **PA-2** in water. (C) The process of the composite hydrogel followed by pellet formation and then attachment of the pellet to the source meter to measure I-V plots.

Organic semiconductors have also been used successfully for gas sensing in the form of semiconducting polymers, semiconducting-SWNT, graphene, or phthalocyanine, but mostly they are limited to oxidative or reductive gases as their electrical conductivity can be modulated in presence of these gases.[168] In this regard, organic *n*-type semiconductors like arylene diimides (ADIs)[131] could be an attractive alternative as appropriate stacking with a specific aromatic hydrocarbon or even a specific structural isomer may cause a substantial change in the conducting property of these ADIs. However, to construct such a device with ADIs, it is essential to create an ordered arrangement of the π-systems of ADIs through controlled self-assembly.[111,112,169(a-c)] In order to create sensors for a specific aromatic hydrocarbon using these ADIs, one thus needs to create a self-assembled system where the target AHC can stack in between the ADI molecules and affect the conductance of the system. Moreover, the ordered arrangement of ADI molecules and their fast and strong binding with specific aromatic gas can lead to room temperature sensors with extremely low response time i.e. in milliseconds (ms). One such possible way is to construct peptide-ADI conjugates which can self-assemble in appropriate media to provide the required arrangement of the π-rings of ADIs. Recently, we have shown that through attachment of small peptide sequences to ADIs the self-assembly and hence the morphology can be fine-tuned.[111-113,170] The conducting property of these aggregates is strongly dependent on the aggregation pattern.[111-113] We envisioned that proper attachment of peptide sequences with naphthalene diimide (NDI) can lead to the ordered arrangement of the NDI core in an aqueous medium and these assembled structures can be used for efficient and selective detection of aromatic organic gases.

With this notion, we have prepared a peptide amphiphile having NDI-peptide conjugate (**PA-2**, **scheme 3.1A**) which self-assembles in water to form high aspect ratio nano-fibers and eventually a self-supporting hydrogel. To this end, carbon-based quantum dot (CQD) have been widely investigated due to their unique chemical stability and interesting electronic properties.[171(a-b)] Recent reports show the presence of CQD as a conducting substance in conjugation with a conducting matrix or polymers affects the electron/hole properties significantly.[172(a-c)] Following these reports, CQD was added in this hydrogel in the presence of a non-interfering polymer and the xerogel of the composite material was tested for detection of VOCs. Interestingly, high sensitivity and selectivity were observed for *p*-xylene. Notably, this is the first example of any organic *n*-type semiconductor as a sensor for organic VOCs.

3.2 Results and Discussion

The peptide amphiphile, (**scheme 1A**) was designed to incorporate an appropriate hydrophobic-lipophilic balance through attachment of a hydrophobic tail and three hydrophilic amino acid

residues (two lysines and one glutamic acid) while keeping the overall charge of (+1) on the molecule at neutral medium. Incorporation of a naphthalene diimide (NDI) unit served two purposes, i) providing π–π stacking interaction and facilitating the self-assembly and ii) introducing the semiconducting property. **PA-2** was synthesized by standard solid phase peptide synthesis protocol (**scheme 3.2**). The C6-NDI-G part was synthesized using one of our previously published work. This fragment of the peptide was then attached to the main peptide sequence following the standard solid phase peptide synthesis (SPPS) protocol on Rink amide resin. The crude product was purified in reverse phase HPLC to obtain the desired product with 70% yield. Characterization was done by NMR and ESI-MS techniques (m/z = 793 $[M+H]^+$ and 397 $[M]^{2+}$). When dissolved in water, **PA-2** formed a self-supporting hydrogel (**scheme 3.1B**) with a recorded minimum gelation concentration (MGC) of 19.6 mM (2 wt%). The hydrogel was thermo-reversible with a gel to sol transition temperature (T_g) of 42 °C at MGC and the T_g value followed a linear relation with the concentration of **PA-2**. Notably, the hydrogel remained stable under ambient conditions over a long period of time (more than 2 months). TEM analysis of matured (24 h) hydrogel samples showed the presence of a fibrous network (**fig. 3.2A**). The fibers are a few nanometers long with a diameter of ~8 nm.

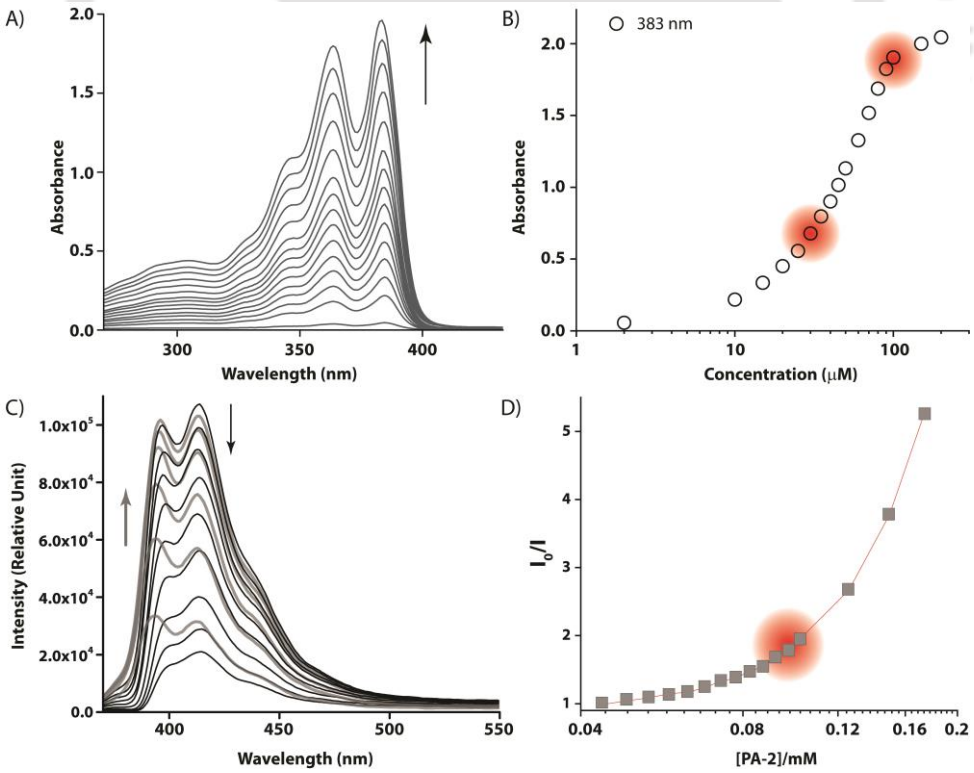

Fig. 3.1 (A) Concentration dependent (A) absorption and (C) emission spectra of **PA-2**. (B) Dependence of absorption at 383 nm and on the concentration of **PA-2**. (D) I_0/I vs concentration of the **PA-2** plot as obtained from the emission spectra; I_0 = emission intensity at 411 nm when [**PA-2**] = 0.04 mM and I = emission intensity at 411 nm at any concentration above 0.04 mM.

To investigate the mechanistic details of the hydrogelation, the spectroscopic properties of **PA-2** were first analyzed in a water medium. Spectroscopic data provides the best clues to interpret the correlation between concentration and aggregation behavior of the molecules while treated in a proper medium. Hence, as a primary experiment, concentration-dependent absorption of **PA-2** was performed first to observe any change in the spectra with increasing concentration of the molecules. **PA-2** showed two well-resolved absorption bands at 362 and 383 nm with a shoulder at 345 nm, which are the characteristic peaks for A_{0-0}, A_{0-1}, and A_{0-2} transitions respectively arising from the NDI core. **Fig. 3.1A** shows the absorption spectra of **PA-2** with increasing concentration. It was observed that, with increasing concentrations of the peptide conjugate, absorbance increases without any shifting or broadening of peaks. However, the absorption (383 nm) vs concentration plot (**fig. 3.1B**) shows two inflection points in the enhancement of absorption. The first change was observed at a concentration of 0.035 mM whereas the second one was found at 0.1 mM.

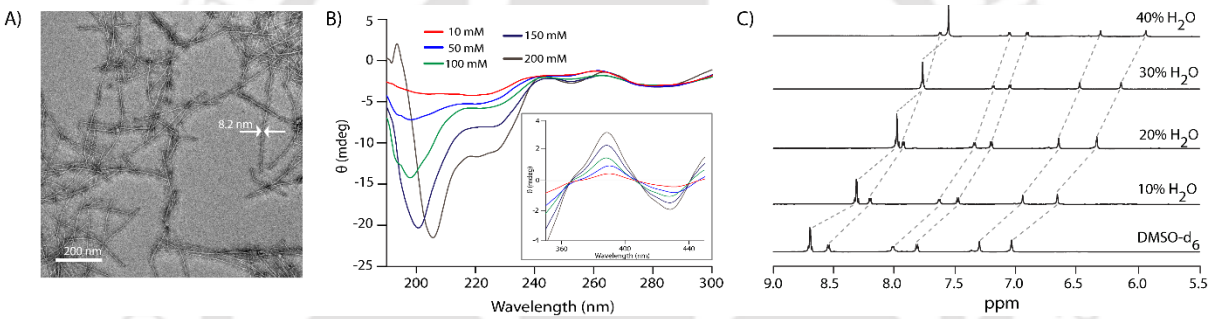

Fig. 3.2 (A) FETEM image of a 2 wt% hydrogel of **PA-2** in water showing the high aspect ratio fibers. All experiments were carried out at room temperature. (B) CD spectra of aqueous solutions of **PA-2** with increasing concentration. Inset: the same for the NDI absorption region. (C) ^{1}H NMR spectra of **PA-2** in DMSO-d_6 with an increasing amount of water (showing only the aromatic region).

Similarly, the fluorescence emission spectra (**fig. 3.1C**) of aqueous solutions of **PA-2** with increasing concentration exhibited (λ_{ex} = 360 nm) two emission bands near 393 and 411 nm whose intensities were found to increase up to a concentration of around 0.040 mM and then gradually decreased up to 0.18 mM. This is a typical feature for NDI-based molecules where the NDI groups form aggregates through π–π interaction. The aggregation begins at the concentration where the intensity is maximum. Due to the electronic transition from π→π* the number of free excited molecules at the first excited state drops and consequently the quenching happens in a continuous way. However, the lower inflection point in the absorption spectra can be considered as the first minimum aggregation concentration i.e. 0.035 mM. The absorbance vs concentration plot has also pointed out the second inflection point at 0.1 mM (**fig. 3.1B**), which was further confirmed from the emission intensity (I_0/I) vs concentration plot (**fig. 3.1D**). Here, the highest intensity at 0.040 mM was considered as I_0, and subsequent intensities were considered as I. When I_0/I was plotted against concentration, a clear inflection point at 0.1 mM was observed for the emission band (411 nm) as

can be seen in **fig. 3.1D**. Hence, the second inflection point can be considered as a second aggregation concentration suggesting for a second order organization.

For further analysis of self-assembly at higher concentrations, we have performed a concentration-dependent DLS experiment (data not shown). However, even after a several time repeat, we were unable to draw any conclusion from the size distributions due to some uneven or irregular changes. Composed of one hydrophobic tail group along with a polar head group, the peptide amphiphile **PA-2** could also behave as a surfactant. Considering the fact, concentration-dependent surface tension has been performed, which showed a linear decrease in intensities after 0.04 mM without any other inflection point (data not being shown). Also, no specific morphology was found in FESEM and TEM experiments. Hence, both the DLS and surface tension experiments were failed to carry over the investigation at higher concentrations.

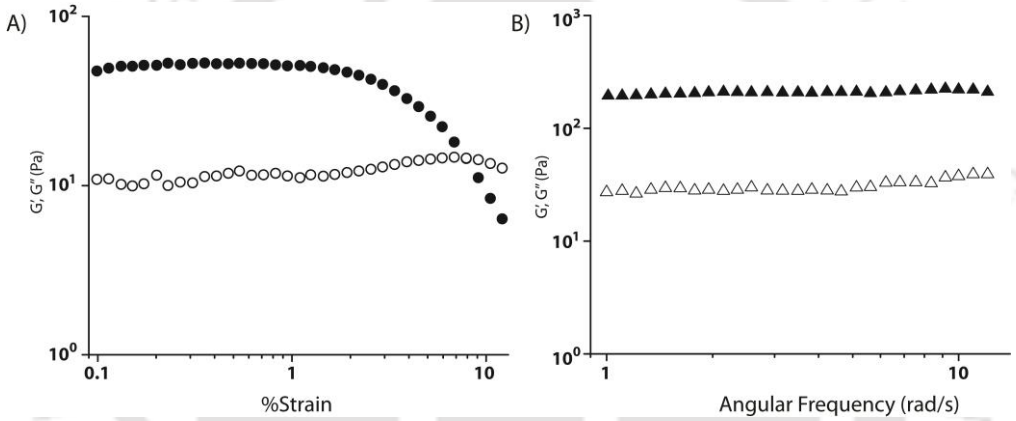

Fig. 3.3 Changes in storage and loss modulus as a function of (A) shear strain and (B) angular frequency for a 2 wt% hydrogel of **PA-2**.

Circular dichroism (CD) spectra of aqueous **PA-2** showed the formation of α-helical structure at a higher concentration as two negative signals typical of α-helix appeared at 206 and 225 nm (**fig. 3.2B**). In the NDI absorption region, a bisignate peak with a positive to negative cross-over point at 411 nm demonstrates the right-handed helicity of the aggregates.[111] Field Emission-Transmission Electron Microscope (FE-TEM) analyses of the hydrogel showed the presence of a network of long fibers (length: ≤1 μm) with a diameter of ~ 7-10 nm (**fig. 3.2A**). The high aspect ratio fibers formed presumably via hierarchical aggregation of **PA-2** through π–π interaction and hydrogen bonding.

^{1}H NMR study of **PA-2** in DMSO-d_6 revealed the involvement of the aromatic protons of NDI group via π–π stacking as the signal corresponding to these protons showed a continuous up-field shift with an increasing amount of water (**fig. 3.2C**). The amide NHs also demonstrated up-field shift which could be attributed to the combination of breakage of intermolecular hydrogen bonds in DMSO-d_6 and formation of hydrogen bonds with water molecules at higher water content.[170]

The mechanical strength of the hydrogel was determined by its viscoelastic properties using rheometer. A strain sweep test was performed first to identify the linear viscoelastic region (LVR) over a range from 0.1 to 100 % strain at a fixed oscillatory frequency of 1 rad/s (**fig. 3.3A**). The LVR can be defined as where strain has no impact upon G′ and G″. From the strain sweep experiment of the gel, it was observed that the gel converts to sol state within 10 % applied strain while the yield point was calculated around 1% under the fixed angular frequency of 1 rad/s at 25 °C. In rheological terminology, it would be said that within the applied range ≤8 % strain, G′>G″, i.e. gel holds its elasticity and remains as a gel. However, after the crossover, when G″>G′, the gel loses its elasticity and converts to sol state. Further, the mechanical strength of the gel was determined from oscillatory test i.e. frequency sweep (**fig. 3.3B**), which was carried out under an appropriate strain (γ = 0.1 %) selected from the LVR at 25 °C. The frequency sweep showed the gel was independent of the frequency over the region and found to be sufficiently strong.

Once the hydrogelation and its properties were established, we wanted to test our hypothesis. Composites were prepared considering the ease of preparation and handling the device. As solid support, polyvinyl alcohol (PVA) was used as the polymer does not contribute to the conductivity but provide stability as well as strength to the materials. Devices were prepared by dissolving 15 mg of **PA-2**, 50 mg of PVA and 10 mg CQD in 0.5 mL of water keeping the concentration of the gelator above MGC. After 12 h of incubation, self-supporting hydrogels were formed and analysis of hydrogels by rheology showed that presence of PVA strengthen the hydrogel as both G′ and G″ were higher than that of the hydrogel without PVA and CQD (**fig. 3.4A**). However, importantly, the gel property remained intact. The composite hydrogels were then lyophilized to get the xerogels. Microscopic analysis of the xerogels using FETEM showed incorporation of CQD of ~ 5-10 nm diameter (inset in **fig. 3.4B**) within the fibrous network of the hydrogel (**fig. 3.4B**). The high-resolution TEM (HR-TEM) image of CQD (inset in **fig. 3.4B**) displays a clear interplanar spacing of 0.354 nm, indicating their high crystallinity. Notably, the presence of PVA and CQD did not affect the fiber dimensions as well as a network structure. The solid was then used to prepare pellets where amounts of all the components remained same and electrodes were attached using silver paste. As controls, experiments from other combinations like xerogel of **PA-2**, **PA-2**/CQD were prepared using the same protocol, where PVA was used just as a binder.

For initial screening, we focused on the conductivity of these samples. As can be seen from **fig. 3.4C**, a potential of -5 to 5 V was applied and current-voltage (I-V) characteristics for each sample were measured both in the air and under vacuum. The samples from the mixture of as-synthesized **PA-2** (solid **PA-2** in presence and absence of solid PVA/CQD) showed irreproducible results with extremely low conductivity within this bias range while samples of the only CQD in PVA did not show any conductivity. Xerogel of **PA-2** showed moderate semiconducting property (conductance,

132 pS) while the presence of CQD (**PA-2**/CQD) improved the conducting property (conductance, 3840 pS) noticeably. Interestingly, measurement under ambient condition resulted in significantly higher conductivity for all the samples compared to that under vacuum (22 and 1180 pS for **PA-2** and **PA-2**/CQD, respectively). It is clear from these results that the higher conductivity can be achieved under the ambient condition when CQD is present in the composite samples.

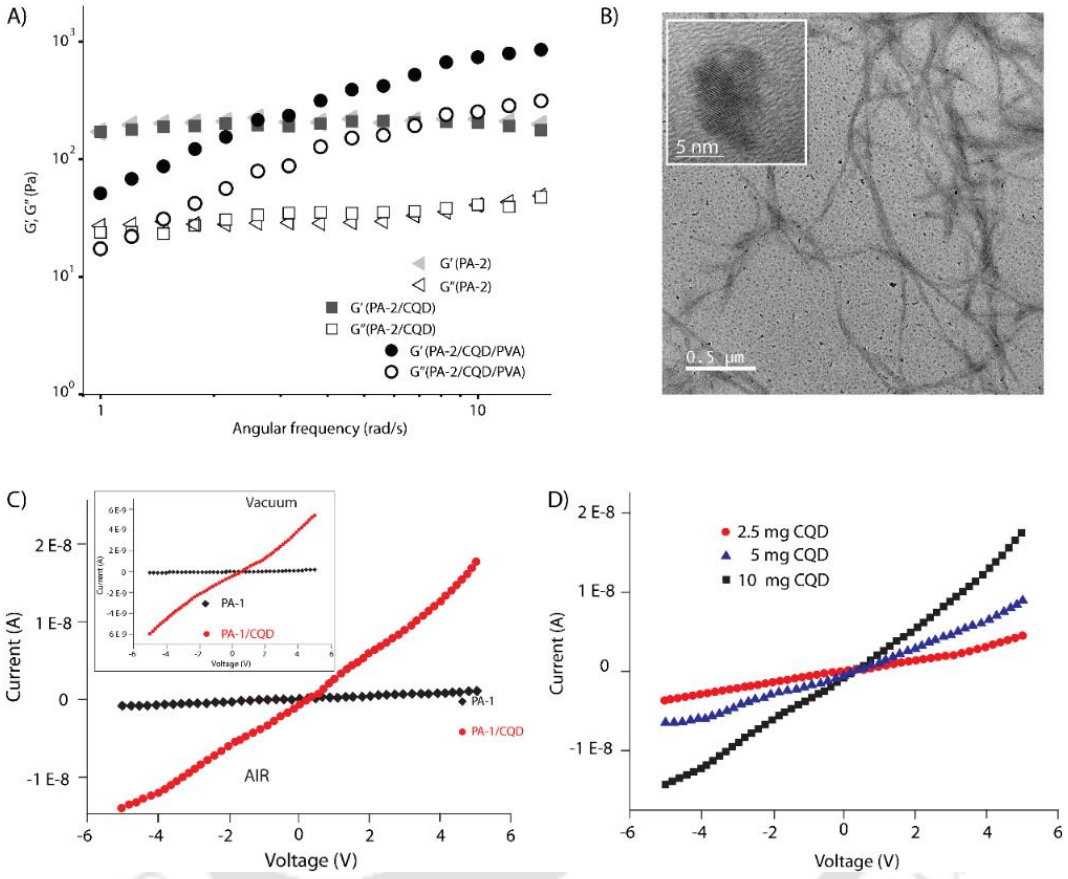

Fig. 3.4 (A) Changes in storage and loss modulus as a function of angular frequency for hydrogels of **PA-2** (2 wt%) in the presence and absence of PVA and CQD. (B) FE-TEM images of a composite hydrogel (15 mg of **PA-2**, 50 mg of PVA and 10 mg of CQD in water) showing the incorporation of CQDs into the hydrogel fibers. Inset: HR-TEM image of CQD showing the clear lattice spacing. (C) I-V plots of different composite devices in the air and under vacuum (inset). (D) Current-Voltage (I-V) plots of prepared devices using varying amounts of CQD. All experiments were performed at room temperature.

Based on these results, the amount of CQD was varied (2.5, 5, 10 and 15 mg) keeping the amounts of other constituents and procedure similar. With 15 mg CQD, handling the device was difficult as it was brittle in nature. However, with an increase in CQD content, the conductivity enhanced from 680 pS (2.5 mg CQD) to 3840 (10 mg CQD) as can be seen from **fig. 3.4D**. Based on these results, for the sensing of VOCs we have selected a composite composition, xerogel of a 24 h matured hydrogel containing 15 mg of **PA-2**, 50 mg of PVA and 10 mg of CQD. A qualitative study of different VOCs showed that the device is highly responsive to xylene vapor and specifically toward *p*-xylene (data not shown). Based on the results, the device was further tested quantitatively for xylene sensing.

Table 3.1. Conductance values for the devices measured at room temperature and under different conditions (all samples contain 50 mg of PVA).

Device composition	*Conductance (pS)*
PA-2	Air: 132 Vacuum: 22
CQD (2.5 mg)/PA-2	Air: 680
CQD (5.0 mg)/PA-2	Air: 2000
CQD (10.0 mg)/PA-2	Air: 3840 Vacuum: 1180

3.2.1 Gas sensing

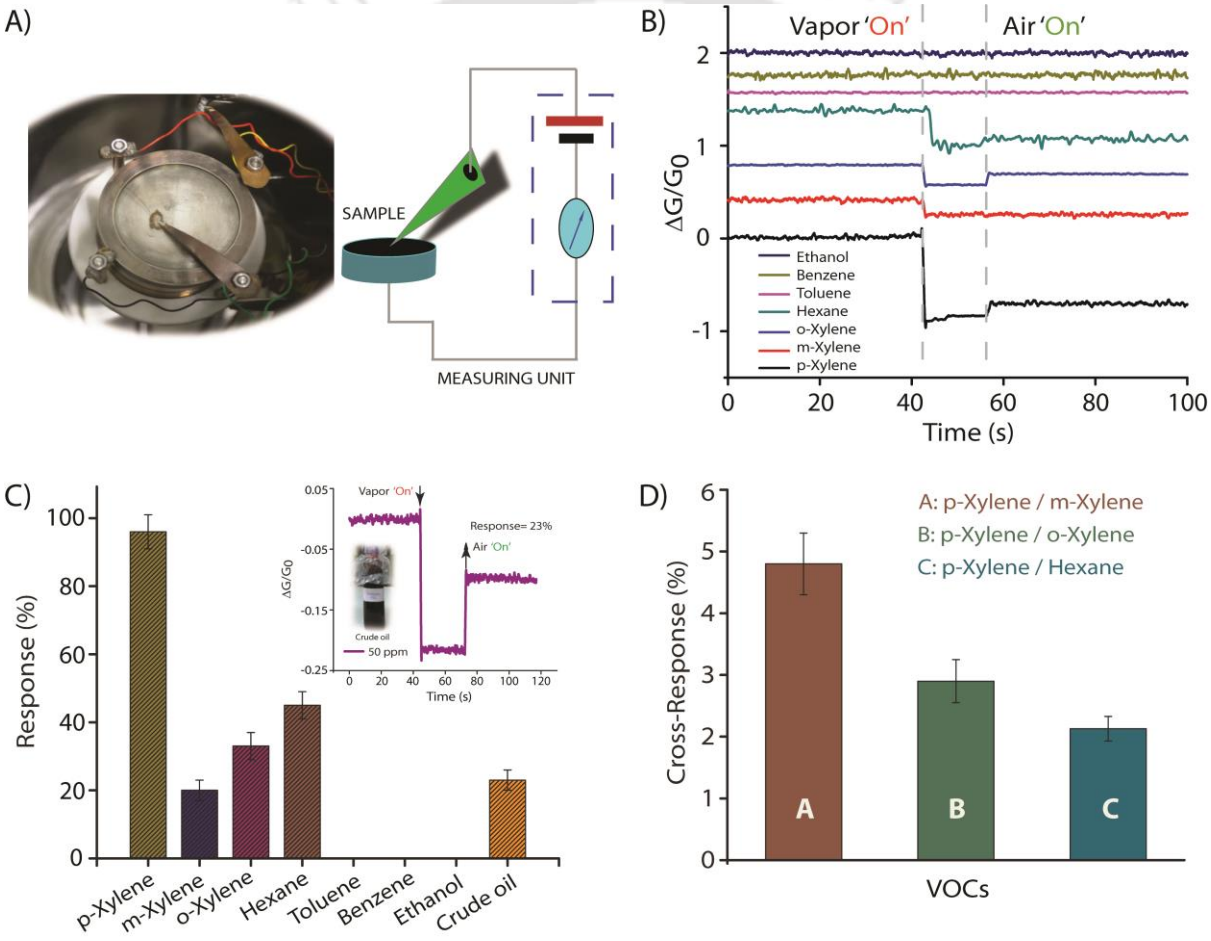

Fig. 3.5 (A) Experimental arrangement for gas sensing measurements with a circuit diagram. (B) Conductance change ($\Delta G/G_0$) of the sensor consisting of 15 mg of **PA-2**, 50 mg of PVA and 10 mg of CQD xerogel composite for different VOCs (50 ppm). (C) Selectivity of the sensor in presence of different VOCs with a fixed concentration of 50 ppm (inset: detection of the crude oil of Indian Oil Corporation Limited using the developed 15 mg of **PA-2**, 50 mg of PVA and 10 mg of CQD Xerogel composite based sensor). (D) Cross-Response characteristics of the sensor (15 mg of **PA-2**, 50 mg of PVA and 10 mg of CQD Xerogel composite) for different VOCs

The experimental arrangement for gas sensing measurements along with the circuit diagram for the present system is shown in **fig. 3.5A**. One of the major concerns for the present day VOC sensors is

their operational inability at room temperature and thus most of them require an additional heating element for successful application of the sensor. Various strategies and experimental methods have been applied to overcome the difficulty and to enhance the sensitivity, particularly at room temperature.[173(a-d)] The present prototype confirms its effectiveness as a VOC sensor at room temperature with high sensitivity. Hence, real-time monitoring of toxic gases can be possible without any pre-heating and that in turn reduces the energy consumption as well as enhances the thermal safety of the system.

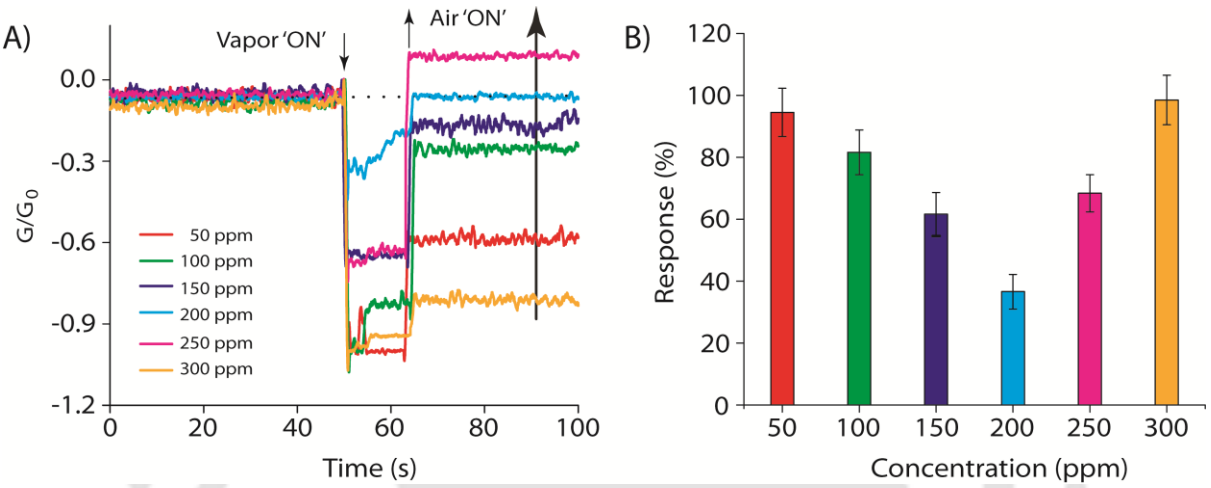

Fig. 3.6 (A) Change in conductance of the sensor at different concentrations of *p*-xylene. (B) Response plot for different concentrations of *p*-xylene.

As mentioned before, selectivity toward a specific gas is another important parameter which needs to be taken care of while developing new sensors. In the present study, the developed sensor is selective toward *p*-xylene even at very low concentration (50 ppm) exposure. **Fig. 3.5B-C** confirms the selectivity as the sensor showed the highest response to *p*-xylene amongst all the VOCs tested (50 ppm of *m*-xylene, *o*-xylene, toluene, benzene, ethanol). For ortho- and meta- isomers, the responses were 33 and 20% respectively. Interestingly, no response was recorded for benzene, toluene, and ethanol under similar experimental conditions. Relatively high cross-response values of the order of 4.8 ($R_{p\text{-xylene}}/R_{m\text{-xylene}}$), 2.9 ($R_{p\text{-xylene}}/R_{o\text{-xylene}}$) also supports the selectivity towards *p*-xylene (**fig. 3.5D**). The detection ability of the developed sensor was not limited to in-lab conventional experiments. We have also tested our developed sensor in the presence of industrial grade crude oil from Indian Oil Corporation Limited, India (IOCL) to check the versatility and ability of direct industrial application of our sensor. The as-received crude oil contains a number of toxic VOCs and the detection or analysis of this type of oils is usually very expensive, time-consuming, and requires complicated sample preparation as well as instrumental support (e.g, gas chromatography, mass spectrometry, infrared spectroscopy etc.). A reliable detection (**Inset, fig. 3.5C**) of the as mentioned crude oil was recorded (**fig. 3.5C**) using the present prototype without any complicated

instrumental arrangement and pre-treatment of the test sample. The sensor possesses inherent direct applicability and could be used as a reliable and inexpensive alternative for fast and real-time detection of samples from industries.

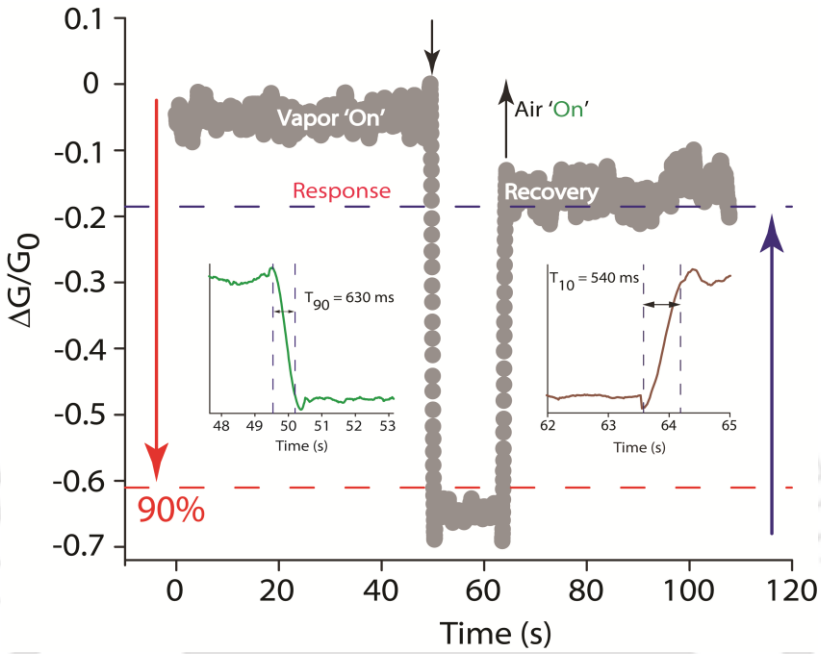

Fig. 3.7 Response & Recovery time characteristics of the sensor for 50 ppm *p*-xylene.

As per the directives of Centers for Disease Control and Prevention (CDC),[174] inhalation of 50 ppm or more xylene for prolong duration could affect human health severely. Thus, for an efficient xylene sensor, it is extremely important to have a detection limit within this range. The present sensor showed relatively high (R≈96%) response at room temperature for low concentration (50 ppm) exposure to *p*-xylene. With increasing concentration, the response at first decreased followed by an enhancement as shown in **fig. 3.6A-B**. For comparison, we have examined the sensing performances of only **PA-2** xerogel without incorporation of CQDs (**fig. 3.8A-D**). At room temperature, the sample showed a very poor response (R ≈ 10-15%) to *p*-xylene which is far below the response obtained for the device prepared using CQD. The result shows that though the xerogel of **PA-2** is capable of sensing *p*-xylene selectively, the incorporation of CQDs in the network of the gel amplifies the response significantly.

Another important parameter for this type of VOC sensors is their reversibility. An irreversible type gas sensor can be understood as a particular one showing a partial recovery of the initial (in absence of the target gas/vapor) signal (current/resistance/conductance) while for a reversible sensor, the recovery should be complete.[175] A reversible sensor is always desirable and in the present case, the sensor showed complete recovery at and above 200 ppm concentration of *p*-

xylene. However, below this concentration, the recovery was ~90 % which is definitely an excellent recovery for practical uses.

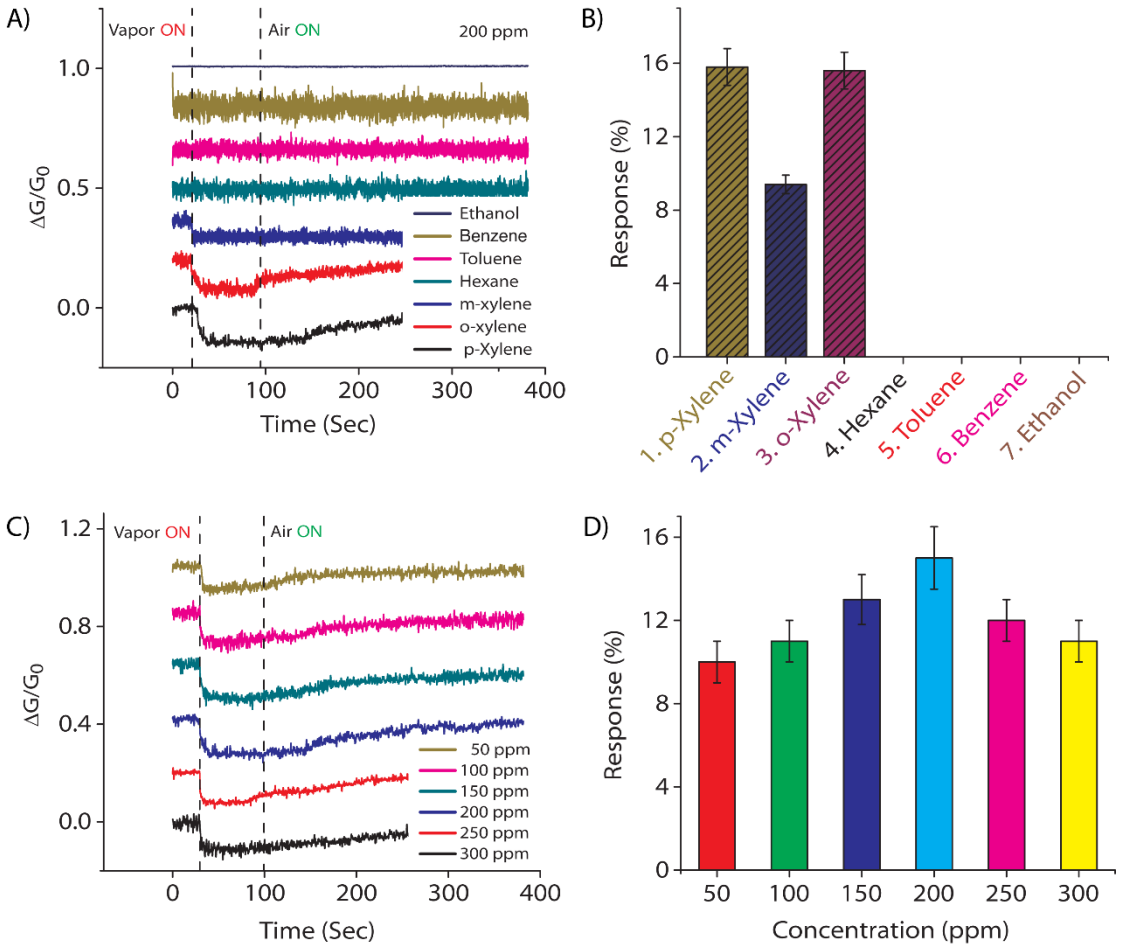

Fig. 3.8 Response characteristics of a sensor with 15 mg of **PA-2** and 50 mg of PVA xerogel composite *i.e.* without CQD. A) Conductance change of the sensor in the presence of different VOCs. B) Variation of responses for different VOCs. C) The response curve for different concentration (50 – 300 ppm) of *p*-xylene. D) Response vs. Concentration plot using a particular VOC of *p*-xylene.

Another important parameter for this type of VOC sensors is their reversibility. An irreversible type gas sensor can be understood as a particular one showing a partial recovery of the initial (in absence of the target gas/vapor) signal (current/resistance/conductance) while for a reversible sensor, the recovery should be complete.[175] A reversible sensor is always desirable and in the present case, the sensor showed complete recovery at and above 200 ppm concentration of *p*-xylene. However, below this concentration, the recovery was ~90 % which is definitely an excellent recovery for practical uses.

Selectivity, operating temperature, response (T_{90}) and recovery time (T_{10}) are the other important parameters for a particular gas sensor. Response time (T_{90}) can be thought to be as the time required to rise up to 90% of the maximum response value (when exposed to target gas) whereas the time duration involved to regain 10% of the base value (in presence of air) is the

recovery time (T_{10}). Fast response and recovery are one of the desired features for a successful gas sensor. **Fig. 3.7** represents the corresponding response & recovery characteristics, where, T_{90} = 630 ms & T_{10} = 540 ms for 50 ppm *p*-xylene. The fast response & recovery characteristics achieved in this present study implies a timely detection for target gases. A comparative summary is provided in **Table 3.2** which reflects different aspects of the present work and previously available similar literatures.

Table 3.2. Comparative summary between the present work and the previous literature.

Materials [Reference]	*VOC, Concentration*	*Response/ Sensitivity*	*Operating Temperature*	*Response Time*	*Recovery Time*
Carbon quantum dots/Peptide Xerogel (current work)	*p*-xylene, 50 ppm	96 %[a]	RT	630 ms	540 ms
NiO/$NiMoO_4$ nanocomposite [167c]	*p*-xylene, 5 ppm	101.5[b]	325 – 425 °C	10 – 50 s	20 – 200 s
Cr_2O_3-$ZnCr_2O_4$ hetero-nanostructures[167b]	*p*-xylene, 5 ppm	69.2[b]	250 – 350 °C	----	----
Co-doped branched ZnO-nanowires[167d]	*p*-xylene, 5 ppm	19.55[c]	400 °C	----	----
Au-loaded $WO_3.H_2O$ nanocubes[167h]	xylene, 5 ppm	26.4[c]	255 °C	1 s	1 s
Fe-doped MoO_3 nanobelts[167f]	xylene, 100 ppm	6.1[c]	136 – 206 °C	20 s	75 s
Ni-deposited metal oxide thin film[167g]	xylene, 10 ppm	10[c]	340 °C	20 s	300 s
SWCNT & cellulose polymer concentrator[167e]	*m*-xylene, 56 ppm	0.5 %[d]	23 °C	7 s	20 s

Response, [a]$R = |\Delta G/G_0|(\%)$; Sensitivity, [b]$S=R_g/R_a$; [c]$S=R_a/R_g$; [d]$R= -\Delta G/G_0(\%)$

It was obvious from the information in **Table 3.2** that majority of the available sensing materials (mainly MOS type) for VOC detection operates at relatively high temperature (>200 °C) utilizing additional heating elements to achieve desired operating condition which is a threat to thermal safety of the system. It is clear from the response and recovery time of other xylene sensors (in seconds to minutes), the present sensor is ultra fast as it operates within the millisecond's range. In this view, the present work introduces a sensor which carries a promising ability to operate truly at room temperature with ultra-fast response and recovery characteristics along with the possibility of moderate response comparable to MOS sensors in the detection of different toxic VOCs.

The diffusion characteristics of xylene isomers inside the sensing material (CQD/**PA-2**) is helpful to explain the sensing mechanism when exposed to these VOCs. In this view, the self-

diffusion coefficient of the three xylene isomers (*m*-, *o*- and *p*-xylene) can be calculated by utilizing the following equation[176]

$$D = \frac{3}{8nd^2}\sqrt{\frac{KT}{\pi m}}$$

where *D* is the self-diffusion coefficient, *n* is the number density, *d* is the diameter of the gas molecules, *m* is the mass of the gas, *K* is the Boltzmann constant and *T* is the operating temperature (Room temperature, T = 300K for this measurement) of the sensor at absolute scale. Among the calculated self-diffusion coefficients, *p*-xylene found to have the highest value of 1.73×10^{-9} m^2/s and this undoubtedly confirms the greater mobility of this particular isomer compared to other two (1.41×10^{-9} m^2/s for ortho and 1.53×10^{-9} m^2/s for meta). The results obtained in the present study are quite consistent with the outcome of the reported work by Zhai *et.al*[177] In that report, the diffusion coefficient was estimated through Molecular Dynamic Simulation of xylene isomers in FAU zeolite. The highly mobile character of *p*-xylene corresponds to its fast diffusion ability through the sensing material compared to other VOCs and presumably the reason behind the highly sensitive and selective detection observed for *p*-xylene at room temperature using the present prototype.

The extremely efficient sensing of *p*-xylene can also be attributed to the binding energies for *p*-xylene@CQD/**PA-2** calculated via density functional theory. The energy optimized structures of complexes of **PA-2** with different xylenes are shown in **fig. 3.9A-C**. The energy optimized structure of **PA-2** showed a much higher affinity (-14.93 kcal $mole^{-1}$) toward *p*-xylene compared to the other isomers (-11.38, -10.42 kcal $mole^{-1}$ for *o*- and *m*- xylenes, respectively). A comparative study for other VOCs shows that the binding energy is significantly higher for benzene or toluene which results in the low to no response in the presence of these VOCs. Based on these observations, it can be concluded that *p*-xylene binds with the NDI moiety of **PA-2** in the fibers of the device more efficiently than any of the VOCs tested. The stronger binding leads to a better signal and thus the selectivity toward *p*-xylene was observed for the device.

As supporting evidence, the reported material (**PA-2** with PVA and CQD) was investigated in the presence and absence of *p*-xylene with the help of Fourier Transform Infrared Spectroscopy (FTIR). In **fig. 3.9D**, the peaks at 2925 and 2856 cm^{-1} are related to the stretching vibrations of $-CH_3$ & $-CH_2$ of CQD/**PA-2**. On the other hand, the peak observed at 3432 cm^{-1} is due to N-H bonds of the material. Other two peaks at 1707 and 1668 cm^{-1} are of amide/imide carbonyls of the peptide. Three peaks out of seven had been shifted (3432 to 3428 cm^{-1}, 1707 to 1704 cm^{-1} and 1668 to 1671 cm^{-1}) by 3-4 cm^{-1} (shown in blue and red color of **fig.3.9D**), when the sensing material was exposed to *p*-xylene vapor, indicating a clear interaction between the respective VOC vapor and the different segment of the material.

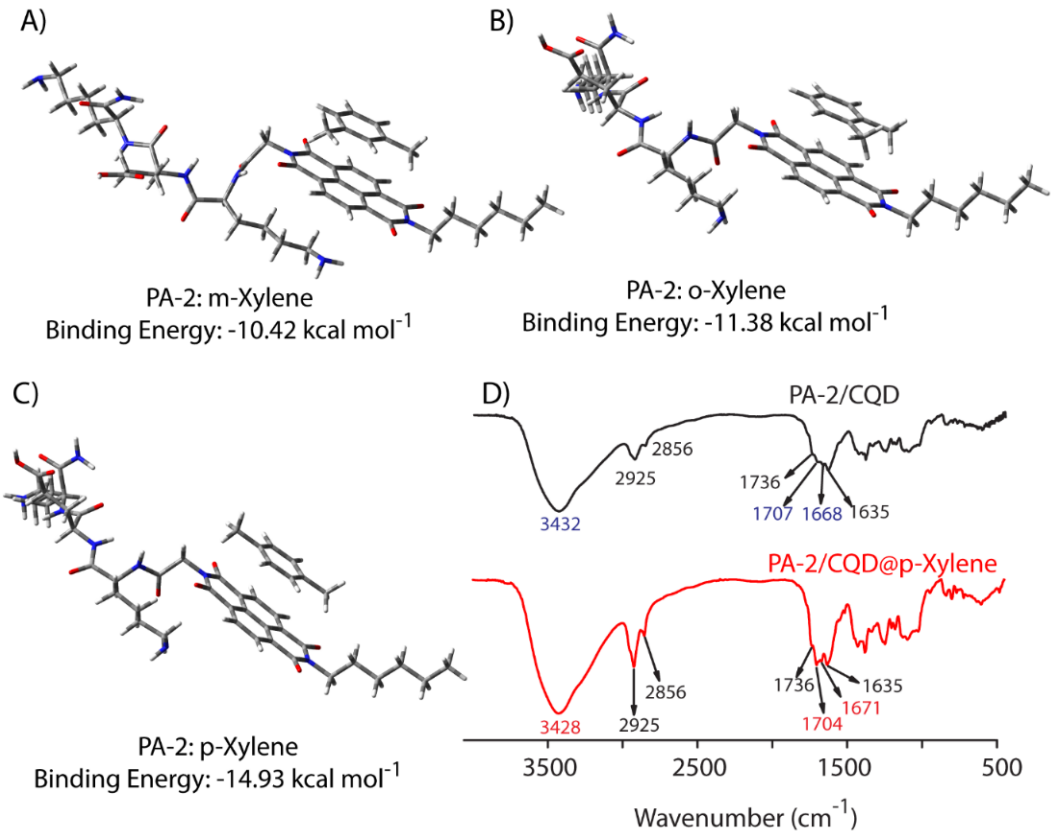

Fig.3.9 (A-C) Energy optimized structures of complexes of **PA-2** with different xylenes obtained from DFT calculations. (D) FTIR Spectrum of CQD/**PA-2** and CQD/**PA-2** when exposed to the *p*-xylene vapor.

3.3 Conclusion

In summary, an all-organic ultra-fast and selective sensor for *p*-xylene are reported. The construction of the sensor was done by incorporating CQD on the high aspect ratio fibers formed by a PA bearing semiconducting NDI group. An ordered arrangement of the NDI group through self-assembly of the PA facilitates the semiconducting property of the system while the presence of CQD amplifies the signal. The sensor is found to be efficiently and selectively sensing *p*-xylene amongst many VOCs tested. The detection limit for *p*-xylene was observed to be 50 ppm with a response of 96%. Moreover, the sensor was reversible in nature and was successfully applied to industrial grade crude oil. The ultra-fast sensing of VOCs at room temperature is the prime advantage over the other reported sensors and the reported system holds promise for future practical applicability.

3.4 Experimental Section

3.4.1 Materials

Fmoc-Rink Amide Resin and protected amino acids were purchased from GL Biochem (China). HBTU, diisopropylethylamine (DIPEA), 1,4,5,8-naphthalenetetracarboxylic acid dianhydride (NDA), n-hexylamine and Betainehydrochloride were obtained from Sigma-Aldrich (USA), glycine and piperidine were purchased from Merck (India) and used without further purification. HPLC grade dimethylformamide (DMF), acetonitrile were procured from Spectrochem (India) and Fisher Scientific (India), respectively. To prepare samples, Milli-Q water with a conductivity of less than 2 $mScm^{-1}$ was used. Chromatographic purification of the peptide was performed on Ultimate 3000 (Dionex). ESI-MS was performed with a Q-tof-Micro Quadrupole mass spectrophotometer (Micromass). UV-Vis data was recorded with a PerkinElmer Lambda 35 spectrometer. Fluorescence measurements were performed with a Fluoromax-4 spectrofluorometer (HORIBA). Current-Voltage measurements and sensing experiments were performed using a Keithley 2612 Sourcemeter.

3.4.2 Synthesis of PA-2

PA-2 was synthesized following the protocol previously reported in chapter 2.[1] The peptide was prepared using solid phase peptide synthesis technique employing Rink-amide MBHA resin as the solid support. Sequence elongation at the N-terminus was performed by coupling the appropriate Fmoc protected amino acids under standard conditions employing HBTU and DIPEA as coupling reagents. Fmoc deprotection was achieved by treating the resin bound peptide with 20% piperidine in DMF. The peptide was cleaved from the resin employing 95% TFA containing 1% triethylsilane. Precipitation from ether followed by purification using semi-prep HPLC, acetonitrile/water system as the eluent and then lyophilization provided the peptides.

3.4.3 Characterization of PA-2

^{1}H NMR (600 MHz, DMSO-d_6) δ/ppm = 8.75 – 8.66 (br, 4H), 8.02 (s, 1H), 7.82 (s, 1H), 7.31 (s, 1H), 7.04 (br, 2H), 4.85 – 4.68 (m, 2H), 4.31 (d, J = 5.3 Hz, 1H), 4.21 (d, J = 5.6 Hz, 1H), 4.12 (d, J = 5.3 Hz, 1H), 4.09 – 4.04 (m, 2H), 2.76 (dt, J = 24.7, 7.6 Hz, 5H), 2.26 (s, 2H), 1.92 (s, 1H), 1.80 (s, 1H), 1.66 (s, 4H), 1.50 (s, 7H), 1.31 (s, 10H), 0.87 (t, J = 6.9 Hz, 3H).**^{13}C NMR** (151 MHz, DMSO-d_6):δ/ppm = 174.51, 173.77, 171.31, 167.17, 163.10, 163.05, 131.16, 130.95, 127.20, 126.40, 118.81, 52.81, 52.70, 52.58, 43.16, 31.78, 31.70, 31.42, 30.65, 27.82, 27.65, 27.11, 27.05, 26.63, 22.66, 22.45, 14.39. **ESI-MS** calcd. for $[M+H]^+$, $C_{39}H_{52}N_8O_{10}$: 793.38, found: 793.42 ($[M+H]^+$), and 397.21 ($[M+2H]^{2+}$). **HPLC**: The peak of **PA-2** appeared at 11.7 min when the column was eluted with a gradient started from 5% to finish at 100% of acetonitrile in water in a 20 min program.

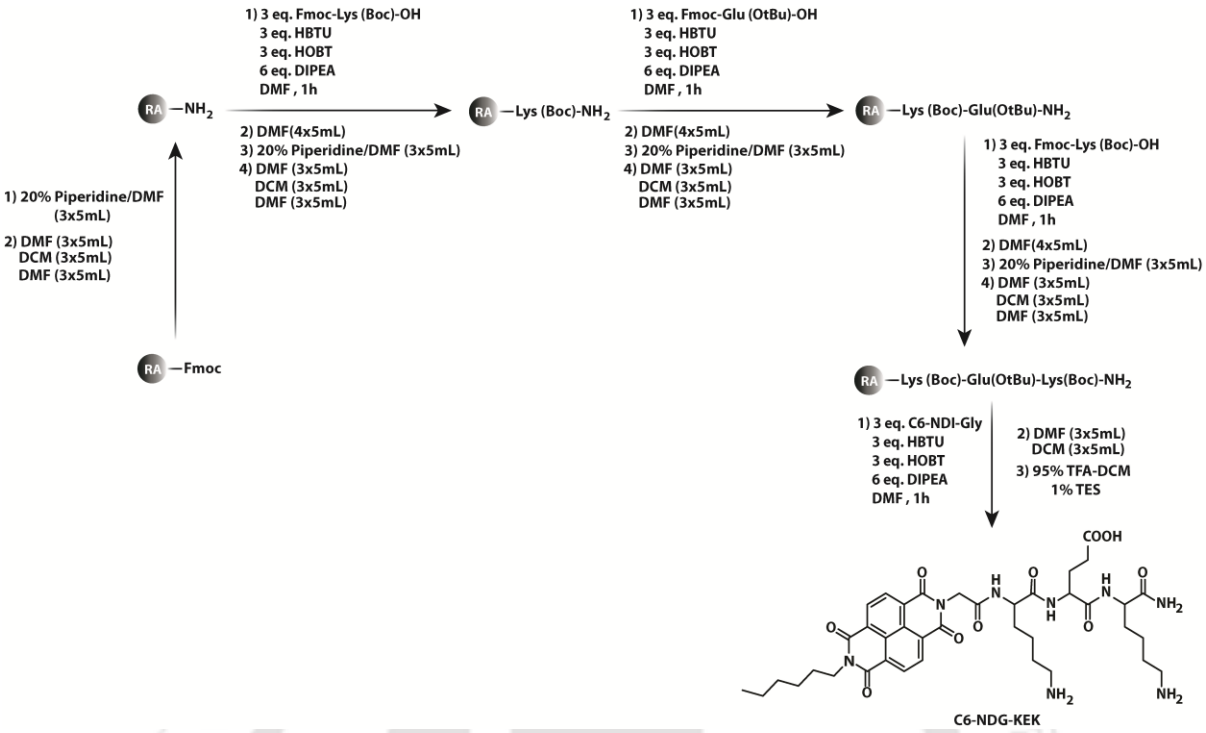

Scheme 3.2 Synthetic route of C6-NDG-KEK

3.4.4 Synthesis of carbon quantum dot (CQD)

Carbon quantum dots were prepared following a literature protocol. Typically, 2 g of Betaine hydrochloride (0.017 mmol) was first dissolved in 5 mL of water and the pH of the solution was adjusted to 1 by slow addition of 1(N) HCl. Then, 1.2 g of Tris-HCl (0.01 mmol) was added to the solution and mixed well by shaking followed by the extraction with 60 mL of isopropanol (3 x 20 mL). Organic parts were mixed, dried over sodium sulfate and evaporated to get a sticky mass. The mass was dried at 80 °C for 3 days. The dried material was heated in a furnace at 250 °C for 2 h in a porcelain crucible and then was cooled to room temperature. Finally, it was extracted with 25 mL of water followed by precipitation in acetone/water mixture (1:10 volume ratio). The combined liquid mixture was centrifuged at 14000 rpm for 30 min to precipitate out the quaternized quantum dot. The supernatant was removed and the precipitated brownish-black mass was further dried in a hot oven at 80 °C until the powder was obtained.

3.4.5 NMR studies

To understand the role of π–π stacking and hydrogen bonding toward the self-assembly of **PA-2**, ^{1}H NMR spectra of **PA-2** (2 wt%) in DMSO-d_6 were recorded in presence of varying amounts of water. The peptide does not assemble in DMSO while the presence of water enhances the assembly

process. As the extent of self-assembly enhances with more and more amount of water, the aromatic and amide protons showed significant shifting in their position.

3.4.6 FETEM

5 μL of the solutions of 1wt% were cast on the carbon-coated copper grid (300 mesh Cu grid with thick carbon film from Pacific Grid Tech, USA) and allowed to air dry for 10 minutes and then the excess sample was blotted with a tissue paper. The grid was then allowed to air dry for 1 day.

3.4.7 Preparation of hydrogel

Typically, 15 mg of **PA-2** was dissolved in 0.5 mL water and incubated at room temperature for 24 h to get a self-supporting hydrogel. For different experiments, different volumes of the hydrogel were prepared to maintain the concentration of **PA-2**.

3.4.8 Preparation of composite devices

To prepare the samples, 15mg of **PA-2** and 50 mg of PVA and different amounts of CQD were dissolved in 0.5 mL of water. The solution was incubated at room temperature to form the self-supporting hydrogel. The hydrogel was then lyophilized to get the xerogel. The solid xerogel was used to prepare the pellets using IR pelletizer. These pellets were used for the sensing purpose as described in the next section.

3.4.9 Rheology

The viscoelastic properties of the hydrogel were characterized using rheometer (Anton-Paar MCR 102) equipped with a 20 mm parallel plate (with 0.3 mm zero gap) measuring system at 25 °C. A strain sweep test was performed first to identify the linear viscoelastic region (LVR) over a range from 1 to 100 % strain at a fixed oscillatory frequency of 1 rad/s. The LVR can be defined as where strain has no impact upon G′ and G″. Further, the mechanical strength of the gel was determined from oscillatory test i.e. frequency sweep, which was carried out under an appropriate strain (γ =1 %) selected from the LVR with the frequency ranging from 1 to 100 rad/s at 25 °C.

3.4.10 Fourier transformed infrared spectroscopy (FTIR)

FTIR spectra of the devices were recorded at room temperature on a Nicolet is 10 spectrometer. For recording the spectra in presence of p-xylene, the device was exposed to p-xylene vapor for 5 min and immediately transferred to the spectrophotometer and the spectrum was recorded.

3.4.11 Density Functional Theory (DFT)

The M06 family of functions were chosen over other conventional DFT functions as they are proven to be more accurate toward geometries and energy calculations for a variety of dispersion dominated systems like DNA base pair stacks. All theoretical calculations were carried out by using the Gaussian 09 package of programs. Energy-minimized structures of the individual solvents (o-Xylene, p-Xylene, m-Xylene, Toluene, Benzene) with C6-NDG-KEK were obtained by DFT calculations at the B3LYP/6-31G (d, p) accuracy level.

3.4.12 Gas sensing measurement

All the gas sensing phenomena were recorded inside a stainless steel chamber as shown in **fig. 3.5A** utilizing the DC two-probe measurement technique at room temperature. No additional heating element was used throughout the measurements. Pellets of circular geometry (Dia-7 mm and thickness-8 mm) were used for all the electrical measurements incorporating a source meter (2612A, Keithley Instruments, USA) to apply a very low fixed bias voltage of 3 mV. Two copper probes were attached with two opposite flat faces of the respective pellets to facilitate a good electrical contact with the source meter. The transient current was measured by a computing system equipped with a software (LabTracer2.9, National Instruments, USA) interfaced with the electrometer. To check the gas sensing performance, the samples were successively exposed to air and respective VOC vapor within the chamber for a fixed interval of time. Primarily, by measuring the transient current in the presence and absence of a particular VOC vapor, the change in the conductance of the material was measured. The sensing performance was characterized in terms of sensor response (R) as: $|\Delta G/G_0|\%$ ($\Delta G=G_g-G_0$, G_g = Conductance in presence of the VOC vapor and G_0 = Conductance in presence of air) at room temperature in presence of different toxic VOC vapors (p-xylene, m-xylene, o-xylene, toluene, benzene & ethanol).

भारतीय प्रौद्योगिकी संस्थान गुवाहाटी
Indian Institute of Technology Guwahati

Chapter – 4

A Water Insoluble Supramolecular Hydrogel with Unique Confinement Ability

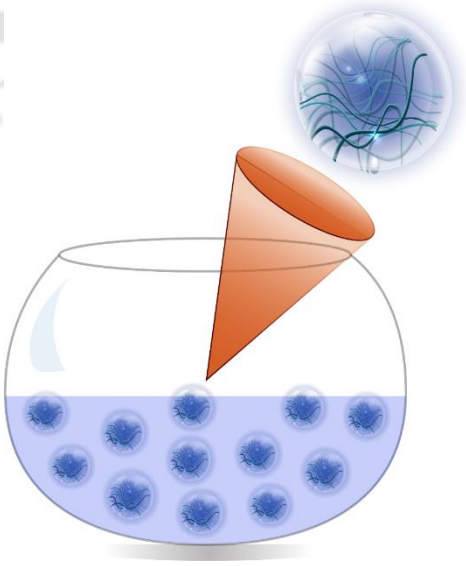

4.1 Introduction

Hydrogels are an important class of soft materials owing to their widespread applications.[35,177,178] Hydrogels consist of physically or chemically cross-linked network and aqueous solutions. Classically, cross-linked networks are formed by covalent linkages within natural or synthetic polymers where water molecules get trapped through cohesive forces.[179-182] However, an attractive alternative is the supramolecular hydrogels of small molecules.[180,182-184] In this case, hierarchical self-assembly of small molecules utilizing non-covalent forces results in fibers which crosslink through supramolecular interactions to form the gel-network. Unlike polymeric hydrogels, owing to the supramolecular nature of the interactions, each constituent molecule in the network retains its physicochemical characteristics.[180,182] Cross-linked polymeric hydrogels, when dispersed in water, depending upon the functional groups present, may not get dissolved as the cross-links are entirely covalent in nature. However, solvent molecules of these hydrogels remain in dynamic motion with the solvent outside.[181] On the other hand, for supramolecular hydrogels, the gel easily dissolves in water as dissolution enhances the overall entropy of the system.[182]

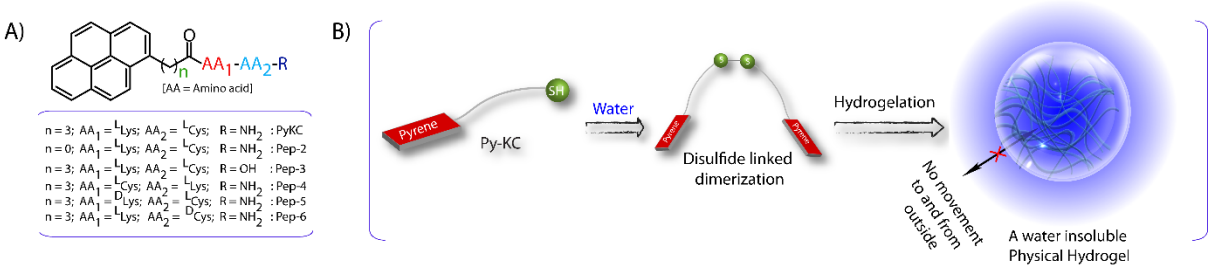

Scheme 4.1 (A) Chemical structures of peptides used in this study. (B) Pictorial presentation of hydrogelation of PyKC in water through dimerization and the insolubility of the formed hydrogel in water.

Supramolecular hydrogels and especially the small peptide-based ones have major advantages over the polymeric hydrogels primarily because of their inherent non-toxic nature and biodegradability.[6,18,35,117,185-189] However, one important issue with the small molecular gels is their ease of dissolution in bio-fluid when applied for biological applications. Prolonged and sustained use of these hydrogels is thus difficult inside the human body.[186] An attractive alternative could be a water-insoluble supramolecular hydrogel made of small peptides which may get dissolved slowly by a biomolecule (stimuli to break the gel) present in the bio-fluid and thus result in sustained application. However, to the best of our knowledge, no supramolecular hydrogel ever been reported which remained insoluble in bulk aqueous medium.

In a serendipitous observation, we found a small peptide-based (**PyKC**, **scheme 4.1A**) water-insoluble supramolecular hydrogel. When immersed in water and various other solutions, the

hydrogel did not dissolve and remained insoluble for more than a year. Herein, we report the hydrogelation of **PyKC**, its insolubility, and the plausible reason behind such unique property

4.2 Results and discussion

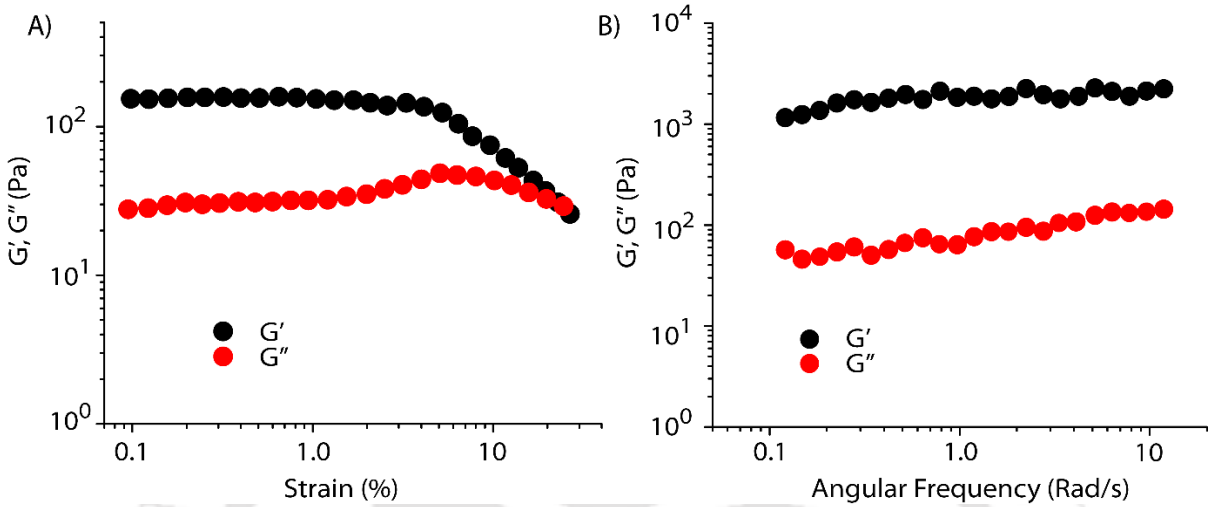

Fig. 4.1 Changes in storage and loss modulus as a function of shear strain (A) and angular frequency (B).

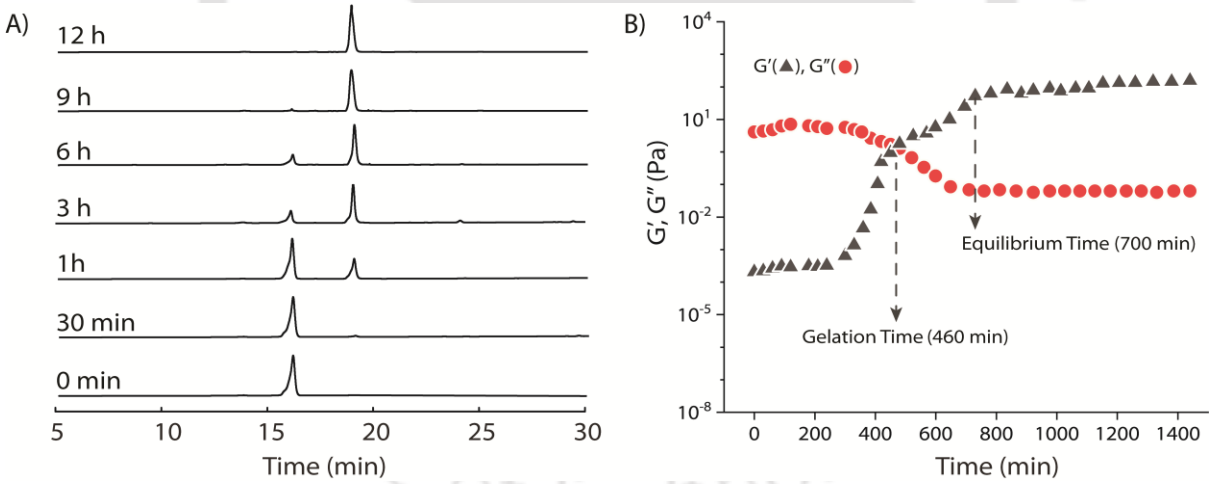

Fig. 4.2 (A) Time-dependent chromatographic analysis of a 0.01 wt% aqueous solution of **PyKC** showing the formation of disulfide-linked dimer formation. (B) Time dependent rheology of a 1 wt% **PyKC** hydrogel showing the sol to gel transition and time required to reach equilibrium.

PyKC forms self-supporting hydrogel in Tris buffer (20 mM, pH 8.0) with minimum gelation concentration (MGC) of 1 wt%. The hydrogel was thermo-reversible and the gel to sol transition temperature (T_g) was obtained as 75 °C. The rheological (**fig. 4.1A** and **B**) analyses showed the gel character as the storage modulus (G′) was found to be considerably higher than the loss modulus (G″) over a range of applied angular frequency.[190] ESI-MS analysis of the hydrogel disclosed the presence of only disulfide-linked dimer of **PyKC** (Pep-7). A time-dependent analytical HPLC analysis

of the solution of **PyKC** revealed that the complete conversion to dimer takes ~12 h at room temperature (**fig. 4.2A**). In the presence of a well-known disulfide bond breaker, dithiothreitol (DTT) (0.1 equivalent), no hydrogelation was observed confirming the critical role of the dimer toward gelation. To further verify the actual time required for gelation, a time dependent rheology was performed which shows sol-to-gel transformation happens at ~ 8 h (**fig. 4.2B**) while the equilibrium was obtained ~ 12 h after that both G" and G' remained constant. The similar completion time for dimerization process and the equilibrium time suggest a critical role of the dimer formation with the gelation process.

Interestingly, a small portion of the hydrogel, when added to water and stirred vigorously, no dissolution of the hydrogel in that bulk water was observed (**fig. 4.3A**). The sample was found to be as it was for more than 12 months when kept at room temperature. This observation is unprecedented for any supramolecular hydrogel and prompted us to quantify the dissolution/insolubility of the hydrogel. A 1 wt% hydrogel of **PyKC** (500 μL) was added to bulk water and incubated with slow shaking at room temperature. Analyses of aliquots of the bulk water taken at different time interval showed up to 5% dissolution of the hydrogel within the first seven days and that remained constant thereafter for more than 1 year (**fig. 4.8A)**. The initial small dissolution of the **PyKC** dimer can be attributed to the residues which connect the hydrophobic layers to form the fiber as seen from the molecular dynamics simulations discussed later. These residues could easily get dissolved in water at the initial stage. However, no further dissolution of the hydrogel proved the insolubility of the hydrogel in water.

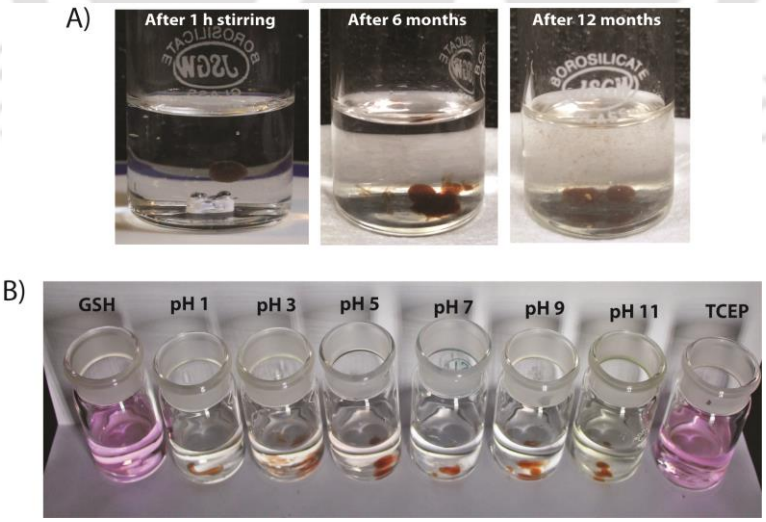

Fig. 4.3 (A) Photographs of a portion of the 1wt% hydrogel prepared from **PyKC** and immersed in bulk water. Photographs taken at different times to show the insolubility of the hydrogel even after 12 months. (B) Photographs of vials containing different aqueous solutions where small portions of the hydrogel (1wt% PyKC) containing Rhodamine B were immersed and stirred for 10 mins. Though the hydrogel dissolved in TCEP and GSH solutions, it remained insoluble in all the buffers.

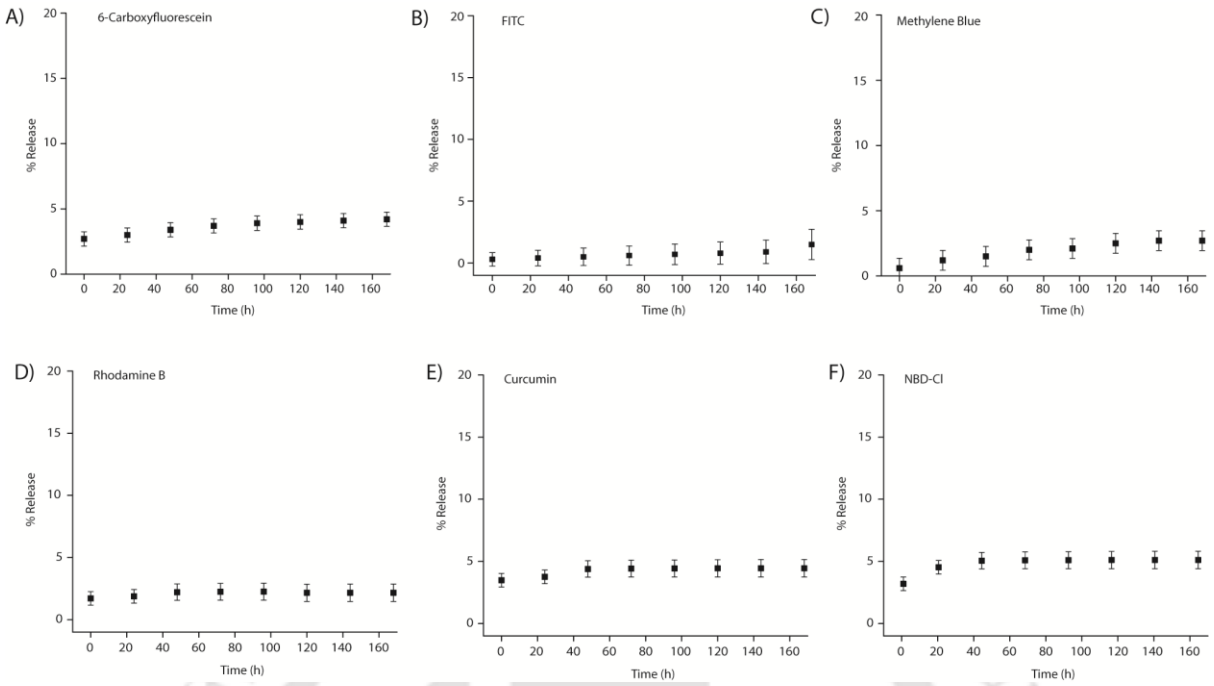

Fig. 4.4 Time dependent % release of entrapped dyes inside1 wt% hydrogel formed by **PyKC** (in 20 mM Tris buffer, pH 8 containing the respective dyes) when dispersed in bulk water.

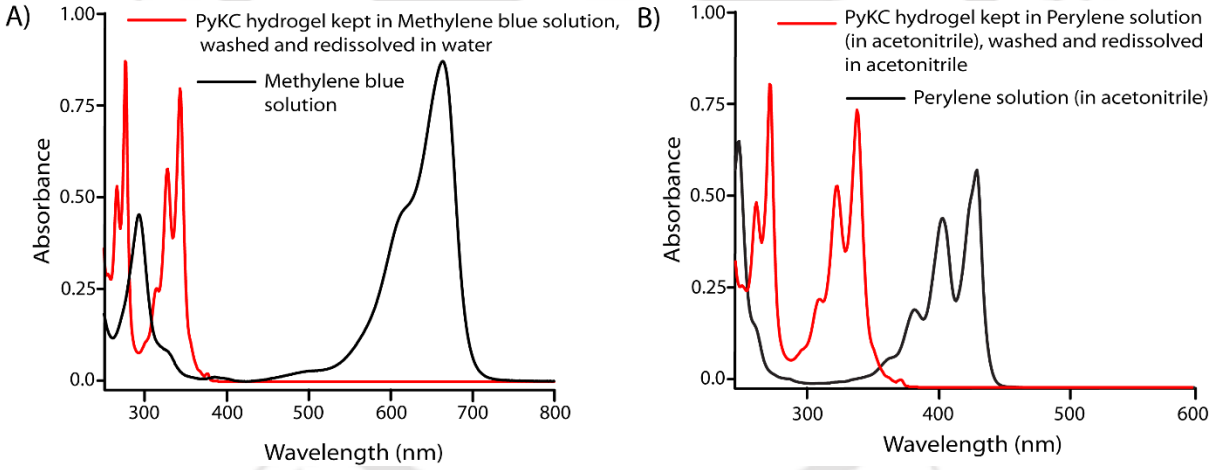

Fig. 4.5 A small portion of **PyKC** hydrogel was dispersed in solutions of methylene blue (in water) and perylene (in acetonitrile) and incubated at room temperature. After seven days, the gels were centrifuged, washed and dissolved in water or acetonitrile with the help of TCEP and the absorption spectra of the solutions were recorded to see any incorporation of the dyes. The absorption spectra of the gel from (A) Methylene Blue test and Perylene test (B) along with the absorption spectra of Methylene Blue and Perylene.

It is worth mentioning that, for a cross-linked polymeric hydrogel, though the network remained insoluble, the water molecules inside the network can move out and that is why xerogels swell in water to form the hydrogel reproducibly.[1,191]

Interestingly, in the present case, the xerogel remained insoluble and unable to swell when water or buffers up to pH 12 were added. Six different dyes (two of each, cationic, anionic and neutral category) were separately entrapped in the gels while preparing the hydrogel and the release

profiles of the dyes showed very similar results as only ~ 5% release over seven days were observed for all these dyes (**Fig. 4.4**). A reverse experiment of incubating the hydrogel (without any dye) in an aqueous solution of Methylene blue for seven days showed no incorporation of dye into the hydrogel (**Fig. 4.5A**). Interestingly, a similar test with Perylene (a fused π–system) in acetonitrile also resulted in similar observation (**Fig. 4.5B**). These results clearly demonstrate that passage of any solute to and from the hydrogel is highly restricted.

The observations also raised the question about the fate of the gel entrapped water molecules. To get an insight about that, we took the help of ^{1}H NMR experiments. Hydrogel prepared in water was added to D_2O, NaOD and DCl solutions and incubated while shaking. The amount of water exchanged from the hydrogels were estimated from ^{1}H NMR spectra of the supernatant deuterated solvents after different time intervals. As can be seen from **fig.4.6** and **4.7**, only ~3% water molecules could come out of the hydrogel within the first day and no further noticeable change was observed after that. The initial increase can be contributed to that of the loosely bound water molecules at the surface of the hydrogel. The results demonstrate that the self-assembly creates a system where both, gel-network as well as the water of gelation, are inaccessible to the surrounding environment. Neither the solvent nor the solute could pass the envelope created by the hydrogel.

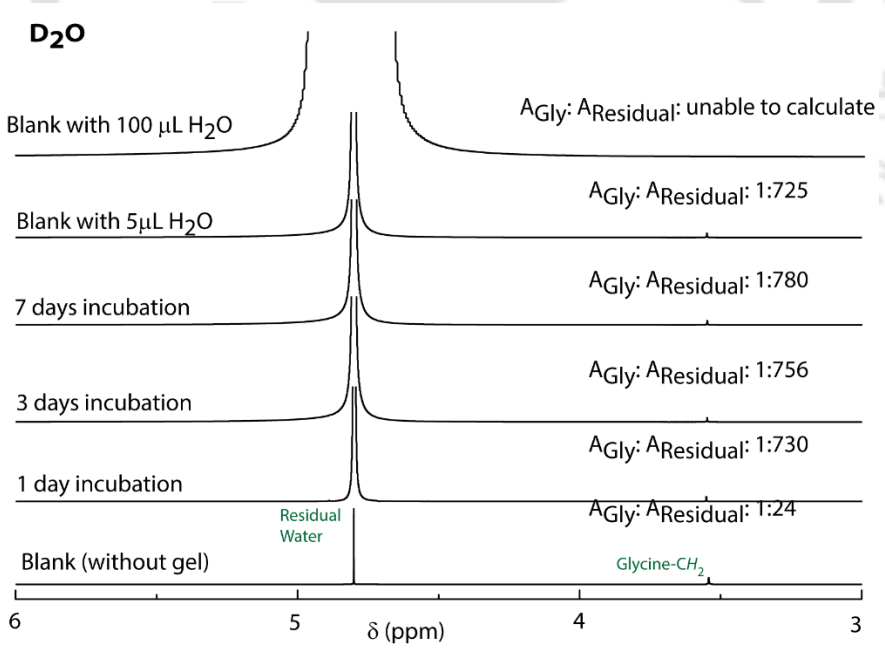

Fig. 4.6 ^{1}H NMR spectra of D2O containing glycine before and after incubating **PyKC** hydrogel inside the solvent for different time period to determine the extent of exchange of water of gelation.

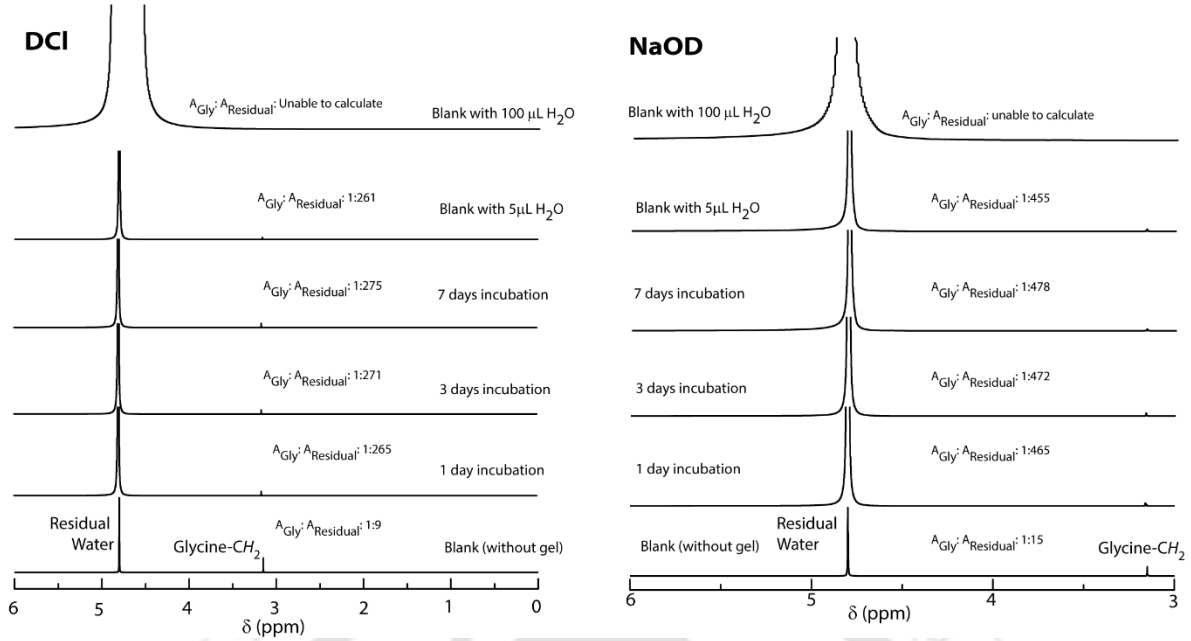

Fig. 4.7 ^{1}H NMR spectra of DCl and NaOD (in D_2O) containing glycine before and after incubating **PyKC** hydrogel inside the solvent for different time period to determine the extent of exchange of water of gelation.

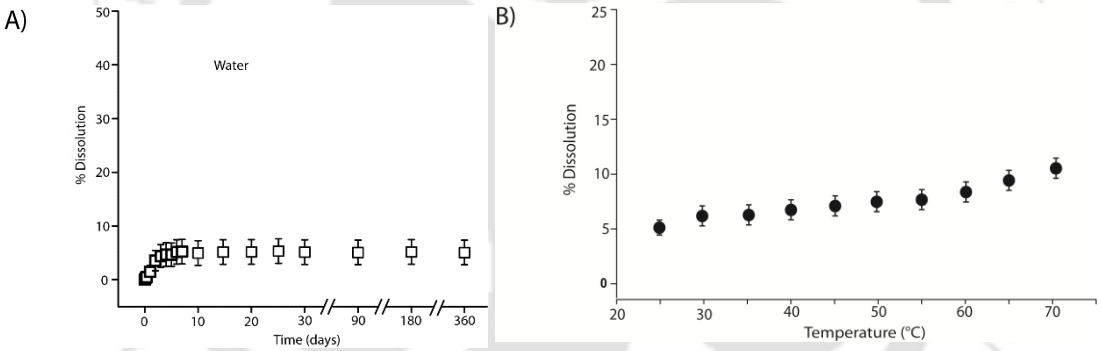

Fig. 4.8 (A) % Dissolution of the 1 wt% hydrogel formed by **PyKC** (in 20 mM Tris buffer, pH 8) when dispersed in bulk water. (B) Percentage dissolution of 1 wt% hydrogel prepared by **PyKC** in Tris-buffer (20 mM, pH 8) in bulk water at different temperatures.

Several water-miscible organic solvents and aqueous solutions were tested to find the solubility of the hydrogel. The results from all these tests are shown in **fig. 4.10**. Interestingly, though DMF and DMSO could dissolve the hydrogel within 5 mins, other solvents showed 4-8% dissolution within the first 24h with no further changes thereafter up to seven days. Buffers of different pH also failed to solubilize the hydrogel (**fig. 4.11**). When exposed to some extreme conditions like 2M NaOH, 12N HCl, and 6M urea, only the acidic solution could solubilize the gel (**fig. 4.12A-C**). The gel also remained insoluble in a biological fluid like human blood serum (HBS) was (**fig. 4.13**). Next, the hydrogel was dispersed in bulk water and the sample was heated at a particular temperature for 1 h with constant shaking and then cooled to room temperature before analyzing the bulk water. As can be seen from **fig. 4.8B**, at 70 °C, only ~8.5% dissolution was recorded. Interestingly at 80 °C,

which is above the T_g of the hydrogel, though the gel melts, the network structure and the insolubility remain intact (**fig. 4.9**). Bringing that sample to room temperature brings back the gel state.

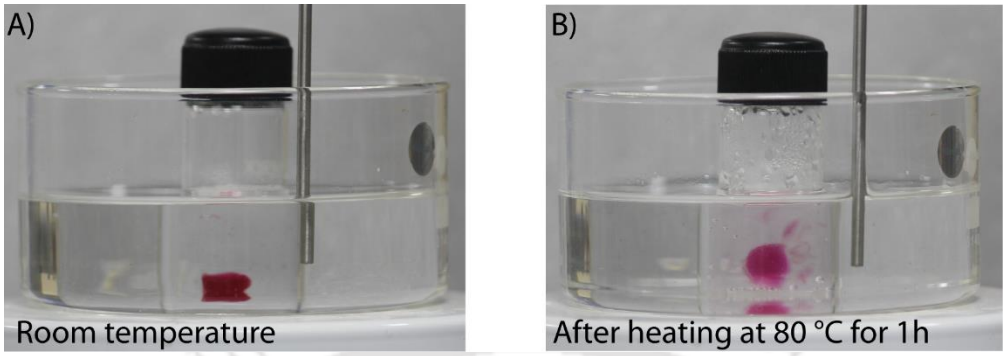

Fig. 4.9 Photographs of a 1 wt% hydrogel of **PyKC** (containing Rhodamine B) before and after heating at 80 °C for 1 h.

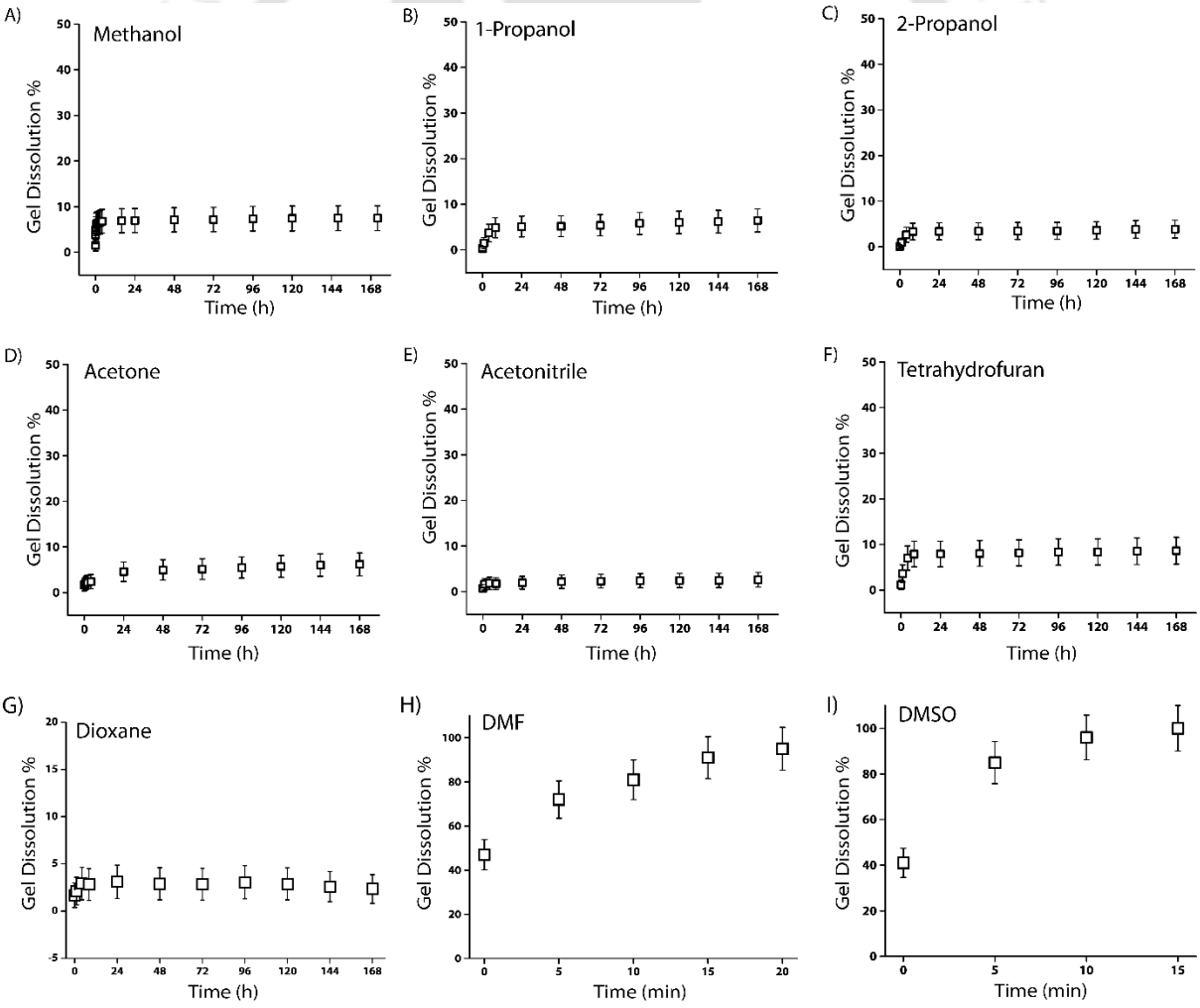

Fig. 4.10 % Dissolution with time for 500 μL of 1 wt% hydrogel of **PyKC** when dispersed in 10 mL of different organic solvents and incubated at room temperature.

Though concentrated acid can dissolve the hydrogel, such extreme condition is not a good choice for future applications. During the search for a suitable system which can break/dissolve the hydrogel, we found aqueous solutions of disulfide breakers, tris(2-carboxyethyl)phosphine hydrochloride (TCEP), (DTT) or glutathione (GSH) can do so effectively (**fig. 4.14**). When subjected to a proteolytic enzyme, Trypsin, the gel dissolve and smaller fragments of the peptide were observed in the ESI-MS spectrum of the solution indicating a breakdown of the peptide (**fig. 4.15** and **fig. S4.17**). Both, Trypsin and GSH, could be interesting options to break the hydrogel during therapeutic applications.

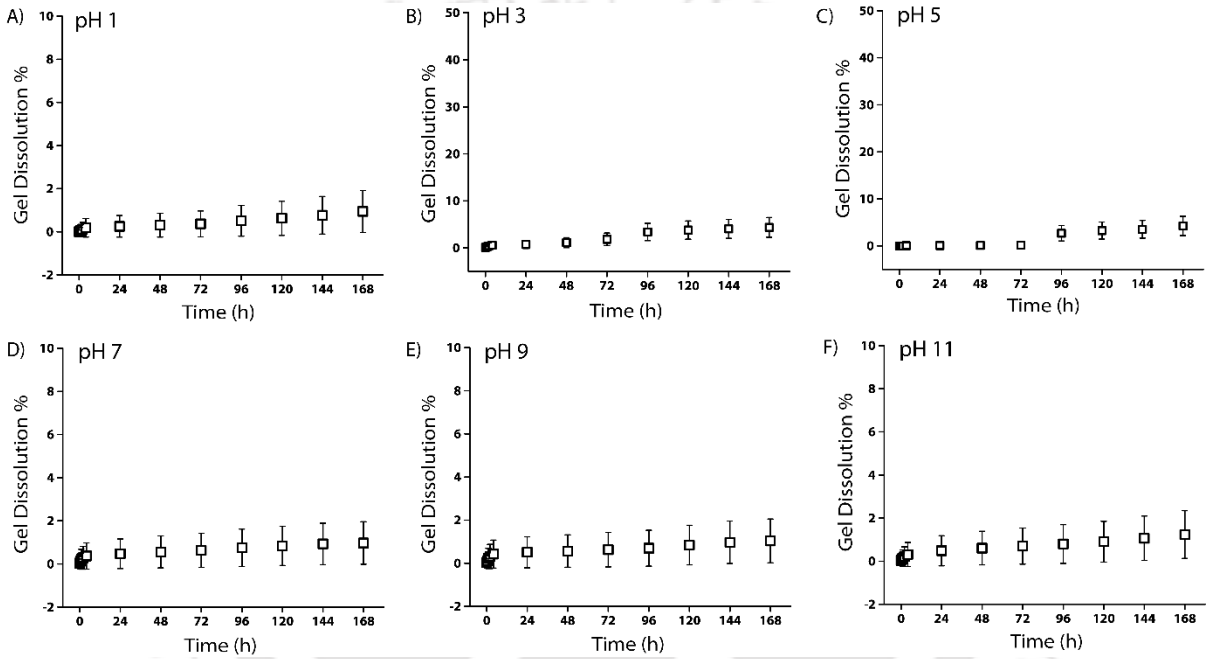

Fig. 4.11 % Dissolution with time for 500 µL of 1 wt% hydrogel of **PyKC** when dispersed in 10 mL of different buffers and incubated at room temperature.

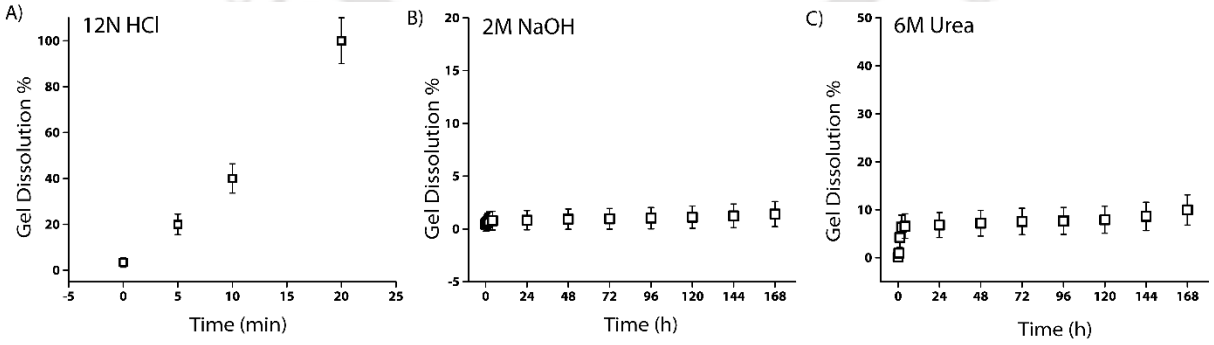

Fig. 4.12 % dissolution with time for 500 µL of 1 wt% hydrogel of **PyKC** when dispersed in 10 mL of aqueous 12 N HCl (A), 2 M NaOH (B) and 6 M urea solutions (C) and incubated at room temperature.

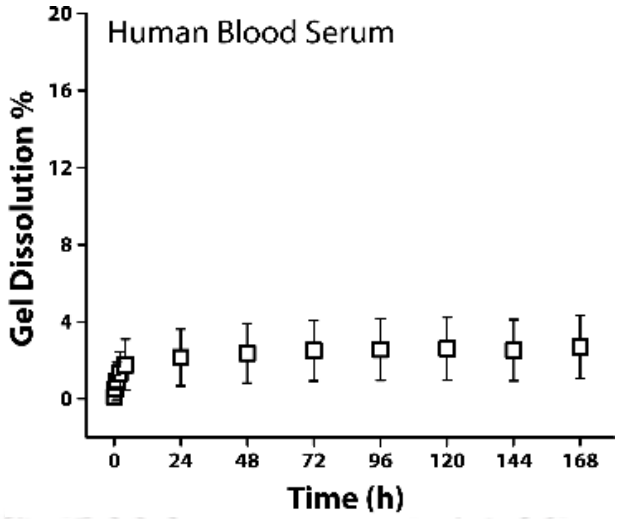

Fig. 4.13 Dissolution with time for 100 µL of 1 wt% hydrogel of **PyKC** when dispersed in 2 mL of human blood serum and incubated at room temperature.

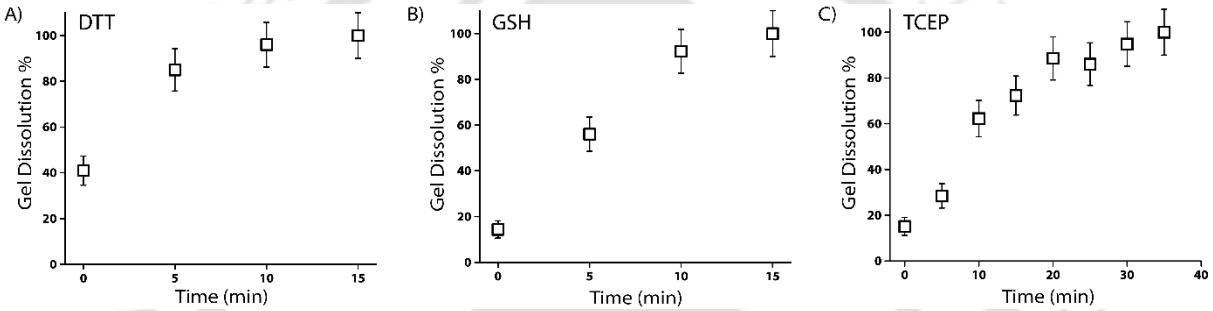

Fig. 4.14 % Dissolution with time for 500µL of 1 wt% hydrogel of **PyKC** when dispersed in 10mL of aqueous solutions of different disulfide bond-breaking agents and incubated at room temperature.

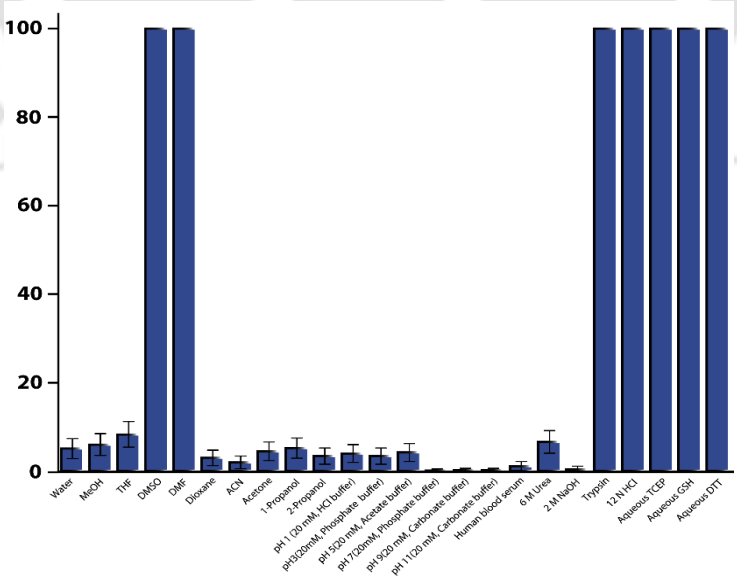

Fig. 4.15 % dissolution of 1 wt% PyKC hydrogel (20 mM Tris-buffer, pH 8) in different media after 168 h.

The insolubility of this hydrogel is fascinating and it is important to evaluate the gelation process. Densely packed thin fibers (diameter ~9 nm) with an average length of ~500 nm were observed

from FETEM of the hydrogel (**fig. 4.16A**) while no such network structure could be found from DTT treated solutions of **PyKC**. Notably, the fibrous network structure was retained by the hydrogel even after keeping it in water for more than 12 months (**fig. 4.16B**). Interestingly, even at a very low concentration of 0.005 wt%, an intense pyrene excimer band (~460 nm, **fig. 4.16C**) was observed.[192] The unusually high intensity of pyrene excimer can be attributed to possible strong π-π stacking. Further insight into the π-π stacking is obtained from the ^{1}H NMR and PXRD analyses of **PyKC**. With the increasing amount of water, the aromatic protons showed a clear up-field shift in the 1H NMR while PXRD of a dried film of the hydrogel showed a π-π stacking distance of 3.4 Å (**fig. 4.16D and E**) representing strong π-π stacking. The stacking distance is in agreement with the distance found from electronic structure calculations (2.97 Å) and from the MD simulations (3.9 Å) discussed later.

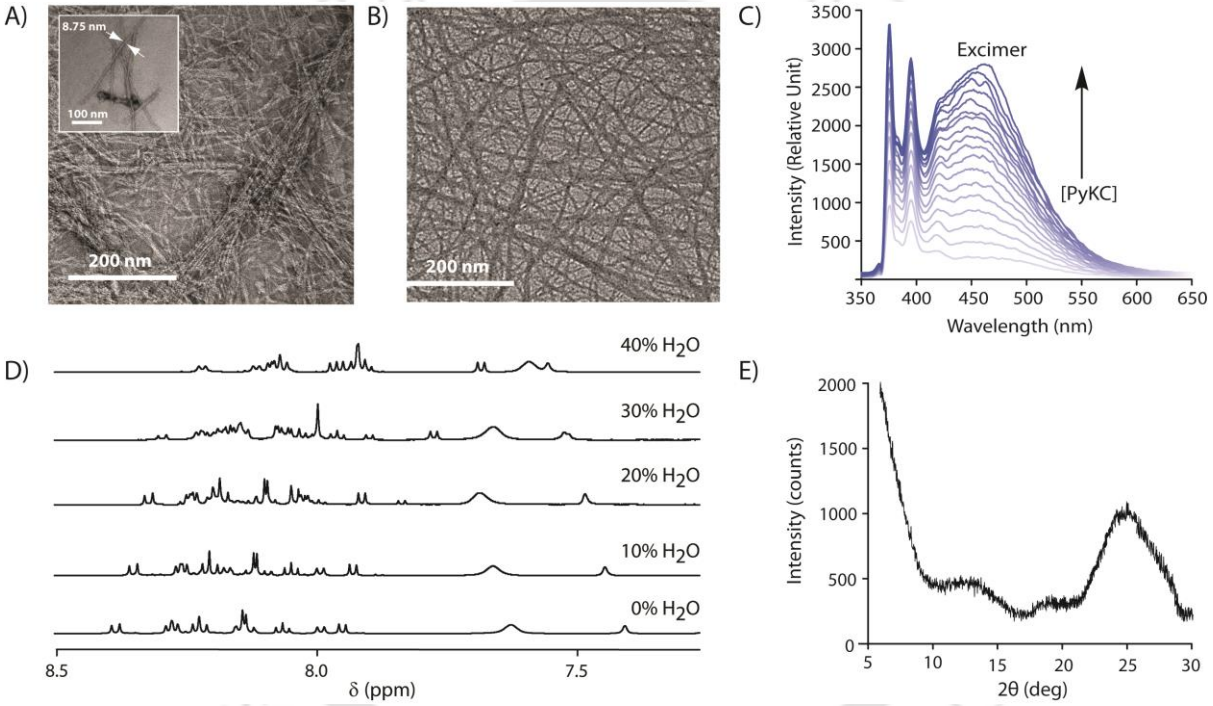

Fig. 4.16 (A) FETEM images of the 1wt% **PyKC**-hydrogel in 20 mM Tris buffer pH 8 (Inset: zoomed-in picture from the same sample showing the diameter of a fiber). (B) FETEM image of the 1wt% **PyKC**-hydrogel in 20 mM Tris buffer pH 8 after incubating in bulk water under ambient condition for 12 months. (C) Concentration (0.001-0.05 wt%) dependent emission spectra of 24h matured **PyKC** solution (in 20 mM Tris buffer pH 8) with increase in concentration (λ_{ex} = 337 nm). (D) ^{1}H NMR spectra of 24 h matured samples of **PyKC** in DMSO-d_6 with varying amounts of water showing strong π-π interaction between the pyrene rings. (E) PXRD profile of a dried film of the 1wt% hydrogel of **PyKC** in 20 mM Tris buffer pH 8. All experiments were carried out at room temperature.

Though the hydrogel forms via dimerization of **PyKC**, separately synthesized **PyKC**-dimer failed to form a hydrogel which suggests that, here dimerization and aggregation proceed simultaneously leading to the network structure. During this process, the water molecules get entrapped within the network and stay immobilized. The entrapment is strong enough to forbid the water molecules to get exchanged with the exterior. In order to obtain information regarding the importance of the peptide sequence, some control molecules (Pep-2-6, **scheme. 4.1A**) were tested for their gelation ability. Only Pep-3, 5 and 6 were able to form hydrogel but all these hydrogels were found to be

spontaneously soluble in water. Hence, it can be concluded that the insolubility is an exclusive property of **PyKC**-hydrogel and the molecular structure certainly plays a significant role in this property.

4.2.1 PyKC-dimer configuration from electronic structure calculation

To understand the molecular origin of the insolubility and unique confinement ability of **PyKC**-hydrogel, the molecular packing of the most stable building block of the hydrogel is analyzed. As a first step, to obtain the most stable conformer, dispersion energies, total energies and the binding energies of the geometry optimized **PyKC** molecules were evaluated using electronic structure calculations. The binding energies for the open and folded conformers were found to be -57.92 and -78.5 kcal/mol respectively (**table 4.1**). This signifies that the stacking of the folded dimer of **PyKC** is energetically more favorable than that of the open dimer. The coordinates of the most stable folded dimer and the charges on each atom are summarized in **table 4.2**. The snapshot of the geometry optimized folded **PyKC** dimer with atom labels is shown in **fig. 4.19**. **Fig 4.18A** and **B** show the optimized geometry of the folded dimer and the stacked dimer respectively. The closest inter-planar distance in the stacked dimer was found to be 2.44 Å which is consistent with the PXRD results (**fig. 4.16E**). The stability of the stacked folded dimer is attributed to both T-type and H-type π–π interactions of the pyrene rings as shown in **fig 4.18B**.

Table 4.1. Energy of the geometry optimized configurations for both open and folded **PyKC** dimers from DFTB calculations.[193-195] The folded conformer has stronger stacking energy. The inter-planar distance is in good agreement with PXRD results (**fig. 4.16E**) and indicates the presence of π–π stacking.

Configuration	Energy (Hartree)				Stacking energy (ΔEb) Kcal/mol	Inter-planar distance (A^0)
	Monomer		Dimer			
	Dispersion	Total	Dispersion	Total		
(a) Open (b) folded	-0.255 -0.275	-168.811 -168.807	-0.571 -0.607	-337.714 -337.740	-57.92 -78.50	2.96 (H-type) 2.44 (T-type)

Table 4.2. Co-ordinates of geometry optimized folded **PyKC** dimer.

1	-14.96449970	3.89450661	-0.89986452
2	-13.51051887	1.98866368	0.25745794
3	-10.93598244	2.48712940	0.87081960
4	-9.87214238	4.89946454	0.32332495
5	-11.36760946	6.73643556	-0.88900660
6	-13.88546051	6.22773251	-1.48616885
7	-9.43040960	0.58335400	2.04128811

8	-6.90276915	1.13322014	2.80644727
9	-5.91015899	3.61798357	2.32112393
10	-7.31734051	5.39871322	1.08285398
11	-14.54585178	-0.45742920	0.80460409
12	-13.07217548	-2.32575681	1.81173969
13	-0.48019603	-1.86267406	2.46350958
14	-8.95139635	-3.75178540	3.54237544
15	-6.48354250	-3.20673841	4.28245445
16	-5.44783603	-0.78783565	3.97662113
17	-2.81192506	-0.28177531	4.88572141
18	-2.74774785	1.16473538	7.36877698
19	-0.10067368	2.10687506	7.92773819
20	0.41470215	4.58841601	6.59858397
21	-1.31273577	6.02465429	5.99736587
22	2.89541784	5.41116188	6.24320464
23	4.98647815	3.79124024	5.49824741
24	4.24516192	2.12025666	3.24562614
25	3.89182992	3.66838773	0.84585862
26	1.26856586	4.80674031	0.63242290
27	0.61865793	5.57799020	-2.06564317
28	-1.97187047	6.40524110	-2.31105645
29	5.98564004	2.24731539	7.71950046
30	8.17003207	0.77712821	7.42762672
31	4.84445349	2.08194430	9.72407291
32	10.47243734	1.43476769	6.08762908
33	10.40450396	0.89255509	3.24356783
34	11.28904629	4.18966971	6.34817342
35	9.89768205	5.95276098	6.84063579
36	13.80036620	4.56457650	5.60100353
37	13.55604511	1.44801648	1.80426088
38	14.03027338	-1.61187969	-0.65594209
39	11.79510474	-0.96485777	-3.27763757
40	10.87553089	-3.44637228	-4.44927035
41	13.26671544	-4.77186872	-5.36490882
42	14.89699970	-5.56276048	-3.42841514
43	13.91619738	-4.79996858	-7.56638344
44	9.52926415	-4.97786397	-2.59904456
45	7.53101753	-4.06618577	-1.12152193
46	7.48720546	-4.67327420	1.11460347
47	5.23029622	-2.65546881	-2.17550926
48	3.20984102	-4.51260416	-2.23656170
49	0.67186070	-3.91603209	-1.98988790
50	-0.93709042	-5.52994485	-2.43807629
51	0.05553022	-1.27945593	-1.07018761
52	-2.70706232	-0.63195803	-1.37263148
53	-3.45690355	-0.49086443	-4.13828772
54	-6.25044081	-0.12041952	-4.40460035
55	5.43129148	-1.21543502	-4.68764224
56	5.07732021	-2.86909171	-7.01654609
57	2.35238252	-2.87769433	-7.90516489
58	1.92259392	-4.63994513	-10.14301521
59	-0.69785872	-4.71325778	-10.90406978
60	-7.20431670	2.24845046	-5.10081768
61	-9.79121693	2.64654649	-5.40293094
62	-11.51132214	0.65917116	-5.00104953
63	-10.58257156	-1.73670283	-4.19129176
64	-7.93476445	-2.13682947	-3.89047630
65	-12.31795360	-3.73160478	-3.66818051
66	-11.41124255	-6.10318190	-2.77415626
67	-8.73805005	-6.46600470	-2.51116640
68	-7.06355864	-4.57974439	-3.07675077
69	-14.17968980	0.98453949	-5.37423819
70	-15.83909675	-0.94027831	-4.90176101
71	-14.96451318	-3.34279789	-3.99101064
72	-16.65050210	-5.30742216	-3.37666899
73	-15.74323801	-7.61493523	-2.47588251
74	-13.15588469	-8.02531866	-2.18453138
75	2.48308919	1.08919462	3.68213874

76	5.69839383	0.65276663	2.95110857
77	5.34685425	5.16769321	0.74257078
78	4.23670537	2.44240184	-0.81599951
79	1.07964135	6.45579584	1.89411059
80	-0.14300095	3.41706844	1.29817291
81	1.91492893	7.10594809	-2.69659739
82	0.93991016	3.95259935	-3.36046748
83	-2.36496195	7.85764313	-1.07632503
84	-3.21437135	4.94737265	-1.95378722
85	6.53385242	5.07740133	4.87568465
86	2.96662991	7.17749996	5.41716337
87	3.96248717	0.27302176	-4.68831715
88	7.23740154	-0.18034547	-4.76288673
89	5.69966294	-4.82563863	-6.61242801
90	6.30109645	-2.17509379	-8.56176432
91	1.09430959	-3.44212867	-6.33681314
92	1.79203568	-0.93151049	-8.42646295
93	2.54976705	-6.57787830	-9.63829019
94	3.10582637	-4.02709266	-11.76507961
95	-1.82898773	-5.38001097	-9.46751230
96	-1.33221515	-2.94991348	-11.42725882
97	4.75896139	-1.24998355	-0.67609914
98	3.61468726	-6.24341715	-3.03185043
99	-16.95321237	3.51887143	-1.36399423
100	-10.54478739	8.58860263	-1.33932350
101	-15.03340690	7.68418132	-2.41916511
102	-4.00017492	4.10916727	2.97573461
103	-6.51752369	7.27908393	0.70720373
104	-16.53637026	-0.82189144	0.33874107
105	-13.86253200	-4.21655872	2.14748995
106	-9.72379283	-5.65810524	3.82153172
107	-5.31679034	-4.69999071	5.13154316
108	-1.78464247	-2.08930142	5.10856123
109	-1.75745724	0.82266128	3.45614415
110	-3.42481277	-0.06439457	8.91449679
111	-4.04164880	2.80076526	7.26650392
112	0.11630623	2.46394441	9.97397272
113	1.31902310	0.66036324	7.44139031
114	8.52496918	-0.25260709	9.04785638
115	11.98486710	0.22639039	6.92163905
116	9.80727413	-1.07336764	2.88371987
117	9.04377586	2.15966821	2.30225136
118	14.38204680	6.41783401	5.59948688
119	15.11254531	3.35220971	6.35894000
120	10.18549733	0.10607897	-2.49840130
121	12.69807678	0.21689882	-4.73807615
122	9.65821002	-3.04538619	-6.11643825
123	14.14266960	-6.66588039	-2.02230530
124	16.60836032	-6.23334574	-4.05861300
125	10.72974335	-6.03183828	-1.47021784
126	0.61762241	-1.14713140	0.94045932
127	1.20837305	0.12233773	-2.10028938
128	-3.10069040	1.21027332	-0.46763828
129	-3.87437798	-2.04414280	-0.37662372
130	-2.42749066	1.08375300	-5.05350871
131	-2.86298776	-2.24489608	-5.11054365
132	-5.87866466	3.81370329	-5.43001009
133	-10.49871388	4.51810454	-5.95533165
134	-8.04536332	-8.31168197	-1.85860031
135	-5.02436722	-4.94009635	-2.88984717
136	-14.87013919	2.82461679	-6.04514587
137	-17.87905473	-0.65940589	-5.17128341
138	-18.69294619	-5.00598945	-3.59429658
139	-17.08190974	-9.12805786	-1.99929953
140	-12.46186471	-9.85472575	-1.48967640

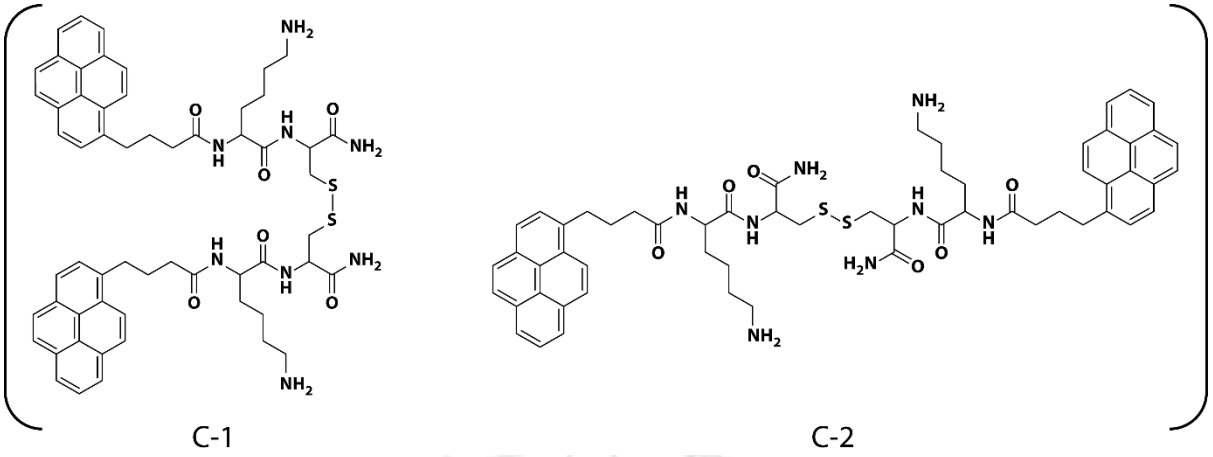

Fig. 4.17 Two different conformers drawn in ChemDraw which were used as the initial configurations for the geometry optimization.

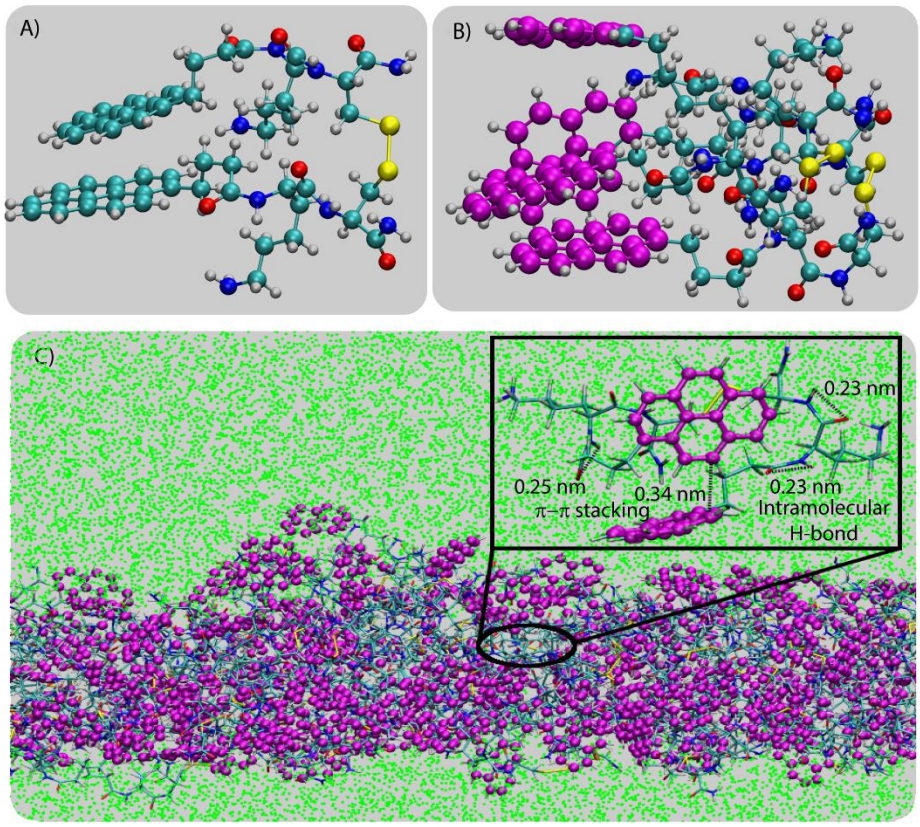

Fig. 4.18 (A) Optimized geometry of a folded **PyKC** dimer showing a parallel stacking of the pyrene rings. (B) Optimized geometry of two stacked folded **PyKC** dimers. Pyrene rings are shown in magenta color. (C) Snapshot of **PyKC** layer in presence of water for system c) from the all-atom MD simulation after 42.5 ns run-length. Color code and representation: pyrene: magenta; peptide-conjugate: lico-rice; water: green. Distinct interfaces of **PyKC**-water are visible showing compartmentalization of water and the hydrogel. The inset shows that the intra-molecular hydrogen bonds in the peptide conjugate and π–π stacking across pyrene rings stabilize the self-assembly of PYKC in the hydrogel.

4.2.2 PyKC-dimers in water from molecular dynamics simulation

The most stable folded conformer of **PyKC** was chosen as the initial structure for Molecular Dynamic (MD) simulations. A snapshot of the final configuration of the self-assembled system from the MD

simulation (as mentioned in simulation details) is shown in **fig. 4.18C** (the equilibration of the system is examined by calculating the potential energy and SASA is shown in **fig. 4.19A** and **B**).[196] We find that **PyKC**-dimers self-assemble into a layer-like structure with two distinct interfaces of water and **PyKC** layers (**fig. 4.18C**). The inset in the figure demonstrates the molecular structure of the interior of the aggregated **PyKC** phase. The pyrene-pyrene distance falls within the $\pi-\pi$ stacking distance where the nitrogens (N) and oxygens (O) of the peptide conjugates form intramolecular hydrogen bonds to each other stabilizing the conformer.

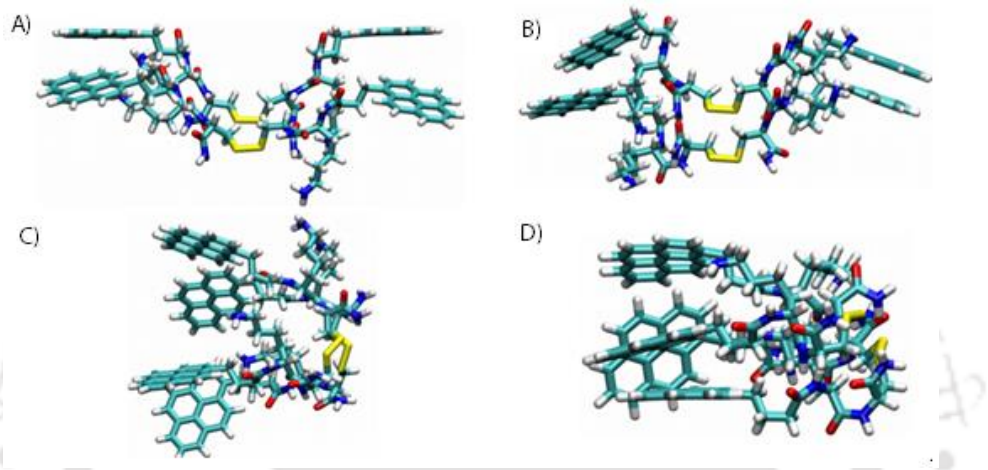

Fig. 4.19 Snapshot of optimized geometries of **PyKC** dimers in open and folded states, (A) Geometry optimized stacked open chain dimer without dispersion correction (B) Geometry optimized stacked folded dimer without dispersion correction, (C) Geometry optimized stacked open chain dimer with dispersion correction and (D) Geometry optimized stacked folded dimer with dispersion correction.

To understand the molecular arrangements of water, pyrene rings and **PyKC** in the self-assembled structure, we calculated density profiles across **PyKC** layers (**fig. 4.20A**) where the direction across the layers is considered as the direction of the normal vector. Distinct interfaces between water and **PyKC** layers are observed demonstrating compartmentalization of water molecules and **PyKC**. Interestingly, there is a strong overlap between the locations of the pyrene rings and the N/O atoms of the peptide. This clearly confirms that the significant part of the hydrophilic atoms of the peptide conjugates is buried in the core region of the hydrophobic aromatic pyrene rings unlike the arrangements of lipids/surfactants in biological membranes/vesicles.[197] The hydrophilic peptide conjugates are stabilized by the intramolecular hydrogen bonds between N-H and O as shown in the inset of the **fig. 4.18C**. The numbers of intramolecular hydrogen bonds of **PyKC** are calculated using the widely accepted geometric criteria where the distance between the donor and the acceptor is ~0.35 nm and the angle between the donor-H-acceptor is 30^0.[198] The numbers of such intra-molecular hydrogen bonds (between N-H---O) are shown in the inset of **fig. 4.20A** for the

production run-length. The inset in **fig. 4.20A** shows the radial distribution function (RDF), g(r), of the pyrene rings calculated using the equation,

$$g(r) = \; < \frac{1}{\rho}\frac{1}{N}\sum_{1}^{N}\sum_{j=1}^{N}\delta(r_{ij} - r) >$$

Where r_{ij} is the distance between two particles i and j, N is the total number of particles. ρ denotes the mean particle density and the angular bracket denotes a time average. The RDF of the pyrene rings from the MD simulation reveals that the nearest distance between pyrene rings is ~0.42 nm across which π–π stacking can operate. Unlike the geometry optimized dimer from electronic structure calculations, aromatic pyrene rings in water form the hydrophobic cluster by both open and closed conformers of **PyKC** as evident from the intra-molecular distance between pyrene rings of individual **PyKC** molecule in the layer (data not shown). On the other hand, the N/O atoms of the peptide conjugates bring very few water molecules inside the **PyKC** layer. These water molecules get trapped within the cluster due to two reasons: a) hydrogen bonds between the trapped water and b) the hydrophobic barrier by the pyrene rings. We identified water molecules which were trapped inside the **PyKC** layers based on the geometric criteria. If a water molecule continuously resides in the core region of **PyKC** (indicated in the density profile by a region (a)) for the entire production run-length of 60 ps, that water is considered as trapped water (TW). TW molecules follow a sub-diffusive dynamics (**fig. 4.21**) demonstrating the extent of confinement and form hydrogen bonds to each other as shown in the inset of **fig. 4.20A**). We calculated intermittent hydrogen bond auto-correlation function for TW and bulk water (BW) following equation,[194,195a]

$$C_{HB}(\boldsymbol{t}) = \frac{< \boldsymbol{h_{TW-TW}(0)h_{TW-TW}(t)} >}{< \boldsymbol{h_{TW-TW}} >}$$

Where, $h_{TW\text{-}TW}(t)$ represents the hydrogen bonds among the trapped water (TW) molecules, and it is 1 if there is a hydrogen bond, otherwise 0. **Fig. 4.20B** shows that the TW relaxes much slower than that of the BW. The change in activation free energy for the breaking of the hydrogen bonds is evaluated using reactive flux correlation analysis.[199] The activation energy ($\Delta \boldsymbol{G^{\#}_{break}}$) for hydrogen bond breaking for the TW is higher than that of the bulk water. The intermittent hydrogen bond relaxation time of TW is much slower than the BW and the relaxation time-scales of TW are comparable to the hydrogen bond relaxation time of confined water near biomolecules.[13] These results clearly indicate the extreme slow dynamics of the trapped water molecules are due to the confinement of water within the **PyKC** layer and are consistent with the experimental observations of least water transport across the hydrogel. Therefore, the insolubility and the unique

compartmentalization ability of the hydrogel are attributed to the specific molecular packing of **PyKC** where peptide conjugates are stabilized by the intramolecular hydrogen bonds and the aromatic pyrene clusters are stabilized by the π–π interactions.

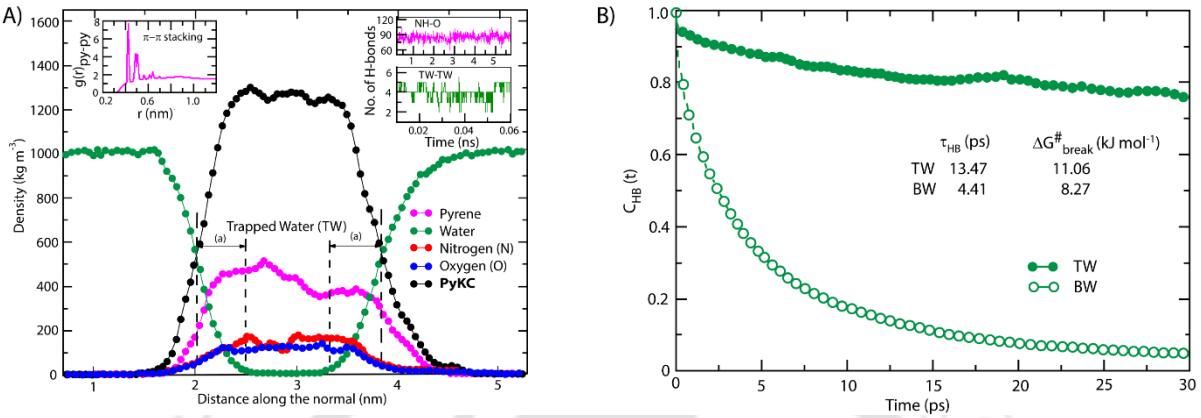

Fig. 4.20 (A) Density profile of **PyKC** layer across the normal from MD simulation. Distinct interfaces of **PyKC**-water are visible showing the compartmentalization of the hydrogel and water. The N/O atoms of the peptide conjugates stay within the layer and bring few waters inside the core of the layer. Water molecules residing continuously in the core region are shown within the vertical lines denoted by the area (a) and labelled as trapped water (TW). Inset: RDF (g(r)) of pyrene-pyrene shows the first peak locates at 0.4 nm where π–π stacking of pyrene rings operate. Numbers of intra-molecular hydrogen bonds among N and O of the peptide conjugate are shown for the production run. These hydrogen bonds contribute in stabilizing the molecular packing of **PyKC** hydrogel. Numbers of hydrogen bonds among trapped water (TW-TW) are shown for the time for which TW remain confined within the core of **PyKC** layer. B) Intermittent hydrogen bond auto-correlation function of TW and bulk water (BW) showing very slow relaxation of the TW. Slow hydrogen bond relaxation time (τ_{HB}) and high activation energy ($\Delta G^{\#}_{break}$) of hydrogen bond breaking of TW compared to that of BW indicate the possibility of less water transport across the hydrogel.

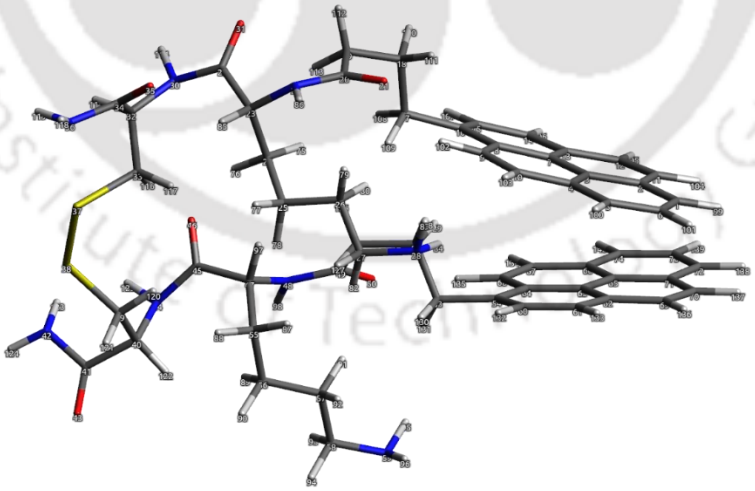

Fig.4.21 Snapshot of geometry optimized folded **PyKC** dimer with atom labels.

Thus **PyKC** forms dimers through a disulfide linkage and the dimers self-assemble to form a water-insoluble hydrogel. The self-aggregation is stabilized through the strong π–π interactions of the pyrene rings and intramolecular hydrogen bonds between the nitrogen and oxygen atoms of the peptide conjugates. Since peptide conjugates are hydrophilic in nature, they bring few water molecules. These water molecules remain confined via hydrogen bonds among trapped water (TW) molecules. The hydrogen bonds among the trapped water molecules and the hydrophobicity of the pyrene rings slow down water transport across the **PyKC** layer resulting in unusual confinement in the system.

4.3 Conclusion

In summary, a unique supramolecular hydrogel is reported which remains insoluble in water and other aqueous or water-soluble systems. Importantly, unlike polymeric cross-linked gels, no exchange of solute or solvent is allowed from and to the hydrogel. The hydrogel remained insoluble for a prolonged time in a bulk aqueous medium as well as in a variety of other solutions. Experimental evidence along with theoretical calculations reveal that the gelator molecule dimerizes and the dimers pack themselves through strong π-π stacking of pyrene rings which leads to the formation of a very tightly knitted network of thin fibers and consequently the hydrogel. The insolubility in water is attributed to the hydrophobic hydration emerged due to the spontaneous self-assembly of **PyKC**-dimer where the water molecules are confined between the hydrophobic cavity of pyrene rings and the peptides.

4.4 EXPERIMENTAL SECTION

4.4.1 Materials

Rink Amide MBHA resin, Fmoc-Cys(Trt)OH, Fmoc-Lys(Boc)-OH, HBTU and HOBT were procured from GL Biochem, China. Rhodamine B, TCEP, 1-Pyrenebutyric acid and Triethylsilane (TES), DTT, GSH, and Trypsin from *Porcine pancreas* were ordered from Sigma Aldrich HPLC-grade dimethylformamide (DMF) and Trifluoroacetic acid (TFA), acetonitrile (ACN), Tetrahydrofuran (THF), Dioxane, Methanol, Ethanol, Dimethylsulfoxide (DMSO), 1-propanol, and 2-Propanol were purchased from Spectrochem. Dichloromethane (DCM) and acetone were purchased from Rankem. To prepare samples, Milli-Q water with a conductivity of less than 2 $mScm^{-1}$ was used. Chromatographic purifications were performed on a Luna 5 µm (C18, 250x10 mm) column (Phenomenex) whereas, analytical HPLC was performed on a Luna 5 µm (C18, 250x4.6 mm) column (Phenomenex) using a

Dionex Ultimate 3000 HPLC. UV-Visible spectra were recorded on a PerkinElmer Lambda 750 spectrometer, while fluorescence measurements were performed on a Fluoromax 4 (Horiba) spectrophotometer. Standard 10 mm-path quartz cuvettes were used for all spectroscopic measurements. ^{1}H NMR, ^{13}C NMR were recorded with a Bruker Ascend 400 MHz (Bruker, Coventry, UK) spectrometer and referenced to deuterated solvents. ESI-MS was performed with a Q-Tof-Micro Quadrupole mass spectrophotometer (Micromass). FETEM images were taken using a JEOL JEM-2100F microscope.

4.4.2 Synthesis of the peptides

The peptides were prepared using solid phase peptide synthesis technique employing Rink-amide MBHA resin as the solid support. Sequence elongation at the N-terminus was performed by coupling the appropriate Fmoc protected amino acids (4 equiv.) under standard conditions employing HBTU (4 equiv.) and DIPEA (8 equiv.) as coupling reagents in presence of HOBT (4 equiv.) in DMF. Fmoc deprotection was achieved by treating the resin bound peptide with 20% piperidine in DMF. The peptide was cleaved from the resin using a cocktail of 95% TFA - 4% dichloromethane - 1% triethylsilane. Precipitation from dry ether followed by purification using semi-prep HPLC (acetonitrile/water system as the eluent) and lyophilization provided the pure peptides. All the control molecules were prepared following a similar protocol.

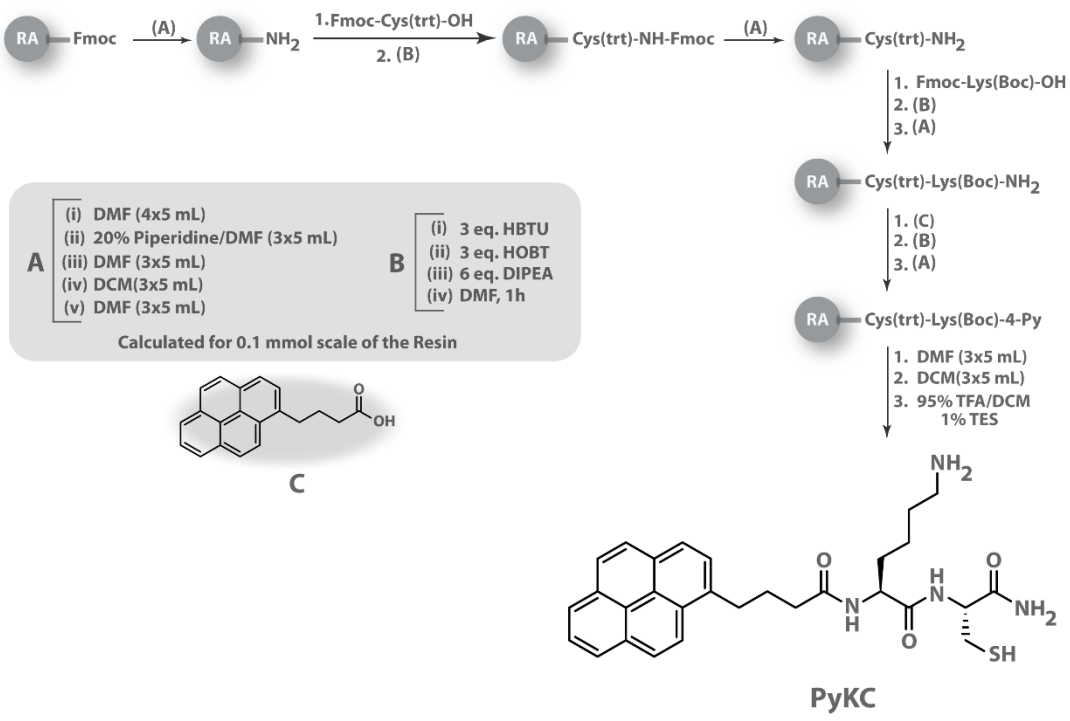

Scheme 3.2 Synthetic route for **PyKC.**

4.4.3 Characterization of synthesized peptides

4.4.3.1 PyKC

^{1}HNMR (DMSO-d_6, 400 MHz): δ/ppm = 8.39 (d, J = 9.3 Hz, 1H), 8.28 (m, 2H), 8.23 (m, 2H), 8.14 (d, J = 2.0 Hz, 2H), 8.07 (t, J = 7.6 Hz, 1H), 7.97 (t, J = 8.2 Hz, 2H), 7.66 (s, 3H), 7.29 (s, 1H), 7.20 (s, 1H), 4.39 – 4.21 (m, 2H), 2.90 – 2.66 (m, 4H), 2.29 (m, 3H), 2.03 (p, J = 7.3 Hz, 2H), 1.69 (m, 1H), 1.55 (m, 3H), 1.35 (d, J = 35.3 Hz, 2H). **^{13}C NMR** (100 MHz, DMSO-d6): δ/ppm = 172.96, 172.31, 171.87, 137.06, 131.36, 130.90, 129.78, 128.06, 127.93, 127.70, 126.99, 126.63, 125.42, 125.26, 124.03, 55.06, 53.19, 39.18, 35.29, 32.71, 31.44, 28.00, 27.10, 26.58, 22.82. **ESI-MS** calcd. for $[M+H]^+$, $C_{29}H_{34}N_4O_3S$: 519.24, found: 519.24 (m/z). **HPLC**: The peak of **PyKC** arrived at 12.8 min retention time when eluted with gradient started from 5% to finish at 100% of acetonitrile in water in a 20 min program.

4.4.3.2 Pep-2

^{1}H NMR (400 MHz, DMSO-d_6): δ/ppm= 8.92 (d, J = 7.5 Hz, 1H), 8.54 (d, J = 9.3 Hz, 1H), 8.42 (s, 1H), 8.36 (dd, J = 7.7, 4.1 Hz, 3H), 8.31 – 8.21 (m, 3H), 8.20 (d, J = 7.9 Hz, 1H), 8.14 (m, 2H), 7.70 (s, 3H), 7.53 (s, 1H), 7.29 (s, 1H), 4.68 – 4.58 (m, 1H), 4.46 (m, 1H), 2.93 (dd, J = 13.5, 5.0 Hz, 1H), 2.88 – 2.79 (m, 3H), 1.85 (s, 2H), 1.72 – 1.48 (m, 2H), 1.54 (s, 2H). **HPLC**: The peak of Pep-2 arrived at 10.1 min retention time eluted with a gradient started from 5% to finish at 100% of acetonitrile in water in a 20 min program.

4.4.3.3 Pep-3

^{1}H NMR (400 MHz, DMSO-d_6): δ/ppm = 8.39 (d, J = 9.3 Hz, 1H), 8.31 – 8.01 (m, 9H), 7.95 (d, J = 7.8 Hz, 1H), 7.69 (s, 3H), 4.38 (m, 2H), 2.90 (dd, J = 13.7, 4.6 Hz, 1H), 2.77 (m, 3H), 2.32 (t, J = 7.2 Hz, 2H), 2.02 (m, 2H), 1.73 – 1.62 (m, 1H), 1.54 (m, 3H), 1.35 (m, 2H). **HPLC**: The peak of Pep-3 arrived at 11.85 min retention time when eluted with a gradient started from 5% to finish at 100% of acetonitrile in water in a 20 min program.

4.4.3.4 Pep-4

^{1}H NMR (400 MHz, DMSO-d_6): δ/ppm = 8.40 (d, J = 9.3 Hz, 1H), 8.33 – 7.99 (m, 8H), 7.96 (d, J = 7.8 Hz, 1H), 7.63 (s, 3H), 7.31 (d, J = 11.9 Hz, 1H), 7.10 (d, J = 14.2 Hz, 1H), 4.40 (td, J = 12.1, 11.2, 7.3 Hz, 1H), 4.16 (m, 1H), 2.82 (s, 1H), 2.73 (s, 3H), 2.42 (s, 1H), 2.33 (s, 2H), 2.40 – 2.26 (m, 0H), 2.07 – 1.95 (m, 1H), 1.70 (d, J = 9.7 Hz, 1H), 1.58 – 1.46 (m, 0H), 1.32 (s, 2H), 1.29 (d, J = 7.5 Hz, 0H). **HPLC**: The peak of Pep-

4 arrived at 11 min retention time when eluted with a gradient started from 5% to finish at 100% of acetonitrile in water in a 20 min program.

4.4.3.5 Pep-5

^{1}H NMR (400 MHz, DMSO-d_6): δ/ppm = 8.37 (dd, J = 9.3, 5.7 Hz, 1H), 8.28 (dt, J = 3.8, 1.9 Hz, 1H), 8.29 – 8.10 (m, 6H), 8.13 – 8.01 (m, 1H), 7.94 (dd, J = 7.8, 5.5 Hz, 1H), 7.67 (s, 3H), 7.42 (d, J = 8.7 Hz, 1H), 7.26 (s, 1H), 4.36 – 4.18 (m, 1H), 2.89 (m, 1H), 2.77 – 2.64 (m, 3H), 2.31 (dd, J = 9.2, 5.2 Hz, 2H), 2.22 (t, J = 8.3 Hz, 1H), 2.02 (m, 2H), 1.66 (dd, J = 13.1, 6.2 Hz, 1H), 1.55 (h, J = 7.5, 6.2 Hz, 4H), 1.37 (d, J = 7.6 Hz, 1H), 1.34 (d, J = 7.7 Hz, 1H). **HPLC**: The peak of Pep-5 arrived at 10.76 min retention time when eluted with a gradient started from 5% to finish at 100% of acetonitrile in water in a 20 min program.

4.4.3.6 Pep-6

^{1}H NMR (400 MHz, DMSO-d_6): δ/ppm = 8.37 (m, 1H), 8.31 – 8.17 (m, 5H), 8.15 (m, 3H), 8.13 – 8.02 (m, 1H), 7.95 (d, J = 7.8 Hz, 1H), 7.67 (s, 3H), 7.41 (s, 1H), 7.26 (s, 1H), 4.38 – 4.18 (m, 2H), 2.89 (m, 1H), 2.74 (s, 3H), 2.32 (t, J = 7.3 Hz, 2H), 2.30 (s, 1H), 2.22 (t, J = 8.4 Hz, 1H), 2.01 (t, J = 7.5 Hz, 2H), 1.67 (s, 1H), 1.55 (m, 3H), 1.36 (m, 7.6 Hz, 2H). **HPLC**: The peak of Pep-6 arrived at 10.9 min retention time when eluted with a gradient started from 5% to finish at 100% of acetonitrile in water in a 20 min program.

4.4.3.7 Pep-7 (PyKC-dimer)

The disulfide-linked dimer of **PyKC** was prepared by incubating a 0.01 wt% solution of **PyKC** in water for 24 h followed by lyophilization and purity check by analytical HPLC and ESI-MS. No further purification was needed and the yield was more than 99.5%. **ESI-MS** calcd. for $[M+H]^+$, $C_{58}H_{66}N_8O_6S_2$: 1035.4580, found: 1035.4574, and 518.2320 $[M]^{2+}$. **HPLC**: The peak for **PyKC**-dimer arrived at 18.9 min retention time when eluted with a gradient started from 5% to reach 30% after 5 min and continued to reach 100% at 40 min.

4.4.4 Preparation of hydrogel

To prepare the hydrogel, appropriate amount of **PyKC** was added in required volume of 20 mM Tris-HCl buffer at pH 8 (to attain a concentration of 1 wt%) and shaken to completely dissolve the solid. The solution was kept undisturbed at room temperature for 12 h to get the self-supporting hydrogel. Unless otherwise mentioned, all the studies were performed with 1 wt% hydrogel at room temperature.

4.4.5 Rheology

The viscoelastic properties of the hydrogel were characterized using rheometer (Anton-Paar MCR 102) equipped with a 20 mm parallel plate (with 0.3 mm zero gap) measuring system at 25 °C. A strain sweep test was performed first to identify the linear viscoelastic region (LVR) over a range from 0.01 to 100 % strain at a fixed oscillatory frequency of 1 rad/s. The LVR can be defined as, where strain has no impact upon G′ and G″. Further, the mechanical strength of the gel was determined from oscillatory test i.e. frequency sweep, which was carried out under an appropriate strain (γ = 0.1 %) selected from the LVR with the frequency ranging from 0.1 to 1000 rad/s at 25 °C. For time dependent gelation studies, the experiment was set up at constant strain of 1% and constant frequency of 5 Hz. The whole experiment was done at 25 °C. The ten batches of gel were prepared in 1 wt% concentration at the same time. Each batch was analysed for one hour. The plot was obtained by combining the G′ and G″ values with time.

4.4.6 NMR studies

The ^{1}H NMR and ^{13}C NMR studies for characterization purpose were performed in DMSO-d_6. The role of hydrogen bonding in gelation was explained from ^{1}H NMR experiment in DMSO-d_6-water complex system at varying percentages of water. For water exchange determination, 750 μL solution of **PyKC** (1 wt%) in water was prepared and 200 μL of it was distributed in three centrifuge tubes and allowed to incubate for 24h to form hydrogel. In a separate experiment, 1.5 mL of fresh D_2O, NaOD (in D_2O) and DCl (in D_2O) solvents were taken and 2 mg of glycine was dissolved in each of these solvents. From these solutions, 500 μL were taken in NMR tubes and the ^{1}H NMR spectra were recorded, a) of these samles, b) after adding 5 μL of water and c) after adding another 95 μL of water (total of 100 μL of water). From the remaining deuterated solvents, 400 μL were added to the centrifuge tubes containing the hydrogels (200 μL each as prepared before) to wash the surface of the hydrogel and after centrifugation, the solvents were discarded. The remaining of the glycine containing deuterated solvents (600 μL) were added to the centrifuge tubes containing hydrogels and sealed. The tubes were incubated at room temperature while shaking at 100 rpm. After 1day of incubation, the samples were centrifuged and 500 μL of the supernatant solvents were taken and ^{1}H NMR spectra were recorded. The solvents were again added back to their respective centrifuge tubes and incubated. The procedure was repeated to get the spectra after 3 and 7 days of incubation. For the analyses of the data, the peak area ratio of glycine -CH_2 peaks (A_{Gly}) and residual water peaks ($A_{Residual}$) were considered. The increase/change in this ratio after incubation of hydrogel samples was considered to calculate the amount of water (H_2O) exchanged from the hydrogel

samples. In order to get the values for 100% exchange, the peak ratios of samples with external water (5 μL and 100 μL) were considered. Unfortunately, with 100 μL water, no ratio could be calculated and thus the ratio corresponding to the 5 μL water samples were extrapolated by multiplying it with 40 (as 200 μL of gels were present).

4.4.7 Determination of Sol–Gel Transition Temperature (T_g)

T_g was determined using a standard ball dropping method. A small steel ball was placed on top of the hydrogel sample (equal volume). The samples were placed in a water bath and the bath was heated at a rate of 0.5 °C/min. The temperature at which the steel ball drops to the bottom was noted as Tg. The experiments were performed in triplicate.

4.4.8 FETEM

5 μL of the samples were cast on the carbon-coated copper grid (300 mesh Cu grid with thick carbon film from Pacific Grid Tech, USA) and allowed to air dry for 10 minutes and then the excess sample was bloated with a tissue paper. The grid was then allowed to air dry for 1 day.

4.4.9 PXRD

Two samples were analyzed by PXRD, a) the gelator in a monomeric state, which was prepared by dissolving in hexafluoroisopropanol (HFIP) followed by drying under ambient condition, and b) a dried thin film of the gel. The samples were analyzed on a Bruker D2 Phaser X-ray diffractometer (30 kV, 10 mA). The Bragg peak λ was extracted from the XRD data and the layer thickness d could be obtained according to the Bragg equation $d = \lambda/2\sin\theta$, $\lambda = 0.15405$ nm.

4.4.10 Dissolution study

In a typical experiment, 500 μL of a 1 wt% hydrogel of **PyKC** (in 20 mM Tris buffer, pH 8) was added to 10 mL of the bulk solvent/solution and the sample was incubated with slow shaking (100 rpm) at room temperature. Aliquots of the bulk solvent/solution were taken time to time and replaced with the same amounts of fresh bulk solvent/solution to keep the overall volume intact. The aliquots were diluted with the same bulk solvent/solution before recording their absorption. Absorbance spectra of freshly prepared solutions of **PyKC**-dimer in the respective bulk solvent/solution were recorded to get the calibration curve to determine the concentrations of **PyKC**-dimer in the aliquots.

The % dissolutions were calculated following the cumulative absorbance at λ_{max} (352 nm). For temperature dependent study, every sample was incubated at a precisely temperature controlled water bath at the respective temperature for 1 h followed by incubation at to room temperature (30 mins). Aliquots were withdrawn from bulk solvent and analyzed. Analyses beyond 70 °C could not be performed as the melting temperature of the hydrogel was found to be 75 °C. All experiments were performed in triplicate.

4.4.11 Electronic Structure Calculations and Molecular Dynamics Simulations

For Folded (C-1, **fig. 4.17**) and open (C-2, **fig. 4.17**) conformations of **PyKC**-dimer were obtained using ChemDraw and used as the initial configurations for the geometry optimization using DFTB+ package. We used density functional tight binding (DFTB-D3) method to get the molecular structure of the PyKC-dimer. DFTB uses minimal atom-centered Slater-type all-valence basis sets and an approximate Hamiltonian matrix based on DFT energy equation. The electrostatic interactions between the partial charges of the molecule were evaluated considering self-consistent charges (SCC). Dispersion corrections were included to consider van der Waals and π–π stacking interactions. C, H, N element pair interactions were obtained from standard DFTB parameters (http://www.dftb.org). Earlier DFTB has been found useful to calculate the stacking energy for pyrene based systems. The total energy of the system in DFTB is written as,

$$\boldsymbol{E_{tot} = E_{BS}[n0] + E_{coul}[\delta n] + E_{rep}(R)}, \qquad (1)$$

Where, E_{BS} [n0] is the band structure energy term, E_{coul} [δn] is the energy due to charge transfer and E_{rep}(R) is the repulsion energy. Dimers of open and folded conformers of **PyKC** are optimized without and with dispersion correction terms. Convergence in the geometry optimization was achieved within 20000 steps. Both the optimized folded and open **PyKC**-dimers (from C-1 and C-2) were separately stacked in such a manner that the pyrene rings remain parallel. The energies of the optimized folded and open dimers were presented in **table 4.1**. The binding energies of the stacked conformers are calculated using the following equation,

$$\boldsymbol{\Delta E_b = E_s - 2E_d}, \qquad (2)$$

Where, ΔE_b is the binding energy, E_s is the energy of the stacked configuration and E_d is the dimer energy. The folded conformer was found to have stronger binding energy and chosen as the initial conformation of the **PyKC**-dimer to perform all-atom molecular dynamics (MD) simulations using GROMACS v4.6.5. Since **PyKC** forms hydrogel at or above 1 wt% concentration, (a) one dimer, (b) two dimers, (c) 60 dimers of geometry optimized **PyKC** each at a concentration of 43.4 wt%, were simulated in presence of SPC/E water model. The bonded parameters of the folded **PyKC**-dimer

were obtained by Automatic topology builder (ATB). Non-bonded parameters were obtained from GROMOS54a7 force-field. For (a), one PyKC dimer was inserted in a box of length 4.16 nm in each xyz direction followed by the random insertion of 75 water molecules. The system was energy minimized using the steepest descent algorithm. Temperature of the system was maintained at 300 K by velocity rescale thermostat in an NVT ensemble for 100 ps. Next a 42.5 ns NPT simulation was performed for equilibration using Parinello Rahman barostat for pressure coupling with a coupling constant of 1 ps. The pressure of the system was held at 1 bar. A time step of 2 fs was used for the simulation and trajectories were collected at every 10 ps and periodic boundary conditions were applied in all 3 directions. The non-bonded interactions were cut-off at a distance of 1 nm. The columbic interactions were determined by Particle mesh Ewald (PME) method. Last 5.5 ns of the total run-length is analyzed for all calculations performed. Systems (b) and (c) were simulated with the same set of parameters. To compare the dynamics of water near **PyKC** with the dynamics of bulk water (BW), a box of bulk SPC/E water molecules is simulated for 2 ns with a time step of 2 fs in an NPT ensemble. Temperature is coupled at 300 K using Nose-Hoover thermostat and Parinello Rahman. barostat is used to maintain the constant pressure of 1 bar. This is followed by an NVT run of 5 ns with a time step of 0.4 fs. The system is coupled to the velocity rescale thermostat with a coupling constant of 2 ps. Non-bonded interactions were cut-off at 0.9 nm. The box length was 1.87 nm in each xyz direction. The last 50 ps of the run were analyzed to calculate the dynamics of BW.

Chapter – 5

Controlled encapsulation, long time protection, and instant triggered release with a minimum damage of biomolecules by a smart tri-peptide hydrogel

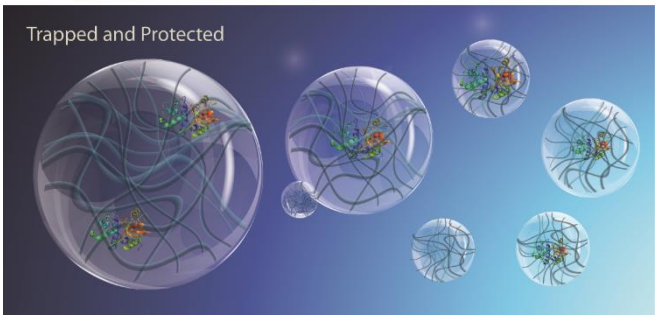

5.1 Introduction

Enzymes are the naturally occurring catalysts which catalyze almost all the biological metabolic processes.[200] The use of enzymes as biocatalysts is a well-established technique in various kind of industries like food,[201,202] textile,[203] cosmetics,[204] pharmaceutical,[205,206] and fine chemicals[207] etc. Enzymes are in general preferred over any other synthetic catalysts since, they are green, noncytotoxic, environmentally friendly, and show greater substrate specificity with high efficiency even under mild reaction conditions.[208] Enzymes are also recognized as efficient catalysts for the resolution of chiral compounds providing a promising alternative to the traditional catalysts.[208] However, even in this 21st century, the industrialization of enzymes are often hampered by a number of factors.[209] The high cost of extraction and purification is one of the major disadvantages of the enzymes to be used as a green catalyst. Secondly, they are relatively unstable and sensitive to conditions, such as a mild fluctuation in the environment, the presence of organic solvents, high temperature, inhibitors, acid, alkaline, and other various extreme conditions.[210,211] This poor stability reduces the natural ability of an enzyme to reboot its own system for the next batch of catalysis. It is important to understand the mechanism behind the functioning of an enzyme. A particular enzyme folds through non-covalent interaction to a particular tertiary structure, known as their native folding. The folding of the polypeptide chain leads to a reactive pocket where the substrates bind and the catalytic reaction takes place.

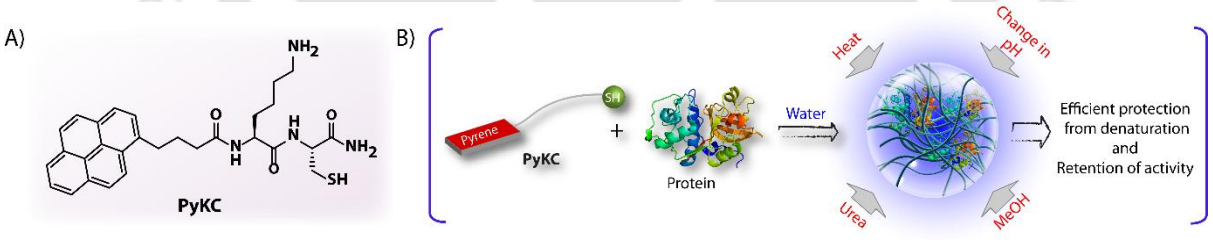

Scheme 5.1 (A) Chemical structure of the **PyKC** tri-peptide. (B) Schematic presentation of the encapsulation of proteins and prevention of denaturation in the presence of various denaturing agents.

However, as the non-covalent bonds are weak in nature, a subtle change in the condition can lead to the unfolding of the polypeptide or a misfolding. The unwinding of the folded enzymes is termed as denaturation while the reagents/conditions are known as denaturants. Thus enzymes are extremely delicate and susceptible toward denaturation. A lot of strategies has so far been taken to develop toward protecting and reusing the enzymes as biocatalysts. The list includes, 1) modification of enzyme structure by changing the amino acid sequence or covalently attaching small molecules to the sequence,[212-219] 2) modification of the microenvironment around the enzyme as per needed,[220] 3) immobilization onto a surface of solid support,[221-224] 4) encapsulation or

entrapment within an insoluble polymeric matrix as hydrogel or nanoparticles.[224-234] Several thousands of reports are published describing the storage and protection of enzymes using the aforementioned techniques.[235] However, all these processes suffer from various flaws including, loss in activity within a short period of time, complicated preparation protocols, short-term storage ability etc. New and efficient techniques and systems are of extremely high demand in this particular area.

Herein, we are reporting the efficient encapsulation of two different types of Lipase in **PyKC** hydrogel (**scheme 5.1**) discussed in Chapter 4. The enzymes are not covalently restricted, rather they are encapsulated inside the tight entanglement of the fibers inside the gel or matrix. The gel is highly capable of enhancing the stability of the enzyme from a wide range of water-soluble organic solvents, different pHs, and even from high temperature. It also can release the enzyme in a triggered way with the help of some disulfide bond-breaking agents. Moreover, the **PyKC** gel protects the enzyme for a long period of time (at least more than 3 months) at room temperature without losing activity.

5.2 Results and Discussion

As discussed in Chapter 4, the hydrogel produced by **PyKC** showed unique insolubility and confinement property. We envisioned that the hydrogel network could be used as a protective capsule for enzymes. We realized that if an enzyme can be entrapped in **PyKC**-hydrogel, a) they can be protected from any external denaturant as any movement of solvent or solute to and from this hydrogel is restricted, and b) because of the tightly knitted network, there may not be enough space for the entrapped enzymes to unwind itself in response to external stimuli.

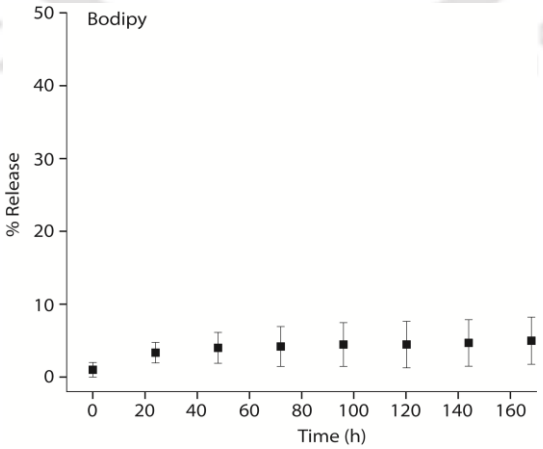

Fig. 5.1 Percentage release of the BODIPY-labelled CV-Lipase with time.

Before evaluating the proposed hypothesis, it was important to check whether the hydrogel is capable of encapsulating proteins and if yes, what the possibility of leaching is. In order to check that, *Chromobacterium viscosum* lipase (CV-Lipase) was labelled with BODIPY dye. A solution of this BODIPY-labelled lapse was used to prepare the hydrogel of **PyKC**. The hydrogel was placed in bulk water and time-dependent release of the protein was monitored following similar protocol mentioned in chapter 4. Importantly, only ~4% leakage of the protein was recorded (**fig. 5.1**) from the absorption spectra within the first day and no further leakage could be observed up to 7 days. The initial leakage can be contributed to the surface bound proteins which could easily get solubilised in the bulk solvent. The experiment clearly demonstrates the hydrogel is capable of encapsulating proteins and no protein molecule can come out of the hydrogel unless it is treated with any disulfide breaking agent.

5.2.1 Stability and retention of structural conformation of the lipase

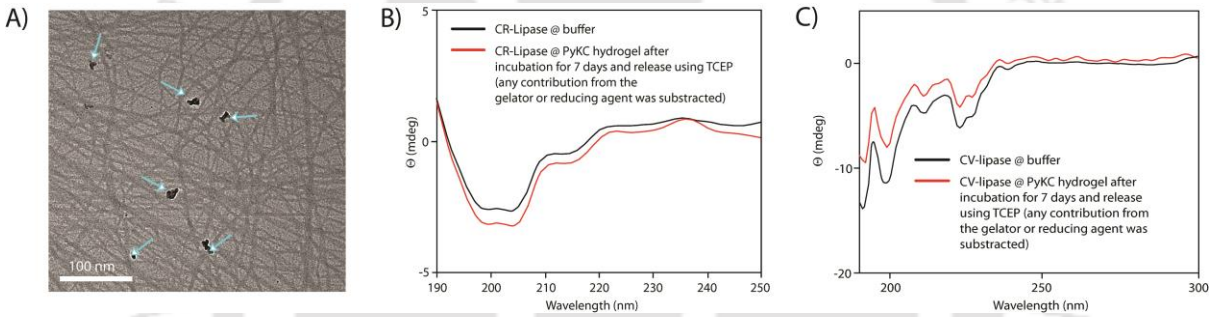

Fig. 5.2 (A) FETEM image of 1wt% hydrogel prepared from **PyKC** in 20 mM Tris buffer of pH 8 containing CV-lipase. The arrows show the enzymes embedded in the network. CD spectra of (B) CR-lipase and (C) CV-Lipase in free and gel-trapped conditions to identify any denaturation due to encapsulation and incubation at room temperature for 7 days.

The FETEM image of enzyme (CR-Lipase) trapped hydrogel is clearly showing the existence of the enzymes inside the cavities of the fiber-network in unfolded condition confirming the stability of the trapped enzymes in the hydrogel environment (**fig. 5.2A**). For further investigation of the retention of structural conformation of the enzymes inside gel-network, we have performed the circular dichroism (CD) experiments. Since breakage/dissolution of the **PyKC** hydrogel can be achieved by using disulfide bond-breaking agents, the enzymes, viz, *Chromobacterium viscosum* lipase (CV-Lipase) and *Candida rugosa* lipase (CR-Lipase) were chosen as treatment with TCEP did not affect their activity. Moreover, lipases are non-proteolytic in nature and hence any catalytic activity on the **PyKC** molecules is not possible. Enzymes were trapped inside the hydrogels and dispersed in required buffers. After seven days, the gels were re-dissolved by TCEP and the released enzymes showed very similar CD to that of the native protein (**fig. 5.2B-C**). The reappearance of

native CD signal demonstrates that the enzymes could retain their conformation inside the gel-network.

5.2.2 Retention of activity of lipase

For enzyme activity studies, several enzyme trapped hydrogel samples were prepared for each of these enzymes and as controls, similar samples of the free enzymes were also prepared in absence of the gelator. At different time intervals, the enzyme activities of the gel entrapped enzyme as well as of the controlled samples were measured (**fig. 5.3** and **5.4**).

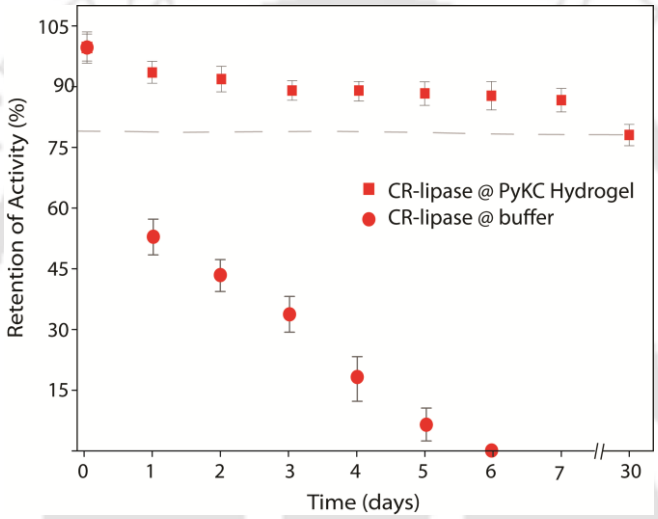

Fig. 5.3 Retention of catalytic activities (%) of the gel-trapped and free CR-Lipase at different time intervals when incubated at room temperature.

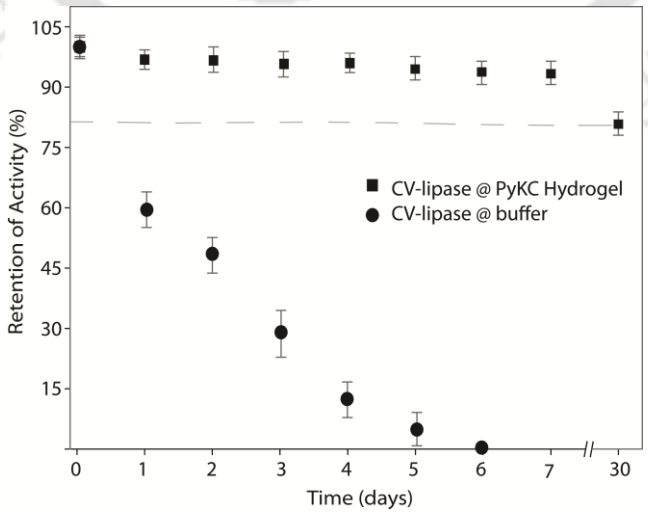

Fig. 5.4 Retention of catalytic activities (%) of the gel-trapped and free CV-Lipase at different time intervals when incubated at room temperature.

To break the gels and bring the entrapped enzymes out of the gel, the samples were treated with the required amount of TCEP before each measurement. Similar treatments were also done for the free enzyme samples. Interestingly, the activity of both free lipases decreased significantly with time and they lost their activities completely within 6 days. However, for the gel trapped enzymes, there is an initial loss of activities (~7-10%) in the first 24h and thereafter no significant change was observed up to 7 days. Importantly, they retained up to ~80% of their activities even after 30 days.

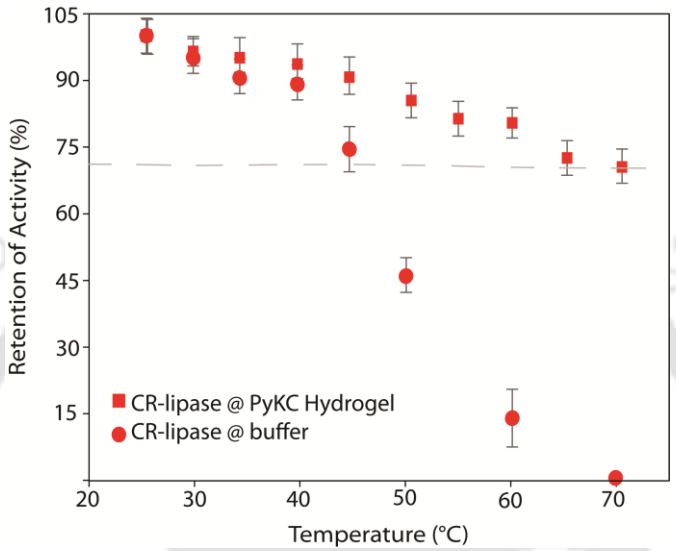

Fig. 5.5 Retention of catalytic activities (%) of the gel-trapped and free CR-Lipase as a function of temperature

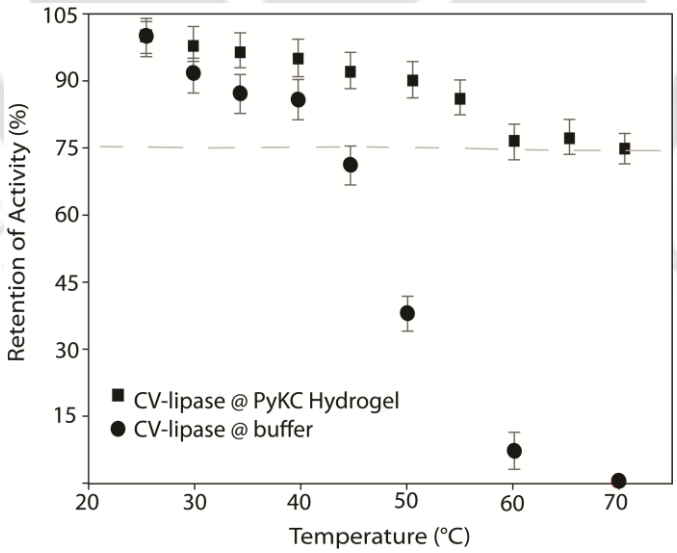

Fig. 5.6 Retention of catalytic activities (%) of the gel-trapped and free CV-Lipase as a function of temperature

Similar experiments were performed for both enzymes where each sample was heated at a particular temperature for 1 h prior to cooling to room temperature and activity measurements. As expected, the free enzymes lost their activities drastically with increase in temperature and at 60 °C,

only ~10% activities were observed while the gel-trapped enzyme retained 75% activity even at 70 °C (**fig. 5.5** and **5.6**). Moreover, maintaining the temperature at 40 °C for seven days resulted only ~18 % loss in activity for gel-trapped CR-Lipase (**fig. 5.7**). However, as the **PyKC** gel is strongly resistant to denaturants, like urea solution, methanol etc. established in chapter 4, we were interested to find its ability to protect the enzymes from these denaturing agents.

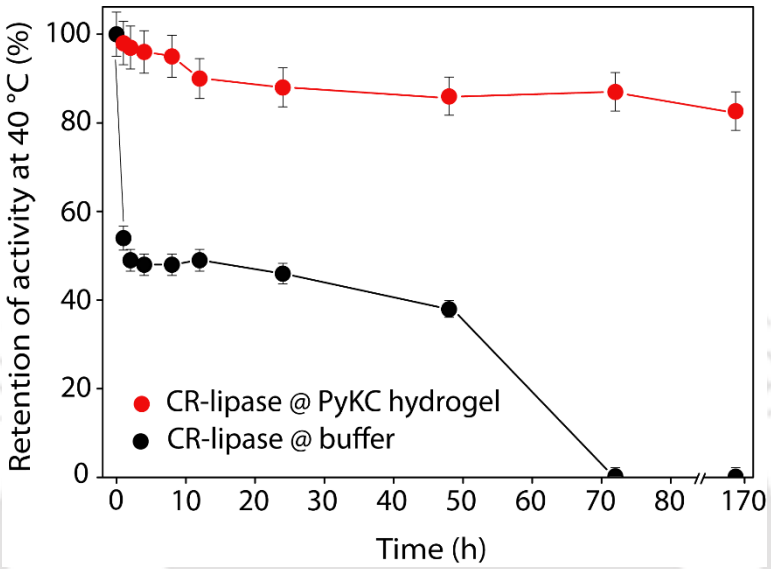

Fig. 5.7 Retention of activity (%) at different time interval by gel-trapped and free CR-lipase when incubated at 40 °C.

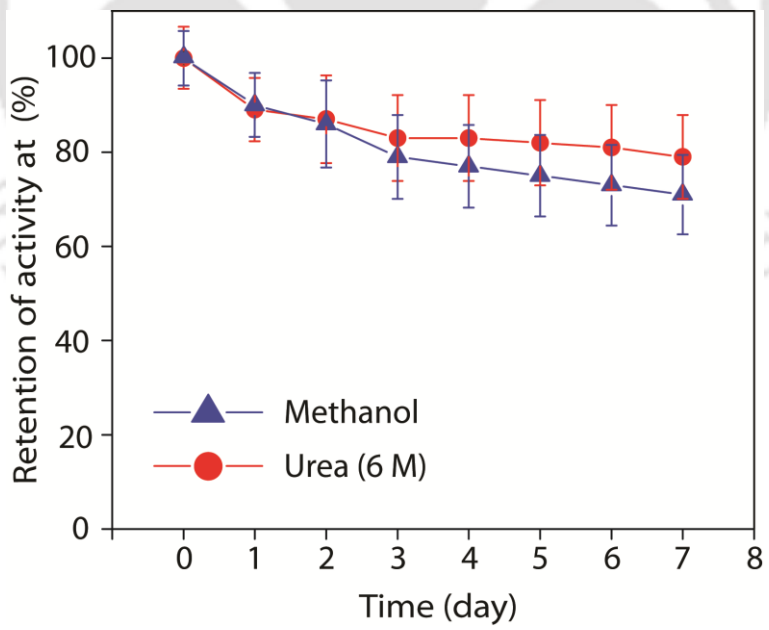

Fig. 5.8 Retention of activity (%) at different time interval by gel-trapped CR-lipase when dispersed in methanol or 6 M urea solutions.

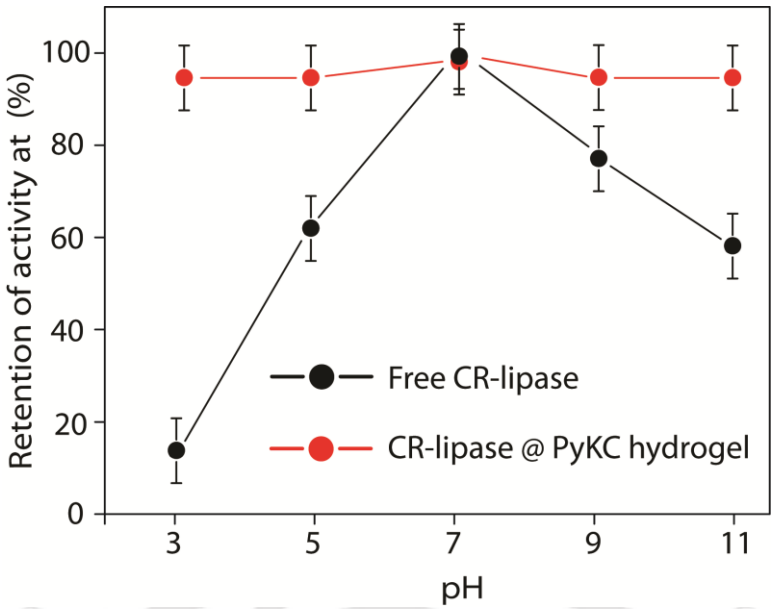

Fig. 5.9 Comparison of retention of activity by CR-lipase under the free and gel-trapped condition when exposed to buffer solutions of different pH for 1h.

Interestingly, exposure to these denaturing agents could not impart any significant changes in the activities of the enzymes as only 10-15% loss were noted after seven days of exposure while the free enzymes were found inactive in presence of these external agents (**fig. 5.8**). Moreover, suspending the hydrogel in buffers of different pH for 1 h could not make any difference in the activity of the trapped-enzyme (**fig. 5.9**).

5.3 Conclusion

The results with these enzymes prove our hypothesis and show that the **PyKC** hydrogel can be used as an effective protecting envelope for biomolecules. The tight packing of the fibers within the hydrogel network and the unusual compartmentalizing property of the hydrogel is efficiently used to confine and protect enzymes from denaturation in the presence of various denaturing agents and stimuli.

5.4 Experimental Section

5.4.1 Materials

The gelator, **PyKC** was synthesized as described in chapter 4. The enzymes, *Chromobacterium viscosum* lipase, *Candida rugosa* lipase, Glutaric anhydride, 2,4-dimethylpyrrole, DMAP, $BF_3.Et_2O$, and *N, N'*-disuccinimidylcarbonate were procured from the Sigma Aldrich. Urea, methanol, tris (2-

carboxyethyl) phosphine hydrochloride (TCEP), and tris hydrochloride (Tris) were purchased from Loba Chemie, Spectrochem, Sigma Aldrich and Spectrochem respectively. To prepare samples, Milli-Q water with a conductivity of less than 2 $mScm^{-1}$ was used. UV-Visible spectra were recorded on a PerkinElmer Lambda 750 spectrometer. Circular Dichroism (CD) experiment was performed by using Jasco J-1500 spectropolarimeter. ESI-MS was performed with a Q-Tof-Micro Quadrupole mass spectrophotometer (Micromass). FETEM image was taken using a JEOL JEM-2100F microscope.

5.4.2 Synthesis and Characterization

5.4.2.1 Bodipy-butyric acid[236]

Glutaric anhydride (68 mg, 0.60 mmol), dry DCM (10 mL), 2,4-dimethylpyrrole (112 mg, 1.20 mmol), and $BF_3{\cdot}OEt_2$ (0.11 g, 0.80 mmol) were added consecutively to a nitrogen-flushed round-bottom flask. The mixture was reluxed for 5 h. The mixture was allowed to cool to room temperature, and then $BF_3{\cdot}OEt_2$ (0.56 g, 4.0 mmol) and Et_3N (0.30 g, 3.0 mmol) were added. The reaction mixture was stirred under nitrogen at room temperature overnight followed by washing with water (2 × 10 mL). The organic phase was dried over Na_2SO_4, and the solvent was evaporated under vacuum. The resulting dark oil was purified by chromatography (hexane/EtOAc 2:1) to give 25 mg (13%) of BODIPY-butyric acid as a dark red solid. **^{1}H NMR** (400 MHz, $CDCl_3$): δ/ppm = 6.06 (s, 2H), 3.05-2.98 (m, 2H), 2.58-2.48 (m, 2H), 2.51 (s, 6H), 2.42 (s, 6H), 2.02-1.93 (m, 2H). **^{13}C NMR** (100 MHz, $CDCl_3$): δ/ppm = 177.9, 154.3, 144.7, 140.4, 131.5, 121.9, 27.4, 26.5, 16.3, 14.5, 14.4. **HRMS** calcd. for $[M+H]^+$, $C_{17}H_{21}{}^{10}BF_2N_2O_2$: 333.1701, found: 333.1702 (m/z).

5.4.2.2 Bodipy-NHS ester[237]

Bodipy-butyric acid (1 eq) and *N, N'*-disuccinimidylcarbonate (3.1 eq) were dissolved in dry DMF under argon and DMAP (3.1 eq) in THF was added at a time. After 1.5 hours at room temperature, the mixture was dissolved in chloroform and washed four times with a 1:1 solution of brine:water. The chloroform was dried over anhydrous sodium sulfate, and concentrated *in vacuo*. The residue was purified on silica gel by elution with MeOH/DCM. Yield = 60%; **^{1}H NMR** (400 MHz, $CDCl_3$): δ/ppm = 6.04 (s, 2H), 3.07 (m, 2H), 2.93 (3H), 2.86 (3H), 2.83 (s, 4H), 2.79-2.73 (m, 2H), 2.49 (s, 3H), 2.40 (s, 3H), 2.06-2.02 (m, 2H), **^{13}C NMR** (100 MHz, $CDCl_3$) δ/ppm = 168.72, 167.56, 154.21, 143.78, 140.23, 132.09, 121.68, 30.68, 26.83, 25.98, 25.36, 16.18, 14.24, 14.21. **HRMS** calcd. for $[M+Na]^+$, $C_{21}H_{24}N_3O_4BF_2Na$: 454.17201, found: 454.17132 (m/z).

5.4.3 Preparation of enzyme incorporated hydrogel

To prepare the enzyme incorporated hydrogel, an appropriate amount of **PyKC** was dissolved in the required volume of 20 mM Tris-HCl buffer at pH 8 and added with the enzyme solution to attain a concentration of 1 wt%. The solution was kept undisturbed at room temperature for 12 h to get the self-supporting hydrogel. Unless otherwise mentioned, all the studies were performed with 1 wt% hydrogel at room temperature.

5.4.4 FETEM

5 μL of the 1 wt% sample containing enzyme incorporated hydrogel was cast on carbon-coated copper grid (300 mesh Cu grid with thick carbon film from Pacific Grid Tech, USA) and allowed to air dry for 10 minutes and then the excess sample was bloated with a tissue paper. The grid was then allowed to air dry for 1 day.

5.4.5 Circular Dichroism (CD)

The CD spectra of all the samples were recorded at room temperature. The data were collected at 1 nm intervals with 2 nm bandwidth. All measurements were done in 0.2 cm path length cuvette with 400 μL sample volume. Each CD profile is an average of 3 scans of the same sample collected at a scan rate of 100 nm min^{-1}, with a proper baseline correction from the respective solvents. In a typical experiment, three samples were prepared and analyzed by CD.

a) PyKC (1 wt%) solution was prepared by dissolving an appropriate amount of PyKC in 20 mM Tris buffer (pH 8) containing 400 μg mL^{-1} of the respective enzyme and 100 μL portions of the solution were incubated separately at room temperature for 12 h to form the hydrogel where the enzyme was encapsulated. The gel was kept at room temperature for seven days and then re-dissolved in 400 μL of Tris buffer containing 7 mg mL^{-1} of TCEP. The CD spectra of this solution were recorded.

b) The CD spectra of native enzyme solution maintaining the enzyme concentration as in the previous case were recorded in presence and absence of TCEP (Importantly, the presence of TCEP did not impart any noticeable change in the structural conformation of the enzymes).

c) CD spectra of a re-dissolved PyKC hydrogel (maintaining the amount of PyKC, buffer, and TCEP as in case of sample (a)) without the enzyme was also recorded and any contribution from this spectrum was subtracted from the CD spectra of sample (a). The spectra obtained from a sample (b)

and (a-c) were compared to find any change in the tertiary structure of the enzyme. These experiments were performed five times to confirm the obtained results.

5.4.6 Enzyme activity

For enzyme activity, 1 wt% **PyKC** solutions were prepared in 20 mM Tris buffer (pH 8) containing the enzyme (70 units/mL). From these solutions, 100 μL portions were taken in 2 mL centrifuge tubes and incubated at room temperature for 12 h to form hydrogels. Similar samples maintaining the buffer and enzyme concentrations were prepared without the gelator. To the hydrogel samples, 1.5 mL of bulk water were added and shaken slowly to suspend the gels in water. Both series of samples were incubated at room temperature and at different time intervals, a pair of gel trapped enzyme and free enzyme sample were taken for analyses. For the gel trapped enzyme samples, the gels were centrifuged and washed with water three times before releasing the enzyme with the help of 0.3 mL of 25 mM TCEP solution and then diluting the sample with appropriate amounts of phosphate buffer (pH 7.2). Free enzyme samples were diluted with phosphate buffer to maintain the overall enzyme concentration as in the case of gel-trapped samples. The enzyme activity was measured by adding 10 μL of 30 mM substrate (PNPA) to these solutions and monitoring the change in absorbance at 400 nm. The loss in activities was calculated with respect to the initial activity of the free enzyme sample at 0 h. For temperature dependent study, the samples were prepared in glass vials and incubated in a precisely controlled water bath maintaining a particular temperature for 1 h. After the incubation period, the samples were allowed to come back to room temperature (30 mins) before doing all the treatments and activity measurements as mentioned before. For the effect of denaturants, only the activity of CR-Lipase was monitored. a) MeOH and Urea: hydrogels were incubated in bulk MeOH or 6 M urea solutions. Samples at different times were centrifuged and washed three times with water before analyzing the activity following a similar procedure as mentioned before. For free enzyme activities, 10 μL of either MeOH or 6 M urea solutions were added to the enzyme solutions before measuring the activities. In both cases, the enzyme showed no activity at all. b) Effect of pH: hydrogel samples containing the enzyme were incubated in buffer solutions of different pH (pH 3: citrate buffer; pH 5: acetate buffer; pH 7: phosphate buffer; pH 9: Tris buffer; pH 11: $NaHCO_3$/NaOH; all 20 mM) for 6 h before centrifugation and washing with water three times. The enzyme activities were then studied following the protocol mentioned before. For free enzyme, the activities were measured in the mentioned buffers.

भारतीय प्रौद्योगिकी संस्थान गुवाहाटी
Indian Institute of Technology Guwahati

NMR, MASS, and HPLC of the Synthesized Compounds

भारतीय प्रौद्योगिकी संस्थान गुवाहाटी
Indian Institute of Technology Guwahati

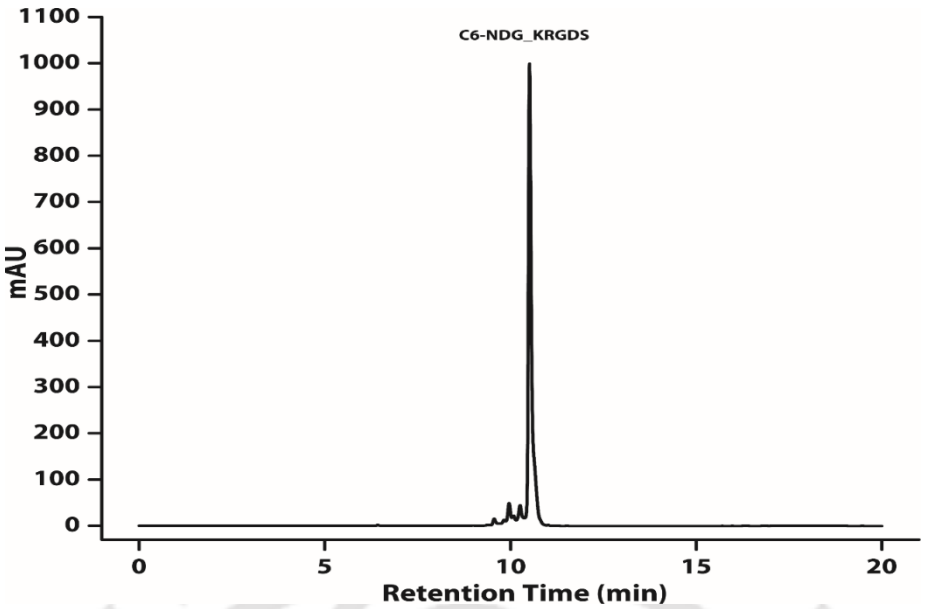

Fig. S2.1. Analytical HPLC chromatogram of **PA-1**.

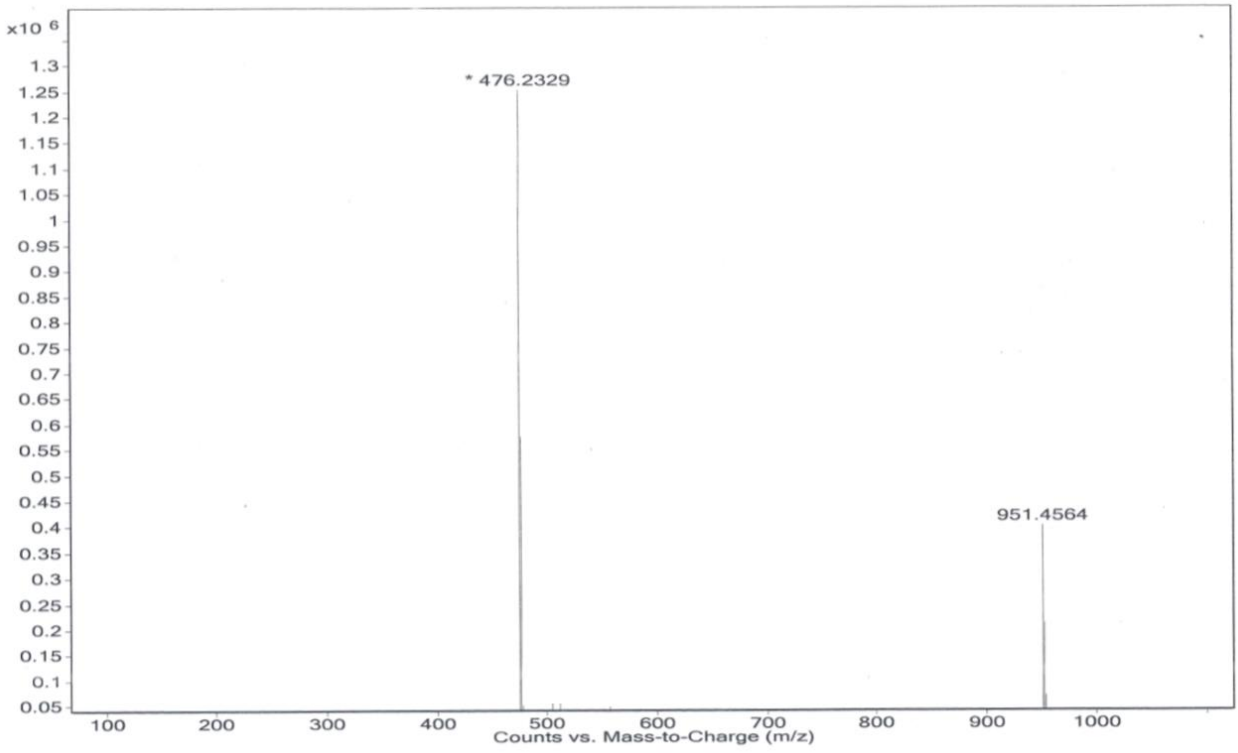

Fig. S2.2. ESI-MS of **PA-1.**

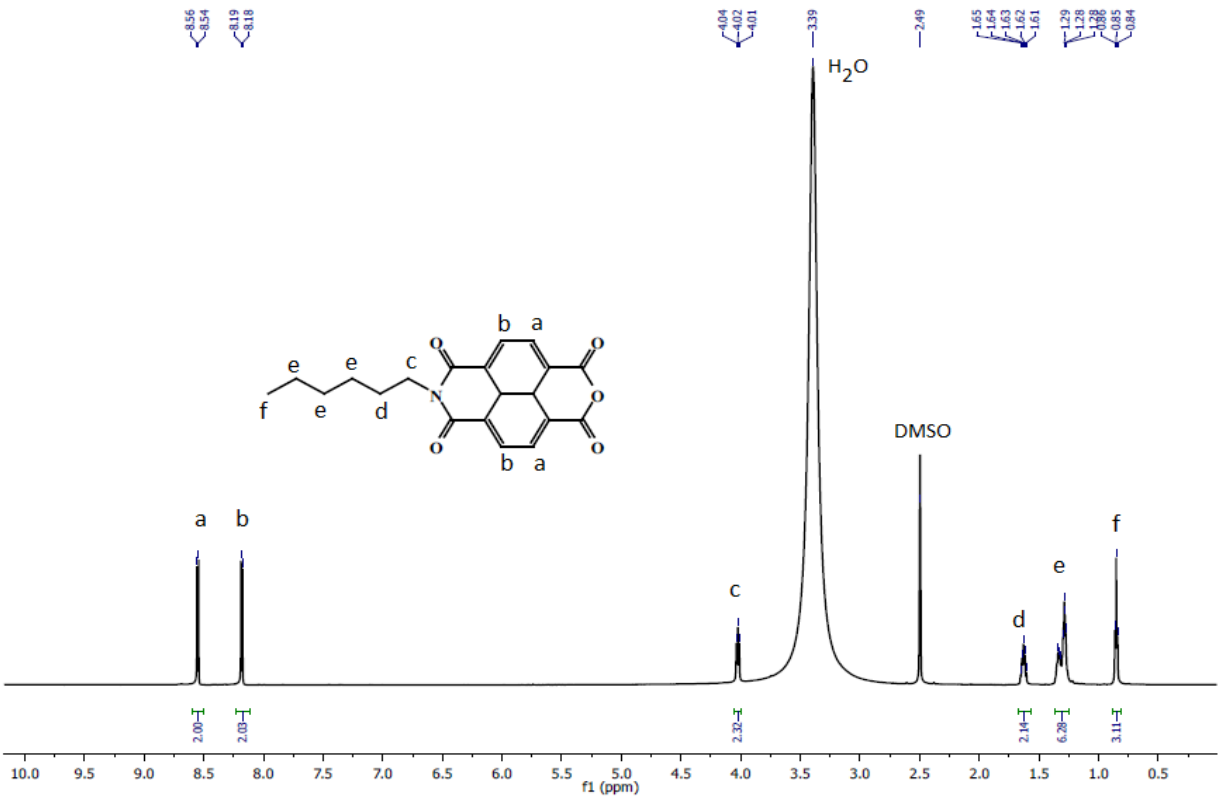

Fig. S2.3. ^{1}H NMR spectra of **1a** in DMSO-d_6.

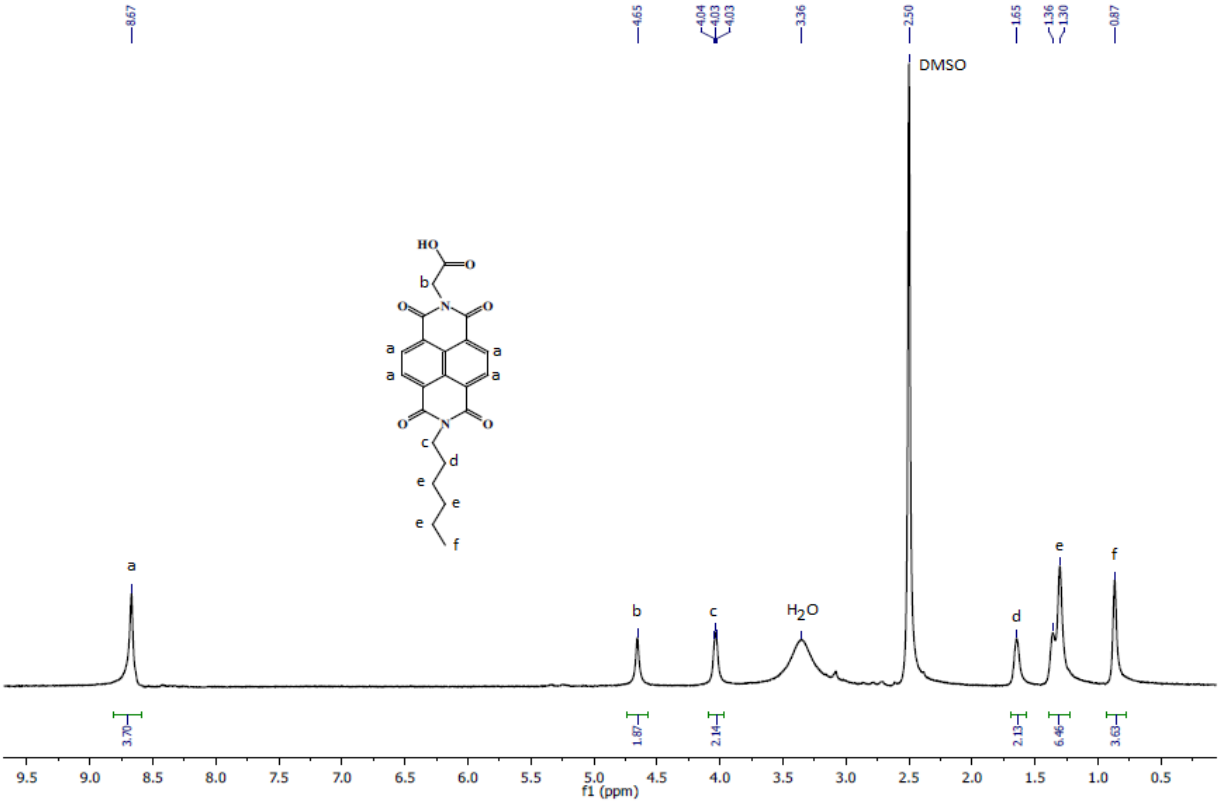

Fig. S2.4. ^{1}H NMR spectra of **1b** in DMSO-d$_6$.

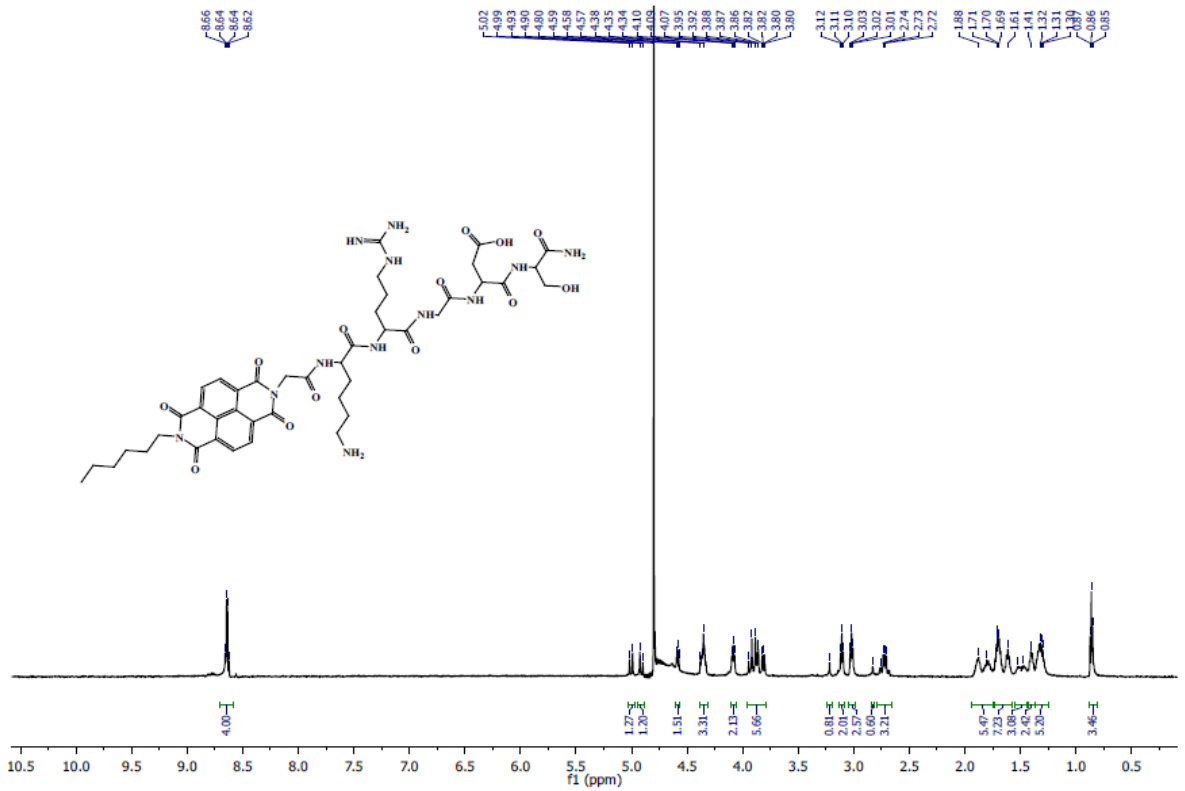

Fig. S2.5. ^{1}HNMR spectra of **PA-1** in D_2O.

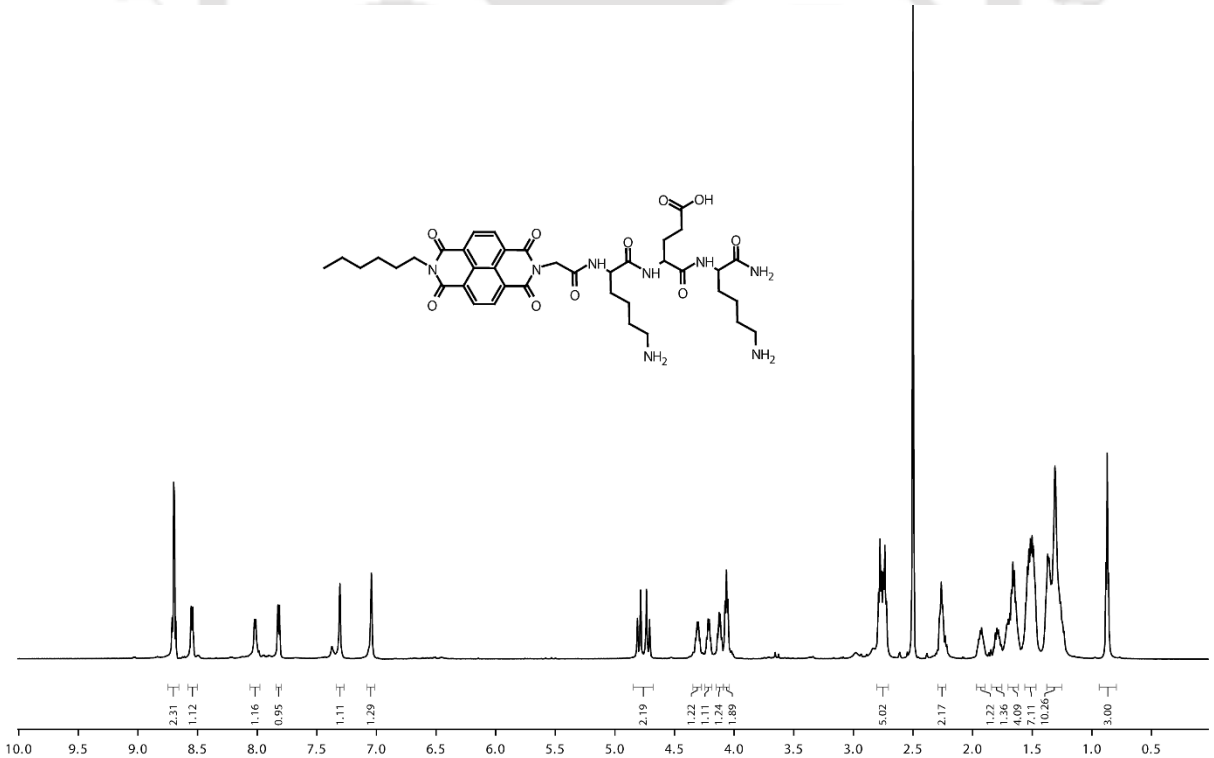

Fig. S3.1. ^{1}H NMR spectra of C6-NDG-KEK.

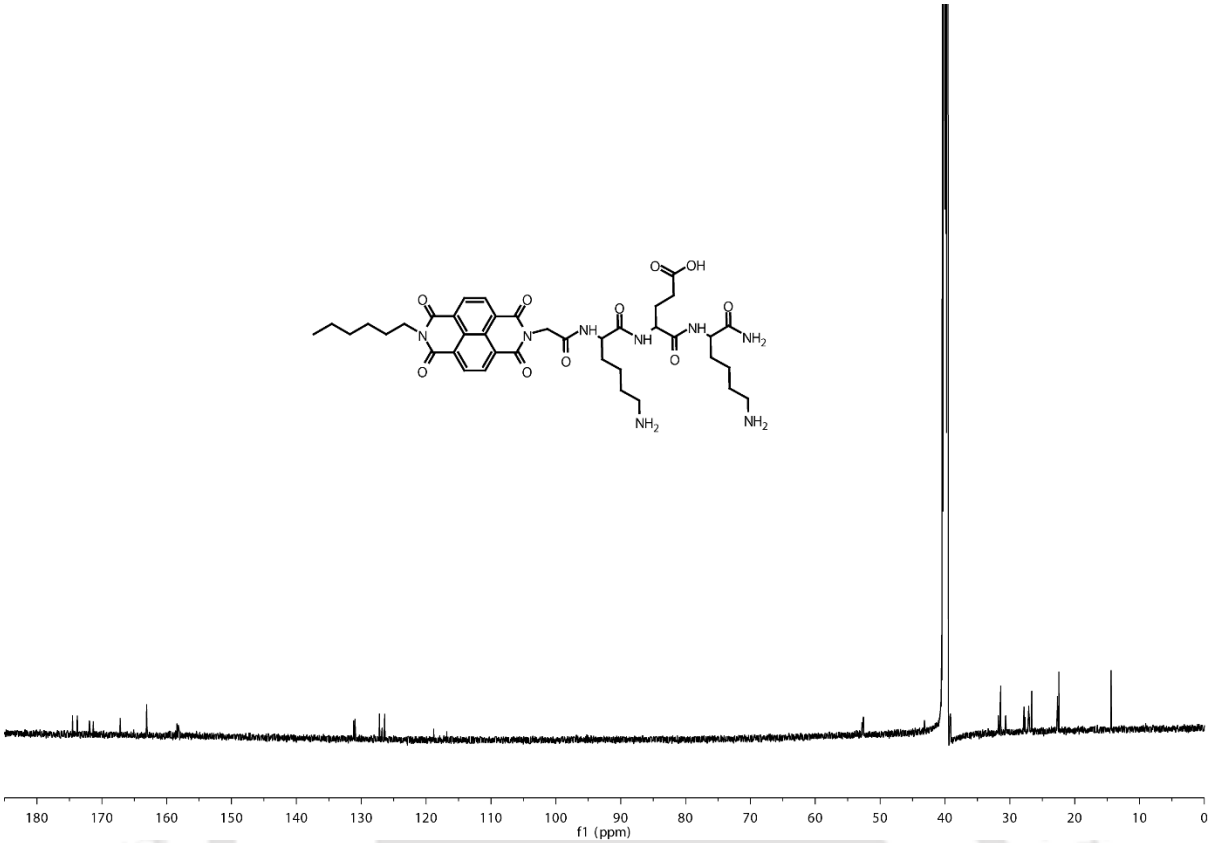

Fig. S3.2. ^{13}C NMR spectra of C6-NDG-KEK.

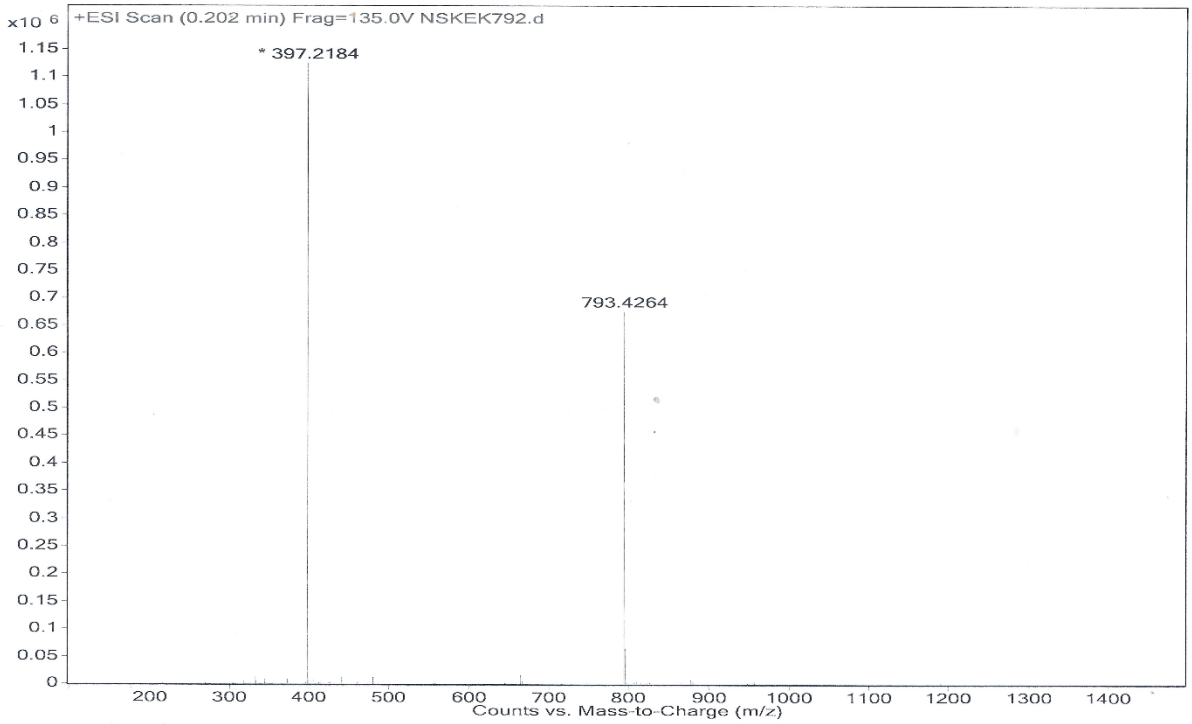

Fig. S3.3. ESI-MS spectra of C6-NDG-KEK.

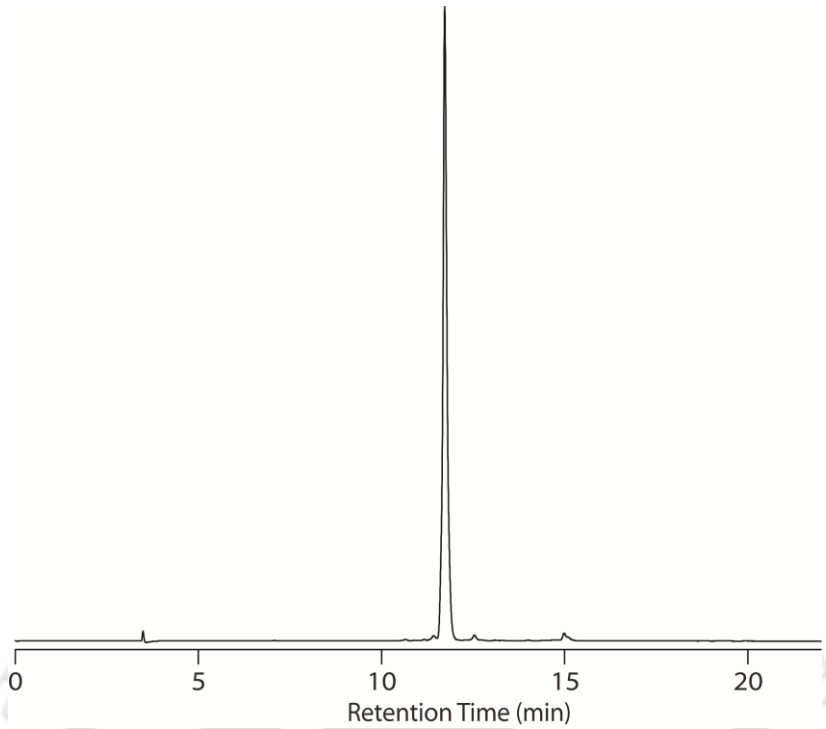

Fig. S3.4. Chromatogram of C6-NDG-KEK.

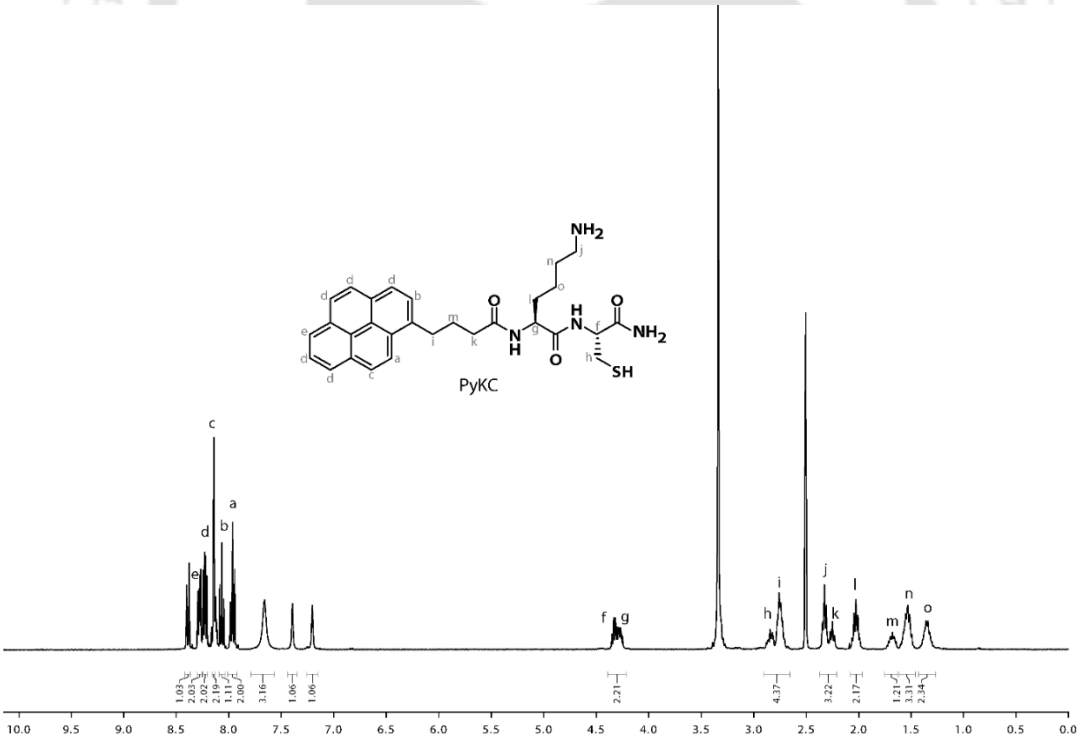

Fig. S4.1. ^{1}H NMR spectra of **PyKC** in DMSO-d_6.

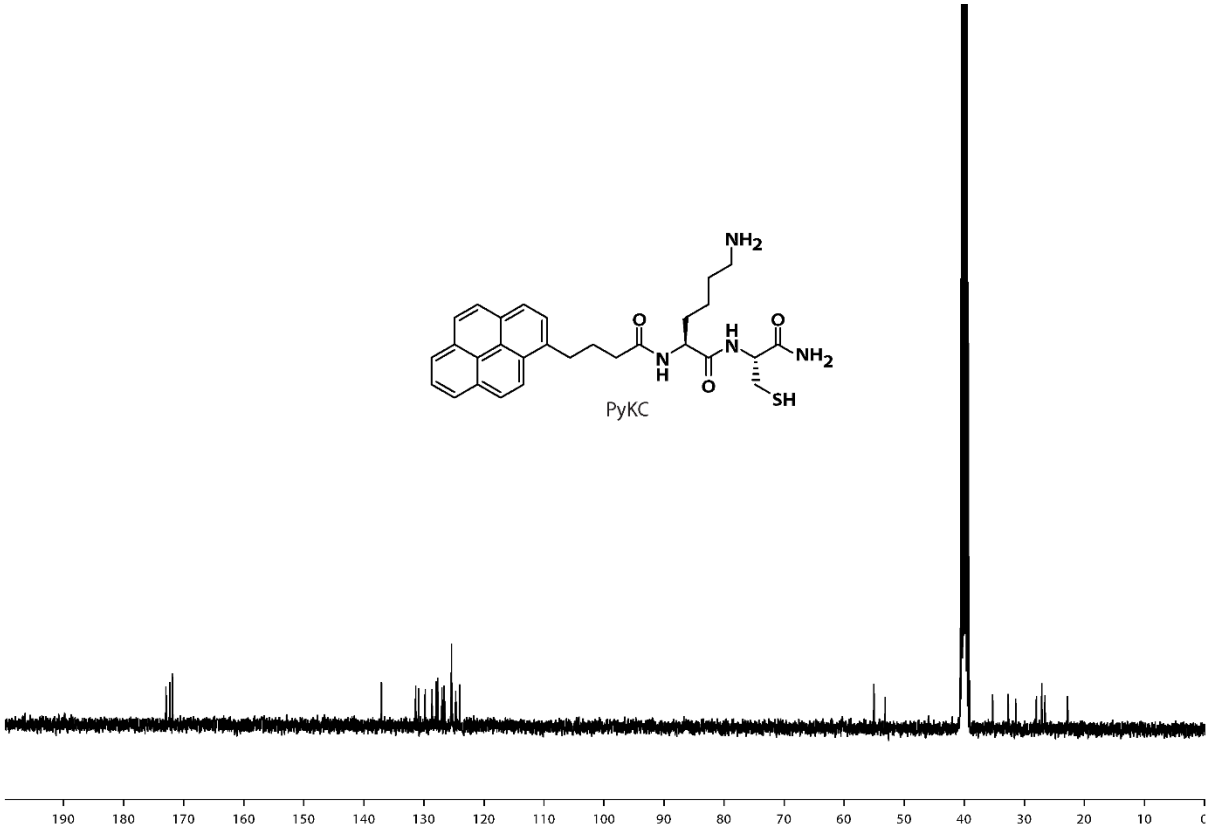

Fig. S4.2. ^{13}C NMR spectra of **PyKC** in DMSO-d_6.

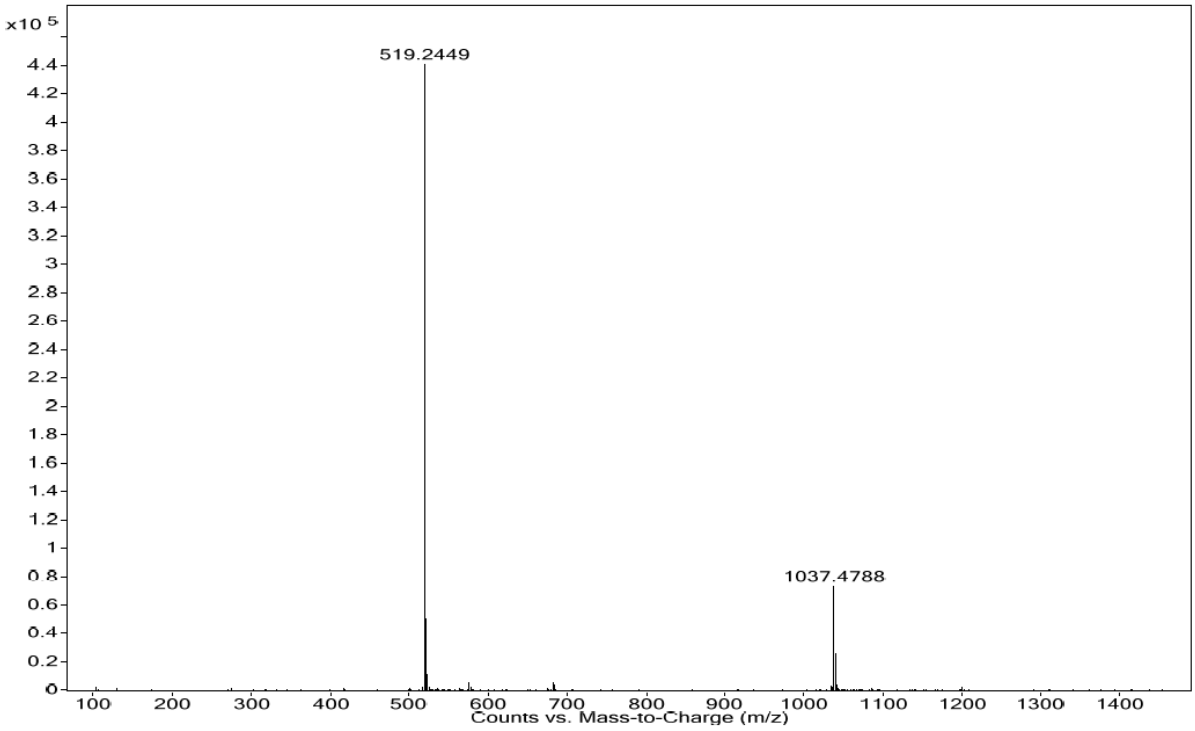

Fig. S4.3. ESI-MS of **PyKC**.

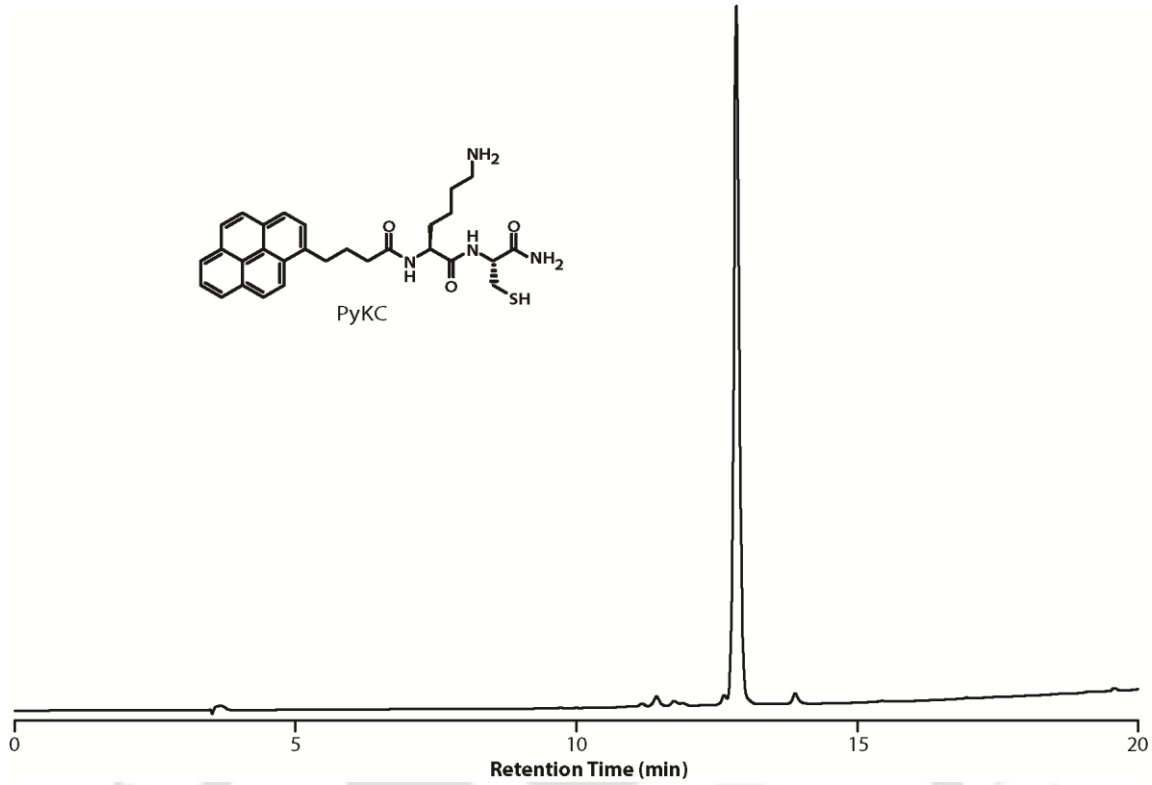

Fig. S4.4. Chromatogram of **PyKC**.

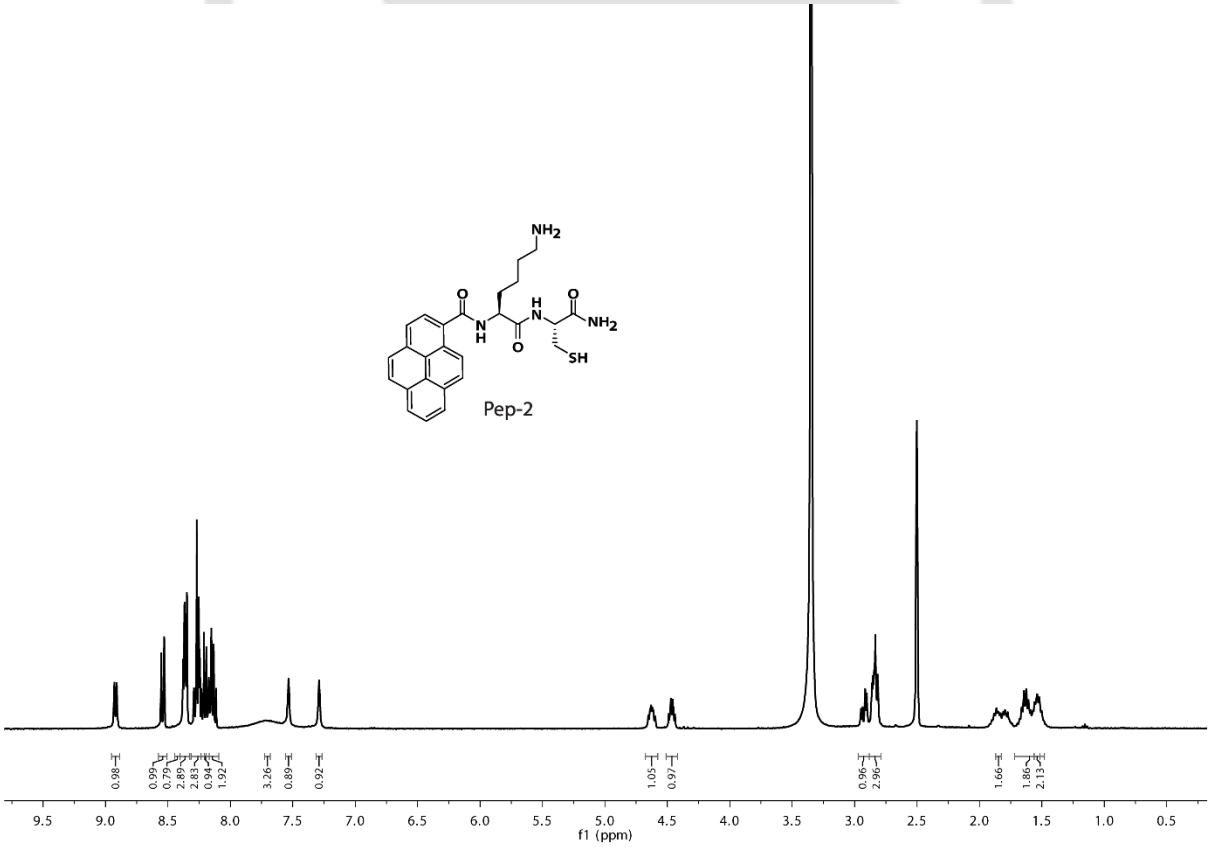

Fig. S4.5. ^{1}H NMR spectra of **Pep-2** in DMSO-d_6.

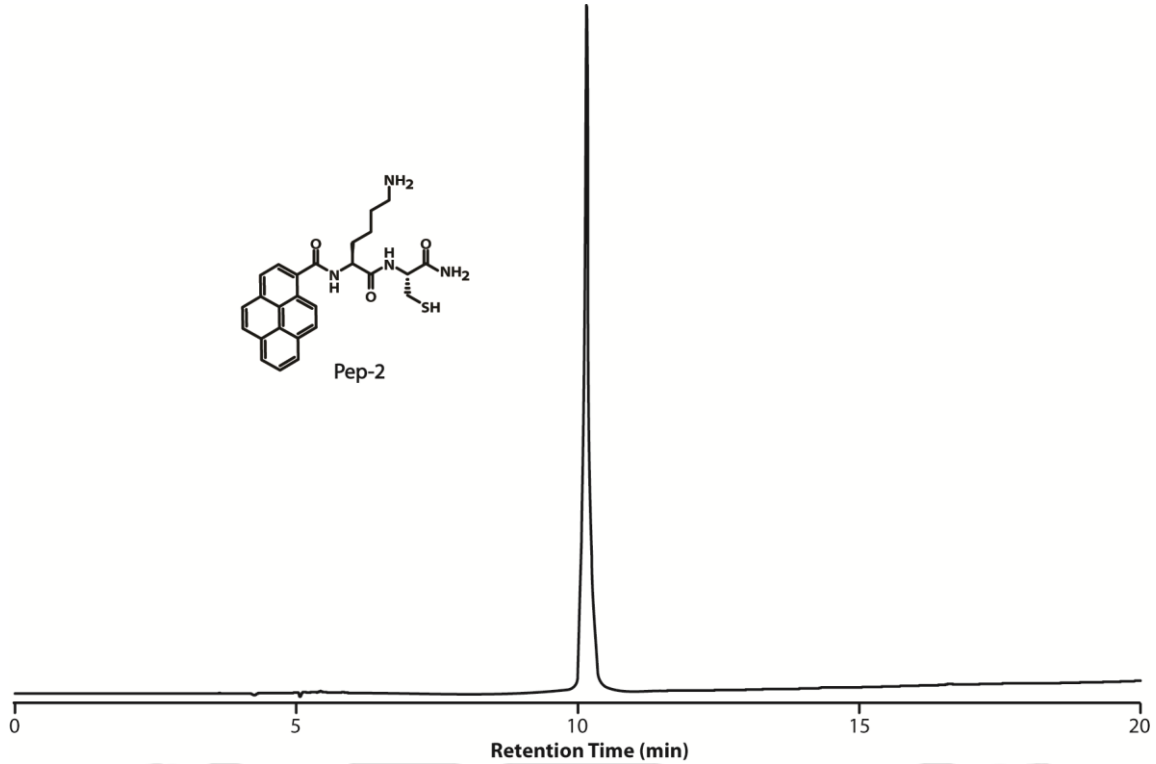

Fig. S4.6. Chromatogram of **Pep-2**.

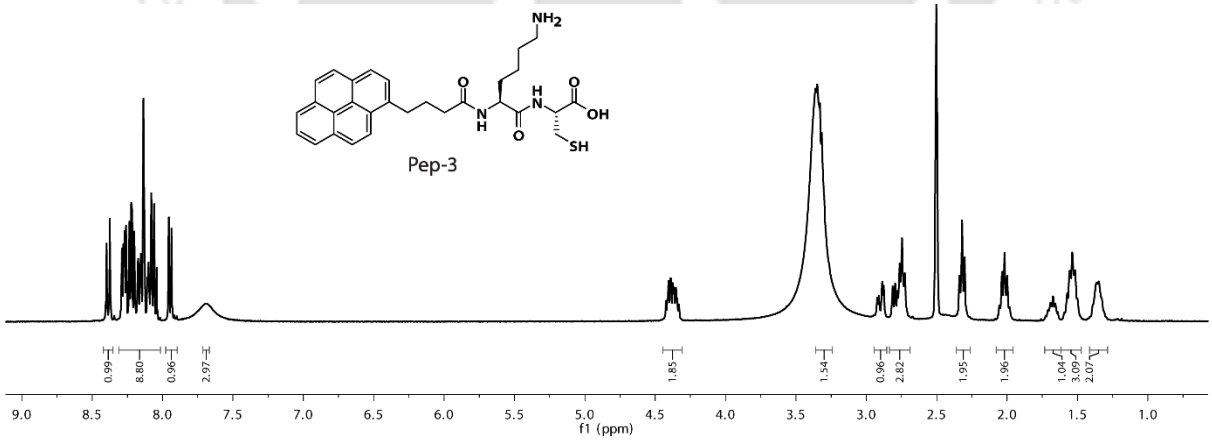

Fig. S4.7. ^{1}H NMR spectra of **Pep-3** in DMSO-d_6.

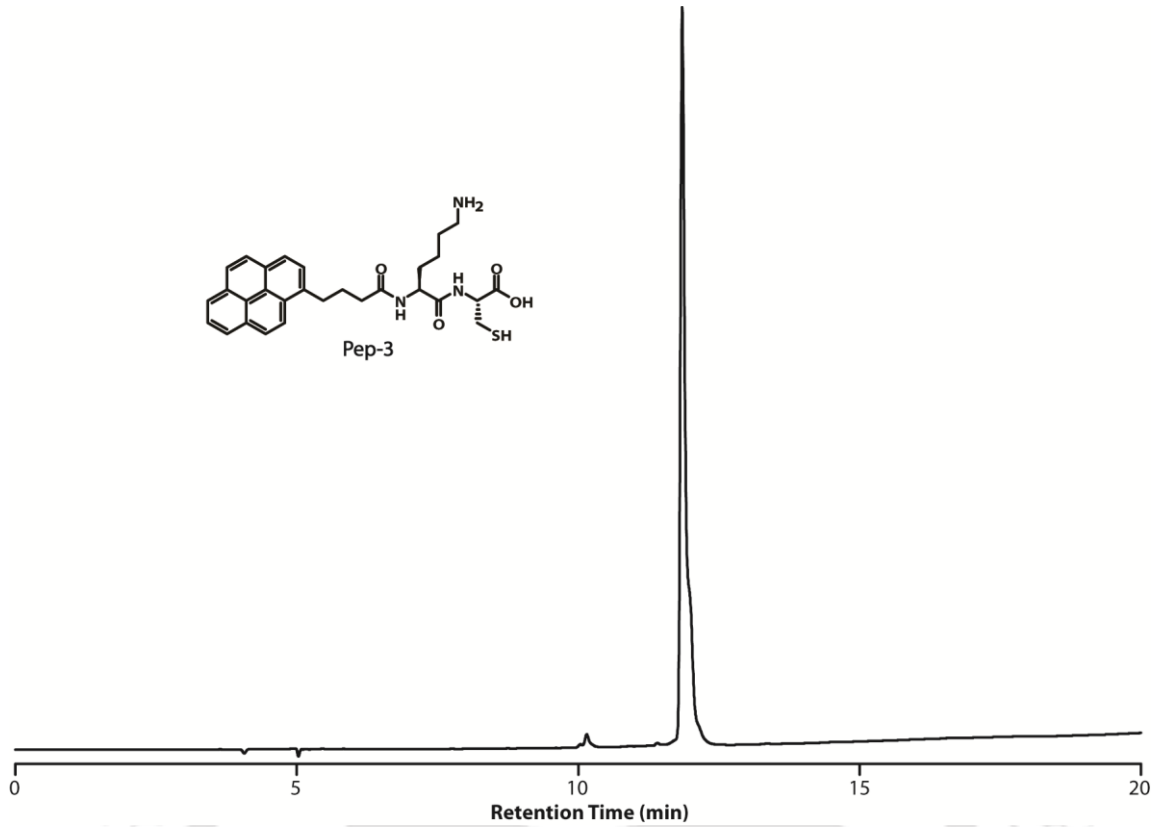

Fig. S4.8. Chromatogram of **Pep-3**.

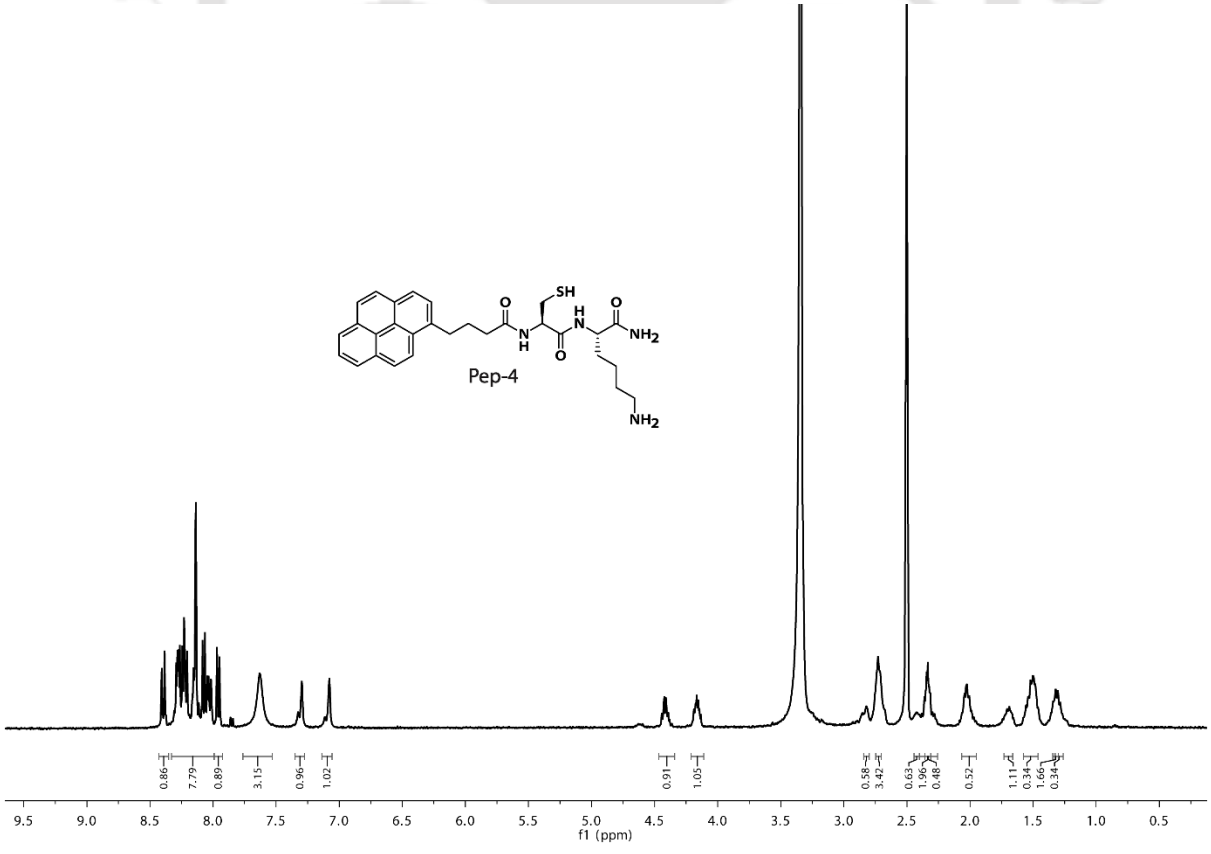

Fig. S4.9. ^{1}H NMR spectra of **Pep-4** in DMSO-d_6.

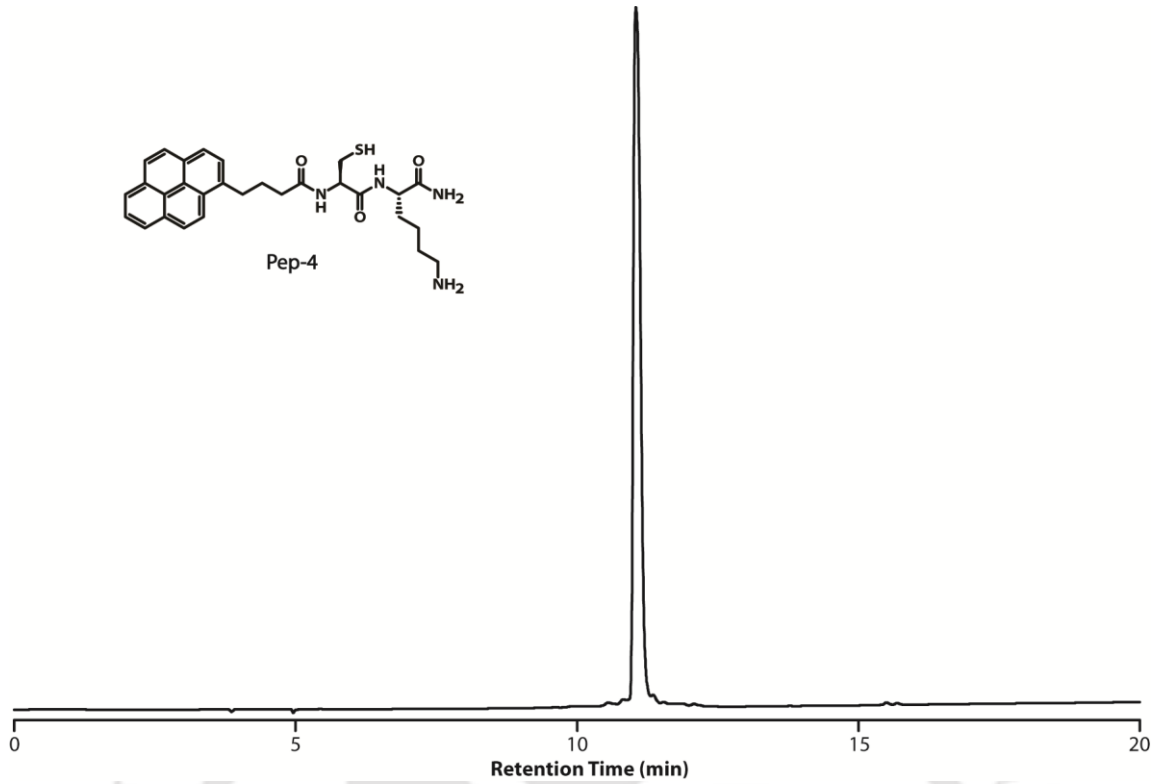

Fig. S4.10. Chromatogram of **Pep-4**.

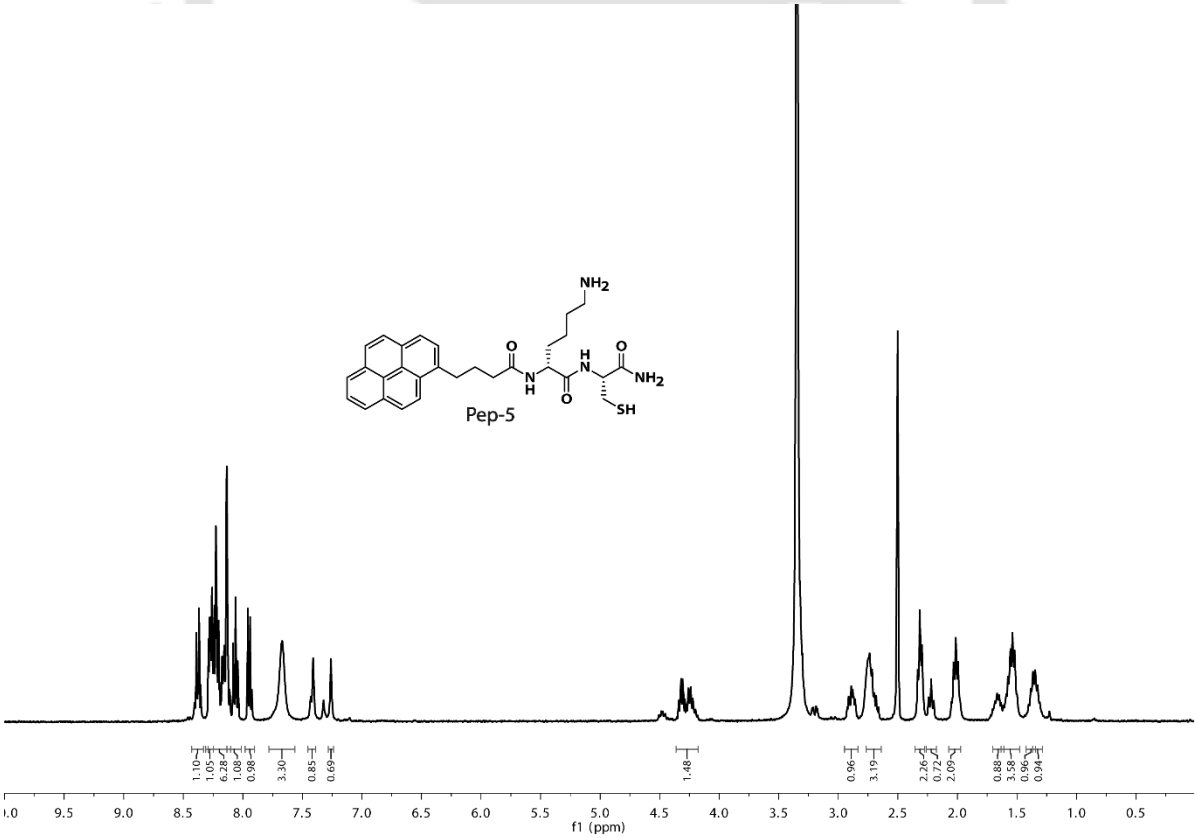

Fig. S4.11. ^{1}H NMR spectra of **Pep-5** in DMSO-d_6.

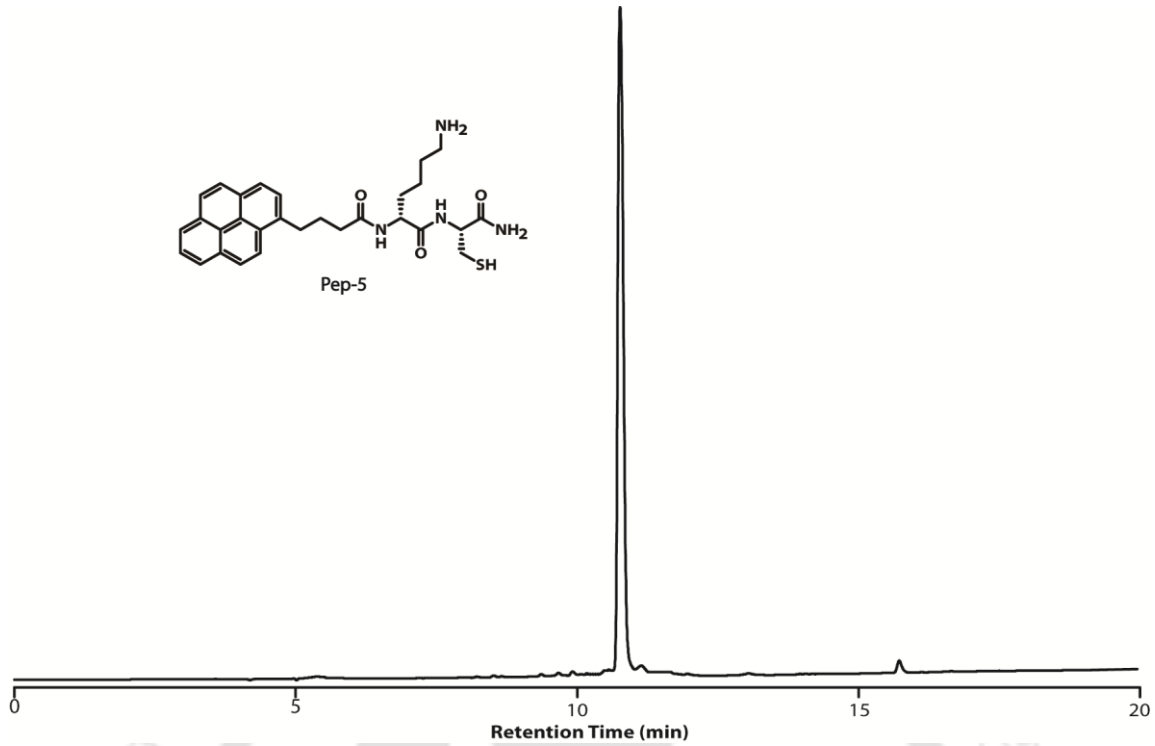

Fig. S4.12. Chromatogram of **Pep-5**.

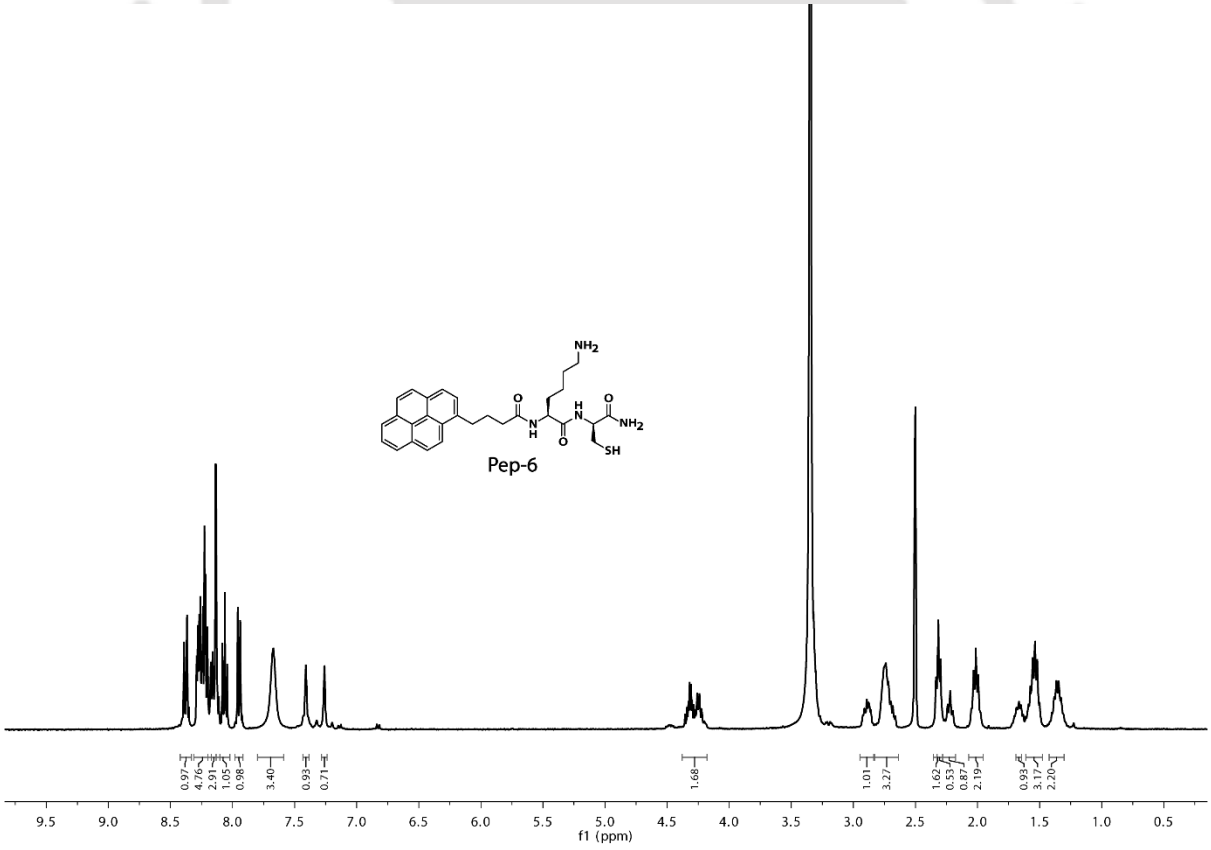

Fig. S4.13. ^{1}H NMR spectra of **Pep-6** in DMSO-d_6.

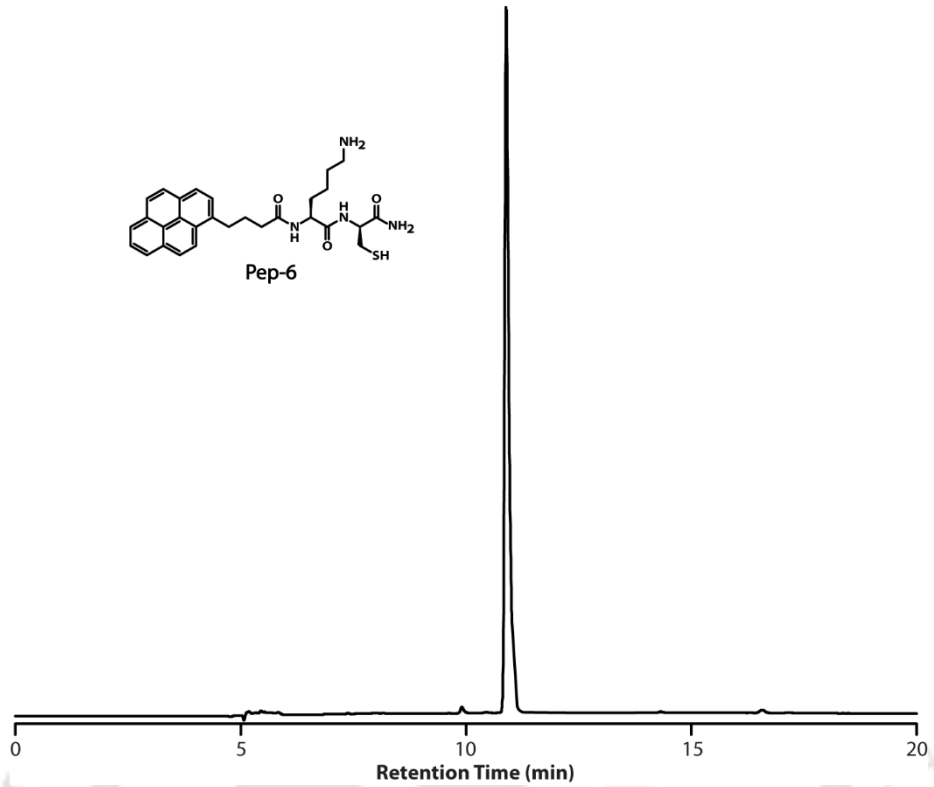

Fig. S4.14. Chromatogram of **Pep-6**.

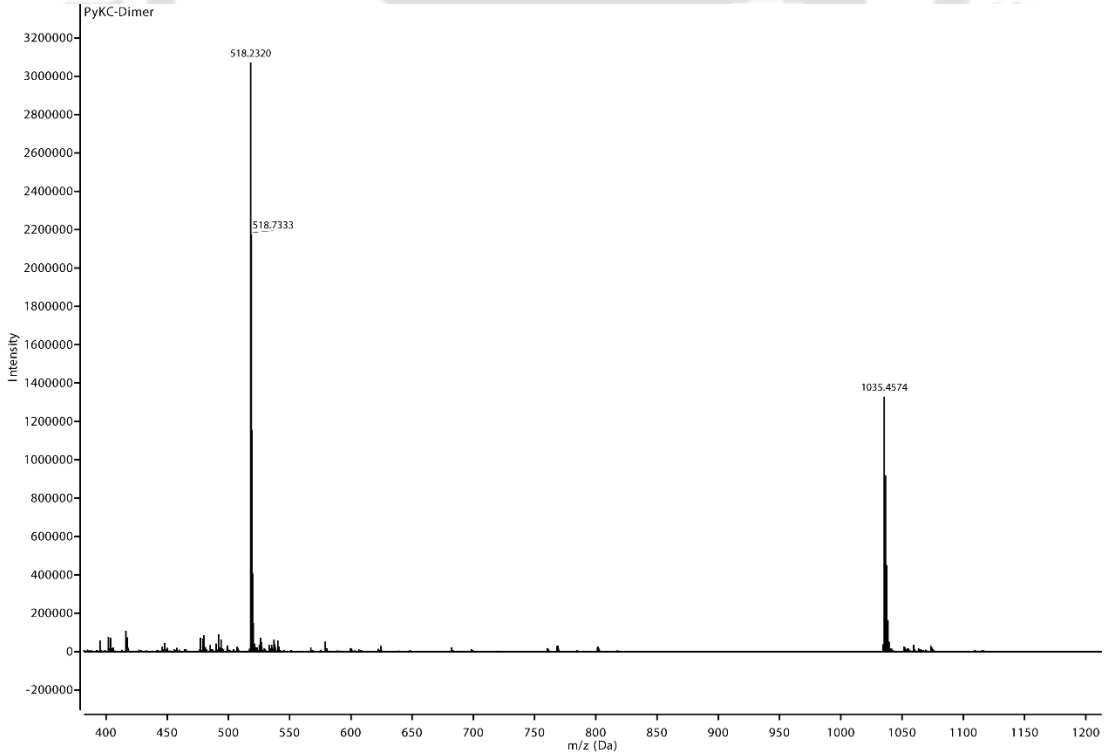

Fig. S4.15. ESI-MS of **PyKC**-dimer.

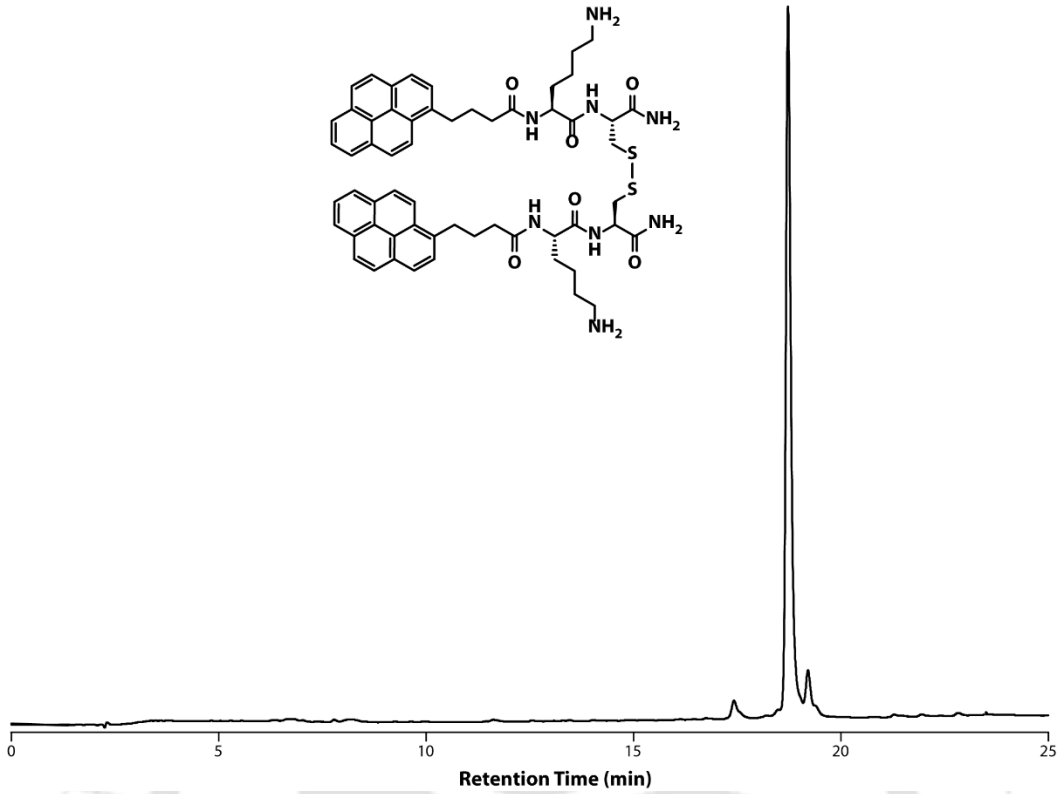

Fig. S4.16. Chromatogram of **PyKC**-dimer.

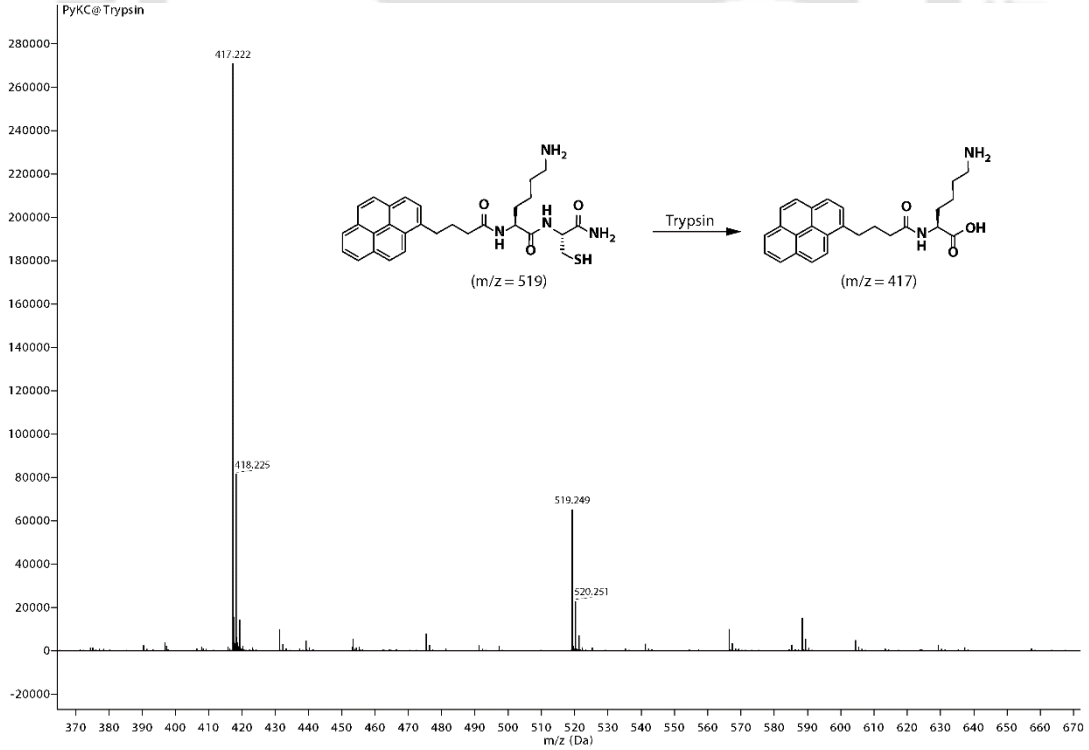

Fig. S4.17. ESI-MS spectrum of a trypsin treated hydrogel of **PyKC**.

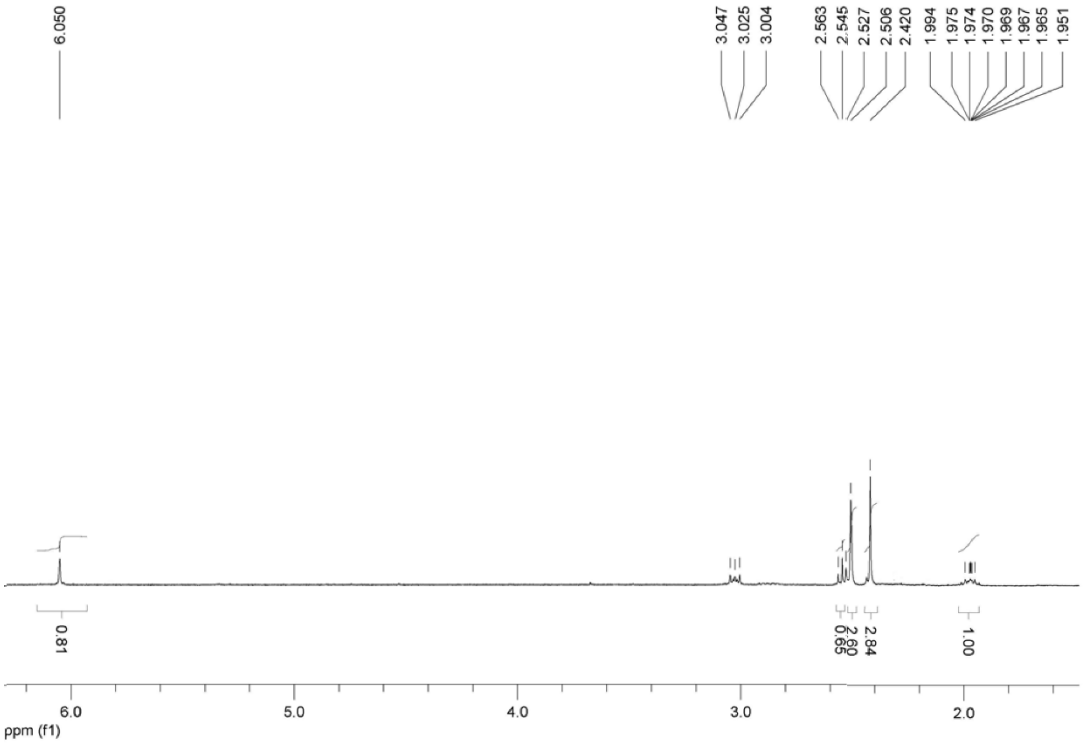

Fig. S5.1. ^{1}H NMR spectra of Bodipy-butyric acid.

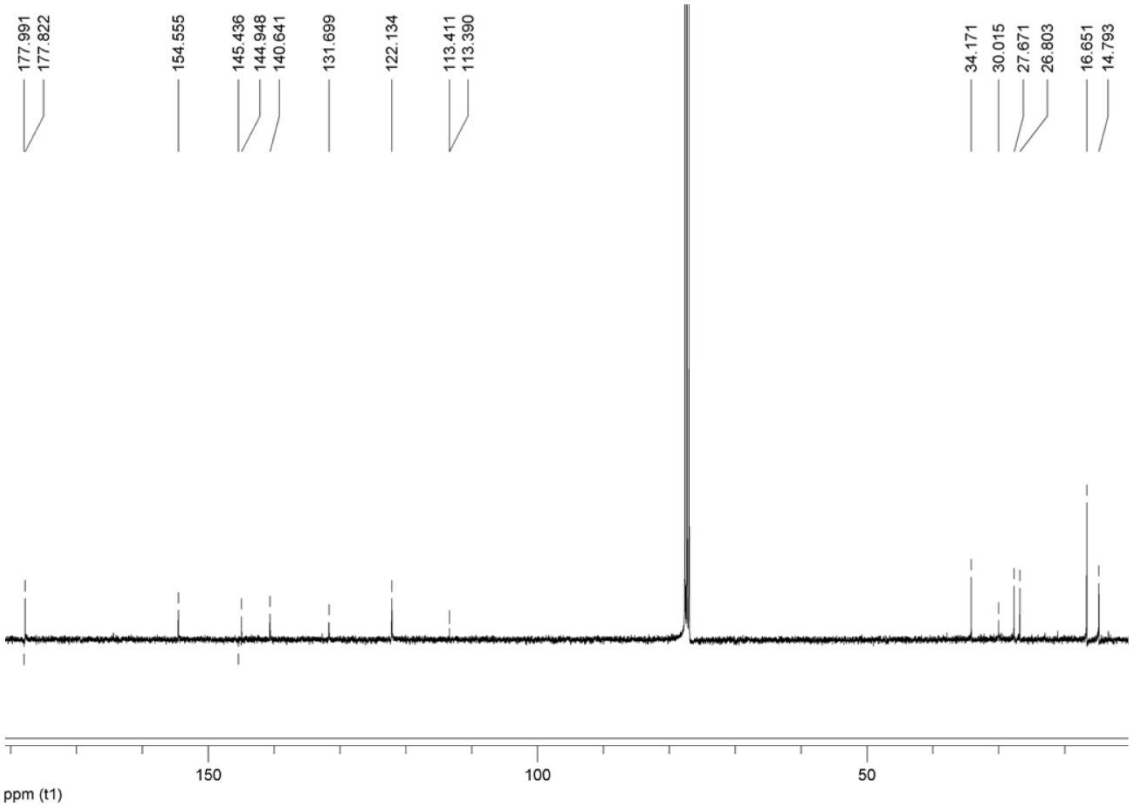

Fig. S5.2. ^{13} C NMR spectra of Bodipy-butyric acid.

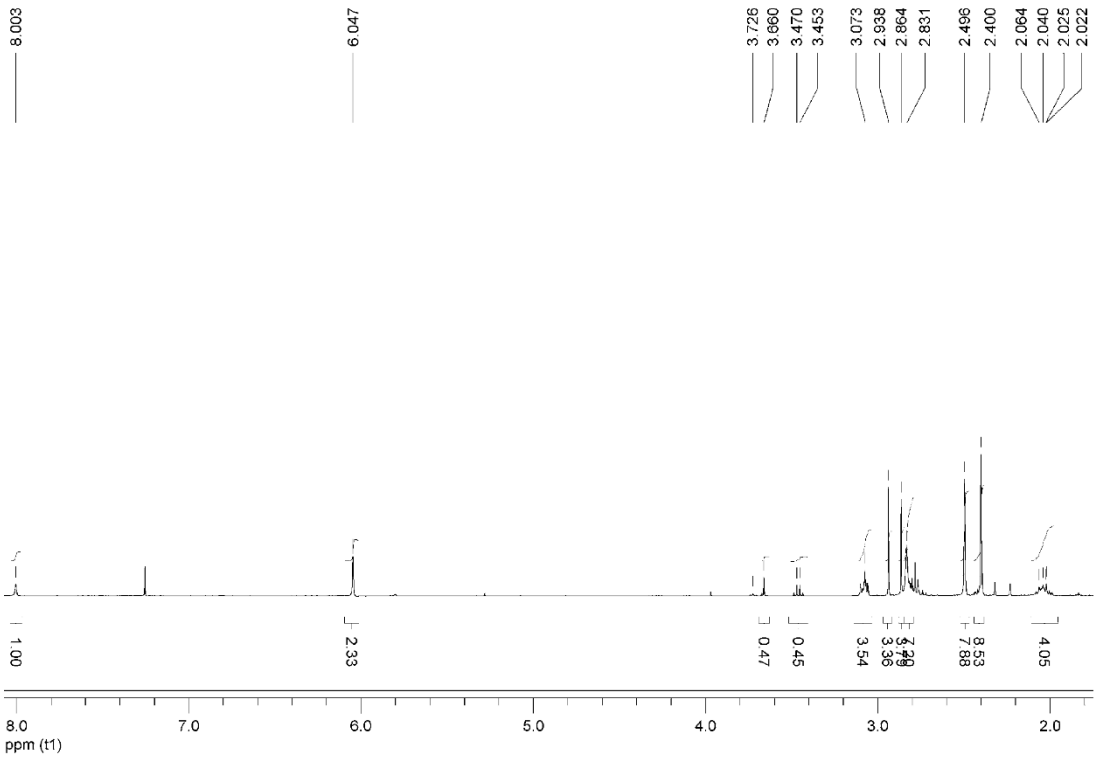

Fig. S5.3. ^{1}H NMR spectra of Bodipy-NHS ester.

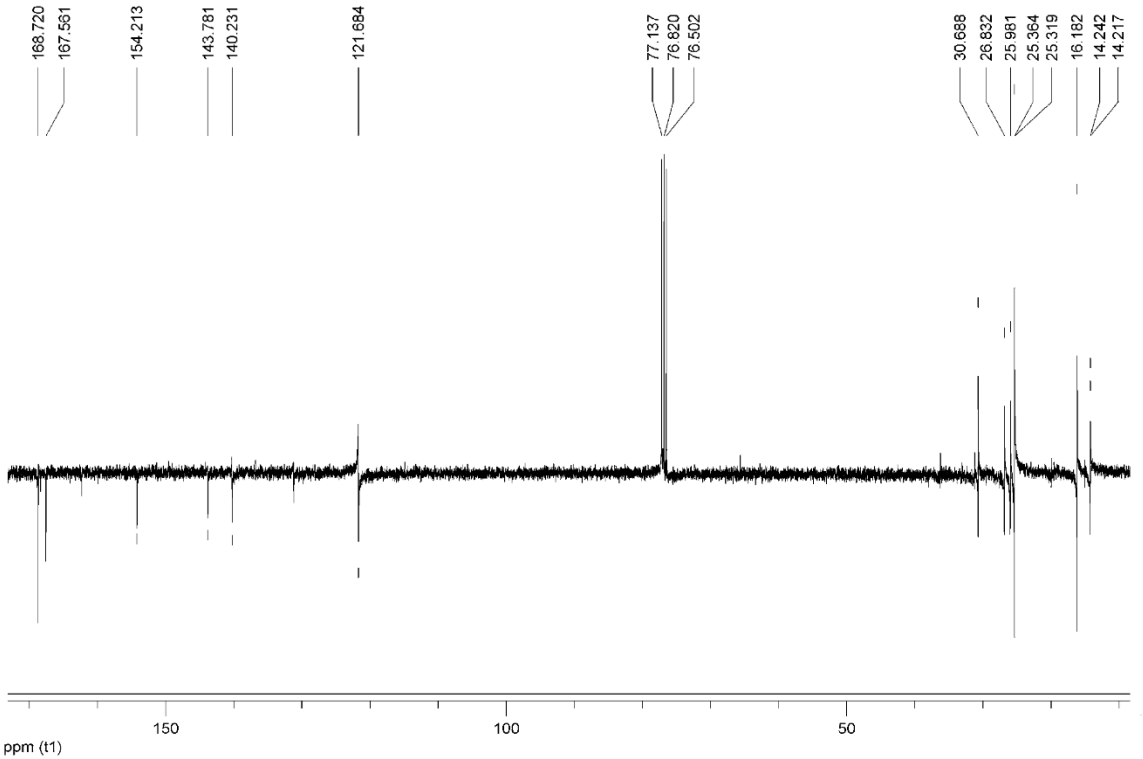

Fig. S5.4. ^{13} C NMR spectra of Bodipy-NHS ester.

भारतीय प्रौद्योगिकी संस्थान गुवाहाटी
Indian Institute of Technology Guwahati

References

भारतीय प्रौद्योगिकी संस्थान गुवाहाटी
Indian Institute of Technology Guwahati

1) Desiraju, G.R. Chemistry beyond the molecule. *Nature*, **2001,** *412*, 397-400.
2) Gao, J.; Tang, C.; Elsawy, M.A.; Smith, A.M.; Miller, A.F.; Saiani, A. Controlling self-assembling peptide hydrogel properties through network topology. *Biomacromolecules*, **2017**, *18*, 826−834.
3) Dasgupta, A.; Mondal. J. H.; Das D. Peptide hydrogels. *RSC Adv.* **2013**, *3*, 9117-9149.
4) Banta, S.; Wheeldon, I.R.; Blenner, M.; Protein engineering in the development of functional hydrogels. *Annu. Rev. Biomed. Eng.* **2010**, *12*, 167–186.
5) Bhattarai, N.; Gunn J.; Zhang, M.Q. Chitosan-based hydrogels for controlled, localized drug delivery. *Adv. Drug Delivery Rev.* **2010**, *62*, 83–99.
6) Jonker, A.M.; Löwik D.W.P.M.; Van Hest, J.C.M. Peptide- and protein-based hydrogels. *Chem. Mater.* **2012**, *24*, 759–773.
7) Oyen, E.; Martin, C.; Caveliers, V.; Madder, A.; Mele, B. V.; Hoogenboom, R.; Hernot, S.; BalletIn, S. In vivo imaging of the stability and sustained cargo release of an injectable amphipathic peptide-based hydrogel. *Biomacromolecules*, **2017**, *18*, 994−1001.
8) Fichman, G.; Gazit, E. Self-assembly of short peptides to form hydrogels: Design of building blocks, physical properties and technological applications. *Acta Biomaterialia*, **2014,** *10*, 1671–1682.
9) Jeon, I.; Cui, J.; Illeperuma W.R.; Aizenberg, J.; Vlassak, J.J. Extremely stretchable and fast self-healing hydrogels. *Adv. Mater.* **2016**, *28*, 4678–4683.
10) Adams, D.J.; Topham, P.D. Peptide conjugate hydrogelators. *Soft Matter*, **2010**, *6*, 3707–3721.
11) Nagai, Y.; Unsworth, L.D.; Koutsopoulos S.; Zhang, S. Slow release of molecules in self-assembling peptide nanofiber scaffold. *J. Controlled Release*, **2006**, *115*, 18–25.
12) Veith, S.R.; Hughes E.; Pratsinis, S.E.; Restricted diffusion and release of aroma molecules from sol-gel-made porous silica particles. *J. Controlled Release*, **2004**, *99*, 315–327.
13) Naskar, J.; Palui G.; Banerjee, A. Tetrapeptide-based hydrogels: for encapsulation and slow release of an anticancer drug at physiological pH. *J. Phys. Chem. B*, **2009**, *113*, 11787–11792.
14) Tran, N.Q.; Joung, Y. K.; Lih, E.; Park, K.D. In situ forming and rutin-releasing chitosan hydrogels as injectable dressings for dermal wound healing. *Biomacromolecules*, **2011**, *12*, 2872–2880.
15) Takei, T.; Nakahara, H.; Ijima, H.; Kawakami, K. Synthesis of a chitosan derivative soluble at neutral pH and gellable by freeze-thawing, and its application in wound care. *Acta Biomater.* **2012**, *8*, 686–693.
16) Hatice, B.-S.; Macias, C.E.; Kung, J.H.; Muratoglu, O.K. Poly(vinyl alcohol)-acrylamide hydrogels as load-bearing cartilage substitute. *Biomaterials*, **2009**, *30*. 589–596.
17) Tasoglu, S.; Demirci, U. Bio printing for stem cell research. *Trends Biotechnol.* **2013**, *31*, 10–19.

18) Hartgerink, J. D.; Beniash, E.; Stupp, S. I. Self-Assembly and mineralization of peptide-amphiphile nanofibers. *Science*, **2001**, *294*, 1684–1688.

19) Lakshmanan, A.; Zhang S.; Hauser, C. A. E. Short self-assembling peptides as building blocks for modern nanodevices. *Trends Biotechnol.* **2012**, *30*, 155–165.

20) Maitra, U.; Sangeetha. N.M. Supramolecular gels: Function and uses. *Chem. Soc. Rev.* **2005**, *34*, 821–836.

21) Yoshimura, T.; Matsuo, K.; Fujioka, R. Novel biodegradable superabsorbent hydrogels derived from cotton cellulose and succinic anhydride: Synthesis and characterization. *J. Appl. Polym. Sci.* **2006**, *99*, 3251–3256.

22) Laftah, W.A.; Hashim, S.; Ibrahim, A.N. Polymer Hydrogels: A Review. *Polymer-Plastics Technology and Engineering,* **2011**, *50*, 1475-1486.

23) Pritchard, C.D.; O'Shea, T.M.; Siegwart, D.J.; Calo, E.; Anderson, D.G.; Reynolds, F.M.; Thomas, J.A.; Slotkin, J.R.; Woodard E.J.; Langer, R. An injectable thiol-acrylate poly(ethylene glycol) hydrogel for sustained release of methylprednisolone sodium succinate. *Biomaterials*, **2011**, *32*, 587–597.

24) Zhang, H.; Qadeer, A.; Mynarcik D.; Chen, W. Delivery of rosiglitazone from an injectable triple interpenetrating network hydrogel composed of naturally derived materials. *Biomaterials*, **2011**, *32*, 890–898.

25) Koutroumanis, K.P.; Avgoustakis, K.; Bikiaris, D. Synthesis of cross-linked N-(2-carboxybenzyl) chitosan pH sensitive polyelectrolyte and its use for drug controlled delivery. *Carbohydr. Polym.* **2010**, *82*, 181–188.

26) Rydholm, A.E.; Bowman C.N.; Anseth, K.S. Degradable thiol-acrylate photopolymers: polymerization and degradation behavior of an in situ forming biomaterial. *Biomaterials*, **2005**, *26*, 4495–4506.

27) Pathak, C.P.; Sawhney, A. S.; Hubbell, J.A. Rapid photopolymerization of immunoprotective gels in contact with cells and tissue. *J. Am. Chem. Soc.* **1992**, *114*, 8311–8312.

28) Kurisawa, M.; Chung, J.E.; Yang, Y.Y.; Gao S.J.; Uyama, H. Injectable biodegradable hydrogels composed of hyaluronic acid–tyramine conjugates for drug delivery and tissue engineering. *Chem. Commun.* **2005**, *0*, 4312–4314.

29) Jin, R.; Hiemstra, C.; Zhong R.; Feijen, J. Enzyme-mediated fast in situ formation of hydrogels from dextran-tyramine conjugates. *Biomaterials*, **2007**, *28*, 2791–2800.

30) DeForest, C.A.; Polizzotti, B.D.; Anseth, K.S. Sequential click reactions for synthesizing and patterning three-dimensional cell microenvironments. *Nat. Mater.* **2009**, *8*, 659–664.

31) Peppas, N. A.; Huang, Y.; Torres-Lugo, M.; Ward, J. H.; Zhang, J. Physicochemical foundations and structural design of hydrogels in medicine and biology. *Annu. Rev. Biomed. Eng.* **2000**, *2*, 9–29.

32) Dong, R.; Pang, Y.; Su, Y.; Zhu, X. Supramolecular hydrogels: synthesis, properties and their biomedical applications. *Biomater. Sci.* **2015**, *3*, 937-954.

33) Appel, E.A.; Barrio, J.; Loh, X.J.; Scherman, O.A. Supramolecular polymeric hydrogels. *Chem. Soc. Rev.*, **2012**, *41*, 6195–6214.

34) Ulijn, R.V.; Smith, A.M. Designing peptide based nanomaterials. *Chem. Soc. Rev.* **2008**, *37*, 664–675.

35) Du, X.; Zhou, J.; Shi, J.; Xu, B. Supramolecular hydrogelators and hydrogels: from soft matter to molecular biomaterials. *Chem. Rev.* **2015**, *115*, 13165–13307.

36) Hamley, I.W. The amyloid beta peptide: a chemist's perspective. Role in Alzheimer's and fibrillization. *Chem. Rev.* **2012**, *112*, 5147–5192.

37) Aggeli, A.; Bell, M.; Boden, N. ; Keen, J.N. ; McLeish, T.C.B.; Nyrkova, I.; Radford, S.E.; Semenov, A. Engineering of peptide -sheet nanotapes. *J. Mater. Chem.* **1997**, *7*, 1135–1145.

38) Carrick, L.M.; Aggeli, A.; Boden, N.; Fisher, J.; Inghamb, E.; Waigh, T.A. Effect of ionic strength on the self-assembly, morphology and gelation of pH responsive β-sheet tape-forming peptides. *Tetrahedron*, **2007**, *63*, 7457–7467.

39) Rapaport, H.; Grisaru, H.; Silberstein, T. Hydrogel scaffolds of amphiphilic and acidic -sheet peptides. *Adv. Funct. Mater.* **2008**, *18*, 2889–2896.

40) Zhang, S.; Holmes, T.; Lockshin, C.; Rich, A. Spontaneous assembly of a self-complementary oligopeptide to form a stable macroscopic membrane. *Proc. Natl. Acad. Sci. U. S. A.*, **1993**, *90*, 3334–3338.

41) Kisiday, J.; Jin, M.; Kurz, B.; Hung, H.; Semino, C.; Zhang, S.; Grodzinsky, A.J. Self-assembling peptide hydrogel fosters chondrocyte extracellular matrix production and cell division: Implications for cartilage tissue repair. *Proc. Natl. Acad. Sci. U. S. A.* **2002**, *99,* 9996-10001.

42) Yokoi, H.; Kinoshita, T.; Zhang, S.G. Dynamic reassembly of peptide RADA16 nanofiber scaffold. *Proc. Natl. Acad. Sci. U. S. A.* **2005**, *102*, 8414–8419.

43) Ozbas, B.; Kretsinger, J.; Rajagopal, K.; Schneider, J.P.; Pochan, D.J. Salt-triggered peptide folding and consequent self-assembly into hydrogels with tunable modulus. *Macromolecules*, **2004**, *37*, 7331–7337.

44) Pochan, D.J.; Schneider, J.P.; Kretsinger, J.; Ozbas, B.; Rajagopal, K.; Haines, L. Thermally reversible hydrogels via intramolecular folding and consequent self-assembly of a de novo designed peptide. *J. Am. Chem. Soc.* **2003**, *125*, 11802–11803.

45) Rajagopal, K.; Lamm, M.S.; Haines-Butterick, L.A.; Pochan, D.J.; Schneider, J.P. Tuning the pH responsiveness of β-hairpin peptide folding, self-assembly, and hydrogel material formation. *Biomacromolecules*, **2009**, *10*, 2619–2625.

46) Larsen, T.H.; Branco, M.C.; Rajagopal, K.; Schneider, J.P.; Furst, E.M. Sequence-dependent gelation kinetics of β-hairpin peptide hydrogels. *Macromolecules*, **2009**, *42*, 8443–8450.

47) Kretsinger, J.; Haines, L.A.; Ozbas, B.; Pochan, D.J.; Schneider, J.P. Cytocompatibility of self-assembled β-hairpin peptide hydrogel surfaces. *Biomaterials*, **2005**, *26*, 5177–5186.

48) Yucel, T.; Micklitsch, C.M.; Schneider J.P.; Pochan, D.J. Direct observation of early-time hydrogelation in β-hairpin peptide self-assembly. *Macromolecules*, **2008**, *41*, 5763–5772.

49) Nagy, K.J.; Giano, M.C.; Jin, A.; Pochan D.J.; Schneider, J.P. Enhanced mechanical rigidity of hydrogels formed from enantiomeric peptide assemblies. *J. Am. Chem. Soc.* **2011**, *133*, 14975–14977.

50) Haines, L.A.; Rajagopal, K.; Ozbas, B.; Salick, D.A.; Pochan, D.J.; Schneider, J.P. Light-activated hydrogel formation via the triggered folding and self-assembly of a designed peptide. *J. Am. Chem. Soc.* **2005**, *127*, 17025–17029.

51) Nagarkar, R.P.; Hule, R.A.; Pochan, D.J.; Schneider, J.P. De novo design of strand-swapped β-hairpin hydrogels. *J. Am. Chem. Soc.* **2008**, *130*, 4466-4474.

52) Hule, R.A.; Nagarkar, R.P.; Hammouda, B.; Schneider, J.P.; Pochan, D.J. Dependence of self-assembled peptide hydrogel network structure on local fibril nanostructure. *Macromolecules*. **2009**, *42*, 7137–7145.

53) Pandya, M.J.; Spooner, G.M.; Sunde, M.; Thorpe, J.R.; Rodger, A.; Woolfson, D.N. Sticky-end assembly of a designed peptide fiber provides insight into protein fibrillogenesis. *Biochemistry*, **2000**, *39*, 8728-8734.

54) Woolfson, D.N.; Raydnov, M.G. Peptide-based fibrous biomaterials: Some things old, new and borrowed. *Curr. Opin. Chem. Biol.* **2006**, *10*, 559–567.

55) Woolfson, D.N. Building fibrous biomaterials from alpha-helical and collagen-like coiled-coil peptides. *Biopolymers*, **2010**, *94*, 118–127.

56) Gotner R.A.; Hoffman, W.F. *J. Am. Chem. Soc.* **1921**, *43*, 2199–2202.

57) Shi, J.; Gao, Y.; Yang, Z.; Xu, B. Exceptionally small supramolecular hydrogelators based on aromatic–aromatic interactions. *Beilstein J. Org. Chem.* **2011**, *7*, 167–172.

58) Yang, Z.; Gu, H.; Zhang, Y.; Wang L.; Xu, B. Small molecule hydrogels based on a class of antiinflammatory agents. *Chem. Commun.* **2004**, *0*, 208–209.

59) Yang, Z.; Liang G.; Xu, B. Enzymatic hydrogelation of small molecules. *Acc. Chem. Res.* **2008**, *41*, 315–326.

60) Orbach, R.; Adler-Abramovich, L.; Zigerson, S.; Mironi-Harpaz, I.; Seliktar, D.; Gazit, E. Self-assembled fmoc-peptides as a platform for the formation of nanostructures and hydrogels. *Biomacromolecules*, **2009**, *10*, 2646–2651.

61) Vegners, R.; Shestakova, I.; Kawinsh, I.; Euell, R.M.; Janmey, P.A. Use of a gel-forming dipeptide derivative as a carrier for antigen presentation. *J. Pept. Sci.* **1995**, *1*, 371–378.

62) Seebach, D.; Matthews, J. L. β-Peptides: a surprise at every turn. *Chem. Commun.* **1997**, *0*, 2015–2022.

63) Yang, Z.; Lianga, G.; Xu, B.; Supramolecular hydrogels based on β-amino acid derivatives. *Chem. Commun.* **2006**, *0*, 738–740.

64) Nanda, J.; Banerjee, A. β-Amino acid containing proteolitically stable dipeptide based hydrogels: encapsulation and sustained release of some important biomolecules at physiological pH and temperature. *Soft Matter*, **2012**, *8*, 3380–3386.

65) Yang, Z.; Liang, G.; Ma, M.; Gao, Y.; Xu, B. Conjugates of naphthalene and dipeptides produce molecular hydrogelators with high efficiency of hydrogelation and superhelical nanofibers. *J. Mater. Chem.* **2007**, *17*, 850–854.

66) Adhikari, B.; Palui G.; Banerjee, A. Self-assembling tripeptide based hydrogels and their use in removal of dyes from waste-water. *Soft Matter*, **2009**, *5*, 3452–3460.

67) Hamley, I.W. Self-assembly of amphiphilic peptides. *Soft Matter*, **2011**, *7*, 4122–4138.

68) Versluis, F.; Marsden, H.R.; Kros, A. Power struggles in peptide-amphiphile nanostructures. *Chem. Soc. Rev.* **2010**, *39*, 3434–3444.

69) Zhang, S. Fabrication of novel biomaterials through molecular self-assembly. *Nat. Biotechnol.* **2003**, *21*, 1171–1178.

70) Katchalski E.; Sela, M. Synthesis and chemical properties of poly-alpha-amino acids. *Adv. Protein Chem.*, 1958, 13, 243–492.

71) Jun, H.-W.; Yuwono, V.; Paramonov, S.E.; Hartgerink, J.D. Enzyme-mediated degradation of peptide-amphiphile nanofiber networks. *Adv. Mater.* **2005**, *17*, 2612–2617.

72) Shroff, K.; Rexeisen, E.L.; Arunagirinathan, A.M.; Kokkoli, E. Enzyme-mediated degradation of peptide-amphiphile nanofiber networks. *Soft Matter*, **2010**, *6*, 5064–5072.

73) Mata, A.; Hsu, L.; Capito, R.; Aparicio, C.; Henrikson, K.; Stupp, S.I. Micropatterning of bioactive self-assembling gels. *Soft Matter*, **2009**, *5*, 1228–1236.

74) Das, D.; Dasgupta, A.; Roy, S.; Mitra, R.N.; Debnath, S.; Das, P.K. Water Gelation of an Amino Acid-Based Amphiphile. *Chem.–Eur. J.* **2006**, *12*, 5068–5074.

75) Cavalli, S.; Albericio F.; Kros, A. Amphiphilic peptides and their cross-disciplinary role as building blocks for nanoscience. *Chem. Soc. Rev.* **2010**, *39*, 241–263.

76) Shao, H.; Parquette, J.R. A π-conjugated hydrogel based on an Fmoc-dipeptide naphthalene diimide semiconductor. *Chem. Commun.* **2010**, *46*, 4285–4287.

77) Nalluri, S.K.M.; Berdugo, C.; Javid, N.; Frederix, P.W.J.M.; Ulijn, R.V. Biocatalytic self-assembly of supramolecular charge-transfer nanostructures based on n-type semiconductor-appended peptides. *Angew. Chem. Int. Ed.* **2014**, *53*, 5882 –5887.

78) Liu, Y.-H.; Hsu, S.-M., Wu, F.-Y.; Cheng, H.; Yeh, M.-Y. Lin, H.-C. Electroactive organic dye incorporating dipeptides in the formation of self-assembled nanofibrous hydrogels. *Bioconjugate Chem.* **2014**, *25*, 1794−1800.

79) Nelli, S.R.; Lin, J.-H.; Nguyen, T. N. A.; Tseng, D.T.-H.; Talloj S.K.; Lin, H.-C. Influence of amino acid side chains on the formation of two component self-assembling nanofibrous hydrogels. *New J. Chem.* **2017**, *41*, 1229-1234.

80) Zhou, M.; Smith, A.M.; Das, A.K.; Hodson, N.W.; Collins, R.F.; Ulijn, R.V.; Gough, J.E. Self-assembled peptide-based hydrogels as scaffolds for anchorage-dependent cells. *Biomaterials*, **2009**, *30*, 2523–2530.

81) Branco, M.C.; Pochan, D.J.; Wagner, N.J.; Schneider, J.P. The effect of protein structure on their controlled release from an injectable peptide hydrogel. *Biomaterials*, **2010**, *31*, 9527−9534.

82) Xu, X.-D.; Liang, L.; Chen, C.-S.; Lu, B.; Wang, N.-l.; Jiang, F.-G.; Zhang, X.-Z.; Zhuo, R.-X. Peptide hydrogel as an intraocular drug delivery system for inhibition of postoperative scarring formation. *ACS Appl. Mater. Interfaces,* **2010**, *2*, 2663−2671.

83) Tang, C.; Miller, A.F.; Saiani, A. Peptide hydrogels as mucoadhesives for local drug delivery. *Int. J. Pharm.* **2014**, *465*, 427−435.

84) Salick, D.A.; Kretsinger, J.K.; Pochan, D.J.; Schneider, J.P. Inherent antibacterial activity of a peptide-based beta-hairpin hydrogel. *J. Am. Chem. Soc.* **2007**, *129*, 14793−14799.

85) Laverty, G.; McCloskey, A.P.; Gilmore, B.F.; Jones, D.S.; Zhou, J.; Xu, B. Ultrashort cationic naphthalene-derived self- assembled peptides as antimicrobial nanomaterials. *Biomacromolecules*, **2014**, *15*, 3429−3439.

86) Ren, C. H.; Wang, H. M.; Zhang, X. L.; Ding, D.; Wang, L.; Yang, Z. M. Interfacial self-assembly leads to formation of fluorescent nanoparticles for simultaneous bacterial detection and inhibition. *Chem. Commun.* **2014**, *50*, 3473−3475.

87) Liu, Y. F.; Yang, Y. L.; Wang, C.; Zhao, X. J. Stimuli-responsive self-assembling peptides made from antibacterial peptides. *Nanoscale*, **2013**, *5*, 6413−6421.

88) Irwansyah, I.; Li, Y.-Q.; Shi, W.; Qi, D.; Leow, W.R.; Tang, M.B.Y.; Li, S.; Chen, X. Gram-Positive antimicrobial activity of amino acid-based hydrogels. *Adv. Mater.* **2015**, *27*, 648−654.

89) Rajagopal, K.; Schneider, J. P. Self-assembling peptides and proteins for nanotechnological applications. *Curr. Opin. Struct. Biol.* **2004**, *14*, 480–486.

90) Zhang, S.; Marini, D. M.; Hwang W.; Santoso, S. Design of nanostructured biological materials through self-assembly of peptides and proteins. *Curr. Opin. Chem. Biol.* **2002**, *6*, 865–871.

91) Yan, X.; Zhu P.; Li, J. Self-assembly and application of diphenylalanine-based nanostructures. *Chem. Soc. Rev.* **2010**, *39*, 1877–1890.

92) (a) Han, T. H.; Kim, J.; Park, J. S.; Park, C. B.; Ihee H.; Kim, S. O. Liquid crystalline peptide nanowires. *Adv. Mater.* **2007**, *19*, 3924–3927. (b) Ryu, J.; Park, C. B. Synthesis of diphenylalanine/polyaniline core/shell conducting nanowires by peptide self-assembly. *Angew. Chem., Int. Ed.* **2009**, *48*, 4820–4823.

93) Aggeli, A.; Bell, M.; Boden, N.; Keen, J. N.; Knowles, P. F.; McLeish, T. C. B.; Pitkeathly M.; Radford, S. E. Responsive gels formed by the spontaneous self-assembly of peptides into polymeric beta-sheet tapes. *Nature,* **1997**, *386*, 259-262.

94) Cui, H.; Muraoka, T.; Cheetham, A. G.; Stupp, S.I. Self-Assembly of giant peptide nanobelts. *Nano Lett.* **2009**, *9*, 945-951.

95) Wang, M.; Wang, J.; Zhou, P.; Deng, J.; Zhao, Y.; Sun, Y.; Yang, W.; Wang, D.; Li, Z.; Hu, X.; King, S. M.; Rogers, S. E.; Cox, H.; Waigh, T. A.; Yang, J.; Lu, J. R.; Xu. H. Nanoribbons self-assembled from short peptides demonstrate the formation of polar zippers between β-sheets. *Nature Communications*, **2018**, *9*, 1-11.

96) Ahmed, S.; Mondal, J.H.; Behera, N.; Das, D. Self-Assembly of peptide-amphiphile forming helical nanofibers and in situ template synthesis of uniform mesoporous single wall silica nanotubes. *Langmuir*, **2013**, *29*, 14274–14283.

97) Lee, S.; Xie, J; Chen, X. Peptide-based probes for targeted molecular imaging. *Biochemistry*, **2010**, *49*, 1364–1376.

98) Gao, Y.; Shi, J.; Yuan, D.; Xu, B. Imaging enzyme-triggered self-assembly of small molecules inside live cells. *Nature Communications,* **2012**, *3*, 1033-1040.

99) Epstein, C. J.; Anfinsen, C. B. The reversible reduction of disulfide bonds in trypsin and ribonuclease coupled to carboxymethyl cellulose. *J. Biol. Chem.* **1962**, *237*, 2175-2179.

100) Jiang, K.; Schadler, L. S.; Siegel, R. W.; Zhang, X.; Zhang, H.; Terrones, M. Protein immobilization on carbon nanotubes via a two-step process of diimide-activated amidation. *J. Mater. Chem.* **2004**, *14*, 37-39.

101) Forde, J.; Tully, E.; Vakurov, A.; Gibson, T. D.; Millner, P.; Ó'Fágáin, C. Chemical modification and immobilisation of laccase from *Trametes hirsuta* and from *Myceliophthora thermophila*. *Enzy. Microbial Technol.* **2010**, *46*, 430-437.

102) Ganguli, S.; Yoshimoto, K.; Tomita, S.; Sakuma, H.; Matsuoka, T.; Shiraki, K.; Nagasaki, Y. Regulation of lysozyme activity based on thermotolerant protein/smart polymer complex formation. *J. Am. Chem. Soc.* **2009**, *131*, 6549-6553.

103) Takahashi, H.; Sawada, S.-I.; Akiyoshi, K. Amphiphilic Polysaccharide Nanoballs: A new building block for nanogel biomedical engineering and artificial chaperones. *ACS Nano*, **2011**, *5*, 337-345.

104) Tao, Q.; Li, A.; Zhang, Z.; Ma, R.; Shi, L. Stabilization of multimeric enzymes against heat inactivation by chitosan-graft-poly(n-isopropylacrylamide) in confined spaces. *ACS Biomateri. Sci. Eng.* **2017**, *3*, 3141-3145.

105) Beierle, J. M.; Yoshimatsu, K.; Chou, B.; Mathews, M. A. A.; Lesel, B. K.; Shea, K. J. Polymer nanoparticle hydrogels with autonomous affinity switching for the protection of proteins from thermal stress. *Angew. Chem. Int. Ed.* **2014**, *53*, 9275-9279.

106) Bayne, L.; Ulijn, R. V.; Halling, P. J. Effect of pore size on the performance of immobilised enzymes. *Chem. Soc. Rev.* **2013**, *42*, 9000-9010.

107) Irim-Vladu, M. "Green" electronics: biodegradable and biocompatible materials and devices for sustainable future. *Chem. Soc. Rev.* **2014**, *43*, 588-610.

108) Cipriano, T.; Knotts, G.; Laudari, A.; Bianchi, R. C.; Alves, W. A.; Guha, S. Bioinspired Peptide nanostructures for organic field-effect transistors. *ACS Appl. Mater. Interfaces,* **2014**, *6*, 21408-21415.

109) Chang, J.-W.; Wang, C.-G.; Huang, C.-Y.; Tsai, T.-D.; Guo, T.-F.; Wen, T.-C. Chicken albumen dielectrics in organic field-effect transistors. *Adv. Mater.* **2011**, *23*, 4077-4081.

110) Xia, Y.; Yang, P.; Sun, Y.; Wu, Y.; Mayers, B.; Gates, B.; Yin, Y.; Kim, F.; Yan, H. One-dimensional nanostructures: synthesis, characterization, and applications. *Adv. Mater.* **2003**, *15*, 353-389.

111) Ahmed, S.; Pramanik, B.; Amba Sankar, K. N.; Srivastava, A.; Singha, N.; Dowari, P.; Srivastava, A.; Mohanta , K.; Debnath A.; Das D. Solvent assisted tuning of morphology of a peptide-perylenediimide conjugate: helical fibers to nano-rings and their differential semiconductivity. *Sci. Reports,* **2017,** *7*, 9485.

112) Ahmed, S.; Amba Sankar, K. N.; Pramanik, B.; Mohanta, K.; Das, D. Solvent directed morphogenesis and electrical properties of a peptide–perylenediimide conjugate. *Langmuir*, **2018**, *34*, 8355–8364.

113) Ghosh, S.; Pramanik, B.; Das, D. Self-aggregation of a naphthalene-monoimide amphiphile and its charge-transfer-complex driven morphogenesis in water. *ChemNanoMat*, **2018**, *4*, 867–873.

114) Babu, S. S.; Praveen, V. K.; Ajayaghosh, A. Functional π-Gelators and their applications. *Chem. Rev.* **2014**, *114*, 1973–2129.

115) Gong, H.-Y.; Rambo, B. M.; Lynch, V. M.; Keller, K. M.; Sessler, J. L. "Texas-Sized" molecular boxes: building blocks for the construction of anion-induced supramolecular species via self-assembly. *J. Am. Chem. Soc.* **2013**,*135*, 6330–6337.

116) de la Rica, R.; Matsui, H. Applications of peptide and protein based materials in bio-nanotechnology. *Chem. Soc. Rev.* **2010**, *39*, 3499–3509.

117) Singh, N.; Kumar, M.; Miravet, J. F.; Ulijn, R. V.; Escuder, B. Peptide-based molecular hydrogels as supramolecular protein mimics. *Chem. Eur. J.* **2017**, *23*, 981–993.

118) Wei, G.; Su, Z.; Reynolds, N. P.; Arosio, P.; Hamley, I. W.; Gazit, E.; Mezzenga, R. Self-assembling peptide and protein amyloids: from structure to tailored function in nanotechnology. *Chem. Soc. Rev.* **2017**, *46*, 4661–4708.

119) Gazit, E. Self-assembled peptide nanostructures: the design of molecular building blocks and their technological utilization. *Chem. Soc. Rev.* **2007**, *36*, 1263–1269.

120) Cui, H.; Webber, M. J.; Stupp, S. I. Self-assembly of peptide amphiphiles: From molecules to nanostructures to biomaterials. *Biopolymers*, **2010**, *94*, 1–18.

121) Fleming, S.; Ulijn, R. V. Design of nanostructures based on aromatic peptide amphiphiles. *Chem. Soc. Rev.* **2014**, *43*, 8150–8177.

122) Dasgupta, A. Exploring architectures at the nanoscale: the interplay between hydrophobic twin lipid chains and head groups of designer peptide amphiphiles in the self-assembly process and application. *Soft Matter*, **2016**, *12*, 4352–4360.

123) Schneider, J. P.; Pochan, D. J.; Ozbas, B.; Rajagopal, K.; Pakstis, L.; Kretsinger, J. Responsive hydrogels from the intramolecular folding and self-assembly of a designed peptide. *J. Am. Chem. Soc.* **2002**, *124*, 15030–15037.

124) Galler, K. M.; Aulisa, L.; Regan, K. R.; D'Souza, R. N.; Hartgerink, J. D. Self-assembling multidomain peptide hydrogels: designed susceptibility to enzymatic cleavage allows enhanced cell migration and spreading. *J. Am. Chem. Soc.* **2010**, *132*, 3217–3223.

125) Jiao, D.; Geng, J.; Loh, X. J.; Das, D.; Lee, T.-C.; Scherman, O. A. Supramolecular Peptide Amphiphile Vesicles through Host–Guest Complexation. *Angew. Chem.* **2012**, *124*, 9771–9775.

126) Goktas, M.; Cinar, G.; Orujalipoor, I.; Ide, S.; Tekinay, A. B.; Guler, M. O. Self-Assembled Peptide Amphiphile Nanofibers and PEG Composite Hydrogels as Tunable ECM Mimetic Microenvironment. *Biomacromolecules*, **2015**, *16*, 1247–1258.

127) Bhosale, S. V.; Jani, C. H.; Langford, S. J. Chemistry of naphthalene diimides. *Chem. Soc. Rev.* **2008**, *37*, 331–342.

128) Bhosale, R.; Misek, J.; Sakai, N.; Matile, S. Supramolecular n/pheterojunction photosystems with oriented multicolored antiparallel redox gradients (OMARG-SHJs). *Chem. Soc. Rev.* **2010**, *39*, 138–149.

129) Sakai, N.; Mareda, J.; Vauthey, E.; Matile, S. Core-substituted naphthalenediimides. *Chem. Commun.* **2010**, *46*, 4225–4237.

130) Che, Y.; Yang, X.; Zhang, Z.; Zuo, J.; Moore, J. S.; Zang, L. Ambient photodoping of p-type organic nanofibers: highly efficient photoswitching and electrical vapor sensing of amines. *Chem. Commun.* **2010**, *46*, 4127–4129.

131) Avinash, M. B.; Govindaraju, T. Amino acid derivatized arylenediimides: a versatile modular approach for functional molecular materials. *Adv. Mater.* **2012**, *24*, 3905–3922.

132) Tumiatti, V.; Milelli, A.; Minarini, A.; Micco, M.; Gasperi Campani, A.; Roncuzzi, L.; Baiocchi, D.; Marinello, J.; Capranico, G.; Zini, M.; Stefanelli, C.; Melchiorre, C. Design, synthesis, and biological evaluation of substituted naphthalene imides and diimides as anticancer agent. *J. Med. Chem.* **2009**, *52*, 7873–7877.

133) Kobaisi, M. A.; Bhosale, S. V.; Latham, K.; Raynor, A. M.; Bhosale, S. V. Functional naphthalene diimides: synthesis, properties, and applications. *Chem. Rev.* **2016**, *116*, 11685–11796.

134) Rhoden Smith, A.; Iverson, B. L. Threading polyintercalators with extremely slow dissociation rates and extended DNA binding sites. *J. Am. Chem. Soc.* **2013**, *135*, 12783–12789.

135) Zhan, X.; Facchetti, A.; Barlow, S.; Marks, T. J.; Ratner, M. A.; Wasielewski, M. R.; Marder, S. R. Rylene and related diimides for organic electronics. *Adv. Mater.* **2011**, *23*, 268–284.

136) Earmme, T.; Hwang, Y.-J.; Murari, N. M.; Subramaniyan, S.; Jenekhe, S. A. All-Polymer solar cells with 3.3% efficiency based on naphthalene diimide-selenophene copolymer acceptor. *J. Am. Chem. Soc.* **2013**, *135*, 14960–14963.

137) Rozanski, L. J.; Castaldelli, E.; Sam, F. L. M.; Mills, C. A.; Jean- Francois Demets, G.; Silva, S. R. P. Solution processed naphthalene diimide derivative as electron transport layers for enhanced brightness and efficient polymer light emitting diodes. *J. Mater. Chem. C* **2013**, *1*, 3347–3352.

138) Yan, H.; Chen, Z.; Zheng, Y.; Newman, C.; Quinn, J. R.; Dotz, F.; Kastler, M.; Facchetti, A. A high mobility electron-transporting polymer for printed transistors. *Nature*, **2009**, *457*, 679–686.

139) Lee, W.-Y.; Oh, J. H.; Suraru, S.-L.; Chen, W.-C.; Würthner, F.; Bao, Z. High-mobility air-stable solution-shear-processed n-channel organic transistors based on core-chlorinated naphthalene diimides. *Adv. Funct. Mater.* **2011**, *21*, 4173–4181.

140) Wurthner, F.; Stolte, M. Naphthalene and perylene diimides for organic transistors. *Chem. Commun.* **2011**, *47*, 5109–5115.

141) Ortiz, R. P.; Herrera, H.; Blanco, R.; Huang, H.; Facchetti, A.; Marks, T. J.; Zheng, Y.; Segura, J. L. Organic n-channel field-effect transistors based on arylene diimide-thiophene derivatives. *J. Am. Chem. Soc.* **2010**, *132*, 8440–8452.

142) Guo, X.; Kim, F. S.; Seger, M. J.; Jenekhe, S. A.; Watson, M. D. Naphthalene diimide-based polymer semiconductors: synthesis, structure–property correlations, and n-channel and ambipolar field-effect transistors. *Chem. Mater.* **2012**, *24*, 1434–1442.

143) Vadehra, G. S.; Wall, B. D.; Diegelmann, S. R.; Tovar, J. D. On-resin dimerization incorporates a diverse array of π-conjugated functionality within aqueous self-assembling peptide backbones. *Chem. Commun.* **2010**, *46*, 3947–3949.

144) Ryan, D. M.; Nilsson, B. L. Self-assembled amino acids and dipeptides as noncovalent hydrogels for tissue engineering. *Polym. Chem.* **2012**, *3*, 18–33.

145) Ma, M.; Kuang, Y.; Gao, Y.; Zhang, Y.; Gao, P.; Xu, B. Aromatic–aromatic interactions induce the self-assembly of pentapeptidic derivatives in water to form nanofibers and supramolecular hydrogels. *J. Am. Chem. Soc.* **2010**, *132*, 2719–2728.

146) Shao, H.; Nguyen, T.; Romano, N. C.; Modarelli, D. A.; Parquette, J. R. Self-assembly of 1-D n-type nanostructures based on naphthalene diimide-appended dipeptides. *J. Am. Chem. Soc.* **2009**, *131*, 16374–16376.

147) Berdugo, C.; Nalluri, S. K. M.; Javid, N.; Escuder, B.; Miravet, J. F.; Ulijn, R. V. Dynamic peptide library for the discovery of charge transfer hydrogels. *ACS Appl. Mater. Interfaces*, **2015**, *7*, 25946-25954.

148) Zhou, J.; Du, X.; Yamagata, N.; Xu, B. Enzyme-instructed self-assembly of small d-peptides as a multiple-step process for selectively killing cancer cells. *J. Am. Chem. Soc.* **2016**, *138*, 3813-3823.

149) Ghule, N. V.; Bhosale, R. S.; Kharat, K.; Puyad, A. L.; Bhosale, S. V.; Bhosale, S. V. A naphthalenediimide-based fluorescent sensor for detecting the pH within the rough endoplasmic reticulum of living cells. *ChemPlusChem*, **2015**, *80*, 485–489.

150) Kapoor, P.; Singh, H.; Gautam, A.; Chaudhary, K.; Kumar, R.; Raghava, G. P. S. TumorHoPe: A database of tumor homing peptides. *PLoS One*, **2012**, *7*, e35187.

151) Bellis, S. L. Advantages of RGD peptides for directing cell association with biomaterials. *Biomaterials*, **2011**, *32*, 4205–4210.

152) Röger, C.; Würthner, F. Core-tetrasubstituted naphthalene diimides: synthesis, optical properties, and redox characteristics. *J. Org. Chem.* **2007**, *72*, 8070–8075.

153) Kim, S.-h.; Shim, N.; Lee, H.; Moon, B. Synthesis of a perylene diimide-viologen dyad (PDI-2V) and its electrochromism in a layer-by-layer self-assembled multilayer film with PEDOT:PSS. *J. Mater. Chem.* **2012**, *22*, 13558–13563.

154) Mondal, J. H.; Ahmed, S.; Das, D. Physicochemical analysis of mixed micelles of a viologen surfactant: extended to water-in-oil (w/o) microemulsion and cucurbit[8]-uril-assisted vesicle formation. *Langmuir* **2014**, *30*, 8290–8299.

155) Satpathi, S.; Sengupta, A.; Hridya, V. M.; Gavvala, K.; Koninti, R. K.; Roy, B.; Hazra, P. A green solvent induced DNA package. *Sci. Rep.* **2015**, *5*, 9137.

156) Hu, J.; Kuang, W.; Deng, K.; Zou, W.; Huang, Y.; Wei, Z.; Faul, C. F. J. Self-assembled sugar-substituted perylene diimide nanostructures with homochirality and high gas sensitivity. *Adv. Funct. Mater.* **2012**, *22*, 4149–4158.

157) Jung, J. H.; Shinkai, S.; Shimizu, T. Spectral characterization of self-assemblies of aldopyranoside amphiphilic gelators: what is the essential structural difference between simple amphiphiles and bolaamphiphiles? *Chem. Eur. J.* **2002**, *8*, 2684–2690.

158) Pramanik, B.; Mondal, J. H.; Singha, N.; Ahmed, S.; Mohanty, J.; Das, D. A viologen–perylenediimide conjugate as an efficient base sensor with solvatochromic property. *ChemPhysChem*, **2017**, *18*, 245–252.

159) Basak, S.; Nandi, N.; Bhattacharyya, K.; Datta, A.; Banerjee, A. Fluorescence from an H-aggregated naphthalenediimide based peptide: photophysical and computational investigation of this rare phenomenon. *Phys. Chem. Chem. Phys.* **2015**, *17*, 30398–30403.

160) Würthner, F.; Kaiser, T. E.; Saha-Möller, C. R. J-Aggregates: from serendipitous discovery to supramolecular engineering of functional dye materials. *Angew. Chem. Int. Ed.* **2011**, *50*, 3376-3410.

161) Weissleder, R.; Nahrendorf, M.; Pittet, M. J. Imaging macrophages with nanoparticles. *Nat. Mater.* **2014**, *13*, 125–138.

162) Lunov, O.; Syrovets, T.; Loos, C.; Beil, J.; Delacher, M.; Tron, K.; Nienhaus, G. U.; Musyanovych, A.; Mailänder, V.; Landfester, K.; Simmet, T. Differential uptake of functionalized polystyrene nanoparticles by human macrophages and a monocytic cell line. *ACS Nano*, **2011**, *5*, 1657–1669.

163) Zhang, J.; Liu, X.; Neri, G.; Pinna, N. Nanostructured materials for room-temperature gas sensors. *Adv. Mater.* **2016**, *28*, 795-831.

164) a) Wagner, T.; Haffer, S.; Weinberger, C.; Klaus, D.; Tiemann, M. Mesoporous materials as gas sensors. *Chem. Soc. Rev.* **2013**, *42*, 4036-4053; b) Tiemann, M. Porous metal oxides as gas sensors. *Chem. Eur. J.* **2007**, *13*, 8376-8388.

165) Zhang, J.; Qin, Z.; Zeng, D.; Xie, C. Metal-oxide-semiconductor based gas sensors: screening, preparation, and integration. *Phys. Chem. Chem. Phys.* **2017**, *19*, 6313-6329.

166) a) Guidelines for drinking-water quality, Vol. 2nd, 2 ed., World Health Organization, Geneva, 1996; b) Rajan, S. T.; Malathi, N. Health hazards of xylene: a literature review. *J. Clin. Diagn. Res.* **2014**, *8*, 271–274.

167) a) Kim, T.-H.; Kwak, C.-H.; Lee, J.-H.; NiO/$NiWO_4$ composite yolk–shell spheres with nanoscale NiO outer layer for ultrasensitive and selective detection of subppm-level p-xylene. *ACS. Appl. Mater. Interfaces*, **2017**, *9*, 32034-32043; b) Kim, J.-H.; Jeong, H.-M.; Na, C. W.; Yoon, J.-W.; Abdel-Hady, F.; Wazzan, A. A.; Lee, J.-H. Highly selective and sensitive xylene sensors using

Cr_2O_3-$ZnCr_2O_4$ hetero-nanostructures prepared by galvanic replacement. *Sensors and Actuators B: Chemical*, **2016**, *235*, 498-506; c) Kim, B.-Y.; Ahn, J. H.; Yoon, J.-W.; Lee, C.-S.; Kang, Y. C.; Abdel-Hady, F.; Wazzan, A. A.; Lee, J.-H. Highly selective xylene sensor based on NiO/$NiMoO_4$ nanocomposite hierarchical spheres for indoor air monitoring. *ACS Appl. Mater. Interfaces*, **2016**, *8*, 34603-34611; d) Woo, H.-S.; Kwak, C.-H.; Chung, J.-H.; Lee, J.-H. Co-Doped branched ZnO nanowires for ultraselective and sensitive detection of xylene. *ACS Appl. Mater. Interfaces*, **2014**, *6*, 22553-22560; e) Im, J.; Sterner, E. S.; Swager, T. M. Integrated gas sensing system of SWCNT and cellulose polymer concentrator for benzene, toluene, and xylenes. *Sensors*, **2016**, *16*, 183; f) Xu, R.; Zhang, N.; Sun, L.; Chen, C.; Chen, Y.; Li, C.; Ruan, S. One-step synthesis and the enhanced xylene-sensing properties of Fe-doped MoO_3 nanobelts. *RSC Adv.* **2016**, *6*, 106364-106369; g) Akiyama, T.; Ishikawa, Y.; Hara, K. Xylene sensor using double-layered thin film and Ni-deposited porous alumina. *Sensors and Actuators B: Chemical*, **2013**, *181*, 348-352; h) Li, F.; Guo, S.; Shen, J.; Shen, L.; Sun, D.; Wang, B.; Chen, Y.; Ruan, S. Xylene gas sensor based on Au-loaded WO_3·H_2O nanocubes with enhanced sensing performance. *Sensors and Actuators B: Chemical*, **2017**, *238*, 364-373.

168) a) Hatchett, D. W.; Josowicz, M. Composites of intrinsically conducting polymers as sensing nanomaterials. *Chem. Rev.* **2008**, *108*, 746-769; b) Zhang, Y.; Kim, J. J.; Chen, D.; Tuller, H. L.; Rutledge, G. C. Electrospun polyaniline fibers as highly sensitive room temperature chemiresistive sensors for ammonia and nitrogen dioxide gases. *Adv. Funct. Mater.* **2014**, *24*, 4005-4014; c) Kong, J.; Franklin, N. R.; Zhou, C.; Chapline, M. G.; Peng, S.; Cho, K.; Dai, H. Nanotube molecular wires as chemical sensors. *Science*, **2000**, *287*, 622-625; d) Schedin, F.; Geim, A. K.; Morozov, S. V.; Hill, E. W.; Blake, P.; Katsnelson, M. I.; Novoselov, K. S. Detection of individual gas molecules adsorbed on graphene. *Nat. Mater.* **2007**, *6*, 652-655; e) Zou, D.; Zhao, W.; Cui, B.; Li, D.; Liu, D. Adsorption of gas molecules on a manganese phthalocyanine molecular device and its possibility as a gas sensor. *Phys. Chem. Chem. Phys.* **2018**, *20*, 2048-2056; f) Huang, L.; Wang, Z.; Zhu, X.; Chi, L. Electrical gas sensors based on structured organic ultra-thin films and nanocrystals on solid state substrates. *Nanoscale Horiz.* **2016**, *1*, 383-393.

169) a) Tayi, A. S.; Shveyd, A. K.; Sue, A. C. H.; Szarko, J. M.; Rolczynski, B. S.; Cao, D.; Kennedy, T. J.; Sarjeant, A. A.; Stern, C. L.; Paxton, W. F.; Wu, W.; Dey, S. K.; Fahrenbach, A. C.; Guest, J. R.; Mohseni, H.; Chen, L. X.; Wang, K. L.; Stoddart, J. F.; Stupp, S. I. Room-temperature ferroelectricity in supramolecular networks of charge-transfer complexes. *Nature*, **2012**, *488*, 485-489; b) Eakins, G. L.; Pandey, R.; Wojciechowski, J. P.; Zheng, H. Y.; Webb, J. E. A.; Valéry, C.; Thordarson, P.; Plank, N. O. V.; Gerrard, J. A.; Hodgkiss, J. M. Functional organic semiconductors assembled via natural aggregating peptides. *Adv. Funct. Mater.* **2015**, *25*, 5640-5649; c) Shang, X.; Song, I.; Ohtsu, H.; Tong, J.; Zhang, H.; Oh, J. H. Morphogenesis and optoelectronic

properties of supramolecular assemblies of chiral perylenediimides in a binary solvent system. *Sci. Rep.* **2017**, *7*, 5508.

170) Singha, N.; Gupta, P.; Pramanik, B.; Ahmed, S.; Dasgupta, A.; Ukil, A.; Das, D. Hydrogelation of a naphthalene diimide appended peptide amphiphile and its application in cell imaging and intracellular pH sensing. *Biomacromolecules*, **2017**, *18*, 3630-3641.

171) a) Bourlinos, A. B.; Stassinopoulos, A.; Anglos, D.; Zboril, R.; Karakassides, M.; Giannelis, E. P. Surface functionalized carbogenic quantum dots. Small 2008, 4, 455-458; b) Antonietti, M.; Oschatz, M. The concept of "Noble, Heteroatom-Doped Carbons," their directed synthesis by electronic band control of carbonization, and applications in catalysis and energy materials. *Adv. Mater.* **2018**, *30*, 1706836.

172) a) Barman, M. K.; Jana, B.; Bhattacharyya, S.; Patra, A. An efficient charge separation and photocurrent generation in the carbon dot–zinc oxide nanoparticle composite. *J. Phys. Chem. C*, **2014**, *118*, 20034-20041; b) Zhang, X.; Zhang, Y.; Wang, Y.; Kalytchuk, S.; Kershaw, S. V.; Wang, Y.; Wang, P.; Zhang, T.; Zhao, Y.; Zhang, H.; Cui, T.; Wang, Y.; Zhao, J.; Yu, W. W.; Rogach, A. L. Color-switchable electroluminescence of carbon dot light-emitting diodes. *ACS Nano*, **2013**, *7*, 11234-11241; c) Bhattacharjee, L.; Manoharan, R.; Mohanta, K.; Bhattacharjee, R. R. Conducting carbon quantum dots – a nascent nanomaterial. *J. Mater. Chem. A*, **2015**, *3*, 1580-1586.

173) a) Lin, Y.; Watson, K. A.; Fallbach, M. J.; Ghose, S.; Smith, J. G.; Delozier, D. M.; Cao, W.; Crooks, R. E.; Connell, J. W. Rapid, solventless, bulk preparation of metal nanoparticle-decorated carbon nanotubes. *ACS Nano*, **2009**, *3*, 871-884; b) Rigoni, F.; Drera, G.; Pagliara, S.; Goldoni, A.; Sangaletti, L. High sensitivity, moisture selective, ammonia gas sensors based on single-walled carbon nanotubes functionalized with indium tin oxide nanoparticles. *Carbon*, **2014**, *80*, 356-363; c) Leghrib, R.; Pavelko, R.; Felten, A.; Vasiliev, A.; Cané, C.; Gràcia, I.; Pireaux, J.-J.; Llobet, E. Gas sensors based on multiwall carbon nanotubes decorated with tin oxide nanoclusters. *Sensors and Actuators B: Chemical*, **2010**, *145*, 411-416; d) Septiani, N. L. W.; Yuliarto, B.; Nugraha; H. K. Dipojono, Multiwalled carbon nanotubes–zinc oxide nanocomposites as low temperature toluene gas sensor. *Appl. Phys. A*, **2017**, *123*, 166.

174) https://www.atsdr.cdc.gov/Toxprofiles/tp71-c2.pdf.

175) Sinha, M.; Mahapatra, R.; Mondal, B.; Maruyama, T.; Ghosh, R. Ultrafast and reversible gas-sensing properties of zno nanowire arrays grown by hydrothermal technique. *J. Phys. Chem. C*, **2016**, *120*, 3019-3025.

176) http://chemeng.iisc.ac.in/kumaran/courses/chap2.pdf.

177) Stoddart, A. Hydrogels: a less than swell time. *Nat. Rev. Mater.* **2017**, *2*, 17018.

178) Zhai, D., Zhao, L., Gao, J., Xu, C. Effect of temperature on the diffusion mechanism of xylene isomers in a FAU zeolite: a molecular dynamics study. *Phys. Chem. Chem. Phys.* **2012**, *14*, 7296-7303.

179) Goodrich, C. P.; Brenner, M. P.; Ribbeck, K. Enhanced diffusion by binding to the crosslinks of a polymer gel. *Nat. Commun.* **2018**, *9*, 4348.

180) Estroff, L. A.; Hamilton, A. D. Water gelation by small organic molecules. *Chem. Rev*, **2004**, *104*, 1201-1218.

181) Chu, L.-Y.; Xie, E.; Ju, X.-J.; Wang, W. Smart hydrogel functional materials. (Springer, **2013**).

182) Draper, E. R. & Adams, D. J. Low-molecular-weight gels: the state of the art. *Chem* **2017**, *3*, 390-410.

183) Hirst, A. R. et al. Low-molecular weight gelators: elucidating the principles of gelation based on gelator solubility and a cooperative self-assembly model. *J. Am. Chem. Soc.* **2018**, *130*, 9113-9121.

184) Raeburn, J.; Adams, D. J. Multicomponent low molecular weight gelators. *Chem. Commun.* **2015**, *51*, 5170-5180.

185) Seow, W. Y.; Hauser, C. A. E. Short to ultrashort peptide hydrogels for biomedical uses. *Materials Today* **2014**, *17*, 381-388.

186) Seliktar, D. Designing cell-compatible hydrogels for biomedical applications. *Science* **2012**, *336*, 1124-1128.

187) Hamley, I. W. Small bioactive peptides for biomaterials design and therapeutics. *Chem. Rev.* **2017**, *117*, 14015-14041.

188) Hirst, A. R.; Escuder, B.; Miravet, J. F.; Smith, D. K. High-Tech applications of self-assembling supramolecular nanostructured gel-phase materials: from regenerative medicine to electronic devices. *Angew. Chem. Int. Ed.* **2008**, *47*, 8002-8018.

189) Liyanage, W.; Vats, K.; Rajbhandary, A.; Benoit, D. S. W.; Nilsson, B. L. Multicomponent dipeptide hydrogels as extracellular matrix-mimetic scaffolds for cell culture applications. *Chem. Commun.* **2015**, *51*, 11260-11263.

190) Yan, C.; Pochan, D. J. Rheological properties of peptide-based hydrogels for biomedical and other applications. *Chem. Soc. Rev.* **2010**, *39*, 3528-3540.

191) Ehrick, J. D. et al. Genetically engineered protein in hydrogels tailors stimuli-responsive characteristics. *Nat. Mater.* **2005**, *4*, 298.

192) Hoche, J. et al. The mechanism of excimer formation: an experimental and theoretical study on the pyrene dimer. *Phys. Chem. Chem. Phys.* **2017**, *19*, 25002-25015.

193) Koskinen, P.; Mäkinen, V. Density-functional tight-binding for beginners. *Comput. Mater. Sci.* **2009**, *47*, 237-253.

194) Goldman, N.; Srinivasan, S. G.; Hamel, S.; Fried, L. E.; Gaus, M.; Elstner, M. Determination of a density functional tight binding model with an extended basis set and three-body repulsion for carbon under extreme pressures and temperatures. *J. Phys. Chem. C*, **2013**, *117*, 7885-7894.

195) (a) Vijay, D.; Sastry, G. N. The cooperativity of cation–π and π–π interactions. *Chem. Phys. Lett.* **2010**, *485*, 235-242. F. (b) Eisenhaber, P. Lijnzaad, P. Argos, C. Sander, M. Scharf, The double cubic lattice method: efficient approaches to numerical integration of surface area and volume and to dot surface contouring of molecular assemblies. *J. Comput. Chem.* **1995**, *16*, 273-284.

196) (a) Debnath, A.; Ayappa, K. G.; Kumaran, V.; Maiti, P. K. The influence of bilayer composition on the gel to liquid crystalline transition. *J. Phys. Chem. B*, **2009**, *113*, 10660-10668; (b) Kanduč, M.; Schlaich, A.; Schneck, E.; Netz, R. R. Water-Mediated interactions between hydrophilic and hydrophobic surfaces. *Langmuir*, **2016**, *32*, 8767-8782; (c) Baoukina, S.; Rozmanov, D.; Tieleman, D. P. Composition fluctuations in lipid bilayers. *Biophys. J.* **2017**, *113*, 2750-2761; (d) Berkowitz, M. L.; Bostick, D. L.; Pandit, S. Aqueous solutions next to phospholipid membrane surfaces: insights from simulations. *Chem. Rev.* **2006**, *106*, 1527-1539.

197) (a) Rey, R.; Møller, K. B.; Hynes, J. T. Hydrogen bond dynamics in water and ultrafast infrared spectroscopy. *J. Phys. Chem. A*, **2002**, *106*, 11993-11996; (b) Lawrence, C. P.; Skinner, J. L. Vibrational spectroscopy of HOD in liquid D_2O. III. Spectral diffusion, and hydrogen-bonding and rotational dynamics. *J. Chem. Phys.* **2003**, *118*, 264-272; (c) Eaves, J. D.; Loparo, J. J.; Fecko, C. J.; Roberts, S. T.; Tokmakoff, A.; Geissler, P. L. Hydrogen bonds in liquid water are broken only fleetingly. *Proc. Natl. Acad. Sci. U. S. A.* **2005**, *102*, 13019-13022; (d) Luzar, A.; Chandler, D. Hydrogen-bond kinetics in liquid water. *Nature*, **1996**, *379*, 55-57.

198) (a) Luzar, A.; Chandler, D. Effect of environment on hydrogen bond dynamics in liquid water. *Phys. Rev. Lett.* **1996**, *76*, 928-931; (b) Chandra, A. Effects of ion atmosphere on hydrogen-bond dynamics in aqueous electrolyte solutions. *Phys. Rev. Lett.* **2000**, *85*, 768-771; (c) Balasubramanian, S.; Pal, S.; Bagchi, B. Hydrogen-Bond dynamics near a micellar surface: origin of the universal slow relaxation at complex aqueous interfaces. *Phys. Rev. Lett.* **2002**, *89*, 115505.

199) Srivastava, A.; Debnath, A. Hydration dynamics of a lipid membrane: Hydrogen bond networks and lipid-lipid associations. *J. Chem. Phys.* **2018**, *148*, 094901.

200) Chapman, R.; Stenzel, M. H. All wrapped up: stabilization of enzymes within single enzyme nanoparticles. *J. Am. Chem. Soc.* **2019**, *141*, 2754−2769.

201) Borrelli, G. M.; Trono, D. Recombinant lipases and phospholipases and their use as biocatalysts for industrial applications, *Int. J. Mol. Sci.* **2015**, *16*, 20774–20840.

202) Shahrestani, H.; Taheri-Kafrani, A.; Soozanipour, A.; Tavakoli, O. Enzymatic clarification of fruit juices using xylanase immobilized on 1,3,5-triazine-functionalized silica-encapsulated magnetic nanoparticles, *Biochem. Eng. J.* **2016**,*109*, 51–58.

203) Varanasi, A.; Obendorf, S. K.; Pedersen, L. S.; Mejldal, R. Lipid distribution on textiles in relation to washing with lipases, *J. Surfactants Deterg.* **2001**, *4*, 135–146.

204) Ozyilmaz, G.; Gezer, E. Production of aroma esters by immobilized *Candida rugosa* and *Porcine pancreatic* lipase into calcium alginate gel. *Journal of Molecular Catalysis B: Enzymatic*, **2010**, *64*,140–145.

205) Hong, S. G.; Kim, H. S.; Kim, J. Highly stabilized lipase in polyaniline nanofibers for surfactant-mediated esterification of ibuprofen, *Langmuir*, **2014**, *30*, 911–915.

206) Li, W.; Wu, H.; Liu, B.; Hou, X.; Wan, D.; Lou, W.; Zhao, J. Highly efficient and regioselective synthesis of dihydromyricetin esters by immobilized lipase, *J. Biotechnol.* **2015**, *199*, 31–37.

207) Khan, N. R.; Rathod, V. K. Enzyme catalyzed synthesis of cosmetic esters and its intensification: a review, *Process Biochem.* **2015**, *50*, 1793–1806.

208) Manzano, M. F. G.; Igarzabal, C. I. A. Immobilization of lipase from *Candida rugosa* on synthesized hydrogel for hydrolysis reaction. *Journal of Molecular Catalysis B: Enzymatic*, **2011**, *72*, 28– 35.

209) Hu, Y.; Yang, J.; Jia, R.; Ding, Y.; Li, S.; Huang, H. Chemical modification with functionalized ionic liquids: a novel method to improve the enzymatic properties of *Candida rugosa* lipase. *Bioprocess Biosyst Eng.* **2014**, *37*, 1617–1626.

210) Somkuti, J.; Mártonfalvi, Z.; Kellermayer, M. S.; Smeller, L. Different pressure–temperature behavior of the structured and unstructured regions of titin, *BBA Proteins Proteomics*, **2013**, *1834*, 112–118.

211) Chen, G.; Wang, L.; Miao, M.; Jia, C.; Feng, B. Coupled effects of salt and pressure on catalytic ability of *Rhizopus chinensis* lipase, *J. Sci. Food Agric.* **2017**, *97*, 5381–5387.

212) Boutureira, O.; Bernardes, G. J. L. Advances in Chemical Protein Modification. *Chem. Rev.* **2015**, *115*, 2174–2195.

213) Morawski, B.; Quan, S.; Arnold, F. H. Functional expression and stabilization of horseradish peroxidase by directed evolution in Saccharomyces cerevisiae. *Biotechnol. Bioeng.* **2001**, *76,* 99–107.

214) Salazar, O.; Cirino, P. C.; Arnold, F. H. Thermostabilization of a cytochrome P450 peroxygenase. *ChemBioChem*, **2003**, *4*, 891–893.

215) Li, Y.; Drummond, D. A.; Sawayama, A. M.; Snow, C. D.; Bloom, J. D.; Arnold, F. H. A diverse family of thermostable cytochrome P450s created by recombination of stabilizing fragments. *Nat. Biotechnol.* **2007**, *25*, 1051–1056.

216) Sun, L.; Petrounia, I. P.; Yagasaki, M.; Bandara, G.; Arnold, F. H. Expression and stabilization of galactose oxidase in Escherichia coli by directed evolution. *Protein Eng., Des. Sel.* **2001**, *14*, 699–704.

217) Arnold, F. H. Directed Evolution: Bringing New Chemistry to Life. *Angew. Chem., Int. Ed.* **2018**, *57*, 4143–4148.

218) Kan, S. B. J.; Lewis, R. D.; Chen, K.; Arnold, F. H. Directed evolution of cytochrome c for carbon-silicon bond formation: Bringing silicon to life. *Science*, **2016**, *354*, 1048–1051.

219) Hammer, S. C.; Kubik, G.; Watkins, E.; Huang, S.; Minges, H.; Arnold, F. H. Anti-Markovnikov alkene oxidation by metal-oxo–mediated enzyme catalysis. *Science*, **2017**, *358*, 215–218.

220) Lancaster, L.; Abdallah, W.; Banta, S.; Wheeldon, I. Engineering enzyme microenvironments for enhanced biocatalysis. *Chem. Soc. Rev.* **2018**, *47*, 5177–5186.

221) Spicer, C. D.; Pashuck, E. T.; Stevens, M. M., Achieving controlled biomolecule–biomaterial conjugation. *Chem. Rev.* **2018**, *118*, 7702-7743.

222) Hoarau, M.; Badieyan, S.; Marsh, E. N. G. Immobilized enzymes: understanding enzyme–surface interactions at the molecular level. *Org. Biomol. Chem.* **2017**, *15*, 9539–9551.

223) Mohamad, N. R.; Marzuki, N. H. C.; Buang, N. A.; Huyop, F.; Wahab, R. A. An overview of technologies for immobilization of enzymes and surface analysis techniques for immobilized enzymes. *Biotechnol. Biotechnol. Equip.* **2015**, *29*, 205–220.

224) Hanefeld, U.; Gardossi, L.; Magner, E. Understanding enzyme immobilisation. *Chem. Soc. Rev.* **2009**, *38*, 453–468.

225) Stepankova, V.; Bidmanova, S.; Koudelakova, T.; Prokop, Z.; Chaloupkova, R.; Damborsky, J. Strategies for stabilization of enzymes in organic solvents. *ACS Catal.* **2013**, *3*, 2823–2836.

226) Sheldon, R. A. Cross-Linked enzyme aggregates as industrial biocatalysts. *Org. Process Res. Dev.* **2011**, *15*, 213–223.

227) Sheldon, R. A.; van Pelt, S. Enzyme immobilisation in biocatalysis: why, what and how. *Chem. Soc. Rev.* **2013**, *42*, 6223–6235.

228) Silva, C.; Martins, M.; Jing, S.; Fu, J.; Cavaco-Paulo, A. Practical insights on enzyme stabilization. *Crit. Rev. Biotechnol.* **2018**, *38*, 335–350.

229) Jegan Roy, J.; Emilia Abraham, T. Strategies in making cross-linked enzyme crystals. *Chem. Rev.* **2004**, *104*, 3705–3722.

230) Adlercreutz, P. Immobilisation and application of lipases in organic media. *Chem. Soc. Rev.* **2013**, *42*, 6406–6436.

231) Walde, P.; Ichikawa, S. Enzymes inside lipid vesicles: preparation, reactivity and applications. *Biomol. Eng.* **2001**, *18*,143–177.

232) Mazur, F.; Bally, M.; Stadler, B.; Chandrawati, R. Liposomes and lipid bilayers in biosensors. *Adv. Colloid Interface Sci.* **2017**, *249*, 88–99.

233) Renggli, K.; Baumann, P.; Langowska, K.; Onaca, O.; Bruns, N.; Meier, W. Selective and responsive nanoreactors. *Adv. Funct. Mater.* **2011**, *21*, 1241–1259.

234) Küchler, A.; Yoshimoto, M.; Luginbühl, S.; Mavelli, F.; Walde, P. Enzymatic reactions in confined environments. *Nat. Nanotechnol.* **2016**, *11*, 409.

235) Cao, L. Carrier-bound Immobilized Enzymes: Principles, *Application and Design*. **2006**, *1–52*, Wiley-VCH Verlag GmbH & Co. KGaA.

236) Li, Z.; Mintzer, E.; Bittman, R. First synthesis of free Cholesterol-BODIPY conjugates. *J. Org. Chem.* **2006**, *71*, 1718-1721.

237) Das, D.; Tnimov, Z.; Ngyen, U.T.T.; Abankwa, D.; Lo, H.; Wu, Y.; Govindaraju, T.; Goody, R.S.; Waldmann, H.; Alexandrov, K. Flexible and general synthesis of functionalized phosphoisoprenoids for the study of prenylation in vivo and in vitro. *ChemBioChem*, **2012**, *13*, 674-683.

भारतीय प्रौद्योगिकी संस्थान गुवाहाटी
Indian Institute of Technology Guwahati

Publications

1. Nilotpal Singha, Samya Neogi, Bapan Pramanik, Antara Dasgupta, Ranajit Ghosh and Debapratim Das, Ultra-fast, Highly Sensitive and Selective Xylene Sensor using Peptide-Xerogel/Carbon Nano-Particle Composite. (Under revision)
2. Nilotpal Singha, Bapan Pramanik, Arpita Srivastava, Sahnawaz Ahmed, Payel Dowari, Basab Kanti Das, Ananya Debnath, Debapratim Das, A water insoluble supramolecular hydrogel with unique confinement property. (Under revision)
3. Bapan Pramanik, Nilotpal Singha, Debapratim Das, Sol, Gel, and Paper Based Detection of Picric Acid at Femtogram Level by a Short Peptide Gelator. ACS Appl. Polym. Mater. 2019, DOI: 10.1021/acsapm.9b00071.
4. Peptide-based water insoluble molecular hydrogel. Nilotpal Singha, and Debapratim Das, Indian patent application no. 201831035121. Kolkata, India: Indian patent office.
5. Bapan Pramanik, Sahnawaz Ahmed, Nilotpal Singha, Basab Kanti Das, Payel Dowari, and Debapratim Das, Unorthodox Combination of Cation- π and Charge-Transfer Interactions within a Donor Acceptor Pair. Langmuir 2019, 35, 478-488.
6. Payel Dowari, Shriya Saha, Bapan Pramanik, Sahnawaz Ahmed, Nilotpal Singha, Anindita Ukil, Debapratim Das, Multiple Cross-Linking of a Small Peptide to Form Size Tuneable Bio-Polymer with Efficient Cell Adhesion and Proliferation Property. Biomacromolecules, 2018, 19, 3994-4002.
7. Nilotpal Singha, Purnima Gupta, Bapan Pramanik, Sahnawaz Ahmed, Antara Dasgupta, Anindita Ukil, Debapratim Das, Hydrogelation of a Naphthalene Diimide Appended Peptide Amphiphile and its Application in Cell-Imaging and Intracellular pH Sensing. Biomacromolecules 2017, 18, 3630-3641. (Invited article for the special issue on Organized Peptidic Nanostructures as Functional Materials)
8. Bapan Pramanik, Sahnawaz Ahmed, Rupam Roy, Basab Kanti Das, Nilotpal Singha, Debapratim Das, A DNA-NDI hybrid to efficiently detect histone in parts per trillion (ppt) level. Chemistry Select 2017, 2, 8911 - 8916.
9. Bapan Pramanik, Sahnawaz Ahmed, Nilotpal Singha, Debapratim Das, Self-Assembly Assisted Tandem Sensing of Pd^{2+} and CN^- by a Perylenediimide-Peptide Conjugate, Chemistry Select 2017, 2, 10061-10066.
10. Sahnawaz Ahmed, Bapan Pramanik, K. N. Amba Sankar, Abhinav Srivastava, Nilotpal Singha, Payel Dowari, Arpita Srivastava, Kallol Mohanta, Ananya Debnath, Debapratim Das, Solvent Assisted Tuning of Morphology of a Peptide-Perylenediimide Conjugate: Helical Fibers to Nano-Rings and their Differential Semiconductivity. Sci. Rep. 2017, 7, 9485.

11.Bapan Pramanik, Julfikar Hassan Mondal, Nilotpal Singha, Sahnawaz Ahmed, Jyotirmayee Mohanty, Debapratim Das, A Viologen-Perylenediimide Conjugate as an Efficient Base Sensor with Solvochromic Property. ChemPhysChem 2017, 18, 245-252.

12.Sahnawaz Ahmed, Nilotpal Singha, Bapan Pramanik, Julfikar Hassan Mondal, Debapratim Das, Redox Controlled Reversible Transformation of a Supramolecular Alternating Copolymer to Radical Cation Containing Homo-polymer. Polymer Chemistry 2016, 7, 4393-4401.

भारतीय प्रौद्योगिकी संस्थान गुवाहाटी
Indian Institute of Technology Guwahati